ELECTRIFICATION BY LIQUID DIELECTRIC FLOW

by

STEVEN MARC GASWORTH

S.B., Massachusetts Institute of Technology
(1976)

S.M., Massachusetts Institute of Technology
(1981)

SUBMITTED IN PARTIAL FULFILLMENT
OF THE REQUIREMENTS FOR THE
DEGREE OF

DOCTOR OF PHILOSOPHY

at the

MASSACHUSETTS INSTITUTE OF TECHNOLOGY

(February, 1985)

Signature of Author______________________________
Department of Electrical Engineering and Computer Science
January 31, 1985

Certified by______________________________
James R. Melcher
Thesis Supervisor

Certified by______________________________
Markus Zahn
Thesis Supervisor

Accepted by______________________________
Arthur C. Smith
Chairman, Departmental Committee on Graduate Students

ELECTRIFICATION BY LIQUID DIELECTRIC FLOW

by

STEVEN MARC GASWORTH

Submitted to the Department of Electrical Engineering and
Computer Science on January 31, 1985 in partial fulfillment of
the requirements for the Degree of Doctor of Philosophy

ABSTRACT

The charging of insulating surfaces by the flow of semi-insulating liquids is investigated with a view towards identifying ways to forestall insulation failure in liquid-cooled power distribution equipment. Both fully developed and fully mixed turbulent flows are considered, the former as a model for the flows in insulating tubes, the latter approximating conditions in certain practical elements such as pumps and expansion regions. Models are developed for the space-time evolution of charge and electrical stress that emphasize the interplay between electrokinetic charge generation, convective transport, ion diffusion and self-precipitation, and conduction driven by the generated fields themselves.

Experiments are designed to allow measurement of the currents influent to the insulating tube or expansion region, and either the accumulating surface charge or the generated electric field. Apart from the imposed flow conditions, the liquid conductivity is controlled by a commercial antistatic agent, while the external configuration of conductors is prescribed with an awareness of the contribution of external image charges to the generated fields. Results indicate that significant electrical stresses stem from the transfer of a net charge to the flow upstream of the insulating element, and migration of the entrained ions in a space charge field that is predominantly normal to the the insulating surface. Leverage over the flow-induced stresses is afforded by the external conductor configuration, control of bulk and surface conductivities, and control of the influent convection current with a properly designed expansion region inserted just upstream of the insulating element.

Physicochemical features of the liquid-insulating solid interface are probed in two supplementary experiments that make use of a multi-phase helical winding around a section of an insulating tube. In the first experiment the flow is imposed and half of the phases are excited with a sinusoidal potential. Convective displacement of the resulting standing-wave perturbation in the entrained volume charge density is detected as an imbalance in the currents carrying perturbation image charge to two of the unexcited phases. The response is interpreted in terms of the undisturbed convection current, the surface conductivity, and the conductivity gradient at the interface. In the second experiment, the flow is induced by a traveling-wave excitation of the winding with the objective of investigating the charge injection process at the same interface.

Thesis Supervisor: James R. Melcher
Title: Stratton Professor of Electrical Engineering and Physics
Thesis Supervisor: Markus Zahn
Title: Associate Professor of Electrical Engineering

ACKNOWLEDGEMENTS

With the fresh perspective that comes from extending my contacts outside of the Continuum Electromechanics Lab, I am struck by the uniqueness and depth of the education I've received, all the more so because so much of it has been shaped by one man, Professor James Melcher. To his credit as an educator, the form of this thesis is as much a product of the careful grounding in fundamentals he has provided over the years, beginning long before this project commenced, as of discussions specific to the thesis.

The balance of the thesis committee included Professors Thomas Lee, Ain Sonin and Markus Zahn. Their participation in discussions and encouragement are deeply appreciated. Professor Sonin's influence was especially strong, through both his insightful comments on the present work, and his own previous publications in the field.

Through MIT's undergraduate research opportunities program, several students participated in various aspects of the project. Of these, three will find their efforts represented here: Yana Kisler, who assisted with the streaming current measurements of Sec. 2.2.3, Steven Lin, who collected essentially all of the traveling-wave pumping data of Sec. B.2, and Lim Nguyen, who obtained the conductivity data of Fig. 3.6.

Despite a remarkable range of projects in the Continuum Electromechanics Lab there is a sense of unity, traceable to the attention paid to fundamental aspects and to a recognition that all of these projects impact on our standard of living. That such a sense is maintained in an academic setting that characteristically emphasizes individual efforts is a credit to the students and faculty of the lab. Only it remains a mystery how our resident computer expert, Eliot Frank, finds enough time for his own thesis; his efforts have greatly simplified the task of preparing documents like the present one.

There can be no understudy for the role played by family and friends. Joel Adler and my father, Kenneth, are two who took the initiative when they saw ways to help.

The stresses that accompany a thesis are shared by the spouse of a married student, and Debbie somehow bore her share patiently while doing so much to lessen mine with her advice and encouragement. The result is as much a joint effort as my department will allow me to admit before revising the name on the diploma.

This work was sponsored by the Electric Power Research Institute, under contract no. RP1536-7.

TABLE OF CONTENTS

LIST OF FIGURES

figure page

LIST OF TABLES

Chapter 1

INTRODUCTION

1.1 Engineering Motivation

A fundamental understanding of the electrification phenomena resulting from the flow of semi-insulating liquids is essential to the safe operation of liquid-cooled power distribution equipment. In transformers and high-voltage direct-current (HVDC) substations these phenomena are manifested as a build-up of electric fields much greater than those allowed for by design, with the prospect of physical damage or fire originating in electrical discharge. What implicates the cooling system is the observation that the field build-up is initiated by the flow of the liquid coolant, whether or not the equipment is energized. Without control over such phenomena, flow rates and hence cooling capacity must be limited, and equipment power ratings will be compromised to a degree that must be determined empirically on a case by case basis.

In transformers, flow-induced fields stress the oil ducts whose oil-impregnated paper surfaces tend to collect a net charge. Experiments with full scale systems (1) typically record the dependence of signals from charge density probes immersed in the oil, and of currents flowing from terminals, on such parameters as oil temperature and flow rate. Even if such in situ measurements had clear interpretations the quantitative and qualitative differences among reported measurements emphasize that their applicabilty is limited to the system at hand. One expedient recognizes the oil as the common element that is most readily replaced, and seeks to correlate flow-induced failure with, and appropriately modify, some oil property. A suggested (2) property is the so-called "charging tendency," which measures the charge separated as a sample volume flows through a paper filter, and which is found to be sensitive to handling and trace chemicals. While it would be a welcome development to find that an identifiable range of charging tendency presages failure in existing units, and that this property can be controlled, there would remain no rational basis for anticipating safe operation of planned units when increased heat transfer capacity is pursued.

The present investigation concerns the electric field build-up initiated by the fully-developed turbulent flow of semi-insulating liquids through insulating tubes. This configuration is of practical interest whenever the coolant must be transferred between metallic elements, such as heat sinks, that are constrained to different potentials. The flow-induced field stresses the wall of the tube, and failure of the insulation may take the form of a pin hole through the wall that allows an exchange between the liquid coolant and the gas that surrounds the tube.

Several factors intensify these problems despite the vast experience with related electrification phenomena acquired in other industrial contexts, notably petroleum processing (3,4) and fueling operations (5). First, because of pressures to use generated power more efficiently, there has been a trend towards locating power substations closer to loads. For such installations to be acceptable near populated areas, they must be increasingly compact, fire-resistant, and benign to the environment, with significant demands upon the capacity and integrity of the cooling system a direct result. Second, because of the sensitivity of electrification phenomena to materials and flow conditions, empirical guidelines evolved from a review of superficially related experiences will be of limited value for purposes of design.

Third, the remedial measures that have been explored in other contexts are not immediately transferable to the high voltage environment. Active systems (6), employing a charge injector and charge density monitor in a feedback arrangement to eliminate any net charge from the flowing liquid, are too cumbersome for compact high voltage equipment. Like the active systems, passive charge injectors (7) are intended to protect flow elements further downstream. However, these schemes require the field generated at grounded points inserted in the flow to exceed a threshold value that is likely to drift as contaminants collect on the points. Both the dielectric strength of the insulation and the heat transfer characteristics of the metallic surfaces in contact with the liquid are also likely to be sensitive to residues. Thus, the antistatic agents (8,9) successfully added to petroleum products and jet fuels must be applied conservatively in high voltage systems until their side effects are fully appreciated. Bonding (10), which aims to provide a controlled charge leakage path by constraining the potential of a conductor in contact with the insulating tube along its length, defeats the insulation function of the tube. Outwardly the simplest approach to neutralizing a liquid stream is the relaxation volume, whose efficiency increases with volume as discussed in Chapter 4 below. The essential point is that without an understanding of the electrification process there is no basis for limiting this volume other than the contraints imposed by the available space.

Traditionally, efforts to maintain safe operating conditions in high voltage equipment have centered on the identification of mechanisms of electrical breakdown and factors which control dielectric strength. Such efforts support designs consistent with applied potentials, but their objective will not be achieved unless flow-induced electrical stresses can be anticipated and controlled as well. While helping to establish a basic understanding of the flow-induced stresses in a specific context, an objective of the present research is to encourage informed design that confronts the electrification problem as an integral step towards meeting heat transfer specifications.

1.2 Flow-Induced Electric Field Generation

The source of the electric field that is not attributable to applied potentials is a distribution of net charge that develops when the liquid flow separates charges of opposite sign. Petroleum processing and aircraft fueling are examples in which the liquid carries a net charge into a partially filled tank. There the absence of a significant mean flow allows the charge to accumulate in the liquid volume and generate an electric field in the vapor-filled space above the liquid (11,12,13). It is typical of these works to neglect the surface charge accumulation at the liquid-vapor interface. However, where the mean flow is significant, as in the insulating tube, it is a surface charge distribution that makes the dominant contribution to the generated field. Thus a specific objective here is a description of the evolution, in space and time, of the surface charge on the insulating tube and of the associated electrical stress.

Whether the accumulating charge is a surface or volume density, and despite differences in materials and configurations, the generation of electric fields by mechanical action can always be analyzed in terms of four basic processes: charge generation, transport, accumulation, and leakage. A simple context for illustrating these processes is the Van de Graaff generator (14) shown in Fig. 1.1a. A net charge is generated at the bottom and imparted to the moving belt which transports the charge to the metal dome at the top. Charge accumulates on the dome and generates an electric field that by design is predominantly outside the region occupied by the belt. A resistive divider running the length of the belt both supports a leakage current from the dome, and ensures that the field associated with the charge in transit will not oppose the transport process. If the dielectric strength of the medium surrounding the dome permits, the maximum generated field is that which drives a leakage current from the dome equal to the convection current carried upward by the belt.

That the Van de Graaff generator and the liquid circulation system have much in common is emphasized most graphically by Boumans (15) who constructed a high voltage generator with the liquid playing the role of the belt, and a closed metal sphere playing that of the dome. What makes the Van de Graaff generator a helpful, though less literal, analogue for

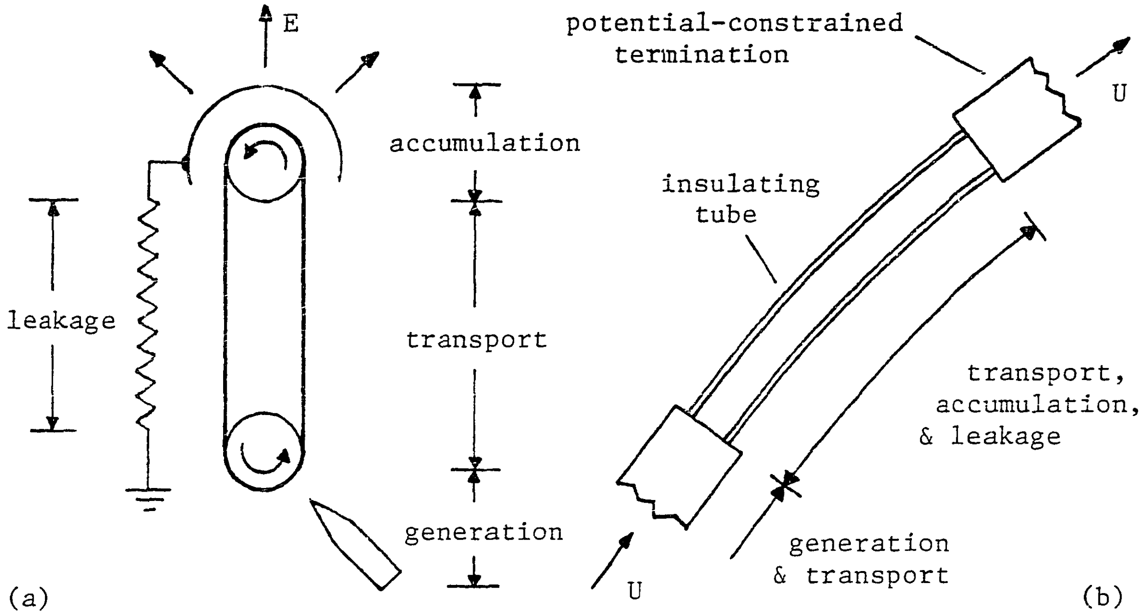

Fig. 1.1 Basic processes in (a) Van De Graaff generator, where various processes are identifiable with physically distinct regions, and (b) section of insulating tube, where processes overlap.

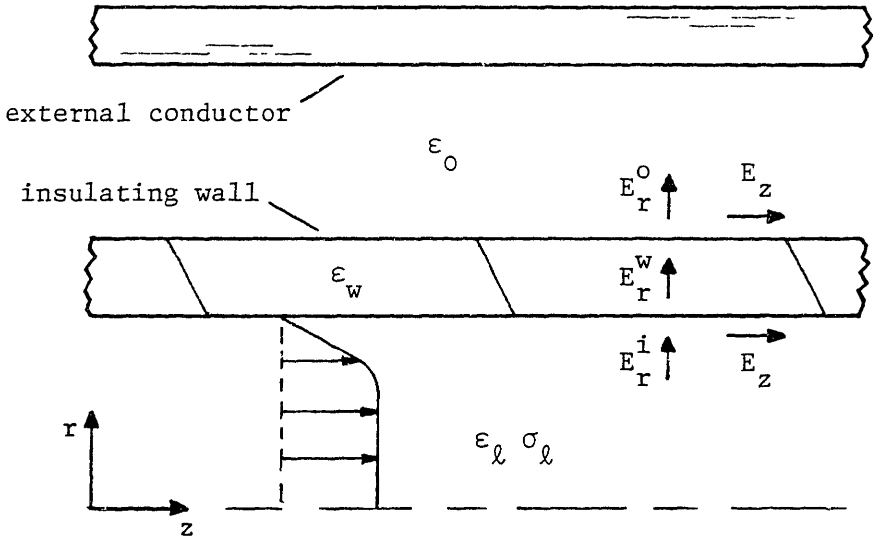

Fig. 1.2 Definition of electric field components at the insulating tube wall. Turbulent velocity profile is shown.

present purposes is the clear spatial separation of the four basic processes (Fig. 1.1a). The same processes underlie the charging of the insulating tube, but here they cannot be identified with physically distinct regions (Fig. 1.1b). It is to contend with this complication that two modes of charging, distinguished by the origin of the collected charge, are defined. In the <u>external</u> mode the collected charge originates in flow elements situated upstream of the insulating tube. In the <u>internal</u> mode, which may operate simultaneously, the insulating tube itself supplies a net charge to the flow while retaining the counter charge which generates an electrical stress.

Much as in the Van de Graaff generator, the external mode is characterized by charge generation and accumulation in separate regions. However, charge generation and transport occur in a common region because both are intimately linked to the mean liquid motion. The flow that shears the diffuse part of the charge double layer that is characteristic of virtually all liquid-solid interfaces also entrains the double layer charge and gives rise to a convection or streaming current. This current can be continuous if there is a mechanism for replacing the charge that is swept away by the flow. Thus, charge generation is likely to be most significant where the flow is bounded by a potential-constrained metallic surface that supports a charge transfer reaction.

Charge transport and accumulation overlap as well, this time in the insulating tube where the potential is free to rise. In the external mode, liquid enters the tube carrying a net charge that, in accordance with Gauss' law, sets up a radial electric field at the inner surface of the tube wall, denoted E_r^i in Fig. 1.2. The entrained charge migrates in its own space charge field to the inner surface of the wall where it accumulates as a surface density. The internal mode is revealed when electrically neutral liquid enters the insulating tube. Now with the space charge field absent near the tube entrance, a rate of change of surface charge there points to the role of the radial diffusion current.

Finally, charge leakage overlaps charge transport and accumulation because all of these processes depend on the presence of ions in the liquid. As indicated in Fig. 1.2, the generated field generally includes components both normal (E_r^w) and tangential (E_z) to the inner surface of the tube wall. While the former stresses the insulation, the latter drives a current through the slightly conducting liquid, and perhaps along the liquid-solid interface, that tends to leak away the collected surface charge. This leakage process is controlled in part by the configuration of conductors in the region outside of the tube because they support image charges that contribute to the generated field. As in the Van de Graaff, the generated field continues to build-up until either the insulation fails or the leakage and accumulation processes reach a balance. It is to ensure that conduction rather than dielectric strength determines the ultimate stress that proper design aims to enhance charge leakage while attenuating charge accumulation.

1.3 Scientific Motivation

A quantitative model for the flow-induced electric field generation in the insulating tube calls for the integration of material drawn from a range of disciplines, and provides an opportunity to address issues that have import beyond the immediate application.

A central concept in classical electrokinetic studies (16,17) is the equilibrium charge double layer in which the net current normal to an interface vanishes by virtue of a balance between ion diffusion and ion migration in the space charge field of the ions themselves. Here, diffusion originates in the thermal motion of the ions, and the familiar Debye length (see Sec. 2.2.1 below) characterizes the thickness of the diffuse part of the double layer where a net charge exists. When the surface that bounds the electrolyte is that of a submicron colloidal particle, the electrophoretic velocity or the sedimentation potential are of interest; if it is that of a capillary, the electro-osmotic flow or the streaming potential may be observed. A description of the equilibrium ion distribution in the highly turbulent flows typical of cooling applications must take account of the turbulent diffusivity profile that is the province of mass transfer studies. This equilibrium distribution defines, for a given flow condition, a fully developed convection or streaming current that is characteristic of a flow element in the sense of being independent of conditions further upstream.

Where charge generation and accumulation proceed, an imbalance between diffusion and migration accounts for a transfer of net charge between the interface and the flowing liquid, and hence a nonvanishing current normal to the interface. The parallels with other convective diffusion processes are not weakened by the fact that here the ions migrate in a space charge field, while in electrodialysis (18), for example, an imposed field dominates. What makes the ion distribution now a nonequilibrium one is the need to specify the rates of both an ionization reaction in the liquid bulk and an electrode reaction if charge is transferred across the liquid-solid interface (see Sec. 2.2.2 below). Unfortunately, even when the chemical identities of the ions are known, as when an antistatic agent supplies their majority, these rate processes remain poorly understood in the semi-insulating liquids typical of high voltage applications.

The leakage process also accounts for ties to apparently unrelated areas of research, because apart from the liquid bulk there are two other potential paths along which charge may leak from the inner surface of the insulating wall. The first is a thin region of enhanced conductivity at that surface that supports a surface current in the presence of a tangential field (E_z in Fig. 1.2). This surface conductivity may itself evolve with time if it stems from the adsorption of a surface-active substance from the liquid. The second path is the bulk of the insulating wall into which charge may be injected under the influence of the normal component of the generated field (E_r^w in Fig. 1.2). The same injection process that may compromise the charge retention capacity of an electret will be beneficial here if it helps relieve the electrical stress within the wall.

1.4 Overview

The guiding objective is to lend a rational basis to the design of a liquid circulation system in which the electrical stresses induced within an insulating tube by the flow must be controlled. Because of their technical importance, the focus is on the specific materials indicated in Table 1.1, which are typical of those selected for current equipment (19). However, to ensure that design guidelines are more broadly applicable, the four basic processes of Sec. 1.2 must be elucidated in terms of standard material parameters. To ensure that these guidelines are easily applied, these processes must be integrated into a picture of the field generation process that is flexible enough to make clear the implications for a general system configuration.

To help outline essential issues, Chapter 2 organizes a review of previous work on the flow of semi-insulating liquids through tubes under section headings that divide the work along conceptual lines rather than by author. That chapter begins by seeking a basis for classifying the tube as conducting or insulating, and finding that a useful classification hinges on the conductivity of the liquid as well. Section 2.2 discusses work on conducting liquid-tube systems in terms that should help clarify the behavior of practical charge generating elements. New data with the liquid fluorocarbon in Table 1.1 are presented here for comparison with the previous experimental work with liquid hydrocarbons. Section 2.3 critiques the previous work on insulating liquid-tube systems to set the stage for the present contribution.

Chapter 3 gives quantitative expression to the picture of the external charging mode introduced in Sec. 1.2, and describes supporting experiments. The model presented in this chapter regards ion migration as the dominant contribution to the normal current at the inner surface of

TABLE 1.1

Cooling System Materials

Element	Materials	Trade Name and Manufacturer	Properties
Liquid	trichlorotrifluoroethane ($C_2C\ell_3F_3$)	Freon 113 Dupont	high dielectric strength, good heat transfer properties, compatibility with other materials
Insulating Tube	ethylene-tetrafluoroethylene copolymer	Tefzel Dupont	chemically inert, good mechanical properties, retains dry surface after exposure to moisture
Additive	polymeric amine salt	DCA-48 Mobil	maintains desired Freon conductivity over extended periods
Metal Sections	aluminum, copper, stainless steel		compatible with Freon 113
Gas Insulation	SF_6		high dielectric strength, nonpolar (so does not enhance ionization when dissolved in Freon)

the tube wall, and leads to a description of the field generation that is appealing because of the small set of material parameters involved. Appendix A helps to limit that set by offering a nonspecific treatment of ionic reaction rates in the liquid bulk. It is left to Chapter 5 to define the range of conditions for which diffusion does not contribute significantly to the normal current, and to Chapter 7 to show that this range encompasses conditions of practical interest. The supporting experiments exploit configurations that are not immediately identifiable with components of an actual system, but for which measured quantities have clear significance and bear direct comparison to theoretical predictions.

Whereas the tube supports a <u>fully developed</u> turbulent flow, Chapter 4 considers flow elements in which the liquid is <u>fully mixed</u> in the sense that the entrained volume charge is uniformly distributed. The random turbulent motions that obscure the mean flow and wipe out gradients in the charge density may be due to obstructions in the flow or to external energy sources, as in a pump. In the expansion element that is considered in detail in this chapter, it is the energy of the influent liquid jet that is presumed responsible. An expansion with insulating walls permits investigation of the basic processes in a context that is simpler than that of the tube because charge transport and accumulation are now separated. Practical interest in both insulating and conducting expansions stems from their potential application as flow elements to be inserted immediately upstream of an insulating tube to attenuate the influent convection current. A theme of this chapter is the relationship between expansion dimensions and its effectiveness in this role.

Experiments reported in Chapter 5 reveal the limitations of the model of Chapter 3 by incorporating an expansion large enough to render the liquid influent to the insulating tube essentially electrically neutral. The diffusion component of the current normal to the liquid-solid interface that was left out of that model is included here in a revised model. Because the revised model introduces an additional boundary condition that brings in phenomenological material parameters, its practical utility is likely to be compromised. Nevertheless, it provides a basis for comparing the contributions of the internal and external modes (see Sec. 1.2 above), as well as a framework into which a physically motivated boundary condition may eventually be incorporated.

It is because of complications inherent in the use of electrodes that other methods are of interest for measuring the surface conductivity whose role in the leakage process was noted in Sec. 1.3. One method, described in Chapters 3 and 5, relates the surface conductivity to the rate of the surface charge relaxation that ensues when flow through the insulating tube is interrupted. Chapter 6 introduces a device that provides the means to continuously monitor changes in the surface conductivity without interrupting the flow. A helical winding on the outer surface of the insulating tube is excited with a standing wave of potential, and simultaneously induces and detects perturbation charge within the flowing liquid to reveal conditions at the interface. The subject of Appendix B is the inverse interaction where liquid convection is induced by electrical forces when the same winding is excited with a traveling wave of potential, again with the objective of probing the interface.

Finally, Chapter 7 is directed primarily to the design engineer who seeks to limit flow-induced electrical stresses without compromising equipment capacity. Here, the objective is to translate the models and results of the previous chapters into concrete design suggestions. This calls for an assessment of the practical value of the migration model of Chapter 3, as well as an argument that results phrased in terms of specific experimental configurations have broader applicability.

Chapter 2

BACKGROUND AND PRELIMINARY EXPERIMENTS

Two factors make the conducting tube a useful context for an introduction to the charge generation process. First, because the fully developed velocity and diffusivity profiles are known, attention can turn directly to the transverse boundary condition that reflects a specific electrochemical attribute of the liquid-solid interface. Second, these profiles and the specialized forms of the equations that govern the volume charge distribution in the liquid are common to the insulating tube, so these can serve as a point of departure for a description of the charge accumulation process. Section 2.1 establishes a basis for classifying a liquid-tube combination as conducting or insulating. A review of previous work with flowing semi-insulating liquids is divided along these lines in Secs. 2.2 and 2.3, with some new streaming current data included in the former section. These reviews emphasize themes that could be the basis for critiques of papers not cited here.

2.1 Classification of Tubes as Conducting or Insulating

It is the engineer's license to classify materials according to their behavior in a particular context without regard for fundamental physical differences. In the following two sections, flow-induced currents are reported for tubes of materials that cover both ends of the conductivity spectrum. However, whether the rate process that establishes these currents forms a significant part of the observations depends in part on the tube's conductivity. In the highly conducting limit, stationary electrical conditions may be established on a time scale even shorter than that needed to attain a steady hydrodynamic flow. In the highly insulating limit, the electrical transient initiated by the flow can be long enough to dominate the observations, and in the extreme case the stationary state never develops because electrical failure terminates the transient.

Intermediate conductivities raise the issue faced by the electric circuit designer who, in considering the step response, would prefer not to model rate processes that proceed quickly on the scale of the excitation rise time, but must do so to verify the ordering of times. Here, the role of the rise time is played by the liquid residence time in the tube (L/U) which typifies the shortest time scale of interest, and it remains to determine the time scale of the electrical transient in terms of the tube's conductivity.

The description of the electric field generation in Sec. 1.2 regards the transient as complete when the leakage process becomes competitive with the accumulation process. So it is natural that in Chapter 3 the transient is found to be characterized by the same time that governs the relaxation of surface charge from the inner surface of the tube wall. For now, regard both the tube material and the liquid as ohmic, with conductivities σ_w and σ_ℓ, respectively, and allow a uniform surface conductivity σ_s at their interface. A detailed treatment in Chapter 3 of the specific configuration shown in Fig. 2.1 leads to a description of electrical quantities in terms of a set of Fourier modes, each of which evolves on its own scale τ_n:

$$\tau_n = \frac{\epsilon_\ell + \epsilon_0 F_n(R,a)}{\sigma_\ell + (2w\sigma_w/a) + (2\sigma_s/a)} \tag{2.1}$$

where

$$F_n(\alpha,\beta) \equiv \frac{2}{ak_n}\left\{ \frac{I_0(k_n\alpha)K_1(k_n\beta) + I_1(k_n\beta)K_0(k_n\alpha)}{I_0(k_n\alpha)K_0(k_n\beta) - I_0(k_n\beta)K_0(k_n\alpha)} \right\} \tag{2.2}$$

and I_n and K_n are the nth order Bessel functions of the first and second kinds, respectively, and $k_n \equiv n\pi/L$ is the wavenumber of the nth Fourier mode. Evidently, the relaxation time is a heterogeneous one in the sense that it depends on the properties of more than one region as well as on their dimensions. It is because the tube wall is regarded as too thin to store appreciable electric field energy that the permittivity of the wall does not enter, and because dissipative processes in the region

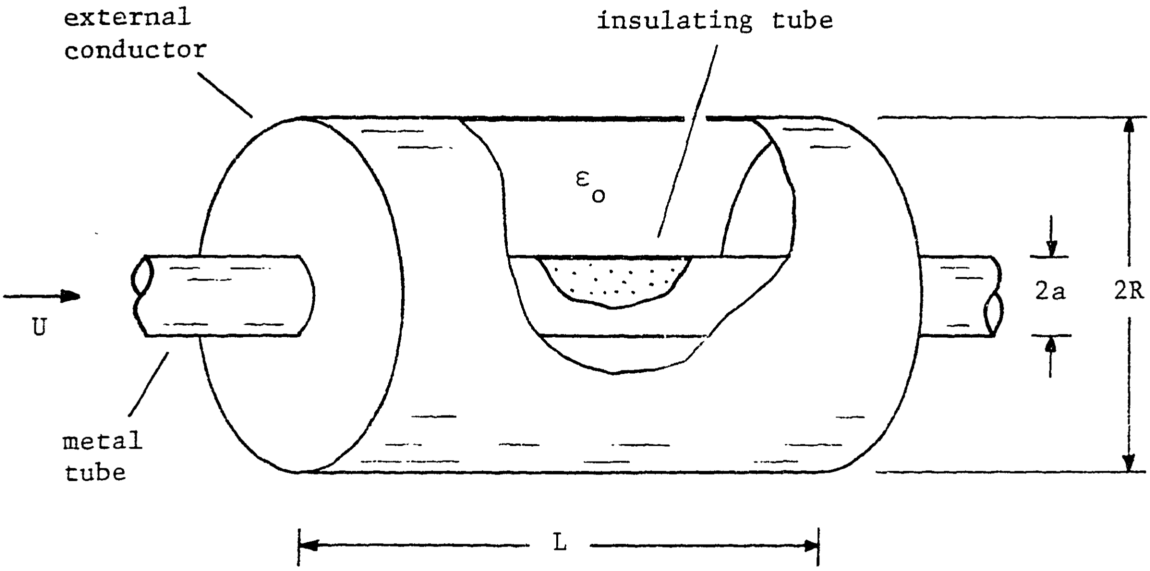

Fig. 2.1 Illustrative external conductor configuration. The axis of the insulating tube coincides with that of a grounded cylindrical conductor. Conducting discs truncate both the cylinder and the insulating tube which conveys the liquid between metal tubes of the same diameter. The liquid and the free space region outside the tube have permittivities ε_ℓ and ε_o respectively.

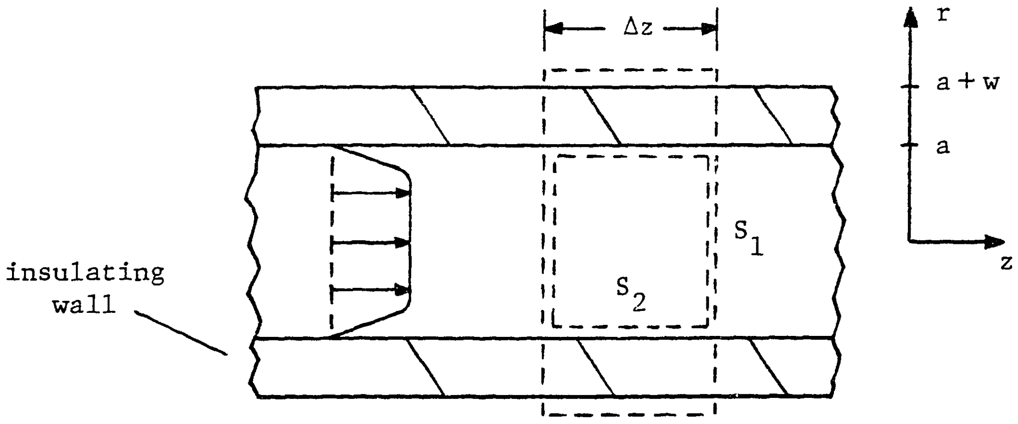

Fig. 2.2 Section of tube showing generators of closed cylindrical control surfaces S_1 and S_2 that are aligned with the tube axis. The curved part of S_1 coincides with the outer surface of the tube and lies within the perfectly insulating gas. The curved part of S_2 coincides with the inner surface, and encloses only volume charge. Mean turbulent velocity profile is shown.

surrounding the tube are neglected that a gas conductivity does not appear. The geometric factor F_n proves to be positive-definite and a decreasing function of n, and thus it is the longest time constant of the series τ_1 that defines the duration of the transient.

For other configurations, the counterpart of Eq. 2.1 can be found in principle by the procedure outlined in Chapter 3. Section 2.2 concerns conducting systems defined as those for which the combined conductivities render $\tau_1 \leq O(L/U)$. Thus Varga's (20) dielectric tubes would be classified as conducting on the basis of the relatively conducting aqueous liquids involved. In practical terms the steady state develops quickly enough to forestall significant charge accumulation, while a steady state charge generation process emerges as the dominant feature. Section 2.3 concerns insulating systems for which the ordering of times is reversed, and now the charge accumulation process will be significant to an extent determined in part by the geometric factor (F_n) that reflects the configuration of external conductors.

2.2 Streaming Currents in Conducting Systems

The charge double layer that resides in the liquid phase at virtually all liquid-solid interfaces consists of an inner layer of molecular dimensions bound to the interface by a combination of specific and coulomb forces, and an outer or diffuse layer held by coulomb forces alone. Thus, essential differences between double layers in semi-insulating liquids and those in the more extensively studied aqueous liquids should be confined to the inner layer (21). Another specific feature of the interface is the charge transfer reaction that sustains the continuous streaming currents observed when the semi-insulating liquid flows through a metal tube (21). The introduction to the charge generation process that follows depends only on the existence of the double layer and the availability of a charge transfer reaction, while their specific attributes are reflected in phenomenological boundary conditions.

The streaming current generated in a fully developed flow is defined as

$$I_s(z) \equiv \int_0^a \rho(r,z)v_z(r)2\pi r dr \tag{2.3}$$

where ρ, v_z and a are the net volume charge density in the liquid, the mean liquid velocity and the tube inside radius, respectively, and r and z are coordinates in a cylindrical coordinate system. To clarify issues inherent in the measurement and prediction of I_s it is necessary to define a total axial current (I) carried by the tube, the liquid and their interface, and that fraction (I_ℓ) carried by the liquid bulk alone. By the definition in Sec. 2.1 a conducting system is characterized by quasistationary electrical conditions, so that

$$\frac{\partial I}{\partial z} = 0 \quad ; \quad I \equiv \int_0^{a+w} (\rho v_z + \sigma E_z)2\pi r dr \tag{2.4}$$

where σ is the local conductivity, E_z is the axial electric field and w is the tube wall thickness. This is just the statement that no net current traverses the closed cylindrical surface S_1 in Fig. 2.2 whose curved part is situated in the perfectly insulating gas. Nor does a steady net current traverse the closed surface S_2 in Fig. 2.2 which encloses only volume charge, so that $I_\ell(z)$ satifies

$$\frac{\partial I_\ell}{\partial z} = -2\pi a J_r(a,z) \quad ; \quad I_\ell(z) \equiv \int_0^a J_z(r,z)2\pi r dr \tag{2.5a}$$

where

$$J_z(r,z) = \left(\rho(r,z)v_z(r) + \sigma_\ell E_z(z)\right) \tag{2.5b}$$

and $J_r(r,z)$ are respectively the axial and radial components of the current density in the liquid. Of course, Eqs. 2.4 and 2.5 do not preclude temporal variations on time scales longer than τ_1 (see Sec. 2.1 above) due to (say) variations in either the upstream or the transverse boundary conditions. The definitions of I and I_ℓ neglect axial diffusion in view of the large Peclet number ($\equiv LU/D_e$) based on the tube length. Also, the mean velocity profile is imposed in the sense that electrical forces are too weak to modify it. Hence, to determine the integrand in Eq. 2.3, it remains only to specify the volume charge profile of which there are two aspects: the developing profile $\rho(r,z)$ that reflects conditions at the tube inlet, and the fully developed profile $\rho(r,\infty)$ that prevails far downstream of the inlet.

2.2.1 Fully Developed Volume Charge Density

Although both the fully developed and the developing charge profiles are governed by the same basic equations, they are considered separately here to emphasize that treatment of the former requires less data of a specific nature. Where the volume charge density is fully developed, Eq. 2.4 indicates that

$$\frac{\partial}{\partial z}\int_0^{a+w} \sigma E_z 2\pi r\,dr = 0 \qquad (2.6)$$

Because the axial field arises from sources distributed over lengths much greater than the tube radius, and is therefore essentially uniform over the tube cross section, Eq. 2.6 requires the axial field to be independent of z. It follows that both J_z (Eq. 2.5b) and I_ℓ (Eq. 2.5a) are fully developed as well, and now to ensure a steady state current density in the liquid that is divergence free, the radial component must satisfy

$$\frac{1}{r}\frac{d}{dr}\left(rJ_r(r,\infty)\right) = 0 \quad \rightarrow \quad J_r(r,\infty) = \frac{A}{r} = 0 \qquad (2.7)$$

with the integration constant set to zero to satisfy Eq. 2.5a. For two ionic species with valences of equal magnitude, this result implies only that the radial flux densities of the individual species are equal. It is left to Sec. A.3 to show that with the additional constraint that the total solute concentration remain independent of z, these flux densities vanish indentically:

$$\Gamma_r^+(r,\infty) = \Gamma_r^-(r,\infty) = 0 \qquad (2.8)$$

Thus, neither ionic species participates in a reaction that transfers a net charge across the interface, and the transverse boundary condition will be an equilibrium one in the sense that <u>rates</u> of charge transfer reactions do not enter. Section A.3 also develops the corollary that chemical equilibrium prevails within the liquid bulk, so that the species conservation equations specialized to the region of fully developed electrical conditions will not call for the <u>rates</u> of the ionization reaction.

As shown in Sec. A.2, the chemical equilibrium condition allows the contributions of migration and diffusion to the vanishing radial current density J_r to be expressed entirely in terms of the unknown fully developed volume charge profile $\rho(r,\infty)$. Abedian and Sonin (22), who summarize the related work prior to 1980, confine attention to the small charge density limit where the liquid conductivity is essentially uniform and equal to its rest value. As a result the equation for $\rho(r,\infty)$ is a linear one, facilitating the development of analytical solutions. Their essential contribution is a consistent account of the role of the turbulent diffusivity in the balance between radial migration and diffusion. Whether the turbulent diffusivity appreciably influences the volume charge distribution is shown to depend on the ratio of the diffusion sublayer thickness δ (see Eq. 3.3 below) to the Debye length

$$\lambda_m \equiv \sqrt{\frac{\epsilon_\ell D_m}{\sigma_\ell}} \qquad (2.9)$$

Figure 2.3 illustrates that when the ratio δ/λ_m is large, the net charge

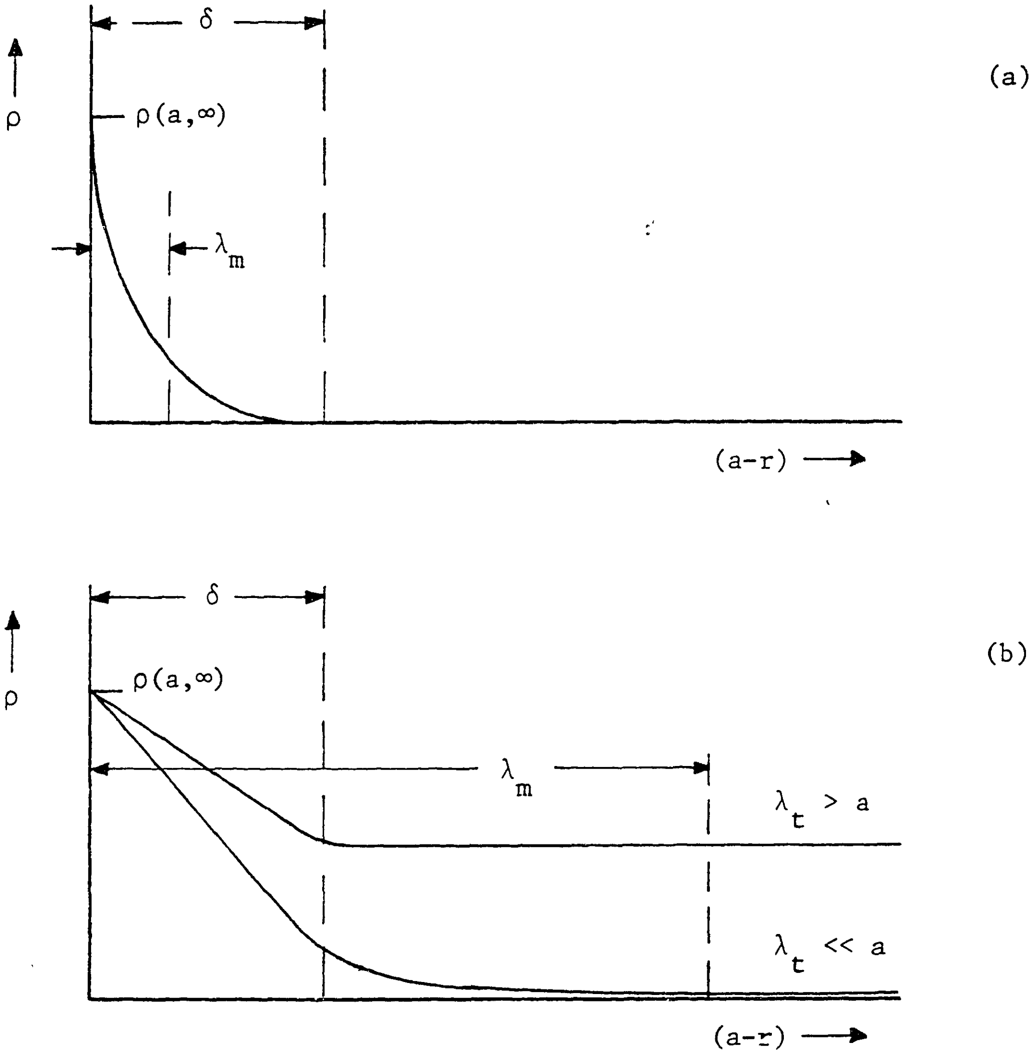

Fig. 2.3 Fully developed charge density profiles in turbulent flow (from reference 22). (a) $\delta/\lambda_m \gg 1$, (b) $\delta/\lambda_m \ll 1$. The Debye length λ_t is given by Eq. 2.9 with the molecular diffusivity D_m replaced by the eddy diffusivity D_t of Eq. 6.9.

is confined to the laminar region near the interface; when it is small the original diffuse layer is exposed to the turbulent motions and drawn into the core. Thus, if the interfacial value $\rho(a,\infty)$ remains fixed, an increase in the mean velocity yields a decrease in this ratio and an increase in the streaming current given by Eq. 2.3.

The charge distributions in Fig. 2.3 are not fully determined until a boundary condition governing $\rho(a,\infty)$ is specified. Abedian and Sonin postulate a linear relation between the charge density and radial current at the interface

$$J_r(a,z) = J_w\left(\frac{\rho(a,z) - \rho_w}{|\rho_w|}\right) \tag{2.10}$$

where J_w and ρ_w are empirical properties of the liquid, solid and ionizable solute combination, but are independent of flow conditions. In view of Eq. 2.7, this condition specializes to $\rho(a,\infty) = \rho_w$ where electrical conditions are fully developed, and leads to the analytical solution

$$\frac{I_s(\infty)}{Q\rho_w} = \left(\frac{R_y\tau_w{\lambda_m}^2}{\rho_m U^2 a^2}\right)\left(1 - \frac{(\delta/\lambda_m)}{\sinh(\delta/\lambda_m)}\right) + \left(\frac{(\delta/\lambda_m)/\sinh(\delta/\lambda_m)}{1 + (a\delta/2{\lambda_m}^2)}\right) \tag{2.11}$$

in terms of the shear stress at the interface τ_w, the hydrodynamic Reynolds number R_y, the volume flow rate Q, the mass density ρ_m and the superficial velocity U. ρ_w has an order of magnitude determined by recognizing that (by assumption) this parameter also characterizes the original stationary double layer. Then equating the total diffuse charge per unit area ($\sim\lambda_m\rho_w$) to the product of the zeta potential (ζ) and the diffuse layer capacity per unit area ($\sim\epsilon_\ell/\lambda_m$) yields

$$\lambda_m\rho_w \simeq \frac{\zeta\epsilon_\ell}{\lambda_m} \quad \rightarrow \quad \rho_w \simeq \frac{\zeta\epsilon_\ell}{\lambda_m^2} = \frac{\zeta\sigma_\ell}{D_m} = 0\left(\frac{\sigma_\ell}{b}\right) \tag{2.12}$$

with the final result exploiting Eq. 2.9, the Einstein relation (which brings in the ion mobility b), and the understanding that the thermal voltage typifies the magnitude of the zeta potential. Nothing is implied here about the sign of ρ_w which must be determined empirically. However, the exchange current density J_w is a positive-definite quantity.

In their theory for the streaming current generated in laminar flow Pribylov and Chernyi (23) regard the bulk concentration of one ionic species at the interface to be constrained independently of flow conditions. Where electrical conditions are fully developed so that chemical equilibrium prevails, this is tantamount to constraining the interfacial concentration of the other species as well. Thus, the net volume charge density at the interface is also independent of the flow, and their boundary condition acquires the same form as that of Abedian and Sonin.

Walmsley and Woodford (24) suggest the boundary condition

$$\Gamma_r^{\pm}(a,z) = K_{\pm}c_{\pm} - K_s^{\pm} \tag{2.13}$$

where $c_{\pm}$ are the concentrations of ionic species, the $K_{\pm}$ are proportionality factors that reflect the fraction of the interface accessible to the ions, while the $K_s^{\pm}$ are proportional to the respective surface concentrations of the ions. In their treatments of the fully developed streaming current in both laminar (24) and turbulent (25) flows these authors specialize Eq. 2.13 by omitting the $K_s^{\pm}$ terms. In addition, they regard the equilibrium value of the product c_+c_- as independent of radial position, which is tantamount to assuming a uniform density of the neutral solute (see Sec. A.2). Consistent with Eq. 2.7 they equate the two ion flux densities in Eq. 2.13. But, because these are nonzero, and because there is no gradient and hence no radial flux of neutral solute, they implicitly allow a change in the total solute concentration along the tube axis. This implies an axial variation of the liquid conductivity which, however gradual, is inconsistent with the fully developed electrical condition.

2.2.2 Spatial Development of the Volume Charge Density

The convection current at the tube inlet generally differs from its fully developed value, and thus $\partial\rho/\partial z \neq 0$ over a section of the tube near the inlet as the current tends towards $I_s(\infty)$. However, as is now shown, the description of the developing profile $\rho(r,z)$ is complicated by more than the addition of an independent variable. Equation 2.4 can be written as

$$\frac{\partial}{\partial z}\int_0^a(\rho v_z + \sigma_\ell E_z)2\pi r dr = -\frac{\partial}{\partial z}\int_a^{a+w}\sigma_w E_z 2\pi r dr \tag{2.14}$$

with surface conduction lumped into the integral on the right. With E_z essentially uniform over the tube cross section, the relative conductivities determine which conduction term balances the nonzero convection term on the left. In the case of present interest the system is rendered conducting (in the sense of Sec. 2.1) by virtue of the tube rather than the liquid, so that typically $\sigma_\ell << (2w/a)\sigma_w$. Thus, the magnitude of the term on the right side of Eq. 2.14 far exceeds the conduction term on the left, and hence the left side must be nonzero. Finally, by definition the left side is $\partial I_\ell/\partial z$, and Eq. 2.5a shows that $J_r(a,z)$ must be nonzero as well. Now the rates of a charge transfer reaction at the interface are needed, and with the argument of Sec. A.3 no longer applicable, rates of the bulk ionization reaction must also be specified. This reliance on additional specific data, which can be circumvented only at the expense of additional assumptions, renders the description of the developing profile $\rho(r,z)$ and convection current $I_s(z)$ more tentative than that of the fully developed current.

Abedian and Sonin's boundary condition (Eq. 2.10) provides a concrete example: in the fully developed region only ρ_w enters, but in the developing region where the wall current density $J_r(a,z)$ is nonzero, the "exchange current density" J_w (which characterizes the rate of interfacial charge transfer) must be specified as well. However, these authors assume that $J_r(a,z)$ remains much less than J_w, which is tantamount to regarding the transport of reactants to and from the interface as the rate limiting process, so that the boundary condition again reduces to $\rho(a,z) \simeq \rho_w$. Their assumption of a volume charge density that is small in the sense that it results from small perturbations of ionic concentrations from equilibrium values obviates the need to specify rates of the ionization reaction. A simple extension of their solution for the developing convection current allows for a finite inlet convection current $I_s(0)$:

$$I_s(z) = I_s(0)\exp(-z/d) + I_s(\infty)\left(1 - \exp(-z/d)\right) \qquad (2.15a)$$

where

$$d \equiv \left(\frac{\epsilon_\ell U}{\sigma_\ell}\right)\left(1 + \frac{2\lambda_m^2}{a\delta}\right)^{-1} \qquad (2.15b)$$

and $I_s(\infty)$ is given by Eq. 2.11. Thus, if the tube length L exceeds the development length d, the fully developed current will emerge, while only if L is less than or of the order of d will the inlet current $I_s(0)$ be reflected in the effluent current $I_s(L)$. Of course, the electrical development described by Eq. 2.15 will be obscured by the hydrodynamic development unless the latter is complete within a distance much less than d.

In his treatment of the electrical development in turbulent flow Walmsley (26) retains the $K_s^\pm$ terms in Eq. 2.13, giving four empirical parameters. He invokes the assumptions of local chemical equilibrium and small charge density, so that in the special case of $K_s^+ = K_s^-$ or if the $K_s^\pm$ are only weakly dependent on surface ion concentrations, it can be shown that Eq. 2.13 reduces to a boundary condition of the same form as Eq. 2.10, with the two parameters expressible in terms of Walmsley's original four. Walmsley divides the flow into a core region where turbulent diffusion is assumed to render the ion distributions uniform, and a diffusion sublayer where molecular diffusion dominates; but he introduces an internal inconsistency in the process of modeling the respective charge distributions. He regards the radial field in the sublayer as independent of radius, consistent with the large radius of curvature of the sublayer relative to its thickness and his assumption that the radial field is essentially imposed by a net charge in the core. However, he simultaneously precludes a net charge in the core by setting $c_+ = c_-$ there when he splices the uniform core distributions to the initially unknown distributions in the sublayer. Nevertheless, the apparent agreement with a portion of the experimental data is not fortuitous, but rather due to the lack of constraints on the empirical parameters. Apart from the inconsistent assumptions, it reveals a lack of predictive capability that to achieve correlations, values assigned to these parameters ranged freely over several orders of magnitude.

Abedian and Sonin (<u>27</u>) test their theory (Eqs. 2.11 and 2.15) against published data, virtually all of which are for doped hydrocarbon liquids in metallic tubes. The shear stress τ_w in Eq. 2.11 is obtained from the Blasius friction-factor correlation (<u>22</u>). Despite the scatter that is characteristic of work with such liquids, satisfactory agreement is discernible for a range of materials and conditions, with ρ_w assigned a value consistent with Eq. 2.12. An exception to the agreement is a consistent tendency of the theory to overestimate the measured currents when $\delta/\lambda_m > 1$. The authors argue that under this condition a significant fraction of the actual effluent convection current is lost to conduction through the effluent liquid jet back upstream to the potential-constrained tube, a possibility discussed previously by Taylor (<u>28</u>).

2.2.3 <u>Preliminary Experiments</u>

Design guidelines for the coolant circulation system cannot be broadly applicable unless qualitative features of the phenomena are common to the various candidate materials. The charge generation process is one basis for comparing the fluorocarbon-additive system of Table 1.1 to the extensively studied hydrocarbon systems. In the experimental arrangement shown in Fig. 2.4 a test section is fed by a tube of twice the diameter to limit the velocity and hence the current generated upstream of the test section. The two electrometers agree closely whether the connection at point A is made or broken, indicating that essentially all of the convection current is generated in the test section. Rather than let the liquid jet exiting the test section flow freely into the receiver, an attempt is made to avoid conduction in the effluent stream back to the test section by channeling the liquid directly into another tube of the same diameter and held at virtually the same potential.

At issue is whether the streaming currents generated by the fluorocarbon liquid parallel the behavior of the hydrocarbon liquids as summarized at the end of the previous subsection. Figure 2.5 presents one third of the collected data (for the extremes of the range of hydrodynamic Reynolds numbers used) along with the predictions of Eqs. 2.11 and 2.15. In the former equation the shear stress τ_w is obtained from the Blasius friction-factor correlation (22). The remaining two thirds of the collected data are for intermediate Reynolds numbers and reveal the same trends. Evident is some discrepancy for $\delta/\lambda_m > 1$, suggesting that the attempt to avoid back conduction was unsuccessful, perhaps due to the finite length of the insulating union at the end of the test section. There are also departures under conditions where the theoretical effluent current is not fully developed, that is, where $I_s(L)$ differs from $I_s(\infty)$. This may be attributed to the more tentative nature of the theory for the spatial development, which in this case apparently overestimates the development length d since the experimental curves tend to follow the theoretical curve for $I_s(\infty)$. Nevertheless, under conditions where a fully developed effluent current is predicted, that is, where the more rigorous aspect of the theory applies, the agreement is satisfactory with both sets of theoretical curves based on a single value of ρ_w that is consistent with Eq. 2.12. Consistent with much of the data for hydrocarbon liquids in metallic tubes, the convection currents are observed to be negative, corresponding to negative values of ρ_w.

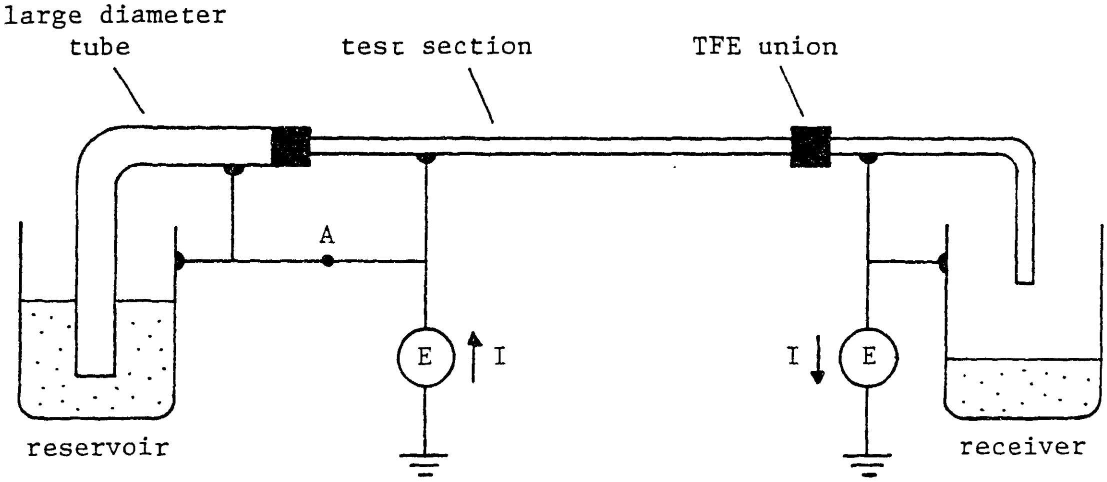

Fig. 2.4 Experimental arrangement for measuring streaming currents. Nitrogen gas pressurizes a stainless steel reservoir to drive liquid from left to right. All tubes are stainless steel joined together by Teflon unions. Inside radius and length of the test section are 1.3 mm and 1.14 m. Electrometers E monitor currents generated in the test section and collected by the stainless steel receiver.

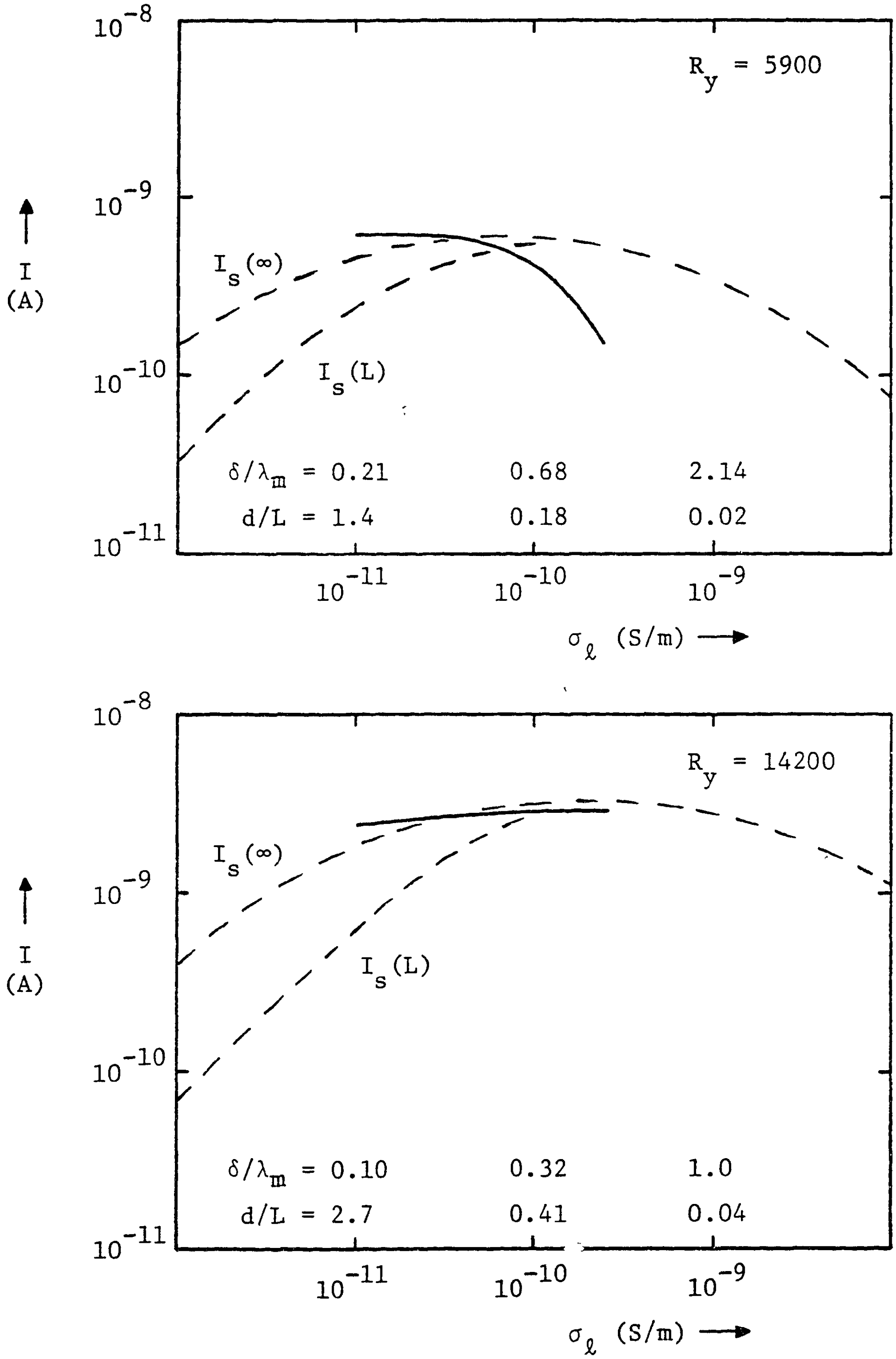

Fig. 2.5 Streaming current data for Freon-113 doped with DCA-48. Solid curves are currents measured by electrometers in Fig. 2.4. Broken curves are predicted values of $I_s(\infty)$ and $I_s(L)$ from Eqs. 2.11 and 2.15 using $\rho_w = 3.0\sigma_\ell/b$. Measured currents are negative, but plotted as positive.

2.3 Streaming Currents in Insulating Tubes

To profitably review the previous work while accomodating a diversity of emphases and perspectives, two essential themes are defined. The first is an elucidation of the rate processes that are initiated by the flow, and which ultimately compete to establish a steady state. The second is the internal charging mode (see Sec. 1.2 above) in which the insulating tube acquires a net charge in excess of the integrated influent convection current. A simple calculation shows that, to be practically significant, this net charge must greatly exceed that contained in the diffuse part of the original double layer along the tube wall before commencement of the flow. The net diffuse charge (Q_{dl}) is approximately the product of the the double layer capacity per unit area (ϵ_ℓ/λ_m), the zeta potential (ζ) and the area of the tube wall ($2\pi aL$):

$$Q_{dl} \simeq 2\pi aL\left(\frac{\zeta\epsilon_\ell}{\lambda_m}\right) \tag{2.16}$$

The maximum stress that can be attributed to the original double layer results when the flow turns the double layer "inside-out" by sweeping out all of the diffuse charge, leaving the fixed charge to find new images outside of the tube. With the magnitude of the net fixed charge also given by Eq. 2.16, Gauss' law yields for the radial electric field within the tube wall of permittivity ϵ_w

$$|E_r| \simeq \frac{Q_{dl}}{2\pi a\epsilon_w L} = \frac{\zeta\epsilon_\ell}{\lambda_m\epsilon_w} \simeq 2.0 \times 10^8\sqrt{\sigma_\ell} \tag{2.17}$$

where the final approximate equality is based on permittivities of $2\epsilon_0$, a diffusivity of 10^{-9}, and a zeta potential equal to the thermal voltage at room temperature. Even for liquid conductivities as high as 1.0 µS/m this field does not approach the dielectric strength of practical insulation. Thus, evidence that a <u>different</u> mechanism is available to generate a significant stress in the absence of upstream charge sources would be the observation that the net accumulated charge exceeds the integrated influent current by an amount much greater than Q_{dl}:

$$\int_0^t |I(0) - I(L)|dt \approx \int_0^t |I(0)|dt >> |Q_{dl}| \qquad (2.18)$$

where the integration limit t is the duration of the experiment. Tables 2.1 and 2.2 summarize the conditions of the previously reported experiments that are the subject of the next four subsections.

2.3.1 Early Work

Keller and Hoelscher (29), who summarize the work prior to 1957, experimented primarily with nominally pure n-heptane in plasticized polyvinyl chloride tubes, and sought to correlate their observations with the Helmholtz-Smoluchowski equation (17) for the streaming current:

$$I_s = \left(\frac{-2\pi a \epsilon_\ell \zeta}{\eta}\right)\tau_w = \left(\frac{-4\pi \epsilon_\ell \zeta v}{a}\right)R_y = \left(\frac{-8\epsilon_\ell \zeta}{a^2}\right)Q \qquad (2.19)$$

where the second equality incorporates Poiseuille's law, and the third brings in the volume flow rate Q. This equation relates the streaming current to the zeta potential under conditions typical of the relatively conducting aqueous liquids for which spatial and temporal developments are short. While the use of Poiseuille's law restricts the validity of Eq. 2.19 to laminar flows, it can be adapted to turbulent flow in the limit $\delta/\lambda_m >> 1$ (see Fig. 2.3a) by inserting an empirical correlation for the wall shear stress τ_w (22).

Consistent with the authors' use of an equation that does not recognize distributed aspects of the phenomena is their experimental arrangement shown in Fig. 2.6 which reveals only the net charge separated by the flow. The capacities with respect to ground of the Faraday cage and receiver, and the parallel resistances which were limited by those of the polystyrene supports, imply time constants that play the role of τ_1 of Sec. 2.1. Because these times are long compared with the duration of

TABLE 2.1

Room Temperature Data for Hydrocarbon Liquids

Properties	n-heptane (C_7H_{16})	iso-octane* (C_8H_{18})	hydrocarbon naptha†	kerosene
ϵ_ℓ/ϵ_0	1.97	1.94	~ 2.	2.09
n	3.86×10^{-4}	5.42×10^{-4}	9.25×10^{-4}	1.35×10^{-3}
ρ_m	683.7	692.	771.	748.7
ν	5.65×10^{-7}	7.83×10^{-7}	1.2×10^{-6}	1.8×10^{-6}
b§	5.2×10^{-8}	3.7×10^{-8}	2.2×10^{-8}	1.5×10^{-8}
D_m¶	1.4×10^{-9}	9.8×10^{-10}	5.8×10^{-10}	3.9×10^{-10}
S_c	400.	800.	2100.	4600.

* $(CH_3)_3C\cdot CH_2\cdot CH{:}(CH_3)_2$ (2,2,4-trimethylpentane)

† MIL-F-7024A, Type II (Shafer et al, (31))

§ $b \simeq (2.0 \times 10^{-11})/n$

¶ $D_m = v_T b \simeq 0.027b$ @ 25 °C

TABLE 2.2

Summary of Experiments with Insulating Tubes

Authors	Liquid & Tube	σ_ℓ (pS/m)	λ_m (μm)	$R_y \times 10^{-4}$	δ/λ_m
Keller & Hoelscher	n-heptane PVC	3.0-?	?-90.	0.03-0.4	0.16-?
Carruthers & Marsh	iso-octane PTFE	17.-362.	6.8-32.	1.8	0.2-0.8
	kerosene rubber	1.2-6.0	35.-78.	17.5	0.08-0.17
Gibson	kerosene PE	100 10,000	8.6 0.86	6.7 6.7	0.3 3.0
Gibbings & Saluja	kerosene PTFE	1.7	65.	0.06-0.55	0.28-0.45
Shafer et al	naptha PTFE	8-200	7.2-36.	1.5-9.1	0.1-3.2
Mason & Rees	kerosene HDPE	1-450	4.0-85.	13.	.07-1.5

notes:

1. conductivities, tube diameters and velocities are those reported by the authors
2. others parameters needed to calculate Debye lengths, Reynolds numbers and diffusion sublayer thicknesses are obtained from Table 2.1.

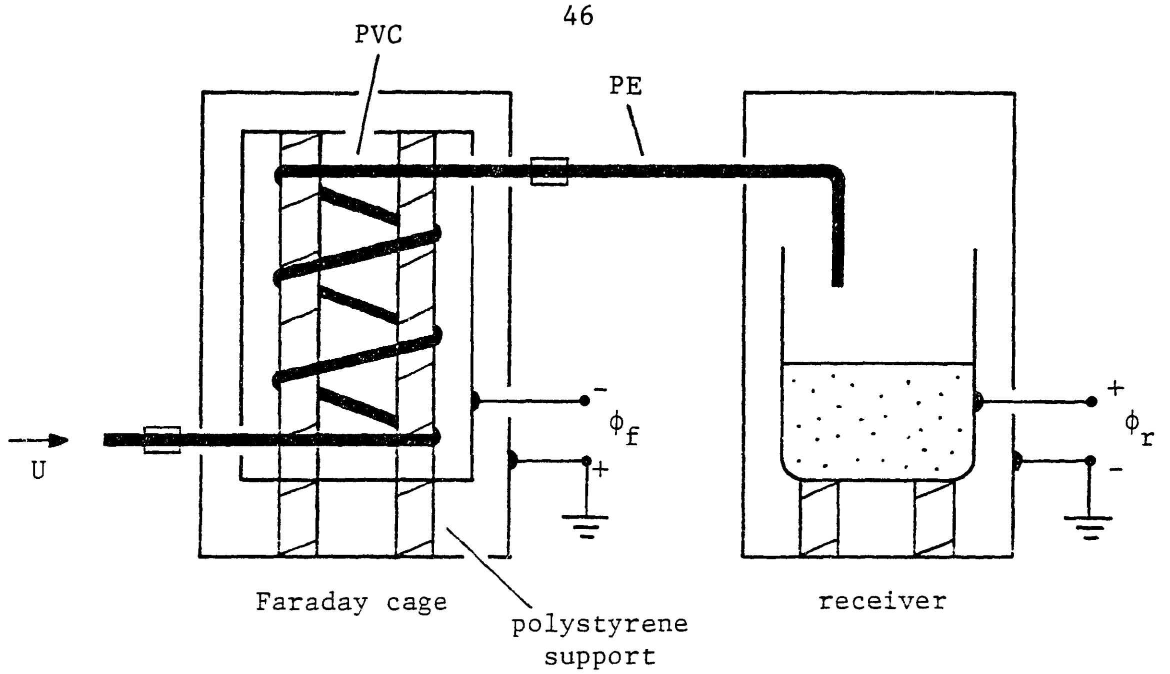

Fig. 2.6 Experimental arrangement of Keller and Hoelscher. A plasticized polyvinyl chloride (PVC) test section communicates with a reservoir and receiver through unplasticized polyethylene (PE) tubes. The Faraday cage and receiver have capacitances C_f and C_r to their respective grounded enclosures.

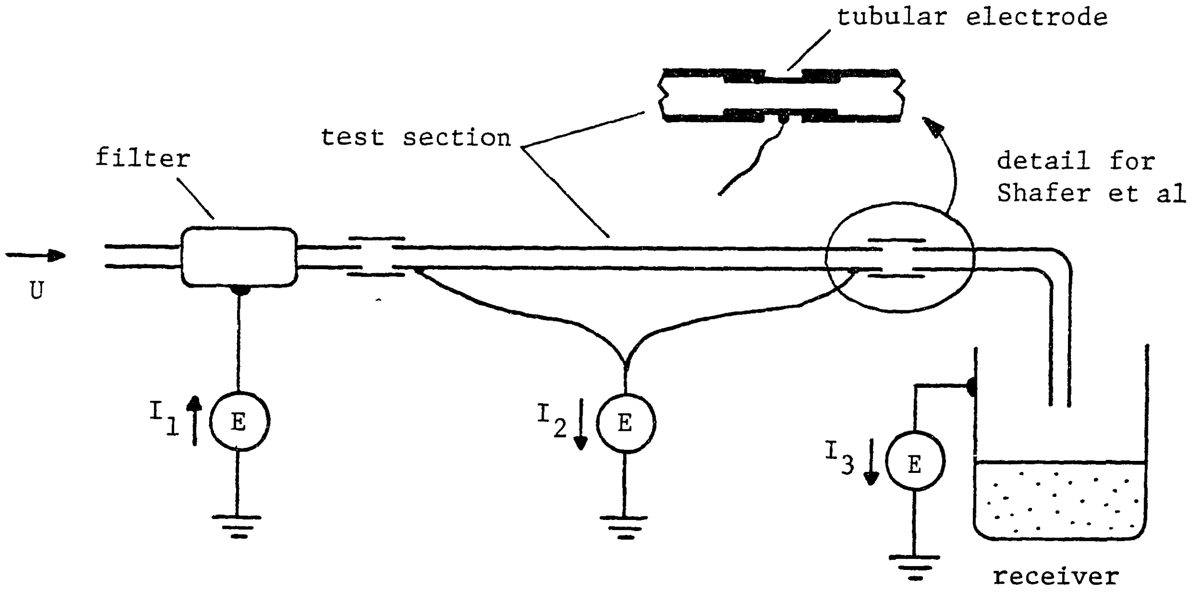

Fig. 2.7 Experimental arrangement of Carruthers and Marsh, and Shafer et al. Carruthers and Marsh used a plain PTFE test section and measured currents I_1 and I_3. Shafer et al measured I_1 and I_2 and used a PTFE test section with a conductive inner lining.

the experiments, the measured rates of change of the Faraday cage and receiver potentials ought to reflect only the *convection* of charge by the liquid. (In conducting systems for which this ordering of times is reversed, leakage is instantaneously on par with convection, and the resulting potentials should be time-independent.) The reported tendency of the liquid to enter the tube wall and extract the plasticizer was manifested in preliminary tests as an increase in the rates of change of these potentials, and a reduction in the resistivity of the tube material. The relatively small contribution of the polyethylene sections to the measured potentials was attributed to the absence of plasticizer.

Consistent with the long time constants, the rates of change of the potentials observed in the formal experiments were essentially independent of time, although the rates increased slightly near the ends of some runs. The authors attributed these departures from fixed rates of change to a redistribution of charge within the Faraday cage and receiver, which they erroneously believed would be reflected in the measurements; they did not suggest that the gradual extraction of plasticizer might be responsible. Nevertheless, the two measured rates of change multiplied by the respective capacities remained equal, indicating that all of the charge collected in the receiver originated in the Faraday cage. Thus, the streaming current issuing from the test section can be calculated from

$$I_s(L) = C_f \frac{d\Phi_f}{dt} = C_r \frac{d\Phi_r}{dt} \qquad (2.20)$$

This current was independent of tube length as L ranged from 6 to 18 feet, and a linearly increasing function of hydrodynamic Reynolds number over a range that encompassed both laminar and turbulent flow.

The authors claim satisfactory agreement between Eqs. 2.19 and 2.20 provided that the zeta potential is regarded as proportional to Reynolds number, with $\zeta \simeq 0.019$ when Ry = 100. However, their claim is compromised by more than this expedient. They assert that the observed dependence of streaming current on tube radius raised to the +1.7 power (based on a single streaming current measurement in each of two tubes) is consistent with Eq. 2.19 when $\zeta \propto R_y$. While it is unclear whether they fixed the Reynolds number or the volume flow rate for these measurements, in neither case is the predicted dependence on radius to the +2.0 power as stated. In fact, with $\zeta \propto R_y$, Eq. 2.19 indicates an exponent of -1.0 if R_y is fixed or -3.0 if Q is fixed.

Enough information is provided to estimate from Eq. 2.16 the net charge in the diffuse part of original double layer; and with $I(0) = 0$ to be consistent with Eq. 2.20, it can be shown that Eq. 2.18 is satisfied. This implies a significant charge generation process within the polyvinyl chloride tube, which the authors attribute to the presence of plasticizer in the liquid. How the charge left behind in the Faraday cage is distributed between the inner and outer surfaces of the tube wall would then depend on the extent to which the PVC tube is rendered conducting by the extraction process.

2.3.2 Steady State

Although by the definition of an insulating system (see Sec. 2.1 above) an observable transient precedes the steady state, the latter remains valid ground for seeking insights. Rutgers et al (30) outline a theory for the steady state distributions of volume charge and potential along the tube axis, which Carruthers and Marsh (10) elaborate in order to explain their experimental results. As discussed in Sec. 2.3.4 below, Shafer et al (31) also invoke the (elaborated) theory to interpret experiments.

Rutgers et al combine integral forms of Gauss' law and a steady state charge conservation statement, both written for the control surface S_2 in Fig. 2.2. In the latter statement the radial diffusion current at the interface is assumed to remain what was for the liquid at rest, independent of flow conditions and the local volume charge distribution. The resulting ordinary differential equation governs the volume charge averaged over the tube cross section $\bar{\rho}(z,\infty)$, and has the solution subject to $\bar{\rho}(0,\infty) = 0$,

$$\bar{\rho}(z,\infty) = \bar{\rho}(\infty,\infty)\left[1 - \exp(-z/LR_e)\right] \tag{2.21a}$$

where

$$\bar{\rho}(\infty,\infty) = \frac{Q_{dl}}{\pi a^2 L} \quad ; \quad R_e \equiv \frac{\varepsilon_\ell/\sigma_\ell}{L/\bar{\upsilon}} \tag{2.21b}$$

Here R_e is the electric Reynolds number based on the mean ion velocity $\bar{\upsilon}$ which bears an unspecifed relation to the mean liquid velocity. With the authors' assumption that the radial diffusion current equals that in the stationary double layer, the fully developed charge density $\bar{\rho}(\infty,\infty)$ is just that which generates a radial migration current of equal magnitude but opposite sign. Thus, $\bar{\rho}(\infty,\infty)$ is also independent of flow conditions, and can be identified with Q_{dl} of Eq. 2.16.

With the axial field $E_z(z,\infty)$ assumed uniform over the cross section of the tube, Eq. 2.4 has the integral

$$I(z,\infty) = \pi a^2\left[\bar{\rho}(z,\infty)\bar{\upsilon} + \sigma_\ell E_z(z,\infty)\right] + I_w(z,\infty) = C \tag{2.22}$$

where I_w is the axial current carried by the tube wall. It remains to substitute Eq. 2.21 and resolve the integration constant C with one of the two boundary conditions suggested by Rutgers et al. If the liquid flows out freely at the end of the tube then $I_w(L,\infty) = 0$ is the recommended condition. Here the authors count on E_z to vanish uniformly over the cross section at the end of the tube, implicitly denying the possibility of a conduction current in the effluent liquid back to the tube (see Sec. 2.2.3 above). Alternatively, if electrodes at each end of the tube are constrained in potential then the integral condition

$\int_0^L E_z dz = \Phi(0) - \Phi(L)$ applies, and now $I_w(z,\infty)$ must be expressed in terms of the axial field and the conductivity of the tube. While neither boundary condition depends for its applicability on the range of this conductivity, the authors associate the former condition with metal tubes and the latter with glass tubes, reflecting what were the traditional modes of experimenting with these materials. Finally, the potential distribution along the tube is obtained from a line integral of the axial electric field, which follows from Eq. 2.22 once the integration constant is determined.

Because it calls for the mean ion velocity which is not directly measurable, and because the assumed radial diffusion current at the interface is physically unrealistic, the theory of Rutgers et al remains unsatisfactory. Making no attempt to rectify these difficulties, Carruthers and Marsh begin by restating the theory, this time allowing for a finite influent convection current. Their counterpart to Eq. 2.21a brings in the finite value of $\bar{\rho}(0,\infty)$ in a straightforward way, and is substituted into Eq. 2.22 to yield

$$I(z,\infty) = I_s(0,\infty)\exp(-z/LR_e) + \left(\frac{\bar{u}Q_{dl}}{L}\right)\left(1 - \exp(-z/LR_e)\right) \qquad (2.23a)$$

$$+ \pi a^2 \sigma_\ell E_z(z,\infty) + I_w(z,\infty) = C$$

where

$$I_s(0,\infty) \equiv \pi a^2 \bar{\rho}(0,\infty)\bar{u} \qquad (2.23b)$$

The first term on the right in Eq. 2.23a accounts for the convection current generated upstream of the tube; the last three correspond to the one convection and two conduction terms in Eq. 2.22. When the tube length L is sufficiently short that the first term in Eq. 2.23a dominates the second, the objections to Rutger's treatment of diffusion can be waived. Moreover, in view of the rigorous steady state theory summarized by Eqs. 2.11 and 2.15, the neglect of radial diffusion in the first term is justifiable under conditions for which $\bar{\upsilon} \approx U$ and $(2\lambda_m^2/a\delta) << 1$.

In fact, Carruthers and Marsh do verify the condition on L by observing the relatively small effluent current that results when their upstream current generating filter is momentarily bypassed. The entries in Table 2.2 indicate that their experimental conditions entailed turbulent flows with the volume charge density distributed as in Fig. 2.3b. Thus, with most of the convection current carried by the core of the flow the authors are justified in replacing the mean ion velocity by that of the liquid. Finally, the above condition on the Debye length and diffusion sublayer thickness can be shown to hold, so that Eq. 2.23 should bear comparison to their experimental results once the conduction terms are resolved.

Unfortunately, the authors invite skepticism even before reporting their experiments, by seeking explicit expressions for quantities that in principle cannot be isolated experimentally. In evaluating the integration constant C in Eq. 2.23, they confine attention to the integral condition that goes with constrained potentials at the ends of the tube. With the conduction terms evaluated on this basis, they write separate expressions for the total axial currents carried by the liquid and by the tube wall. However, their plan to compare the former with the measured effluent current is ill-founded because it requires the conduction currents in the liquid and the wall to channel through different electrometers from a point where the potential is constrained.

In their experiments, Carruthers and Marsh conveyed iso-octane through both copper and PTFE tubes in the arrangement shown in Fig. 2.7, and measured the current ratio I_3/I_1 as a function of liquid conductivity. The range of liquid conductivities was such that the axial conduction current was carried entirely by the tube, in the case of copper, and by the liquid, in the case of PTFE. Despite the expected scatter, a trend towards higher current ratios with the PTFE tube can be discerned in the data. This is the basis for the authors' claim of satisfactory confirmation of the theory which predicts an increase in the ratio $I_\ell(L,\infty)/I_S(0,\infty)$, that is, the ratio of the total axial current in the liquid at the outlet to the convection current at the inlet, with decreasing tube conductivity. The authors also performed full scale experiments with aviation kerosene flowing through rubber hoses, but found it necessary to adjust the measured conductivity by a multiplicative factor of 0.08 to make results conform to the theory.

The prediction of a higher value of the ratio $I_\ell(L,\infty)/I_S(0,\infty)$ with the PTFE tube is easily explained. In the steady state, Eq. 2.4 requires the axial conduction current to be distributed to render the net axial current at $z = L$ the same as that at $z = 0$. Then because the convection component decreases with z in accordance with the first term on the right in Eq. 2.23, the conduction component will tend to supplement convection at $z = L$ and oppose it at $z = 0$. With the copper tube, the conduction component is excluded from the liquid, and hence $I_\ell(L,\infty)$ reflects only the convection component. With the PTFE tube, the net axial current is carried entirely by the liquid, and now $I_\ell(L,\infty)$ is larger in magnitude because it includes the conduction component. The authors obscure this explanation by labeling the ratio in question the "fraction of charge unrelaxed." In a review article, Gibson (32) perpetuates the misnomer by asserting that insulating tubes constitute a greater hazard for receiving vessels further downstream because the higher ratio implies a "decrease in charge relaxation." What they failed to recognize is that the ratio is higher by virtue of a conduction current, not an increase in the effluent convection current.

That the data didn't reveal more clearly a higher ratio with the PTFE tube is likely due to a combination of two factors. First, is the possibility discussed earlier that a portion of the conduction current attributed to the liquid is diverted from the effluent stream by the electrode that constrains the potential at $z = L$. Second, is an indication from their measurements of the potential along the PTFE tube that the steady state modeled by the theory had never developed. They found that discharges prevented the potential measured at the midpoint of the tube from exceeding roughly 2.5% of that predicted by their modification of Rutgers' theory. If these discharges contributed to the leakage process, the observed steady currents were not the result of the balance between axial convection and conduction that underlies the theory.

2.3.3 Transient

Keller and Hoelscher confine attention to such early times that only the convection current is revealed, while the steady state theory of Rutgers et al can only apply after long enough times that conduction and convection are already in balance. Bridging the temporal gap between these extremes is the transient where conduction is important, though not yet sufficient to offset the rate of increase of surface charge. Both Gibson (32) and Gibbings and Saluja (33) explicitly consider the transient, though neither do so in a satisfactory way.

In unpublished work summarized in (32), Gibson and co-workers investigate the effects induced by kerosene flowing through a polyethylene tube that directly connects a conducting reservoir and receiver. The effluent current and the surface charge density on the tube for two typical runs are shown in Fig. 2.8. Gibson does not report the influent current, nor does he indicated where the surface charge density is measured, what the external conductor configuration is, or whether the reservoir is grounded.

Gibson offers the following interpretation of the results in Fig. 2.8a. For the low conductivity liquid, the "charge that separates to the pipe surface cannot migrate quickly along the pipe and its presence impedes the progress of further charge separation." While for the high conductivity liquid, "the layer of conducting liquid adjacent to the pipe wall

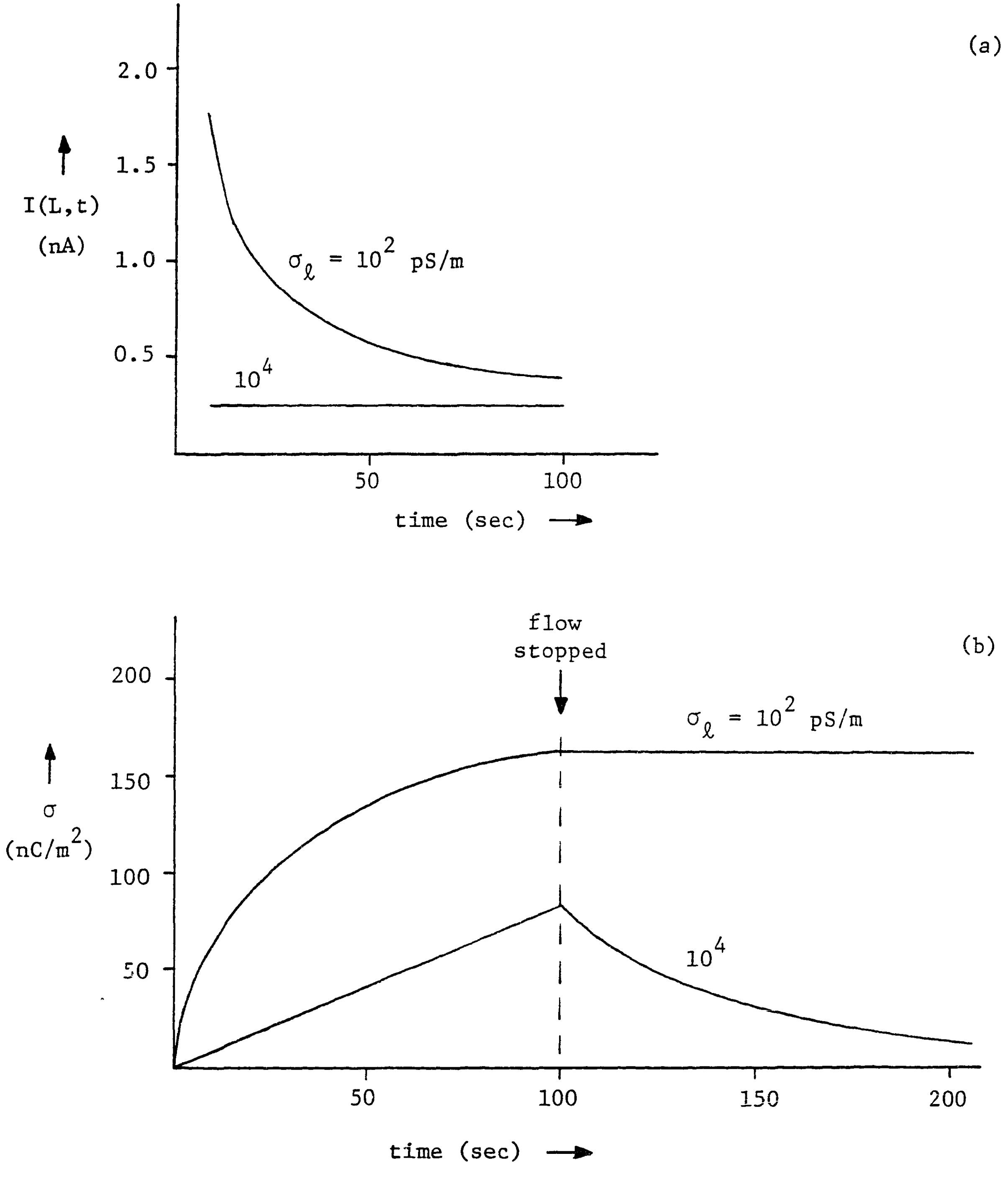

Fig. 2.8 Experimental results of Gibson. (a) Effluent current. (b) Surface charge density on polyethylene tube.

may be considered to provide a leakage path to earth and so reduce charge accumulation at the liquid-solid interface." He then suggests that the results in Fig. 2.8b "confirm this general picture," noting in particular the more rapid decay of charge in the high conductivity liquid after the flow has ceased, but ignoring the fact that for the same liquid under flow conditions the linear increase of charge with time contradicts his account of the constant effluent current.

In fact, it is readily shown that Gibson's interpretation has no basis in the data as presented. A charge conservation statement written for a surface that encloses the entire tube is

$$I(0,t) = (2\pi aL)\frac{d\bar{\bar{\sigma}}}{dt} + I(L,t) \tag{2.24}$$

where $\bar{\bar{\sigma}}$ is the charge per unit inside surface area of the tube averaged over that area. If the surface charge density reported in Fig. 2.8b approximates this averaged value, then the right side of Eq. 2.24 is fully specified by the given data. For the high conductivity liquid Eq. 2.24 yields

$$I(0,t) \simeq 4.3 \times 10^{-10}$$

For the low conductivity liquid, the given curves are regarded as exponential with time constant $\tau \simeq 30$ (sec), and thus

$$I(0,t) \simeq \left(2.5 \times 10^{-10}\right) + \left(32.0 \times 10^{-10}\right)\exp(-t/\tau)$$

Because the estimated influent currents are in each case apparently comparable to the effluent currents in Fig. 2.8a, it is inconceivable that the latter can be explained without reference to the former. Even if the signs of the quantities on the right in Eq. 2.24 are misrepresented by

Fig. 2.8 this conclusion stands, because for both runs the magnitude of the effluent current exceeds that of the rate of change of the net charge by at least 50%, again indicating significant influent currents. The entries in Table 2.2 are based on the maximum liquid velocity (10 m/s) possible with Gibson's apparatus. If the given data was obtained at this velocity, then an additional factor behind the qualitative differences in the runs with the high and low conductivity liquids may have been their correspondence to Figs. 2.3a and 2.3b, respectively.

Gibbings and Saluja performed experiments on apparatus similar to that of Gibson, and present a quantitative theory for the transients in the effluent current and in the surface charge density. In the experiments, undoped kerosene was withdrawn from a stainless steel reservoir by a straight section of PTFE tube and conveyed to a stainless steel receiver into which the liquid flowed freely. The authors measured only the effluent current and the potential in the liquid at the tube exit, the former with an electrometer attached to the receiver, and the latter by means of a probe inserted in the effluent stream. A monotonic decrease with time of the effluent current was observed under both turbulent and laminar flow conditions. In the former case, a plot of the logarithm of the current against time suggested to the authors a piecewise linear curve which they interpreted as a succession of exponential segments, each implying a longer time constant than the preceding segment. On this basis they extrapolated the ultimate current to zero. In the laminar case, following an erratic transient, the effluent current abruptly settled to a finite asymptote within one hour.

The authors do not state whether the reservoir was grounded. Nor do they attempt to measure either the influent current or the accumulating charge, and thus the comment on Gibson's work applies here as well: the effluent current alone is insufficient basis for a comparison with theory. Nevertheless, it is instructive to outline the theory because it differs on a fundamental level from the picture introduced in Secs. 1.2 and 1.3 above, and detailed below in Chapters 3 and 5.

Gibbings and Saluja's theory attributes a rate of change of the surface charge density at the inner surface of the tube wall to a competition between "charging" and "rejection" components of the radial current density. The charging component is an adaptation of the initial normal current at a wall bounding a weakly ionized gas, which arises because the mean electron velocity exceeds that of the positive ions (34). For a binary electrolyte, this component acquires the form (35)

$$J_{ch} \equiv \frac{3z_i RT}{4\ell_i}\left(c_+b_+ - c_-b_-\right) \tag{2.25}$$

where R, T, and ℓ_i are respectively the gas constant, absolute temperature, and ionic mean free path, while $c_\pm$ are the molar concentrations of the two ionic species with valencies $\pm z_i$ and mobilities $b_\pm$. The rejection component is proportional to the product of the liquid conductivity and the local surface charge density $\bar{\sigma}$

$$J_{rej} \equiv - k\sigma_\ell\bar{\sigma} = - kz_iF(c_+b_+ + c_-b_-)\bar{\sigma} \tag{2.26}$$

where F is Faraday's constant and k is a "positive coefficient expressing the radial component of the field at the wall resulting from the surface charge deposited on the wall per unit area." Neglecting conduction through the wall or along the liquid-solid interface, conservation of surface charge is expressed by

$$\frac{\partial\bar{\sigma}}{\partial t} = J_r(a,z,t) = J_{ch} + J_{rej} \tag{2.27}$$

"To simplify the discussion," the authors "consider only ions of one negative valency adjacent to the wall," and apply Eqs. 2.25 and 2.26 with c_+ set to zero. In addition, c_- is approximated as independent of both time and position along the tube, so that subject to the initial condition of vanishing surface charge Eq. 2.27 has a solution

$$\bar{\sigma}(z,t) = \frac{-3RT}{4\ell_i kF}\left(1 - \exp(\alpha t)\right) \quad ; \quad \alpha \equiv (-z_i c_- b_- kF) \qquad (2.28)$$

and

$$J_r(a,z,t) = (-z_i c_- b_-)\left(\frac{3RT}{4\ell_i}\right)\exp(\alpha t) \qquad (2.29)$$

that is independent of z. Finally, the influent current is assumed to remain zero, and thus the effluent current follows from Eqs. 2.24, 2.27 and 2.29 as

$$I(L,t) = I(L,0)\exp(\alpha t) \quad ; \quad I(L,0) = (2\pi aL)(z_i c_- b_-)\left(\frac{3RT}{4\ell_i}\right) \qquad (2.30)$$

To argue that this result supports their interpretation of the decaying effluent current in turbulent flow as a succession of exponential segments, the authors restate a hypothesis from an earlier publication (36): ions of several different valencies are present, and these deposit on the wall in batches, with ions of higher valency deposited first. The progressively longer time constants of successive segments are then accounted for by the dependence of $1/\alpha$ (Eq. 2.28) on the reciprocal of the valence. Objections to this hypothesis and to the description of the data as a succession of exponential curves are raised in the discussion following (36).

Of immediate concern is whether the theory captures the physics of the charging process. Two obvious difficulties are perhaps more issues of presentation than substance. First, is the clear inconsistency in neglecting positive ions while assuming that the influent current vanishes. Second, there is nothing apparent in the theory that restricts it to turbulent flow, yet it cannot account for the finite asymptote of the effluent current observed in laminar flow. The authors recognized that the finite asymptote implies a leakage process, but they did not incorporate one in the theory. Nor did the finite asymptote lead them to question whether the influent current was actually negligible.

But two more substantive criticisms reveal the essential inadequacy of the theory. First, the postulated rejection current arises from a radial electric field that is proportional to the local surface charge density and independent of the local volume charge density. That Gauss' law is generally violated is seen by writing its integral form for the surface S_2 in Fig. 2.2

$$E_r(a,z) = \frac{a}{2}\left(\frac{\bar{\rho}}{\epsilon_\ell} - \frac{\partial E_z}{\partial z}\right) \quad ; \quad \bar{\rho} = z_i F(c_+ - c_-) \qquad (2.31)$$

which relates the radial field at the interface to both the local volume charge and the axial field which arises from distributed sources, including those on external conductors. Second, because the charging current density of Eq. 2.25 is generally finite even when the net volume charge $\bar{\rho}$ vanishes, the postulated transient can be initiated simply by filling the tube with stationary liquid, and can proceed to completion before the flow commences. If the theory is to imply that commencement of the flow will initiate a new transient, then the ion concentrations ($c_\pm$) in the influent liquid must differ from those in the stationary liquid. Because there is nothing in the theory to relate these concentrations to flow conditions, it fails to account for the characteristic feature of observed electrification phenomena, namely, their initiation by the flow.

2.3.4 Flow-Induced Failure

Both Shafer et al (31) and Mason and Rees (37) identified experimental conditions that produced pin-hole failures in insulating tubes, as well as conditions under which the responsible discharges could be suppressed or rendered less energetic.

Mason and Rees measured the charge transferred by discharges between the surface of a high density polyethylene tube with an outer diameter of 63 mm and a movable grounded brass sphere of 28 mm diameter. The discharges were induced by circulating kerosene around a closed loop with a filter and filter bypass line just upstream of the polyethylene tube, and a relaxation tank just downstream to avoid recirculating charge. A pump situated upstream of the filter was thought to contribute negligible charge to the flow. The 15 foot length of tube was supported at regular intervals by a frame made of the tube material, and was arranged, according to the authors' schematic, in a zig-zag pattern. Liquid conductivity was controlled by clay filtering and an unspecified antistatic agent over the range indicated in Table 2.2.

A field mill showed that the potential at the tube surface increased with time following commencement of the flow and reached a steady state after about ten minutes. In this state equal currents were drawn from ground by the filter and returned to ground by the relaxation tank, consistent with Eq. 2.24 if these currents represent respectively the influent and effluent currents in the tube. A bulk charge relaxation time of the tube wall of about twenty seconds, based on the wall conductivity reported by the authors, suggests that accumulated charge resided on the <u>outer</u> surface of the tube. The steady state potential distribution was nonuniform with sign reversals about the tube circumference and along the axis, perhaps due partly to the uncontrolled arrangement of external conductors and partly to undetected discharges during the transient.

In this steady state, discharges of both signs were induced by the approach of the brass sphere with its radius of curvature just under half that of the outer tube surface. The charge transferred between the tube surface and the sphere was insensitive to their spacing in the range of 0.7 to 7.0 sphere diameters. At the lowest liquid conductivities (~2 pS/m) discharges were energetic enough to puncture the tube wall, permitting the escape of liquid. With the objective of identifying conditions that would limit the tranferred charge below the threshold of 75.0 nC which the authors considered incendive, they investigated the influence of liquid conductivity, conductive coatings on the outer tube surface, and the spacing of grounded tube supports.

Their finding that the transferred charge decreased linearly with increasing liquid conductivity, does not have a clear-cut interpretation. While enough information is provided to show that the tube wall contributed a larger resistance per unit axial length than the liquid so that the latter controlled the leakage process, the effects of liquid conductivity on charge separation in the upstream filter were not reported. The application of a conductive coating to the outer surface of the tube was found to increase or decrease the transferred charge, respectively, if the coating was isolated or continuous. In the former case, the coating creates "hotspots" by shorting out the local axial conduction current. In the latter, the resistance per unit length attributable to the coating undercuts that of the tube wall and liquid, thus enhancing the leakage process. The linear decrease of transferred charge with decreasing spacing of (and hence increasing number of) grounded tube supports is at least qualitatively consistent with the notion that the steady state stress is reduced by enhancing the leakage process.

Based on these findings the authors offer specific recommendations, but caution that they apply only to their specific experimental configuration. Perhaps the most significant observation was the pin-hole puncture produced in a tube wall having a short enough bulk charge relaxation time that the discharge may have been initiated at the outer surface of the tube. This would suggest that to avoid insulation failure it is not enough to relieve the stress within the wall.

Shafer et al provide a vivid description of pin-hole failures induced in plain tetrafluoroethylene (TFE) tubes by the flow of a white hydrocarbon naptha. With a liquid conductivity of 165 pS/m and a hydrodynamic Reynolds number of 45,000 a visible discharge appeared within about 4 minutes of the start of the flow that left multiple pin-hole punctures through which the liquid could seep. These pin holes became enlarged if the flow continued, or the phenomenon could be reproduced if a fresh tube was used. In contrast to the later study of Mason and Rees, the bulk charge relaxation time of the tube wall far exceeded the duration of the experiment. Inspection of the inner surface of the tube revealed "paths" branching out from each pin hole and covering practically the entire surface, suggesting that the discharge originated at the inner surface and engaged essentially all of the accumulated surface charge.

The significance of the Reynolds number and liquid conductivity were determined in preliminary experiments that related the charge generated in a paper filter just upstream of the tube to flow rate and additive type and concentration. The authors observed "bell" curves similar to those shown in Fig. 2.5 for the streaming current, and noted that the currents generated by the filter easily exceeded those generated by the insulating tube alone. They also found that the results of a "charging tendency" test (like that mentioned in Sec. 1.1 above, but with a steel capillary in place of the filter) bore no relation to the charge generating behavior of their filter in situ, confirming that such tests do not reflect an intrinsic property of the liquid-additive combination.

In a second set of experiments, with essentially the same arrangement as that of Carruthers and Marsh shown in Fig. 2.7, Shafer et al measured the maximum steady state potential developed along the tube under various flow conditions. Unlike Carruthers and Marsh, however, Shafer et al achieved a steady state without discharges by using TFE tubes with inner liners rendered sufficiently conducting by carbon particles to provide the dominant axial conduction path. Thus, the leakage process is controlled independently of the liquid conductivity, but because of the nonlinear current-voltage characteristics of the liners, their effective conductance varies with each run. Despite this complication the results support the view of the steady state as the result of a balance between charge generation and leakage by showing that the steady state potential increases with the former and decreases with the latter. Note that in contrast to the outer coatings used by Mason and Rees, the inner liners always enhance leakage regardless of the conductivity of the wall bulk.

A third set of experiments, also with the apparatus in Fig. 2.7, was intended to measure the ratio of the effluent to influent convection currents under conditions where the entrained charge originates entirely upstream of the tube. The authors' implicit assumption that the effluent current I_3 was entirely convective was likely based on the expectation that the large conductance of the tube liner would preclude a significant conduction component in the liquid. The effluent current was not measured directly, but rather inferred from the difference between the influent current I_1 and the current I_2 drawn from the tubular electrodes at each end of the test section which presumably made contact with the inner liner. There is no mention of a transient in the measured currents, probably because the large conductance of the liner rendered τ_1 (see Sec. 2.1 above) sufficiently short.

Shafer et al obtained a satisfactory correlation between these results and the model represented by the first term on the right in Eq. 2.23a. For the measured ratio

$$\frac{I_2}{I_1} = \frac{I_1 - I_3}{I_1} = 1 - \frac{I_3}{I_1}$$

that model predicts

$$1 - \frac{I_s(L)}{I_s(0)} = 1 - \exp(-1/R_e) \quad ; \quad R_e \equiv \frac{\varepsilon_\ell/\sigma_\ell}{L/\bar{\upsilon}} \qquad (2.32)$$

The conditions under which this represents a limit of the more rigorous steady state theory of Abedian and Sonin are discussed in Sec. 2.3.2 above. In view of Fig. 2.3, the entry in the last column of Table 2.2 indicates that the identification $\bar{\upsilon} \simeq U$ made by the authors is valid only over part of the experimental range of flow rate and liquid conductivity, with $\bar{\upsilon} < U$ over the remainder. This may help explain their finding that Eq. 2.32 tends to slightly underestimate the measured ratio (I_2/I_1), a tendency which the authors tentatively attributed to ambiguous dc liquid conductivity measurements in which steady applied voltages did not yield steady currents.

2.3.5 Summary

Perhaps more unfortunate than the paucity of work addressed to the flow-induced failure of insulating tubes are the limited perspectives that characterize the existing work. The experiments reviewed above typically measure "terminal" currents from which the net charge on an insulating tube may be inferred, but they fail to capture the distributed character of the phenomena. Nor do the previous models reflect the interplay among the four basic processes outlined in Sec. 1.2. For example, Rutgers et al decouple the radial diffusion current at the tube wall from flow conditions (Sec. 2.3.2), while the transient postulated by Gibbings and Saluja may proceed to completion even before the flow commences (Sec. 2.3.3). The need remains for controlled experiments that support a self-consistent account of the space-time evolution of the flow-induced electrical stress within the insulating tube wall.

On the positive side, two results from the previous work are germane because they are suggestive of the practical value of the model introduced in the next chapter. That model attributes the charge accumulating on the insulating tube wall exclusively to sources upstream of the tube, and regards the radial current density at the wall as being dominated by migration. The first germane result addresses an issue raised in connection with Eq. 2.18: in each experiment that produced discharges, including those of Carruthers and Marsh, Mason and Rees, and Shafer et al, an essential element was an upstream charge generator, typically a filter. The second such result, the reasonable correlation secured by Shafer et al with Eq. 2.32, encourages the expectation that practical situations exist that are adequately represented by a model that neglects the diffusion component in the radial current density.

Chapter 3

FLOW-INDUCED CHARGING OF THIN INSULATING TUBES: MIGRATION LIMIT

3.1 Introduction

The limiting condition that underlies the model of this chapter for the flow-induced electric field generation in the insulating tube is one that would naturally be introduced for the sake of simplicity, yet it proves a satisfactory representation for a range of practical conditions. Without prior justification, the normal current density in the liquid at the liquid-tube interface that accounts for a rate of increase of surface charge is regarded as due entirely to ion migration. In this limit the insulating tube is no more than a passive charge collecting surface, in that no surface charge accumulates unless an upstream flow element supplies a net charge to the flow. It is when this limit applies that flow-induced electrical stresses will be reduced by insertion of a "charge trap" in the flow immediately upstream of the insulating tube; Chapter 4 outlines the conditions under which an expansion volume will be effective as a trap. The normal diffusion current that generally competes with ion migration is accounted for in Chapter 5, leading to clarification of the conditions under which the latter is actually dominant.

Section 3.2 addresses the question: given the total axial current in the liquid at the entrance to the insulating tube, what is the space-time evolution of the electrical stress within the tube wall. Conditions on the liquid conductivity (the Debye length) and the hydrodynamic Reynolds number (the diffusion sublayer thickness) are such that most of the convection current is carried in the core of the turbulent flow. The condition on the conductivity also renders the electrical transient initiated by the flow long enough (see Sec. 2.1 above) that it dominates the experimental observations. Thus, to help interpret experiments the model must retain time rates of change of electrical quantities. Analysis of the temporal transient also highlights the essential role of the external conductor configuration, which supports image charges that contribute to the generated field. While the *steady state* potential distribution along the tube (but not the radial electric field in the wall) can be determined independently of that configuration, the latter must be specified at the outset to determine any *transient* quantity. Nevertheless, the steady state stress distribution is of interest because it proves to be a convenient basis in Sec. 7.1.1 for deducing general guidelines from the model.

In Sec. 3.3 two versions of the experiment are described, distinguished by the external conductor configurations. The first configuration, pictured in Fig. 3.1, is a close fitting coaxial sleeve that accentuates the role of the radial electric field component in the liquid by eliminating the axial component at the *outer* surface of the insulating tube wall. The extreme aspect ratio of the tube is the justification for neglecting the axial field at the *inner* surface of the wall as well. In terms of the basic processes of Sec. 1.2, charge accumulation proceeds unopposed by leakage; in terms of the characteristic times of Sec. 2.1, establishment of a steady state is delayed well beyond the duration of the experiment. The role of the small but finite axial field at the inner surface of the wall is not recognized until this configuration is taken up again in Chapter 5. The second configuration, pictured in Fig. 3.2, relaxes the constraint on the axial field and renders the leakage process competitive with the accumulation process on a short enough time scale that the approach of the steady state can be discerned experimentally.

There is no pretense that either configuration represents, let alone idealizes, any practical configuration, nor would that be desirable. Moreover, while the model of Sec. 3.2 could in principle be applied to other configurations, including those identifiable as practical ones, to do so would contribute nothing to a clarification of the phenomena that underlie the flow-induced field generation. Rather, the view is taken here that these phenomena are most profitably explored in the simplest

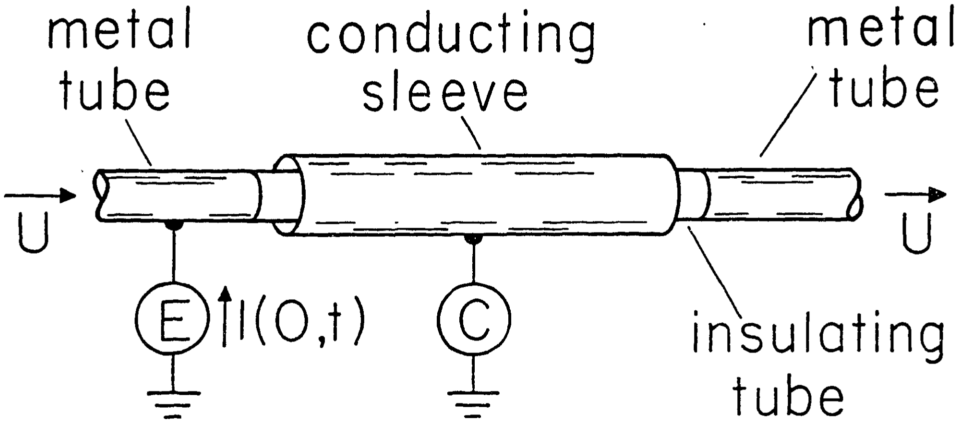

Fig. 3.1 Experimental arrangement with close fitting coaxial conducting sleeve. For clarity the length of insulating tube is exaggerated relative to that of the sleeve.

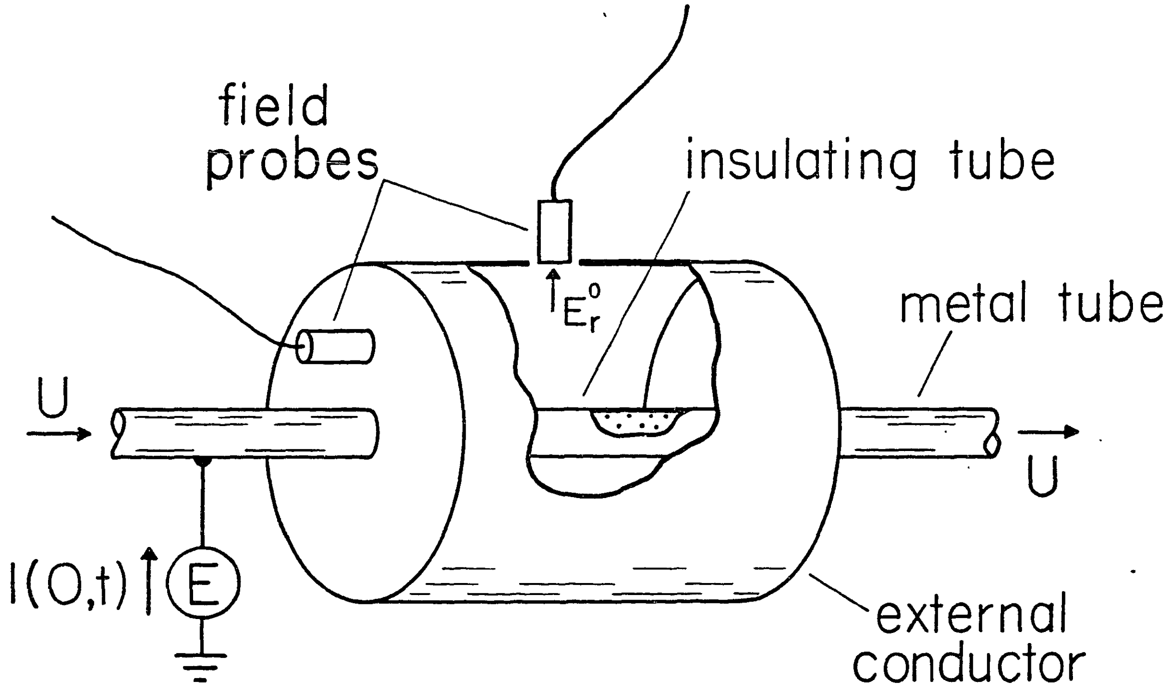

Fig. 3.2 Experimental arrangement with capped cylinder.

possible context, and that once clarified, their implications for other configurations will be clear.

3.2 Migration Model

What makes the specific external conductor configuration shown in Fig. 3.2 an ideal context for presenting the model is the relatively simple mathematical description of the potential distribution in the external region. The insulating tube lies on the axis of a cylindrical conducting annulus, and extends between conducting caps that truncate the annulus. Upstream of the insulating tube, a potential-constrained metallic section generates the convection current that drives the charging process. A similar section downstream collects the liquid as well as part of the leakage current driven by the rising potential of the insulating tube.

The objective is to predict the temporal and spatial evolution of both the charge distribution along the insulating tube and the electric field within the tube wall. Fields at the inner surface of the external conductor are more conveniently measured than those that stress the insulation, so expressions for the former are sought as well. Two dependent variables are needed to specify the charge distribution, and natural choices are the volume and surface charge densities. It proves convenient, however, to eliminate the latter in favor of a new variable, an effective line charge density representing the total charge per unit length of tube, with contributions from both the volume and surface charge densities. After the assumptions are clarified, a pair of coupled partial differential equations expressing conservation of the volume and line charge densities is identified (Sec. 3.2.2). The axial electric field component within the tube (E_z in Fig. 3.3) enters these equations as a third dependent variable. The additional relation called for comes from solving Laplace's equation for the potential distribution in the external region and expresses the field in terms of the line charge density (Sec. 3.2.3). When the influent convection current can be regarded

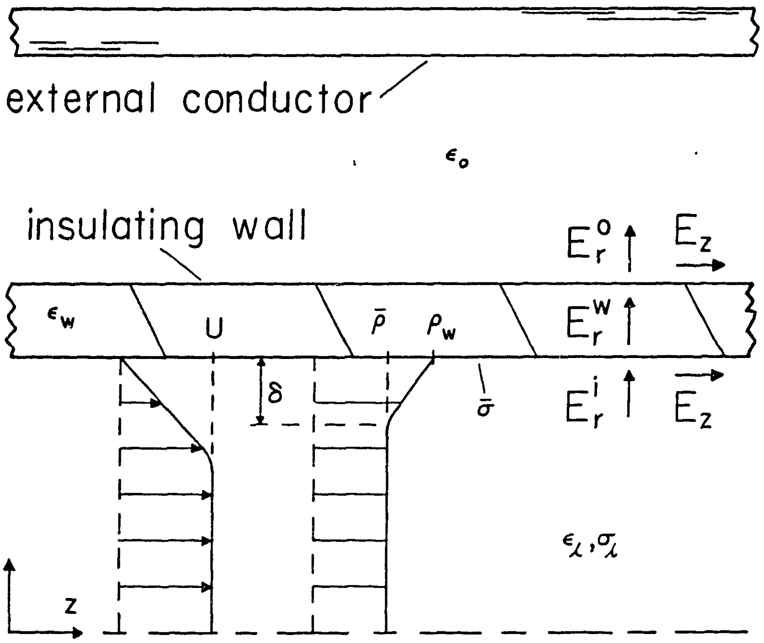

Fig. 3.3 Definition of electric field components at the insulating wall. Cylindrical coordinate system is defined, and typical velocity and volume charge density profiles are shown.

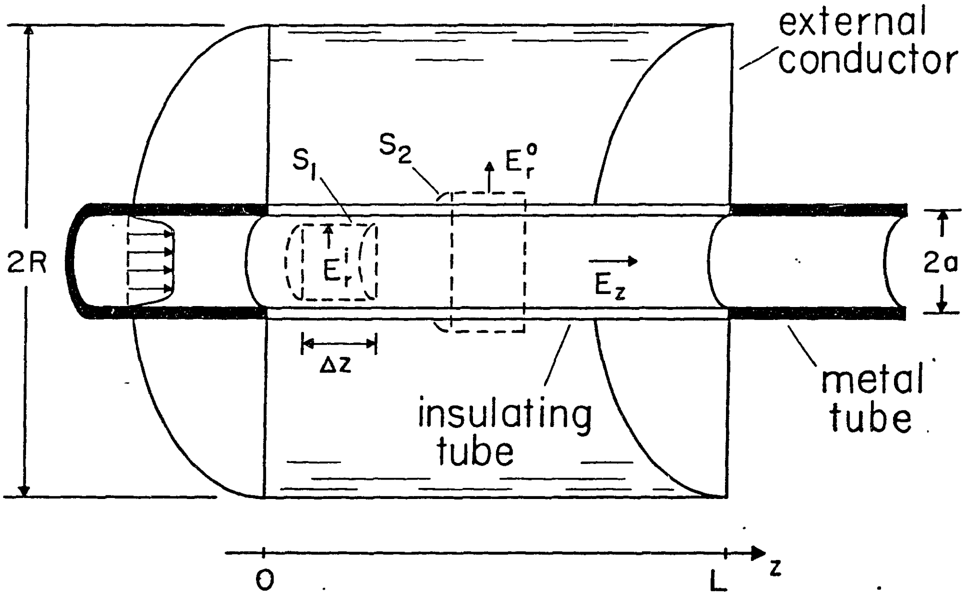

Fig. 3.4 Cross sectional view of capped cylinder and insulating tube with control surfaces S_1 and S_2 defined. For clarity the tube radius (a) is exaggerated relative to the radius (R) of the external conductor.

as imposed, an analytical solution of these equations is available for the transient electrical quantities (Sec. 3.2.5). Numerical treatment is required if that current varies on a time scale comparable to that of the charging transient, perhaps through its dependence on the generated field.

3.2.1 Assumptions

[a] The flow is turbulent and fully developed. Fully turbulent flow occurs for hydrodynamic Reynolds numbers in the approximate range

$$R_y \equiv \frac{2aU}{\nu} > 4000 \qquad (3.1)$$

Here a, U and ν are respectively the tube inside radius, the mean liquid velocity, and the kinematic viscosity. Hydrodynamic conditions become independent of position along the tube axis beyond a development length of the order of 100 tube radii. Thus, either the length of the tube under study greatly exceeds this length, or a metal entrance section of the same inside diameter, and of sufficient length to complete the development, lies just upstream of the insulating tube.

[b] The Debye length exceeds the diffusion sublayer thickness,

$$\lambda_m^2 \gg \delta^2 \qquad (3.2)$$

For the high Schmidt numbers typical of liquids of interest (see Table 2.1) there is a thin layer near the phase boundary of thickness (22)

$$\delta \simeq \left(118\, R_y^{-7/8}\, S_c^{-1/3}\right) a \qquad (3.3)$$

within which the turbulent fluctuations are diminished so that molecular diffusion outweighs the turbulent contribution to mass transfer. The

Debye length (Eq. 2.9) characterizes the width of the region near the wall within which, by virtue of a balance between conduction and diffusion, the net volume charge would remain if the flow were laminar throughout. As a consequence of Eq. 3.2, the entrained volume charge is not confined to the Debye layer but extends into the core of the flow where its distribution is influenced by the eddy diffusivity (Fig. 2.3b). It is perhaps tempting to relax the inequality of Eq. 3.2 by arguing that the field ($E \simeq \zeta/\lambda_m$) internal to the "laminar" double layer is weak enough that the generated fields will disrupt the layer and eject the diffuse charge into the core of the flow. However, the same condition on the liquid conductivity that renders the internal fields weak also strengthens the inequality of Eq. 3.2. Moreover, the transient described by the model includes the initial portion where the generated fields are not yet significant, and thus the inequality in question must be retained.

[c] Most of the convection current is carried in the core of the flow where the mean liquid velocity is essentially the superficial velocity:

$$\pi a^2\bar{\rho}(z,t) >> 2\pi a\delta\rho(a,z) \tag{3.4}$$

Here, $\bar{\rho}$ is the volume charge density averaged over the core of the flow ($0 < r < a-\delta$) and $\rho(a,z)$ is the volume charge density at the liquid-solid interface that typifies the density within the diffusion sublayer. As discussed in (22) this inequality is consistent with Eq. 3.2, and facilitates an integral approach in the description of the volume charge distribution along the axis of the tube.

[d] The migration component of the radial current density within the diffusion sublayer completely dominates the diffusion component. Conditions that justify this assumption are outlined in Sec. 5.5.2. In view of the large Peclet number (LU/D_e) axial diffusion is neglected as well.

[e] Departures of ionic concentrations from their respective values in an undisturbed solution remain small compared with those values. Thus, the liquid conductivity σ_ℓ is essentially uniform and remains close to its value σ_0 where the net volume charge density vanishes. This condition appears to breakdown at the liquid-solid interface where if $J_r(a,z) << J_w$, Eqs. 2.10 and 2.12 suggest that the net charge density ($\rho(a,z) \simeq \rho_w$) is of the order of the individual densities ($\rho_\pm \simeq \sigma/b$). However, as discussed below in Sec. 6.3.2 chemical equilibrium can be expected to prevail within the diffusion sublayer, and now Eqs. A.11 and 2.12 yield an approximate value for the bulk conductivity at the interface

$$\sigma_\ell(a,z) = \sigma_0\sqrt{1 + (\rho_w b/\sigma_0)^2} \simeq 1.4\sigma_0 \qquad (3.5)$$

that is still close to the assumed value.

[f] The bulk charge relaxation time ($\tau_w \equiv \epsilon_w/\sigma_w$) of the tube wall is long compared with the time that characterizes the charging transient (τ_1 of Sec. 2.1). As a consequence charge precipitated from the flow is stored at the liquid-solid interface as a surface density ($\bar{\sigma}$) that can be reduced only by conduction through the liquid and perhaps along the interface. This condition is relaxed in Sec. 5.3.

[g] The gas that surrounds the insulating tube is perfectly insulating on the time scale of interest (τ_1 of Sec. 2.1). Coupled with assumption [f], this implies that there is no net charge anywhere other than in the liquid bulk, at the liquid-solid interface, and on the external conductors.

[h] The axial electric field is essentially uniform over the tube cross section. This presumes that the local axial field arises primarily from distant sources (image charges on external conductors) distributed over length scales large compared to the tube radius, while the local volume and surface charge densities make no signficant <u>net</u> contribution.

[i] The influent convection current $I_s(0,t)$ varies slowly on the scale of the liquid residence time (L/U) in the tube. While probably of general validity, this assumption is certainly appropriate if variations in $I_s(0,t)$ relate to the rising potential of the insulating tube relative to the grounded upstream section that generates the convection current. The time scale for variation of the potential is τ_1 which, by the definition in Sec. 2.1 of an insulating system, is much greater than L/U.

3.2.2 Conservation Laws

Conservation of volume charge is expressed by Eq. A.9 specialized to reflect the assumptions of the previous section. Assumptions [d] and [e] justify neglect of both the diffusion term and the term containing the gradient of the liquid conductivity. Integrating the remainder of Eq. A.9 over the tube cross section yields

$$\frac{\partial\bar{\rho}}{\partial t} = -\frac{\bar{\rho}}{\tau_\ell} - U\frac{\partial\bar{\rho}}{\partial z} \quad ; \quad \tau_\ell \equiv \frac{\varepsilon_\ell}{\sigma_\ell} \tag{3.6}$$

where assumption [c] allows the simple form of the convection term. To complete the specification of the charge distribution along the tube, an effective line charge density

$$\lambda(z,t) \equiv \pi a^2\bar{\rho}(z,t) + 2\pi a\bar{\sigma}(z,t) \tag{3.7}$$

is introduced instead of the surface charge density ($\bar{\sigma}$) at the inside surface of the tube. This choice leads most directly to evaluation of the axial electric field, and to application of the boundary condition at the tube entrance when $\bar{\rho}(0,t)$ is unknown (see Sec. 3.2.5, case C). Conservation of line charge is expressed by

$$\frac{\partial\lambda}{\partial t} = -\frac{\partial I}{\partial z} \tag{3.8a}$$

where the net axial current

$$I(z,t) \equiv \pi a^2\left[U\bar{\rho} + \sigma_e E_z(a,z,t)\right] \quad ; \quad \sigma_e \equiv \left[\sigma_\ell + (2\sigma_s/a)\right] \qquad (3.8b)$$

includes conduction and convection in the liquid volume, and conduction along the inside surface of the tube via a uniform surface conductivity σ_s, but excludes conduction within the tube wall (assumption [f]). Assumption [h] allows the simple form of the conduction term and the definition of an effective axial conductivity σ_e. Equation 3.8 simply recognizes that no current flows across the curved part of the surface S_2 in Fig. 3.4 which lies within the perfectly insulating gas.

With $\bar{\rho}(0,t)$ slowly varying on the scale of the liquid residence time (assumption [i]), the temporal derivative in Eq. 3.6 is small compared with the convection term and Eq. 3.6 can be integrated immediately:

$$\bar{\rho}(z,t) = \bar{\rho}(0,t)\exp(-z/\tau_\ell U) \qquad (3.9)$$

This is substituted into Eq. 3.8 to yield

$$\frac{\partial\lambda}{\partial t} + (\pi a^2\sigma_e)\frac{\partial E_z}{\partial z}(a,z,t) = \left[\frac{\pi a^2\bar{\rho}(0,t)}{\tau_\ell}\right]\exp(-z/\tau_\ell U) \qquad (3.10)$$

That Eq. 3.10 is written with the "excitation" on the right and the "response" terms on the left is made clear in the next section where the local axial field is shown to be a linear integral function of the line charge density. This inhomogenous equation is the starting point for the analyses in the remaining sections. In Sec. 3.2.4 surface charge relaxation is treated by setting $\bar{\rho}(0,t) = 0$. In Sec. 3.2.5, Eq. 3.10 is applied to describe the charging transient for the capped cylinder configuration (Fig. 3.2), and then specialized to the sleeve configuration (Fig. 3.1) by setting $E_z(a,z,t) = 0$. Finally, the steady state governed by Eq. 3.10 with $\partial\lambda/\partial t = 0$ is discussed in Sec. 3.2.6.

3.2.3 External Fields

To complete the description of the model, Eq. 3.10 must be supplemented by a relation between $\lambda(z,t)$ and $E_z(a,z,t)$, and this comes from solution of Laplace's equation,

$$\nabla^2\Phi = 0 \quad ; \quad \Phi = \Phi(r,z,t) \tag{3.11}$$

for the potential Φ in the region outside the insulating tube. Gauss' law applied to a cylindrical volume of differential axial extent and coincident with the outer surface of the tube (S_2 in Fig. 3.4) yields

$$2\pi a(\Delta z)\varepsilon_o E_r^o + \pi a^2\varepsilon_\ell(\Delta E_z) = \lambda\Delta z \tag{3.12}$$

where ε_o and ε_ℓ are the permittivities of the free space region surrounding the tube and of the liquid, respectively. The simple form of the axial field term is allowed by assumption [h]. Neither the thickness nor the permittivity of tube wall appear in Eq. 3.12 because the former is regarded as small compared with the inner diameter (a). The electric field satifies the electro-quasistatic limit of Faraday's law if it is the negative gradient of the potential:

$$E_z(r,z,t) = -\frac{\partial\Phi}{\partial z} \quad ; \quad E_r^o(r,z,t) = -\frac{\partial\Phi}{\partial r} \tag{3.13a,b}$$

With the axial field continuous at the tube-gas interface, the field components in Eq. 3.12 are just those of Eq. 3.13 evaluated at $r = a$. Combining these two equations, and taking the limit of $\Delta z \rightarrow 0$, yields the boundary condition on the potential at the outer surface of the insulating tube

$$(\varepsilon_o)\frac{\partial\Phi}{\partial r} + \left(\frac{\varepsilon_\ell a}{2}\right)\frac{\partial^2\Phi}{\partial z^2} = -\frac{\lambda}{2\pi a} \quad ; \quad r = a \tag{3.14}$$

with additional boundary conditions on the potential being imposed by the external conductors. For the specific configuration shown in Fig. 3.4, the additional boundary conditions on the potential are

$$\Phi(r,0,t) = 0 \quad ; \quad \Phi(r,L,t) = 0 \quad ; \quad \Phi(R,z,t) = 0 \tag{3.15}$$

The complete set of solutions to Laplace's equation satisfying Eq. 3.15 is the series

$$\Phi(r,z,t) = \sum_{n}^{\infty} \Phi_n(t)B_n(R,r)\sin(k_n z) \quad ; \quad k_n = \frac{n\pi}{L} \tag{3.16}$$

where

$$B_n(\alpha,\beta) \equiv \left(I_0(k_n\alpha)K_0(k_n\beta) - I_0(k_n\beta)K_0(k_n\alpha)\right) \tag{3.17}$$

and I_n and K_n are the nth order modified Bessel functions of the first and second kinds, respectively. Application of the boundary condition Eq. 3.14 is facilitated by expressing the line charge density as a Fourier series:

$$\lambda(z,t) = \sum_{n}^{\infty} \lambda_n(t)\sin(k_n z) \tag{3.18a}$$

where

$$\lambda_n(t) \equiv (2/L)\int_0^L \lambda(z,t)\sin(k_n z)dz \tag{3.18b}$$

Now, substituting Eqs. 3.16 and 3.18a into Eq. 3.14 yields a relation among Fourier coefficients

$$\Phi_n(t) = \frac{\lambda_n(t)}{2\pi a k_n\left((\epsilon_\ell a/2)k_n B_n(R,a) + \epsilon_o C_n(R,a)\right)} \tag{3.19}$$

where

$$C_n(\alpha,\beta) \equiv \left[I_0(k_n\alpha)K_1(k_n\beta) + I_1(k_n\beta)K_0(k_n\alpha)\right] \tag{3.20}$$

Field components in the external region are expressed in terms of these coefficients by substituting Eq. 3.16 into Eqs. 3.13:

$$E_z(r,z,t) = - \sum_{n}^{\infty} \Phi_n(t)k_nB_n(R,r)\cos(k_nz) \tag{3.21}$$

and

$$E_r^o(r,z,t) = + \sum_{n}^{\infty} \Phi_n(t)k_nC_n(R,r)\sin(k_nz) \tag{3.22}$$

With no surface charge density at the <u>outer</u> surface of the insulating wall (assumption [g]), an expression for the radial electric field within the wall (Fig. 3.3) follows from Gauss' law as

$$E_r^w(z,t) = \frac{\epsilon_o}{\epsilon_w} E_r^o(a,z,t) \tag{3.23}$$

The desired relation between $\lambda(z,t)$ and $E_z(a,z,t)$ is given by Eq. 3.21 (evaluated at $r = a$) with Eqs. 3.19 and 3.18b substituted.

3.2.4 <u>Surface Charge Relaxation</u>

Unlike the bulk conductivity, the surface conductivity is not readily determined with confidence in advance. However, this parameter can be deduced from observation of the surface charge relaxation that follows interruption of the flow. When the flow, and hence the convection current at the tube inlet, is interrupted the residual volume charge relaxes to the liquid-solid interface within a few bulk relaxation times ($\epsilon_\ell/\sigma_\ell$), leaving only surface charge within the tube. Thus, the ensuing surface charge relaxation* is governed by Eq. 3.10 with $\bar{\rho}(0,t) \to 0$:

$$\frac{\partial\lambda}{\partial t} + (\pi a^2\sigma_e)\frac{\partial E_z}{\partial z} = 0 \tag{3.24}$$

---

[*] An explicit statement of surface charge conservation attributes a rate of change of surface charge to a divergence of the surface current and a bulk conduction current normal to the interface. To represent the latter contribution would require the introduction of a Laplacian potential

$$\Phi^i(r,z,t) = \sum_n^{\infty} \Phi_n^i(t) I_0(k_n r)\sin(k_n z)$$

for the charge-free region inside the tube. In terms of this potential, and that given by Eq. 3.16 for the external region, surface charge conservation is expressed by

$$\frac{\partial}{\partial t}\left[-(\epsilon_o)\frac{\partial \Phi}{\partial r} + (\epsilon_\ell)\frac{\partial \Phi^i}{\partial r}\right] = -(\sigma_\ell)\frac{\partial \Phi^i}{\partial r} + (\sigma_s)\frac{\partial^2 \Phi^i}{\partial z^2}$$

To deduce the relaxation times of the spatial modes, a second relation between the Fourier coefficients Φ_n and Φ_n^i would be obtained from the requirement that the potential be continuous, $\Phi(a,z,t) = \Phi^i(a,z,t)$.

The purpose of this footnote is to show that Eq. 3.24 is consistent with the explicit treatment. The left side of the conservation statement is equivalent to $(1/2\pi a)(\partial\lambda/\partial t)$, and it is in the same limit ($k_n a \ll 1$) that renders the axial field uniform over the tube cross section (assumption [h]) that the right side reduces to

$$\left[-(\sigma_\ell)\frac{\partial \Phi^i}{\partial r} + (\sigma_s)\frac{\partial^2 \Phi^i}{\partial z^2}\right] \rightarrow -\left(\frac{a}{2}\sigma_\ell + \sigma_s\right)\frac{\partial E_z}{\partial z} \equiv -\left(\frac{a}{2}\sigma_e\right)\frac{\partial E_z}{\partial z}$$

as can be seen by substituting the series expression for Φ^i, taking the indicated limit and making use of Faraday's law Eq. 3.13a. That the condition on $k_n a$ fails for large enough n is unimportant because the amplitudes of these higher order modes are strongly attenuated.

The generality of Eq. 3.24 could be emphasized by using Eqs. 3.13a and 3.14 to eliminate the axial field and the line charge density, giving a boundary condition on the potential in the external region that applies regardless of the external conductor configuration. This boundary condition could then be applied to the specific form Eq. 3.16 to determine the surface charge relaxation times (38). However, with a specific configuration in mind at the outset it is more direct to insert Eqs. 3.18a, 3.19, and 3.21 in Eq. 3.24, which yields the homogeneous differential equation for each Fourier coefficient:

$$\frac{d\lambda_n}{dt} + \frac{\lambda_n}{\tau_n} = 0 \quad ; \quad \lambda_n(t) = \lambda_n(0)\exp(-t/\tau_n) \qquad (3.25a,b)$$

where

$$\tau_n = \frac{\epsilon_\ell + \epsilon_o F_n(R,a)}{\sigma_\ell + (2\sigma_s/a)} \qquad (3.26)$$

and

$$F_n(\alpha,\beta) = \frac{2C_n(\alpha,\beta)}{ak_n B_n(\alpha,\beta)} \qquad (3.27)$$

The external configuration evidently plays an essential role in controlling the charge relaxation process, reflecting the fact that while dissipative processes are confined to within the tube, energy storage is primarily in the free-space region outside the tube. The more general result given by Eq. 2.1 is obtained if axial conduction within the bulk of the tube wall is included in Eq. 3.8b.

All field quantities are expressible in terms of the same set of Fourier coefficients, and hence they decay with same relaxation times. Because τ_n proves to be a decreasing function of n, the relaxation time for the fundamental spatial mode, τ_1, can be determined from relaxation data if the initial portion ($0 < t < \sim 2\tau_2$) is excluded. Thus, τ_1 can be determined from fields measured at the surface of the conducting enclosure, and σ_s follows from Eq. 3.26 as

$$\sigma_s = \frac{\epsilon_\ell + \epsilon_0 F_1(R,a)}{(2\tau_1/a)} - \frac{a}{2}\sigma_\ell \tag{3.28}$$

The surface conductivity appears only in Eqs. 3.8 and 3.26, which indicate that it must be of the order of $(a\sigma_\ell/2)$ to be significant.

3.2.5 Charging Transient

The system of equations to be solved is Eqs. 3.10 and 3.21 (supplemented by Eqs. 3.18 and 3.19). If the influent convection current $Q\bar{\rho}(0,t)$ can be regarded as imposed, then an analytical solution is available, though not in closed form. To illustrate this solution for the two experimental external conductor configurations, both cases A and B below regard the charge density at the inlet $\bar{\rho}(0,t)$ as slowly varying over the duration τ_{ex} of the experiment. Case C allows for an effect of the generated fields on the influent convection current by allowing an arbitrary temporal variation of $\bar{\rho}(0,t)$, which necessitates a numerical treatment.

A. Capped Cylinder and Imposed Influent Convection Current: While $\bar{\rho}(0,t)$ varies slowly on the scale of τ_{ex}, the latter is presumed long enough compared with τ_1 that the entire transient is of interest. The homogeneous solution to Eq. 3.10 is given by Eqs. 3.18a and 3.25b. The particular solution can be expressed as an exponential function, but to facilitate application of the initial condition, the right side of Eq. 3.10 is represented as a Fourier series of the same form as the homogeneous solution:

$$\exp(-z/d) = \sum_{n}^{\infty} e_n \sin(k_n z) \tag{3.29}$$

where

$$e_n = \left(\frac{2}{n\pi}\right)\left[\frac{1 - (-1)^n \exp(-L/d)}{1 + (L/n\pi d)^2}\right] \quad ; \quad n \text{ odd} \tag{3.30}$$

and $e_n = 0$ for n even. The characteristic length $d \equiv \tau_\ell U$. Substituting

Eqs. 3.18a, 3.19, 3.21 and 3.29 into Eq. 3.10 yields

$$\frac{d\lambda_n}{dt} + \frac{\lambda_n}{\tau_n} = \left(\frac{\pi a^2 \bar{\rho}(0,t)}{\tau_\ell}\right) e_n \tag{3.31}$$

where the τ_n are given by Eq. 3.26. With the right side of Eq. 3.31 essentially constant on the scale of the longest time constant (τ_1), and subject to the initial condition of $\lambda(z,0) = 0$, the complete solution to Eq. 3.31 is

$$\lambda_n(t) = \frac{\pi a^2 \bar{\rho}(0,t)}{\tau_\ell}\left(1 - \exp(-t/\tau_n)\right)\tau_n e_n \tag{3.32}$$

Finally, the field components are obtained from Eqs. 3.19, 3.21 and 3.22 with Eq. 3.32 substituted. These can be evaluated at points on the surface of the external conductor with appropriate values of (r,z), or evaluated at (a,z) to apply Eq. 3.23 for the electrical stress within the insulation. In retrospect, the assertion in Sec. 2.1 that the charging (Eq. 3.32) and relaxation (Eq. 3.25b) transients are characterized by the same time constants holds only as long as the influent convection current is stationary on the scale of τ_1.

B. <u>Close Fitting Sleeve and Imposed Influent Convection Current</u>: As in case A, the influent convection current varies slowly on the scale of τ_{ex}. However, the extreme aspect ratio of the tube and the proximity of the equipotential surface (Fig. 3.1) render the time that now plays the role of τ_1 (Sec. 5.3.3) long enough compared with τ_{ex} that axial conduction remains negligible. Letting $E_z \rightarrow 0$ in Eq. 3.10 yields

$$\frac{\partial\lambda}{\partial t} = \left(\frac{\pi a^2 \bar{\rho}(0,t)}{\tau_\ell}\right)\exp(-z/\tau_\ell U) \tag{3.33}$$

The assumption that $\bar{\rho}(0,t)$ is independent of the generated fields is perhaps more plausible here than in case A because the experiment ends before the axial field at the inlet becomes appreciable. In fact, this assumption receives strong support from experiments with the sleeve configuration reported in Secs. 3.3.2 and 6.2.

With the condition on $\bar{\rho}(0,t)$, Eq. 3.33 is immediately integrated with respect to time to yield

$$\lambda(z,t) = t\left[\frac{\pi a^2\bar{\rho}(0,t)}{\tau_\ell}\right]\exp(-z/\tau_\ell U) \qquad (3.34)$$

The measured quantity in this case is the rate of change of the total charge accumulated within the tube (Q_t), which is obtained by integrating Eq. 3.33 over the length of the tube

$$\frac{dQ_t}{dt} = Q\bar{\rho}(0,t)\left[1 - \exp(-L/\tau_\ell U)\right] \quad ; \quad Q \equiv \pi a^2 U \qquad (3.35)$$

With $E_z \simeq 0$ the electrical stress within the insulating wall

$$E_r^w(z,t) = \frac{\lambda(z,t)}{2\pi a\epsilon_w} = t\left[\frac{a\bar{\rho}(0,t)}{2\epsilon_w\tau_\ell}\right]\exp(-z/\tau_\ell U) \qquad (3.36)$$

follows immediately from Gauss' law and Eq. 3.34. The essentially linear increase in electrical stress with time reflects the dominance of the charge accumulation process over the leakage process for times short compared with (the counterpart of) τ_1.

C. Capped Cylinder and Arbitrary Influent Convection Current: In Abedian and Sonin's theory (Sec. 2.2) for the convection current in a conducting tube, steady electrical conditions are assumed to prevail well away from the ends of the tube. However, where the upstream conducting tube joins to the entrance of the insulating tube, the rising potential of the latter produces an unsteady electric field that penetrates into the conducting tube a distance of the order of the tube diameter. It is for now an open question whether the unsteady field in the neighborhood of the outlet of the conducting tube affects the effluent convection current communicated to the insulating tube. Thus, it is essential to allow for such an effect if tests of the model for processes in the insulating tube are to be unambiguous.

As in case A the full transient is of interest ($\tau_l < \tau_{ex}$) but now an arbitrary time dependence of $\bar{\rho}(0,t)$ is allowed to account for an effect on the influent convection current of the generated electric field. Thus, the upstream boundary condition is now expressed in terms of the measured influent current (which reflects <u>both</u> convection and conduction) rather than the initially unknown $\bar{\rho}(0,t)$. Since the generated field varies essentially on the time scale of τ_l it is reasonable to expect that $\bar{\rho}(0,t)$ does as well, and hence the latter still varies slowly relative to the liquid residence time (assumption [i]). Thus, $\bar{\rho}(z,t)$ is still given by Eq. 3.9 so that Eq. 3.10 still holds. Now, however, Eq. 3.8b must be used to eliminate the unknown $\bar{\rho}(0,t)$ in Eq. 3.31 in favor of the experimentally accessible $I(0,t)$:

$$\frac{d\lambda_n}{dt} + \frac{\lambda_n}{\tau_n} = \left[\frac{I(0,t) - \pi a^2 \sigma_e E_z(a,0,t)}{\tau_\ell U} \right] e_n \qquad (3.37)$$

where

$$E_z(a,0,t) = \sum_m^{\infty} \left[\frac{-\lambda_m(t) B_m(R,a)}{2\pi a\left[(\epsilon_\ell a/2) k_m B_m(R,a) + \epsilon_o C_m(R,a)\right]} \right] \qquad (3.38)$$

follows from Eqs. 3.19 and 3.21. As in case A only the odd spatial modes are excited. To apply this result, the series Eq. 3.38 can be truncated after k terms so that Eq. 3.37 represents a set of k coupled linear ordinary differential equations for the coefficients λ_n to be integrated numerically with the given $I(0,t)$.

3.2.6 Steady State Solution

The steady state results when axial conduction offsets the rate of increase of surface charge due to the space charge field in the liquid. Thus, there is no basis for a steady state solution for the sleeve configuration because the corresponding axial electric field has not yet been determined. That solution emerges from analysis of the same configuration in Sec. 5.3 where the small but finite axial electric field is recognized. Here, attention is confined to the capped cylinder configuration, and the steady state solution that is governed by Eq. 3.10 with $\partial\lambda/\partial t \rightarrow 0$

$$(\pi a^2 \sigma_e)\frac{\partial E_z}{\partial z} = \left[\frac{\pi a^2 \bar{\rho}(0,\infty)}{\tau_\ell}\right] \exp(-z/\tau_\ell U) \tag{3.39}$$

Substituting Eqs. 3.21 and 3.29 into Eq. 3.39 yields the relation among Fourier coefficients

$$\Phi_n(\infty) = \frac{e_n \bar{\rho}(0,\infty)}{\sigma_e \tau_\ell B_n(R,a) k_n^2} \tag{3.40}$$

where e_n is given by Eq. 3.30. With Eq. 3.40 inserted in Eqs. 3.21 and 3.22 the steady state fields are expressed in terms of the average volume charge density at the inlet. The latter can be expressed in terms of the steady state influent current I(0,∞) by recognizing that in the steady state Eq. 3.8a requires the total axial current

$$I(z,\infty) \equiv \pi a^2 \left[U\bar{\rho}(z,\infty) + \sigma_e E_z(a,z,\infty)\right] = I(0,\infty) \tag{3.41}$$

to be independent of axial position. The integration constant I(0,∞) is resolved by substituting Eq. 3.9 into Eq. 3.41 and requiring that the line integral of the axial field over the length of the tube vanish (in view of the grounded terminations):

$$\bar{\rho}(0,\infty) = \left[\frac{L/\tau_\ell U}{1 - \exp(-L/\tau_\ell U)}\right]\frac{I(0,\infty)}{\pi a^2 U} \qquad (3.42)$$

The quantity in the large parentheses is evidently the fraction of the net influent current carried by convection.

It is notable that if only the steady state potential distribution along the tube is of interest, a closed form expression can be obtained without specifying the external conductor configuration. Equations 3.9 and 3.42 are combined and the result is used to eliminate $\bar{\rho}(z,\infty)$ from Eq. 3.41, which then gives the explicit dependence of $E_z(a,z,\infty)$ on z and $I(0,\infty)$:

$$E_z(a,z,\infty) = \left\{1 - \left[\frac{L/\tau_\ell U}{1 - \exp(-L/\tau_\ell U)}\right]\exp(-z/\tau_\ell U)\right\}\frac{I(0,\infty)}{\pi a^2 \sigma_e} \qquad (3.43)$$

With respect to the grounded terminations, the potential $\Phi(a,z,\infty)$ at any point along the tube follows immediately from a line integral of E_z:

$$\Phi(a,z,\infty) = -\int_0^z E_z(a,z,\infty)dz \qquad (3.44)$$

If now the radial electrical stress $E_r^w(z,\infty)$ is desired, Laplace's equation for the potential $\Phi(r,z,\infty)$ in the external region must be solved subject to boundary conditions dictated by the specific external conductor configuration and the known potential along the tube. Then the stress follows from Eqs. 3.13b and 3.23.

3.3 Experiments

Because the model of Sec. 3.2 is phrased in terms of known material parameters (with the exception of the surface conductivity) and simple external configurations, support for the view of the charging process as a competition between accumulation and leakage tendencies can come from simple controlled experiments. Following an overview of the experimental arrangement and materials, results for the configurations shown in Figs. 3.1 and 3.2 are summarized in Secs. 3.3.2 and 3.3.3, respectively.

3.3.1 Arrangement and Materials

The experimental facility shown in Fig. 3.5 is designed with three objectives in mind: to accommodate a range of experiments, including those pictured in Figs. 3.1 and 3.2 as well as those reported in later chapters, to ensure that all significant net charge and currents can be accounted for, and to maintain the liquid conductivity. Immediately upstream and downstream of the experimental section are stainless steel tubes of the same diameter as the insulating tube and joined to the latter by Teflon unions that provide a smooth hydrodynamic transition. The upstream section serves to complete the development of the velocity profile and to generate a convection current at the inlet to the insulating tube. Under nitrogen gas pressure, liquid is forced out of the reservoir at a velocity calculated from the measured rate of change of liquid height in the glass level indicator. After the liquid inventory is exhausted, liquid is returned to the reservoir through a separate tube (not shown in Fig. 3.5) also under gas pressure.

The liquid comes into contact only with potential-constrained stainless steel surfaces and the insulating tube under test. Observed rates of change of net charge are confined to the latter because the capacitances of the metallic elements (with respect to the pressure vessels and aluminum screens) charge through the electrometer input impedances quickly on the scale τ_1 of the transient in the insulating tube. It is to allow measurement of the influent and effluent currents in the insulating tube

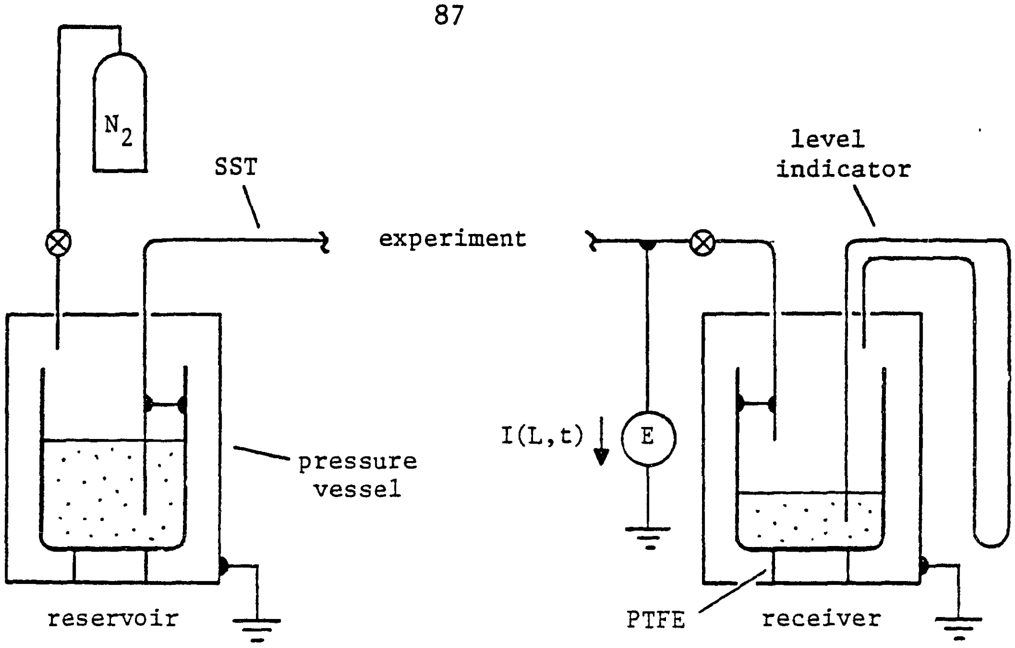

Fig. 3.5 Experimental test facility. Flow path is completed by experiments shown in Figs. 3.1 and 3.2. All tubes and beakers are stainless steel. Not shown are a dedicated three-terminal conductivity cell on the floor of the beaker in the reservoir, a PTFE tube through which spent liquid is returned to the reservoir, and sections of aluminum screen "wrapped" around the tubes and grounded to provide electrostatic shielding.

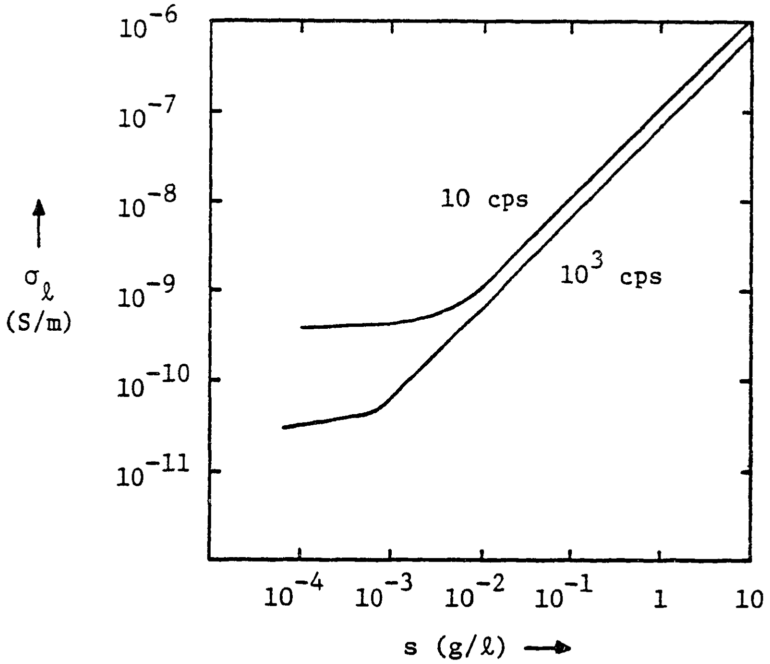

Fig. 3.6 $C_2Cl_3F_3$ conductivity measured at the indicated frequencies as a function of additive concentration. All conductivities reported in the text are measured at 200.0 cps.

that the liquid is not recirculated. The upstream section draws initially quiescent, and hence electrically neutral liquid from a reservoir of large enough dimensions compared with the tube radii that the liquid presumably remains quiescent. The influent current I(0,t) is measured by the electrometer shown in both Figs. 3.1 and 3.2, which maintains at ground potential all of the metallic sections upstream of the test section, including the reservoir. The effluent current I(L,t) returns to ground through the electrometer shown in Fig. 3.5, which is connected to all of the metallic sections downstream of the test section, including the receiver.

The insulating tubes under study are Tefzel, an ethylene-tetrafluoroethylene copolymer developed by Dupont (39, 40) with slightly superior mechanical properties than, but otherwise similar to, Teflon (polytetrafluoroethylene). The liquid is Dupont's Freon TF (41), which is a relatively pure grade of Dupont's refrigerant Freon 113 ($CC\ell_2F$-$CC\ell F_2$) with the properties indicated in Table 3.1. Liquid, as received, is filtered through silica gel into the closed experimental system, after which it is exposed only to its own vapor and the nitrogen gas. A dedicated three terminal cell immersed in the reservoir typically indicates an initial liquid conductivity of about 1.0 pS/m, as measured at 200.0 cps with a capacitance bridge. In addition to its sensitivity to moisture, the liquid conductivity can be dominated by the effects of trace materials, so once the liquid has been filtered and sealed, pumps are avoided, as are materials containing plasticizers, antioxidants, etc. In successive experiments the conductivity is gradually raised by the addition of an antistatic agent, Ethyl Corporation's DCA-48 (42) (also available from Mobil). Very small additive concentrations are involved (see Fig. 3.6) so the additive is diluted with Freon TF before being injected by syringe through a small port in one of the pressure vessels.

The conductivity as a function of additive concentration is shown in Fig. 3.6 where the linear dependence suggests a bimolecular dissociation reaction (Sec. A.2) that is not uncommon in hydrocarbon liquids (43).

TABLE 3.1

Room Temperature Data for Freon TF

formula	$CC\ell_2F\text{-}CC\ell F_2$
$\varepsilon_\ell/\varepsilon_o$	2.4
η	6.8×10^{-4}
ρ_m	1565.0
ν	4.4×10^{-7}
b^*	3.0×10^{-8}
D_m^*	8.0×10^{-10}
S_c	550.0
λ_m	$1.3 \times 10^{-10}/\sqrt{\sigma_\ell}$

* calculated as in Table 2.1

This is consistent with the polymeric structure of the additive molecules which contain 24 to 28 amine - carboxylic acid functional groups, and are thought to produce ions by a proton transfer reaction (44). This structure and ionization process make it plausible that positive and negative ions have similar mobilities, because their molecular weights will typically differ by that of the transferred proton which is small compared with the total molecular weight (~6000). Perhaps more likely is a spectrum of molecular weights and mobilities, which may still imply similar effective mobilities for positive and negative ions.

3.3.2 Close Fitting Sleeve

In the arrangement shown in Fig. 3.1, the electrometer (E) measures the influent current I(0,t) while the charge amplifier (C) records the net charge on sleeve (= $-Q_t$). As a check on the instrumentation prior to the formal experiments, the second electrometer shown in Fig. 3.5 aids in a demonstration that the relation

$$\frac{dQ_t}{dt} = I(0,t) - I(L,t) \qquad (3.45)$$

is satisfied instantaneously, as required by the law of charge conservation. Subsequently, only two of the quantities in Eq. 3.45, the influent current and net charge, are recorded.

Table 3.2 summarizes the conditions of two runs for which assumptions [a] and [b] of Sec. 3.2.1 are satisfied. The record of run 36 is shown in Fig. 3.7, where after an initial transient the measured influent current tends to a constant value. Two factors suggest that the transient in I(0,t) reflects a temporal development of the convection current generated in the upstream metallic section. First, the same transient is observed in experiments in which there are no insulating sections, like those reported in Sec. 2.2.3. Second, the fixed rate of change of Q_t following the transient indicates that conduction driven by

TABLE 3.2

Experiments with Close Fitting Sleeve

Parameter				Equation
Run Number:		36	37	
Measured:	a (mm)	1.3	1.3	
	L (m)	0.38	0.38	
	σ_ℓ (pS/m)	4.7	4.7	
	U (m/s)	0.66	1.60	
	I(0,t) (nA)	-0.15	-0.7	
	Q_t/t (nC/min)	-1.42	-4.0	
Calculated:*	$\bar{\rho}(0,t)b/\sigma_\ell$	-0.3	-0.5	3.46
	R_y	3900.0	9450.0	3.1
	λ_m (μm)	60.0	60.0	2.9
	δ (μm)	14.0	6.2	3.3
	τ_1 (min)	6030.0	6030.0	5.30†
	Q_t/t (nC/min)	-1.1	-2.1	3.35 & 3.46
Adjusted:	Q_t/t (nC/min)	-1.47	-3.0	3.5 & 3.35

* with data from Table 3.1

† with $w = 0.3$ mm and $\epsilon_w = 2.6\epsilon_o$

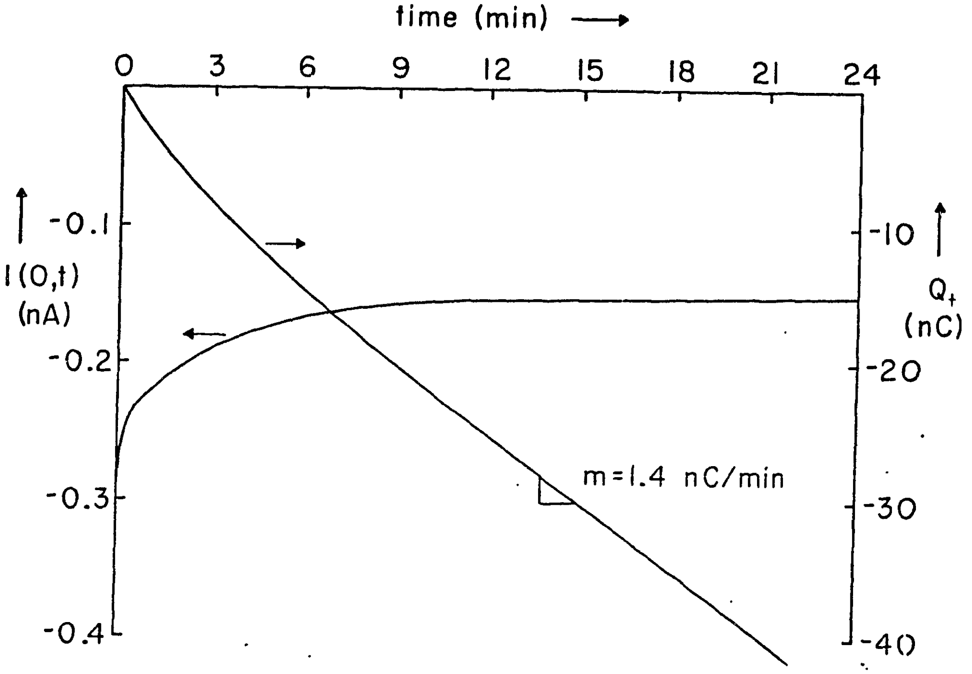

Fig. 3.7 Experimental results with close fitting sleeve configuration of Fig. 3.1. Conditions are given in Table 3.2 as run 36.

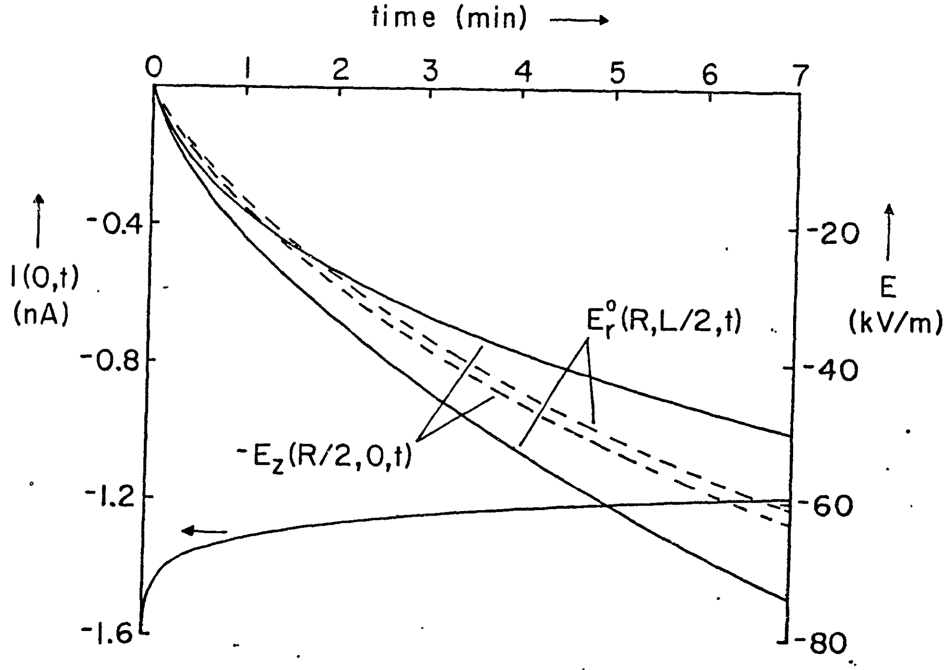

Fig. 3.8 Experimental results with capped cylinder configuration of Fig. 3.2. Conditions are given in Table 3.3 as run 60.

the generated field does not yet contribute significantly to the influent current. Thus, the ordering of times $\tau_l \gg \tau_{ex}$ and the assumption of an imposed volume charge distribution, both of which underlie case B of Sec. 3.2.5, are confirmed. Calculated values of τ_l given in Table 3.2 are also consistent with the assumed ordering of times. Results in Sec. 3.3.3 indicate that surface conduction is negligible, at least in relatively fresh tube samples used here, and thus τ_l is calculated from Eq. 5.30 with $\sigma_s = 0$ (and $\tau_w \to \infty$).

With axial conduction negligible, the volume charge density at the inlet follows from Eq. 3.8b (with $\sigma_e E_z \to 0$) as

$$\bar{\rho}(0,t) = \frac{I(0,t)}{\pi a^2 U} \tag{3.46}$$

Because $I(0,t)$ and hence $\bar{\rho}(0,t)$ vary slowly on the scale of the residence time L/U, Eq. 3.35 applies even through the transient, but is most easily applied where $I(0,t)$ is constant. Table 3.2 indicates that agreement between the measured dQ_t/dt and that calculated from Eq. 3.35 is improved by adjusting the latter to take account of the slightly enhanced conductivity at the interface. This is consistent with the integral approach used to arrive at Eq. 3.9, which actually calls for the conductivity at the interface (Eq. 3.5) when τ_ℓ is evaluated for Eq. 3.35.

3.3.3 Capped Cylinder

The external conductor in Fig. 3.2 is large enough to accommodate field probes that "view" the interior through flat tips mounted flush with, and held at the same potential as, the inside surface of the enclosure. Thus, the probes do not distort the local field, and because they are situated in regions of relatively low field intensity, discharges can be permitted to develop in the vicinity of the insulating tube without jeopardizing the instrumentation. Experiments consist of initiating the flow and recording the inlet current $I(0,t)$ and the normal fields incident on the probes, $E_r^o(R,L/2,t)$ and $-E_z(R/2,0,t)$. Just before the liquid inventory is exhausted, the flow is interrupted by a downstream valve, leaving the insulating tube full of liquid and allowing the accumulated surface charge to relax in a controlled way.

Results are found to be fairly reproducible provided that successive runs are initiated from the same electrical conditions by allowing surface charge to relax completely prior to commencing a new experiment. Table 3.3 summarizes the conditions of selected runs, and tabulates the two lowest order (and hence longest) relaxation times as calculated from Eq. 3.26 with $\sigma_s = 0$, making these values upper limits. Provided that $\bar{\rho}(0,t)$ varies on a longer time scale than τ_1, the latter characterizes both the charging and relaxation transients (see Sec. 3.2.5).

Relaxation Transient: Calculated values of τ_1 and τ_2 are disparate enough that the exponential form of the fundamental mode should be discernible in recordings of the probe responses following interruption of the flow, and this is the case. With the amplitude $A(t_o)$ and slope $m(t_o)$ of either probe response measured after a time t_o ($\sim 2\tau_2$) has elapsed since interruption of the flow, the fundamental mode relaxation time is determined from $\tau_1 = -A/m$. Indicative of the agreement between calculated and measured values of τ_1 in Table 3.3 are the small values of $2\sigma_s/a$ (from Eq. 3.28) compared with the bulk conductivities. Thus, at least for the materials and conditions investigated here, surface conduction is unimportant.

Charging Transient: The solid lines in Fig. 3.8 represent the charging transient of run 60, with flow conditions as given in Table 3.3. The calculated fundamental mode time constant (τ_1) is comparable to the duration of the natural transient in the influent convection current discussed in connection with Fig. 3.7. Thus, the latter will tend to interfere with the exponential form of the charging transient, and the analysis of case A in Sec. 3.2.5 cannot be applied. An alternative to

TABLE 3.3

Selected Experiments with Capped Cylinder

Run	R (m)	σ_ℓ	τ_1^m	τ_1^c	τ_2^c	$\|2\sigma_s/a\|$
48	0.076	2.4	173.0	176.0	48.0	0.043
51	0.051	2.4	202.0	192.0	50.0	0.12
59	0.076	41.0	12.0	10.3	2.8	5.8
60	0.076	47.0	8.0	9.0	2.4	5.8
62	0.076	52.0	8.6	8.1	2.2	2.9

notes:

time constants are in minutes; conductivities are in pS/m

superscripts 'm' and 'c' denote measured and calculated values, the latter from Eq. 3.26 with $\sigma_s = 0$

for all runs, tube radius a = 1.3 (mm) and tube length L = 0.3 (m)

Flow Conditions for Run 60

$R_y = 12000.0$ $\lambda_m = 20.0$ (μm) $\delta = 5.0$ (μm) the procedure given as case C of Sec. 3.2.5 is a direct numerical integration of Eqs. 3.6 and 3.8, as outlined in (38), with the results shown as broken lines in Fig. 3.8. As in case C, the measured influent current $I(0,t)$ supplies the upstream boundary condition. While better agreement might be obtained from more refined experimental or numerical procedure, there is strong encouragement from the favorable comparison between the experimental time scale discernible in Fig. 3.8 and that calculated for τ_1.

3.4 Discussion

The experiments tend to support a model in which the flow-induced electrical stress arises from a surface charge distribution determined by competing charge accumulation and leakage processes. The former is driven by the space charge field of charge entrained in the liquid; the latter is controlled by geometric factors and the conductivities of the liquid bulk and liquid-solid interface. The fundamental mode relaxation time τ_1 emerges as the time scale on which the surface charge and electrical stress tend towards a steady state where the axial component of the generated field drives a conduction current through the liquid that offsets the local rate of change of surface charge due to the space charge field. It is to enhance the axial field at the expense of the radial field in the tube wall that the external conductors should be configured to support image charges primarily near the ends of the tube rather than along the transverse boundary. Thus, the sleeve configuration of Fig. 3.1 illustrates to an extreme the "hotspot" created by a conductor in close proximity to the tube as it shorts out the local axial field.

The ultimate stress is that of the steady state, so Eq. 3.40 can be the basis for suggesting other steps to avoid flow-induced insulation failure. Because the bulk conductivity helps determines e_n in the numerator as well as $\bar{\rho}(0,t)$ as discussed in Sec. 2.2, its appearance in the denominator in Eq. 3.40 (through the effective conductivity) is deceptive, and further discussion is reserved for Sec. 7.1. Also left to Sec. 7.1 is a clarification of the apparently complicated dependence of the ultimate stress on tube radius (with the volume flow rate fixed). However, the surface conductivity appears only in the denominator (through σ_e), and to the extent that it exceeds $a\sigma_\ell/2$ it tends to reduce the ultimate stress. The proportionality between the stress and the influent volume charge density $\bar{\rho}(0,\infty)$ is also notable because of the leverage over the latter afforded by the antistatic additives.

It is because of side effects implied by the gradual depletion (44) of the additive from the liquid bulk that an alternative way to limit $\bar{\rho}(0,\infty)$ would be desirable. Thus, in the next chapter, the subject is the charge trapping tendency of an expansion volume when inserted in the flow just upstream of the insulating tube. To be effective, its own characteristic time must be short compared with that which governs the transient in the insulating tube (τ_1). The rest of what is required for the expansion to be effective is an indication that the accumulating charge originates primarily upstream of the insulating tube, as already suggested by previous work (Sec. 2.3.5). Thus, in Chapter 5 the sleeve configuration is taken up again, but now an expansion volume at the tube entrance limits the influent current to reveal convection currents generated within the insulating tube itself.

Chapter 4

CHARGE TRAPPING AND GENERATION IN FULLY MIXED FLOWS

4.1 Introduction

In the sense that the mean flow is obscured by essentially random turbulent motions, the flows in pumps and perhaps heat exchangers and certain other practical flow elements are best characterized as fully mixed. Much like the radial charge density profile in the fully developed pipe flow, species concentrations and the net charge density tend to be uniform in a turbulent core, while suffering variation across a diffusion sublayer at the solid boundary. This chapter explores the behavior of an expansion region where the resident liquid is presumed to be entrained and mixed by the influent liquid jet. When the diffusion sublayer thickness exceeds the Debye length the expansion region is shown to function as a charge <u>trap</u>, in the sense that the effluent convection current is less than that at the inlet. As discussed in Sec. 3.4, such an element inserted in the flow just upstream of an insulating tube can help limit the flow-induced electrical stress within the tube wall.

Limits to the trapping tendency are anticipated when the energy of the influent liquid jet increases to the point where the turbulent motions approach within a Debye length of the expansion wall. Under this condition, double layer charge is swept into the turbulent core and withdrawn by the effluent liquid stream, rendering the expansion volume a charge <u>generator</u> in that the effluent convection current can exceed that at the inlet. Thus, the ratio of the diffusion sublayer thickness to the Debye length plays a role here that is analogous to that in the charge generation process in a conducting tube (Fig. 2.3).

Without specifying whether the expansion wall is conducting or insulating, Sec. 4.2 develops an expression for the effluent convection current in terms of the influent convection current and the volume charge density at the liquid-solid interface. This general result is the basis for associating charge trapping and generating behavior with the appropriate limits of the ratio of diffusion sublayer thickness to Debye length. In experiments reported in Sec. 4.3, liquid-filled expansions uniformly exhibit charge trapping behavior, while those filled with porous media permeated by the liquid generally behave as charge generators. To show that these results are consistent with the model, empirical mass transfer correlations are invoked in Sec. 4.4 to relate the Sherwood number (diffusion sublayer thickness) to the mechanical power input and to a characteristic dimension of the expansion. The discussion in Sec. 4.5 recognizes that the trapping tendency of the liquid-filled expansion does not rule out charge generation in a pump where the mechanical power is supplied externally, and proposes modifications of the liquid-solid interface intended to inhibit charge generation for any power input.

4.2 Charge Distributions

Based on assumptions summarized next, an expression is derived in Sec. 4.2.2 for the resident volume charge in terms of the influent convection current and material and flow parameters. In Sec. 4.2.3 the electrical stress within the wall of an insulating expansion, pictured in Fig. 4.1, is related to operating conditions, but is shown to be controlled independently of the volume charge by proper design.

4.2.1 Assumptions

[a] The net charge density ρ is uniform in a turbulent core region that essentially fills the expansion volume. This presumes that turbulent motions in the core are intense enough that a Debye length based on the turbulent diffusivity ($\lambda_t \equiv \sqrt{\tau_\ell D_t}$) exceeds the characteristic linear dimension of the expansion (L_e). Thus, in the core $\rho = \bar{\rho}(t)$, a function of time alone.

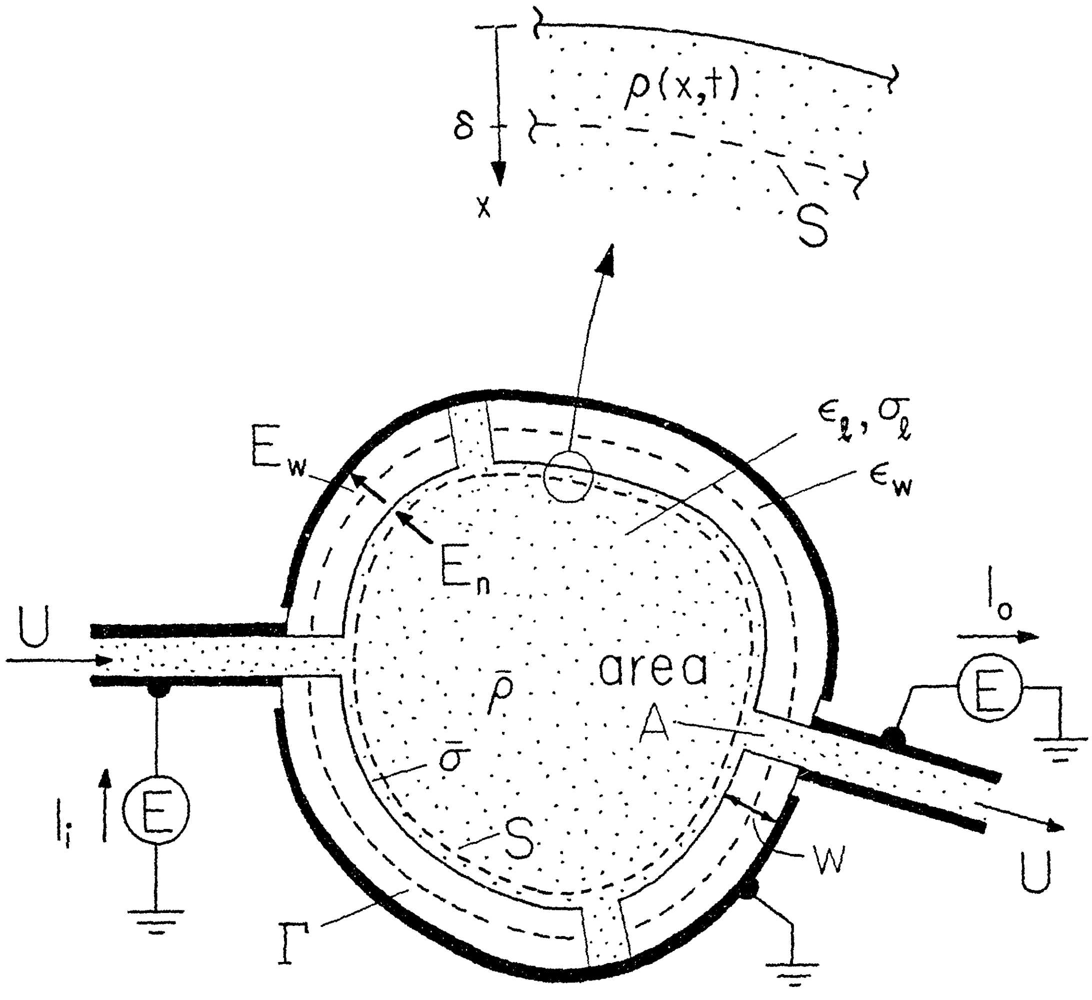

Fig. 4.1 Insulating expansion with internal volume V, bounded by the surface S. At the outer surface of the insulating wall is a grounded conducting layer. Two types of leakage channels are shown: the dead-end type containing stationary liquid in contact with the conducting layer, and those carrying the influent and effluent liquid streams.

[b] The turbulent core is bounded by a diffusion sublayer of uniform thickness δ that is small compared with the local radius of curvature of the expansion wall. The molecular diffusivity is assumed to dominate the turbulent one throughout the sublayer.

[c] Convection is negligible within the sublayer so that charge transport there is entirely by diffusion and migration.

[d] The charge density remains small (in the sense of assumption [e] of Sec. 3.2.1) so that the liquid conductivity σ_ℓ is essentially uniform throughout the expansion volume and close its value where the net charge density vanishes.

[c] The influent convection current $\bar{\rho}_i Q$ varies slowly on the scale of the charge relaxation time τ_ℓ ($\equiv \epsilon_\ell/\sigma_\ell$). This is consistent with observations. With the lowest conductivity in the vicinity of 1.0 pS/m (see Sec. 3.3.1) the longest relaxation time is of the order of 20.0 seconds. Meanwhile, transients in the flow-induced convection currents are characterized by time constants of the order of minutes (see Sec. 3.3.2).

4.2.2 Volume Charge

With assumption [d], the term in Eq. A.9 containing the gradient of the conductivity can be neglected, and with Gauss' law, this equation can be written in a form more convenient for present purposes as

$$\frac{\partial \rho}{\partial t} = -\bar{v}\cdot\nabla\rho - \nabla\cdot\bar{J} \tag{4.1a}$$

where

$$\bar{J} = \sigma_\ell \bar{E} - D_e \nabla\rho \tag{4.1b}$$

is the net current density, in which D_e is the local diffusivity. The convection of charge by the turbulent velocity fluctuations is accounted for by the diffusion term in Eq. 4.1, while the explicit convection term involves the mean velocity $\bar{v}$ which is presumed to be negligible everywhere except at the ports.

Core Region: With assumption [a] the effluent liquid contains volume charge of the uniform density $\bar{\rho}(t)$ prevailing through out the expansion, and carries a convection current $\bar{\rho}Q$, where Q is the volume flow rate. Integration of Eq. 4.1a over the volume V enclosed by the surface S in Fig. 4.1 yields

$$\frac{d\bar{\rho}}{dt} = -\frac{1}{V}\int_S (\bar{J}\cdot\bar{n})da + \frac{(\bar{\rho}_i - \bar{\rho})}{\tau_r} \quad ; \quad \tau_r \equiv \frac{V}{Q} \qquad (4.2)$$

where $\bar{n}$ is the outward directed normal vector, τ_r is the liquid residence time in the expansion, $\bar{\rho}_i Q$ is the influent convection current and Gauss' theorem was used to convert the volume integral to one over the bounding surface. It remains to relate the normal current density $\bar{J}\cdot\bar{n}$ to $\bar{\rho}$ by solving Eq. 4.1 for the volume charge distribution $\rho(x,t)$ in the diffusion sublayer.

Diffusion Sublayer: With the surface S in Fig. 4.1 coincident with the edge of the diffusion sublayer at $x = \delta$, the surface integral in Eq. 4.2 can be elaborated using Eq. 4.1b

$$\int_S (\bar{J}\cdot\bar{n})da = \int_S \left(\sigma_\ell \bar{E}\cdot\bar{n} + D_m\frac{\partial\rho}{\partial x}(\delta)\right)da = \frac{\bar{\rho}V}{\tau_\ell} + D_m\int_S \frac{\partial\rho}{\partial x}(\delta)da \qquad (4.3)$$

where x is defined within the sublayer as the distance measured from the interface into the liquid (Fig. 4.1), and Gauss' law was used to write the second equality. With assumption [e], the time derivative in Eq. 4.1 can be neglected compared with the conduction term. To specialize Eq. 4.1 for the diffusion sublayer, the convection term is also neglected (assumption [c]) and $D_e \rightarrow D_m$ (assumption [b]):

$$\frac{\partial^2\rho}{\partial x^2} - \frac{\rho}{\lambda_m^{\,2}} \simeq 0 \quad ; \quad \rho = \rho(x,t) \tag{4.4}$$

where λ_m is the Debye length given by Eq. 2.9. With $\rho(\delta,t) \simeq \bar{\rho}(t)$ the solution to Eq. 4.4 is expressed in terms of the values of ρ at the boundaries of the sublayer as

$$\rho(x,t) = \left[\frac{\bar{\rho}(t) - \rho(0,t)\cosh(\delta/\lambda_m)}{\sinh(\delta/\lambda_m)}\right]\sinh(x/\lambda_m) + \rho(0,t)\cosh(x/\lambda_m) \tag{4.5}$$

With Eq. 4.5 substituted, Eq. 4.3 yields

$$\int_S (\bar{J}\cdot\bar{n})da = \bar{\rho}(t)\left[\frac{V}{\tau_\ell} + \frac{SD_m}{\lambda_m}\coth(\delta/\lambda_m)\right] - \rho(0,t)\left[\frac{SD_m}{\lambda_m}\operatorname{csch}(\delta/\lambda_m)\right] \tag{4.6}$$

where the uniformity of δ, $\rho(0,t)$, and $\bar{\rho}(t)$ on S allowed immediate evaluation of the surface integral.

<u>Effluent Convection Current</u>: Substituting Eq. 4.6 into Eq. 4.2 yields a differential equation for volume charge in the turbulent core

$$\frac{d\bar{\rho}}{dt} + \frac{\bar{\rho}}{\tau_a} = \frac{\bar{\rho}_i}{\tau_r} + \frac{\rho(0,t)}{\tau_b} \tag{4.7a}$$

where

$$\tau_a \equiv \tau_\ell\left[1 + \frac{\tau_\ell}{\tau_r} + \frac{\lambda_m}{L_e}\coth(\delta/\lambda_m)\right]^{-1}$$

and (4.7b)

$$\tau_b \equiv \tau_\ell\left[\frac{\lambda_m}{L_e}\operatorname{csch}(\delta/\lambda_m)\right]^{-1}$$

where $L_e \equiv V/S$ is the linear dimension of the expansion. Although $\rho(0,t)$ remains to be specified, it does not vary independently of $\bar{\rho}$ or $\bar{\rho}_i$. Thus, the particular solution of Eq. 4.7a prevails because the homogeneous solution is characterized by a time $\tau_a < \tau_\ell$, while $\bar{\rho}_i(t)$ varies slowly on the scale of τ_ℓ (assumption [e]). In the limit $\lambda_m << \delta$, and exploiting the inevitable inequality $\lambda_m << L_e$, the particular solution reduces to

$$\bar{\rho}(t) \simeq \frac{\bar{\rho}_i(t)}{1 + \tau_r/\tau_\ell} \tag{4.8}$$

Because this limit implies a short charge relaxation time (τ_ℓ) compared with a diffusion time (δ^2/D_m) based on the sublayer thickness, it is not surprising that Eq. 4.8 is what would result if diffusion is neglected at the outset. In this migration limit the effluent convection current ($\bar{\rho}Q$) is less than that at the inlet ($\bar{\rho}_iQ$) and a trapping efficiency can be defined:

$$E \equiv \frac{\bar{\rho}_i - \bar{\rho}(t)}{\bar{\rho}_i} = \frac{1}{1 + \tau_\ell/\tau_r} \tag{4.9}$$

which increases as the ratio of the residence to relaxation times increases. In the opposite limit ($\lambda_m >> \delta$) the particular solution to Eq. 4.7 reduces to

$$\bar{\rho}(t) \simeq \frac{\tau_\ell}{\tau_r}\left[\frac{\bar{\rho}_i(t) + (\lambda_m^2/\delta L_e)\rho(0,t)}{1 + \tau_\ell/\tau_r + (\lambda_m^2/\delta L_e)}\right] \tag{4.10}$$

Unless the two terms containing the Debye length are significant, this result is no different from the migration limit Eq. 4.8. Thus, the condition $\lambda_m >> \delta$ is evidently a necessary but insufficient one for charge generation. An additional condition emerges in Sec. 4.4 where a boundary condition is suggested for $\rho(0,t)$, and empirical mass transfer correlations are invoked to relate δ to the power in the influent liquid jet.

4.2.3 Surface Charge in Insulating Expansions

As long as the steady state influent and effluent convection currents differ there will be a tendency for the inner surface of the insulating wall to collect a surface charge. The surface charge generates both an electrical stress within the insulating wall and a leakage current through conduction paths in the liquid that tends to reduce the surface charge density. If the dielectric strength of the wall permits, both the electrical stress and the leakage current increase until the latter offsets the difference in convection currents. The objectives of this section are to relate the ultimate electrical stress to operating conditions, and to show how that stress can be rendered tolerable regardless of the required trapping efficiency by creating additional leakage paths through the insulating wall.

In the configuration shown in Fig. 4.1, a conducting layer applied directly to the outer surface of the wall plays the role of the sleeve in Fig. 3.1 by constraining the electric field in the wall E_w to be essentially normal to the wall. The same layer seals and terminates the dead-end liquid channels that form leakage paths of predictable conductance. The resistance encountered by the net leakage current (I_N) is assumed to be dominated by that of the channels, and thus the variation in the potential Φ over the inner surface of the insulating wall is small compared with the potential drop across the wall. With the potential regarded as essentially uniform over the inner surface, the net leakage current is given by

$$I_N \simeq \sum_{i}^{N} \Phi G_i = \Phi N G = \Phi N \left(\frac{\sigma_\ell A}{w} \right) \tag{4.11}$$

where the summation is over N channels, and G_i is the conductance of the ith channel. For simplicity, all channels are taken to be identical, each with cross sectional area A and length w equal to the wall thickness (Fig. 4.1). Of course, the channels that carry the influent and effluent liquid contribute to the total conductance as well.

An estimate of the steady state stress is obtained by equating the net leakage current I_N to the difference between the steady state convection currents $(\bar{\rho}_i - \bar{\rho})Q$. Then from Eqs. 4.2 and 4.11

$$E_w \simeq \frac{\Phi}{w} \simeq \frac{1}{NA\sigma_\ell}\int_S (\bar{J}\cdot\bar{n})da \tag{4.12}$$

where the condition is implicit that the typical radius of curvature ($\sim L_e$) greatly exceeds the wall thickness (w). With Eq. 4.6 substituted, and in the migration limit $\lambda_m \ll \delta$ where Eq. 4.8 applies, the steady state stress is given by

$$E_w \simeq \frac{\bar{\rho}_i V}{NA\epsilon_\ell(1 + \tau_r/\tau_\ell)} \simeq \frac{(\bar{\rho}_i Q)E}{NA\sigma_\ell} \tag{4.13}$$

Here, the inequality $\lambda_m \ll L_e$ was used again, and the efficiency E was introduced using Eq. 4.9. The result indicates that, for a given efficiency and influent convection current $(\bar{\rho}_i Q)$, the stress can always be reduced by increasing either the number (N) or the cross sectional areas (A) of the dead-end channels. It is this leverage over the leakage process that makes it possible to regard the efficiency (Eq. 4.9) and the steady state stress (Eq. 4.13) as independent design issues. If it is of interest, the steady state stress generated in the thin sublayer limit ($\lambda_m \gg \delta$) can also be obtained from Eqs. 4.6 and 4.12.

While the transient in the electrical stress is of no practical consequence, it provides additional basis for testing the model. The rate of change of the average stress is related to that of the average surface charge density ($\bar{\sigma}$) by Gauss' law applied to the closed surface Γ in Fig.

4.1:

$$\frac{dE_w}{dt} = \frac{1}{\varepsilon_w}\frac{d\bar{\sigma}}{dt} \simeq \frac{1}{\varepsilon_w S}\left[\int_S (\bar{J}\cdot\bar{n})da - I_N\right] \qquad (4.14)$$

The first equality recognizes that the volume charge typically makes a negligible contribution to a stress that is significant on the scale of the dielectric strength. The time that plays the role here that τ_1 plays for the insulating tube in Chapter 3 is identified from Eq. 4.14 by using Eqs. 4.11 and 4.12 to express I_N and E_w in terms of the potential Φ. The result

$$\tau_1 = \left[\frac{w}{NA\sigma_\ell}\right]\left[\frac{S\varepsilon_w}{w}\right] \qquad (4.15)$$

is written so as to make clear its origin in the "lumped" resistance associated with the N channels, and capacitance formed by the liquid and the outer conducting layer as electrodes and the wall as the dielectric. This time, which characterizes the transient in the electrical stress, is longer than that characterizing the transient in the effluent convection current ($\tau_a \simeq E\tau_\ell < \tau_\ell$) essentially by a factor of

$$\frac{\tau_1}{\tau_a} \simeq \frac{S}{NA}\frac{\varepsilon_w}{\varepsilon_\ell}\frac{1}{E}$$

that is, the ratio of the surface area of the expansion to the net cross sectional area of the channels, multiplied by two factors that are close to unity.

4.3 Experiments

There are two ways in which the experiments can lend support to the model of the preceding section. First, at issue for both insulating and conducting expansions, is whether the influent and effluent convection currents conform to or depart from the migration limit (Eq. 4.8) under the conditions consistent with those identified by the model. Second, for the insulating expansion, an indication that the ultimate electrical stress is correctly represented by Eq. 4.13 can come from comparison of the observed time constants with those predicted by Eq. 4.15.

4.3.1 Arrangement and Procedure

Experiments were conducted with five cylindrical expansions, two with insulating, and three with conducting walls, as described in Table 4.1. In the 2-port expansions, liquid is injected and withdrawn through ports at opposite ends of the cylinder axis. Mixing is likely to be more complete in the 3-port expansions, like that illustrated in Fig. 4.2, where liquid is injected through ports at both ends of the cylinder axis, and withdrawn through a port on the curved part of the cylinder midway between the ends. For the insulating expansions, a close fitting conducting enclosure at the outer surface of the insulating wall is maintained virtually at ground potential by a charge amplifier. There are no dead-end channels like those illustrated in Fig. 4.1, so the controlled leakage paths include only those channels through which liquid enters and exits the expansion. The expansions are either filled with liquid or packed with a biphasic material such as steel wool or fiberglass permeated by the liquid. In the latter case, the packed expansion is flushed with samples of the liquid under study before installation in the flow loop.

The experimental arrangement is essentially that described in Sec. 3.3.1 but with the insulating tube replaced by an expansion volume, as shown in Fig. 4.3. The tubes that communicate liquid to the expansion are electrically isolated from the latter (conducting expansion) or its con-

TABLE 4.1

Descriptions of Experimental Expansions

expansion	material	volume (m^3)	$\tau_1 \sigma_\ell$	inlet ports	outlet ports
A	Teflon	3.3×10^{-5}	$\sim 2.0 \times 10^{-8}$	1	1
B	Plexiglas	1.0×10^{-3}	$\sim 1.2 \times 10^{-7}$	2	1
C	Brass	3.3×10^{-5}	—	1	1
D	Brass	3.3×10^{-5}	—	2	1
E	Brass	1.0×10^{-3}	—	2	1

notes:

$\tau_1 \sigma_\ell$ is calculated from Eq. 4.15

tubes connected to the expansions have radii a = 1.3 (mm)

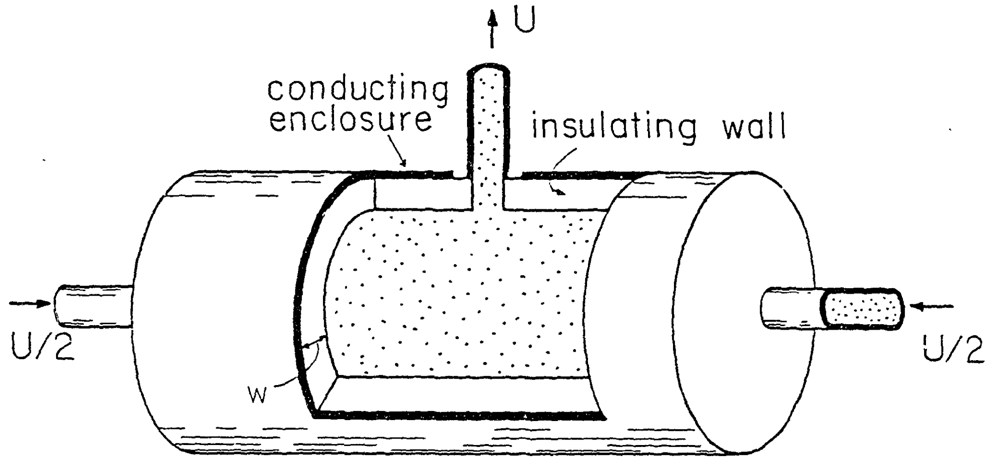

Fig. 4.2 Three-port insulating expansion corresponding to expansion B in Table 4.1.

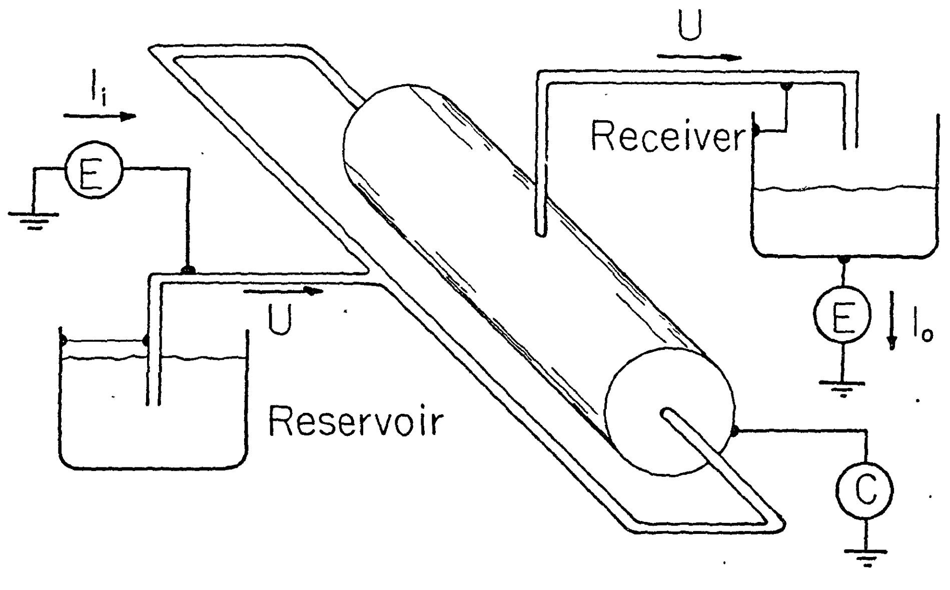

Fig. 4.3 Experimental arrangement showing three-port expansion, electrometers E and charge amplifier C. The stainless steel tubes are electrically isolated from the expansion or its conducting enclosure.

ducting enclosure (insulating expansion). Three measurable quantities are the net influent and effluent currents and either the current drawn by a conducting expansion or the net charge on the conducting enclosure of an insulating expansion. As a check on the instrumentation, these three quantities are shown to be consistent with a statement of charge conservation like Eq. 3.45, after which only two (typically the influent current and the expansion charge or current) need be recorded. With no dead-end channels in the insulating expansions, and provided that the wall is perfectly insulating on the time scale of the experiment, all of the leakage current (I_N) reaches ground through the electrometers via the stainless steel tubes. Thus, all of the charge on the conducting enclosure is "counted" by the charge amplifier which then indicates the (negative of the) net charge within the insulating expansion and, with Gauss' law, the electrical stress in the wall. Because charge convection and leakage proceed through common channels, the convection currents can be isolated only for times much <u>shorter</u> than the time constant τ_1 identified in Sec. 4.2.3. Meanwhile, for both the conducting and insulating expansions, the quasistationary charge densities in Eqs. 4.8 to 4.10 can only be measured <u>after</u> a time τ_a (Eq. 4.7b) has elapsed since commencement of the flow.

4.3.2 <u>Results</u>

Results for the expansions described in Table 4.1 are arranged in Table 4.2 according to their letter designations. Along with the influent and effluent currents, I_i and I_o, the Reynolds number R_y of the flow in the stainless steel tubes is tabulated to give an idea of the relative residence times, as well as for reference in Sec. 4.4. Measured and calculated efficiencies, E_m and E_c, are determined respectively from the first and second expressions for E in Eq. 4.9 using

$$\bar{\rho}_i = I_i/Q \quad ; \quad \bar{\rho} = I_o/Q$$

TABLE 4.2

Selected Experiments with Expansions*

Run†	σ_ℓ	R_y	$\tau_1\sigma_\ell$	$-I_i$	$-I_o$	E_m	E_c
31 A	4.7	7300.0	1.0×10^{-8}	0.35	0.15	0.57	0.54
32 A	4.7	11000.0	1.0×10^{-8}	0.65	0.35	0.46	0.44
33 A	4.7	14000.0	1.4×10^{-8}	0.90	0.60	0.33	0.38
34 A	4.7	16000.0	0.5×10^{-8}	1.1	0.75	0.32	0.36
69 B	47.0	16000.0	4.1×10^{-7}	2.1	0.1	0.95	0.99
81 B	130.0	16000.0	3.1×10^{-7}	0.9	0.1	0.90	0.998
21 C	4.7	6500.0	—	0.6	0.23	0.62	0.56
22 C	4.7	11000.0	—	1.1	0.48	0.56	0.45
23 C	4.7	14000.0	—	1.5	0.70	0.53	0.40
151 D	7.6	12000.0	—	0.62	0.3	0.52	0.54
152 D	7.6	18000.0	—	1.1	0.68	0.38	0.44
153 D	3.3	12000.0	—	0.44	0.32	0.27	0.34
154 D	3.3	18000.0	—	0.85	0.65	0.24	0.26
155 D	7.6	12000.0	—	0.55	2.4	steel wool	
156 D	7.6	18000.0	—	0.88	4.0	steel wool	
134 E	1.4	12000.0	—	—	0.015	—	—
138 E	7.0	12000.0	—	—	0.002	—	—
142 E	17.0	12000.0	—	—	0.004	—	—

* subscripts 'm' and 'c' denote measured and calculated efficiencies
σ_ℓ in pS/m ; $\tau_1\sigma_\ell$ in s-pS/m ; I_i and I_o in nA

† letters identify corresponding entry in Table 4.1

For the insulating expansions these currents are measured at a time such that $\tau_a << t << \tau_l$, while for the conducting expansions only the condition $t >> \tau_a$ is required. Much as in experiments with the insulating tube (Sec. 3.3.3) τ_l is calculated from the amplitude and slope of the charge amplifier response following interruption of the flow by a valve downstream of the expansion. Three features of the results are notable:

First, for the runs with liquid-filled expansions (that is, excluding the last five entries in Table 4.2) the satisfactory agreement between E_m and E_c is evidence that the migration limit Eq. 4.8 applies, either because $\lambda_m << \delta$ or because the terms containing the Debye length in Eq. 4.10 are sufficiently small. Agreement is found for both conducting and insulating expansions, consistent with the absence of any wall parameter in Eq. 4.8. For one of the runs with an insulating expansion, the record shown in Fig. 4.4 illustrates (1) the expected transient in the effluent current characterized by a time of the order of τ_a, (2) the transient in the influent current generated upstream that is familiar from Sec. 3.3.2 and (3) the relaxation of the accumulated surface charge (following interruption of the flow) from which τ_l is calculated.

Second, for the runs in which steel wool fills the expansion (155 and 156) the effluent current exceeds that at the inlet, indicating that Eq. 4.8 does not apply. As illustrated in Fig. 4.5 for one of these runs, the effluent current is not characterized by a single value, so those reported in Table 4.2 are final values. Results for expansions packed with fiberglass were too erratic to characterize, but for at least some of these runs the effluent current was the larger.

Third, the measured values of $\tau_l\sigma_\ell$ are in fair agreement with the approximate calculated values in Table 4.1, lending support to the simple picture in Sec. 4.2.3 of the surface charge evolution. The consistency between runs 69 and 81 with significantly different conductivities gives some confirmation that leakage through the insulating wall does not compete with that through the liquid.

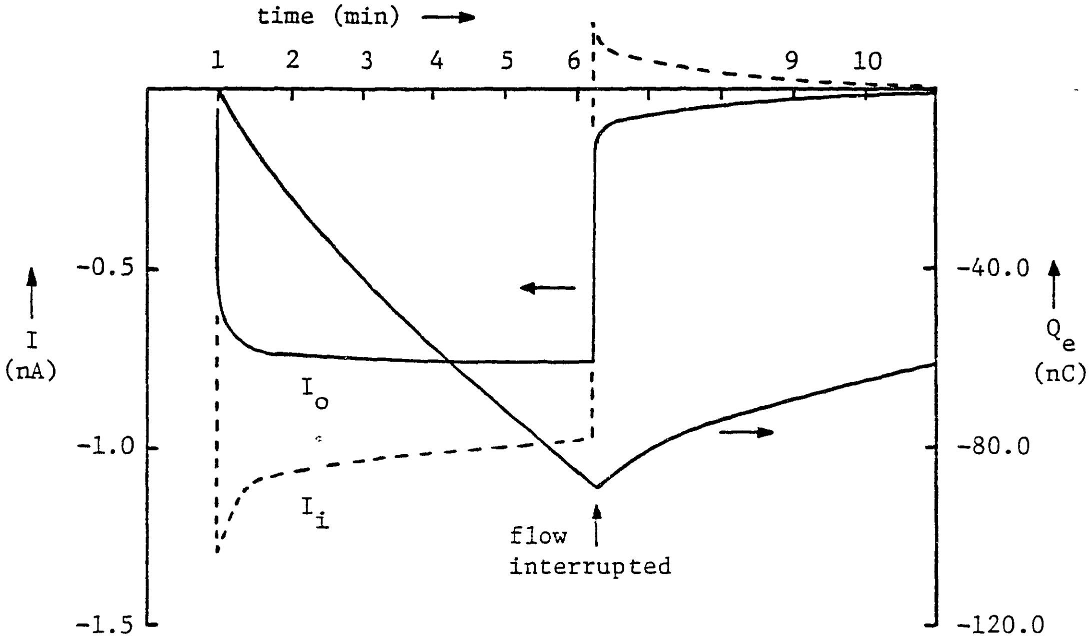

Fig. 4.4 Experimental results with liquid-filled insulating expansion. Q_e is the net charge within the expansion. Conditions are given in Table 4.2 as run 34. Residence time $\tau_r = 2.5$ s and relaxation time $\tau_\ell = 4.5$ s.

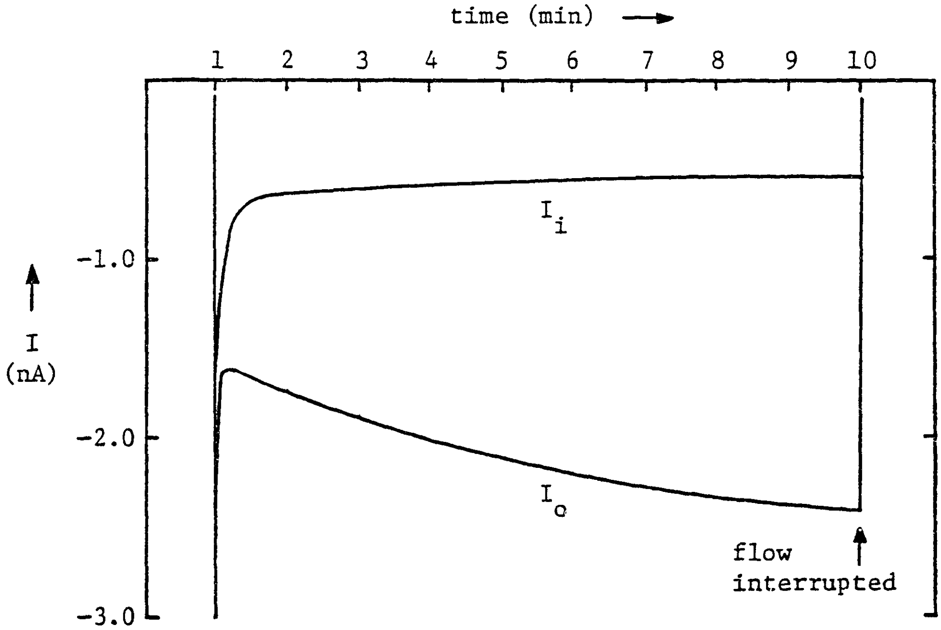

Fig. 4.5 Experimental results with conducting expansion packed with steel wool. Conditions are given in Table 4.2 as run 155. Residence time $\tau_r = 3.2$ s and relaxation time $\tau_\ell = 2.8$ s.

With a view towards experiments discussed in Chapter 5, which call for a negligible current at the entrance to an insulating tube, the objective in the runs with the liquid-filled expansion E was to minimize the effluent current. Accordingly, an effort was made to minimize the current generated upstream of the expansion, much as for the test section in the experiment of Sec. 2.2.3. Because that influent current was not measured, there is no comparison of efficiencies in Table 4.2. Nevertheless, the effluent currents are given for comparison with the typically much larger currents encountered in the experiments with insulating tubes in Sec. 3.3.

4.4 Criteria for Trapping and Generation

The particular solution of Eq. 4.7 is a general result whose usefulness is compromised by uncertainty about the wall charge density $\rho(0,t)$ and by the tenuous assumption of a well-defined diffusion sublayer of uniform thickness δ. Nevertheless, when δ is large enough to justify the migration limit (Eq. 4.8), neither $\rho(0,t)$ nor δ enters explicitly, which ultimately accounts for the satisfactory agreement between measured and calculated efficiencies in experiments with liquid-filled expansions. In the next two subsections, values are suggested for $\rho(0,t)$ and δ with the limited objectives of clarifying the condition under which Eq. 4.10 reduces to Eq. 4.8, and of showing that this condition is satisfied for the liquid-filled expansions but not for those packed with steel wool.

4.4.1 Conditions on the Sherwood Number

To exploit mass transfer correlations reported in the literature, δ must be eliminated from Eq. 4.10 in favor of the Sherwood number. From the definitions of the mass transfer coefficient k_m and the Sherwood number S_h (45) the latter is related to the effective diffusion sublayer thickness δ by

$$S_h \equiv \frac{k_m L_e}{D_m} \equiv \frac{r_m L_e}{(\Delta c) D_m} \simeq \frac{L_e}{\delta} \qquad (4.16)$$

Here, Γ_m is the flux density due to diffusion, Δc is the concentration difference between the interface and the solution bulk, and δ is assumed to characterize the concentration gradient so that $\Gamma_m \simeq (\Delta c)D_m/\delta$. Introducing this relation into Eq. 4.10 yields

$$\bar{\rho}(t) \simeq \frac{\tau_\ell}{\tau_r}\left[\frac{\bar{\rho}_i(t) + (\lambda_m/L_e)^2 S_h \rho(0,t)}{1 + \tau_\ell/\tau_r + (\lambda_m/L_e)^2 S_h}\right] \quad ; \quad \delta << \lambda_m \qquad (4.17)$$

To draw conclusions from this result, it is postulated that the wall charge density remains close to its value for an undisturbed double layer, so that $\rho(0,t) \simeq \rho_w$ where ρ_w is given by Eq. 2.12. To be definite about the influent volume charge, which is supplied by a conducting tube in the experiments, the associated convection current $\bar{\rho}_i Q$ is identified with the fully developed convection current given by Eq. 2.11 in the limit of highly turbulent flow ($\delta_u << \lambda_m$) in the tube:

$$\bar{\rho}_i = \frac{I_s(\infty)}{Q} \simeq \rho_w\left[1 + \frac{a\delta_u}{2\lambda_m^2}\right]^{-1} \qquad (4.18)$$

The subscript 'u' identifies the variable with the upstream tube. It is omitted from ρ_w and λ_m because their magnitudes are independent of both flow conditions and the solid phase, by assumption in the case of ρ_w. For the experimental conditions of Sec. 4.3, the factor multiplying ρ_w in Eq. 4.18 ranges from about 0.1 to unity, the upper limit corresponding to the lowest conductivities. With these characterizations of $\rho(0,t)$ and $\bar{\rho}_i$, Eq. 4.17 reduces to Eq. 4.8 when

$$S_h << \left[\frac{L_e}{\lambda_m}\right]^2 \quad \text{or} \quad \frac{\lambda_m^2}{\delta L_e} << 1 \qquad (4.19)$$

Thus, Eq. 4.19 is one of two sufficient conditions for validity of the migration limit (Eq. 4.8), the other condition being $\delta \gg \lambda_m$. Accordingly, there are two <u>necessary</u> conditions for departure from charge trapping behavior: $\delta \ll \lambda_m$ and

$$S_h \gg \left[\frac{L_e}{\lambda_m}\right]^2 \quad \rightarrow \quad \bar{\rho}(t) \simeq \rho(0,t) \simeq \rho_w \qquad (4.20)$$

for which the effluent convection current ($\sim\rho_w Q$) is of the order of the fully developed convection current predicted for a conducting tube, independent of conditions upstream of the expansion. To assess the practical importance of these limits it remains only to relate the Sherwood number to flow conditions.

4.4.2 Mass Transfer Correlations

In a large number of empirical studies involving agitated liquids, the Sherwood number has been found to be proportional to the product of powers of other dimensionless numbers that characterize the configuration, liquid properties and flow conditions. The conditions which justify the Chilton-Colburn analogy (<u>46</u>, p. 645) are not too restrictive, so the mass transfer counterparts of the heat transfer correlations developed from related studies (<u>47</u>) can be cited as well. In the majority of these studies the mixing is induced by a driven impeller, so the correlations as formulated are most directly applicable to pumps. Nevertheless, when the condition for local isotropic turbulence (<u>45</u>, p. 20) is satisfied, these correlations can be expressed in terms of the mechanical power input per unit volume, permitting application to a jet-mixed expansion.

The mass transfer correlations proposed for a variety of configurations are similar enough that the magnitude of S_h can be estimated without specifying details of the configuration. An expression for the mass transfer coefficient that has successfully correlated data on heat and mass transfer to fixed bodies (e.g. heat transfer jackets) submerged in agitated liquids is (<u>45</u>, p. 78)

$$k_m = 0.13\ (S_c)^{-2/3} \left[\frac{(P/V)\eta}{\rho_m^2}\right]^{1/4} \quad ; \quad S_c \equiv \frac{\nu}{D_m} \tag{4.21}$$

where P/V is the mechanical power input per unit volume and η, ν and ρ_m are, respectively, the absolute and kinematic viscosities and the mass density. The Sherwood number follows from Eq. 4.16 as

$$S_h = 0.13\ (S_c)^{1/3} \left[\frac{L_e P}{\nu^3 \rho_m}\right]^{1/4} \tag{4.22}$$

where the relation $V \simeq L_e^3$ was used. For the jet-mixed expansion, the power input is expressible in terms of the the volume flow rate Q and the pressure drop from the inlet (p_i) to the outlet (p_o) channel (48, p. 176):

$$P = (\Delta p)Q \quad ; \quad \Delta p \equiv p_i - p_o \tag{4.23}$$

With the expansion dimension (L_e) large compared with the channel radius (a), the contraction at the outlet accounts for practically the entire pressure drop, which is approximately (49, p. 67)

$$\Delta p \simeq 0.75 \rho_m U^2 \tag{4.24}$$

With Eqs. 4.23 and 4.24 substituted, Eq. 4.22 becomes

$$S_h \simeq 0.1\ (S_c)^{1/3} (R_y)^{3/4} (L_e/a)^{1/4} \quad ; \quad R_y \equiv \frac{2aU}{\nu} \tag{4.25}$$

For the expansions in Table 4.1 the factor involving L_e/a ranges from about 2.4 to 3.2, and thus Eq. 4.25 is essentially the same as the correlations proposed for heat transfer to jacketed walls in impeller-mixed vessels (47, p. 284), if the Schmidt number is replaced by the Prandtl number and the Reynolds number is replaced by one based on the impeller dimension and angular velocity. As noted, use of Eq. 4.21 is justified only under conditions of local isotropy, that is, when the scale of the primary eddies (L_e) vastly exceeds the Kolmogoroff scale (L_k):

$$L_k \equiv \frac{(\eta)^{3/4}}{(\rho_m)^{1/2}\,(P/V)^{1/4}} \simeq \frac{(a)^{1/4}\,(L_e)^{3/4}}{(R_y)^{3/4}} << L_e \qquad (4.26)$$

where Eqs. 4.23 and 4.24 have been used, and the final inequality holds in view of the high Reynolds numbers involved (Table 4.2).

With the Schmidt number of Table 3.1, Eq. 4.25 specializes to

$$S_h \simeq (R_y)^{3/4}\,(L_e/a)^{1/4} \qquad (4.27)$$

For the experimental conditions summarized in Tables 4.1 and 4.2 ($L_e \leq 0.1$, $a \simeq 10^{-3}$, $R_y < 2 \times 10^4$) S_h is at best of the order of 10^4. With δ obtained from Eq. 4.16, and λ_m from Table 3.1, the ratio δ/λ_m ranges from less than to greater than unity. However, the inequality Eq. 4.19 is easily satisfied which is sufficient to validate Eq. 4.8, consistent with the experimental results for the liquid-filled expansions.

The charge trapping tendency of the liquid-filled expansions does not preclude charge generation in a pump for which the Sherwood number given by Eq. 4.22 must be re-evaluated based on the externally supplied mechanical power. It is also tempting to apply the developments of Secs. 4.2 and 4.4 to the expansions packed with steel wool (and to some practical filter elements) by recognizing that the characteristic length (L_e) emerges in Eq. 4.10 from the ratio of the liquid volume to the area of the liquid-solid interface. Relative to the liquid-filled expansion, that volume is decreased while the surface area is vastly increased by the inserted material, leading to a much smaller characteristic length and a greater likelihood that the conditions for charge generation are satisfied. Here again, the power input must be re-evaluated, but more important is the recognition that as long as the liquid "ports" are localized, the flow and hence the mass transfer process are now likely to be highly nonuniform.

4.5 Discussion

Two aspects of the behavior of the liquid-filled expansion render it a candidate for use in the coolant circulation system. First, both of the sufficient conditions for charge trapping ($\lambda_m << \delta$ or $\lambda_m^2 << \delta L_e$) and the condition for high trapping efficiency ($\tau_r >> \tau_\ell$) are consistent in their dependence on σ_ℓ, L_e and R_y, and one of the sufficient conditions was easily satisfied with modest experimental volumes. Second, Eq. 4.7 indicates that the expansion operates at full efficiency within a time ($\tau_a < \tau_\ell$) short compared with that which characterizes the charging transient in the insulating tube ($\tau_1 >> \tau_\ell$, Sec. 3.2.5).

As noted in Sec. 4.4.2, charge generation is more likely in both filters (due to the small characteristic length) and in pumps (due to the externally supplied mechanical power). In the case of the pump, an alternative to trapping the generated charge by means of a downstream liquid-filled expansion, is to circumvent a necessary condition for charge generation ($\delta < \lambda_m$) by displacing the edge of the diffusion sublayer relative to the interface from which λ_m is measured. Thus, the solid surface could be "extended" into the liquid in the form of a "web" or "tangle" of the solid material tenuous enough to allow the liquid and ions to permeate, but dense enough to exclude the turbulent liquid motions. To prevent re-entrainment of the "trapped" ions and allow their escape to ground by conduction along the interface, the extended surface layer must be thick compared with λ_m. The suitability of an adsorbed polymer layer as the extension of the solid surface is demonstrated by its ability to reduce the electrophoretic mobility of host particles, indicating displacement of the plane of shear (50,51). That such layers can extend the region at the interface within which molecular diffusion dominates is also demonstrated by the attendant reduction in the Sherwood number measured for a rotating disc in turbulent flow (52). It is to preserve flexibility in the choice of the solid "substrate" for the polymer layer that insulating walls are accommodated in the development of Sec. 4.2 by evaluation of the generated electrical stress in Sec. 4.2.3.

Apart from anticipating the behavior of practical elements where the flow is well mixed, there are two ways in which the developments in this chapter relate to phenomena in the insulating tube. First, the migration model of Chapter 3, whose range of validity has yet to be defined, has its parallel in the migration limit represented by Eq. 4.8; this parallel is formalized in Sec. 5.5.2. Second, outside the range of validity of the migration model, a boundary condition involving the wall charge density must be specified for both the expansion and the insulating tube. To the extent that flow conditions are uniform over a section of the expansion wall serving as an electrode, and to the extent that those conditions can be controlled by an external energy source, the expansion offers the possibility of a relatively direct empirical investigation of that boundary condition.

Chapter 5

FLOW-INDUCED CHARGING OF THIN INSULATING TUBES: DIFFUSION EFFECTS

5.1 Introduction

It is the premise of the model of Chapter 3 that practical situations exist for which diffusion makes a negligible contribution to the normal current density in the liquid at the liquid-insulating solid interface. In these situations, where space charge entrained in the influent liquid drives the charging process in the insulating tube, a charge trapping expansion is usefully inserted at the tube inlet. In this chapter, the importance of the diffusion current is demonstrated in experiments in which an insulating tube acquires a net charge in the absence of a significant influent convection current. The results motivate a revised model which, despite its more tentative character, serves as the basis for defining the range of validity of the migration model. A consistent argument that this range includes practical conditions must reconcile with the charge generation process in a conducting tube (Sec. 2.2) where the normal diffusion and migration current densities are generally comparable.

Like the experiments of Sec. 3.3.2, those reported below in Sec. 5.2 incorporate a close fitting sleeve to attenuate the axial conduction current so that measurements will reflect primarily the radial current density in the liquid and bear more direct comparison to processes in conducting tubes. Now, however, a large expansion volume at the entrance to the insulating tube limits the influent current, while the sleeve is split into electrically isolated segments to reveal distributed aspects of the phenomena. The observed effluent current is generated within the insulating tube itself, and differs from that generated by conducting tubes in at least two respects. First, whereas Abedian and Sonin's theory appears to overestimate the spatial development length for streaming currents generated by the Freon TF/DCA-48 combination in stainless steel tubes (Sec. 2.2.3), it appears to underestimate that length for Tefzel tubes. Second, there is a history dependent transient response to the flow that suggests an uncontrolled leakage process driven by the small axial electric field within the tube.

The model developed in Sec. 5.3 incorporates diffusion in a way that closely parallels the model of Sec. 4.2.2 for the expansion region. The long spatial development length is accounted for with a revised boundary condition on the volume charge density within the diffusion sublayer that no longer regards radial charge transport through the liquid bulk as the rate limiting step of the spatial development. Time constants characterizing the observed temporal transients are too short to be accounted for by bulk conduction driven by a quasi-one-dimensional axial electric field. Thus, the model allows for a significant surface conductivity at the liquid-insulating solid interface, which is regarded as fixed and uniform for the duration of a single experiment, but which evolves over a much longer time scale as indicated by a gradual shortening of the observed time constants. While the role of surface conduction in the experiments remains a matter of contention, an important implication of the model is that a controlled surface conductivity tends to reduce the ultimate electrical stress regardless of whether the accumulating charge originates upstream or within the insulating tube itself.

5.2 Experiments

The main purpose of the experiments described below is to qualitatively characterize the charging process internal to the insulating tube within the framework developed for conducting tubes (Sec. 2.2). Viewed in their entirety, the experimental observations are sufficiently rich in information that experiments are most helpful the greater their simplicity and degree of repetition. A preliminary interpretation in Sec. 5.2.3 of certain features of the results guides the development of the model in Sec. 5.3.

5.2.1 Arrangement and Procedure

With details as given in Sec. 3.3.1, the experimental arrangement is as shown in Fig. 5.1. The electrometer connected to the expansion (or its conducting enclosure) also constrains to ground potential the liquid reservoir (not shown) and the stainless steel tube that feeds the expansion. Thus, the indicated current is identified as the net axial current $I(0,t)$ at the entrance to the insulating tube. A second electrometer virtually grounds the receiver and the communicating stainless steel tube to indicate the net axial current $I(L,t)$ at the outlet of the insulating tube. In most of the experiments the close fitting sleeve illustrated in Fig. 3.1 is split into electrically isolated segments; in Fig. 5.1 seven segments are shown. These are grounded directly or virtually through a third electrometer which monitors, on a time-sharing basis, the currents flowing to ground from the individual segments.

The current I_i flowing from the ith sleeve segment can be related to quantities of interest by recognizing that to zero order the electric field within the tube is entirely radial (see Sec. 5.3.2 below). Thus, over the entirety of surface S_1 in Fig. 5.2 the normal component of the (zero order) field vanishes, and by Gauss' law, so must the net charge enclosed and its rate of change:

$$\Delta_i I(z,t) + I_i(t) = 0 \qquad (5.1)$$

where

$$\Delta_i I(z,t) \equiv I(i\ell,t) - I(\{i-1\}\ell,t)$$

and $I(z,t)$ is the local axial current and ℓ is the length of each segment. To check the instrumentation and verify that the impedance levels of uncontrolled current paths are sufficiently high, the formal experiments are preceded by a demonstration that at any instant the summation over all N sleeve segments

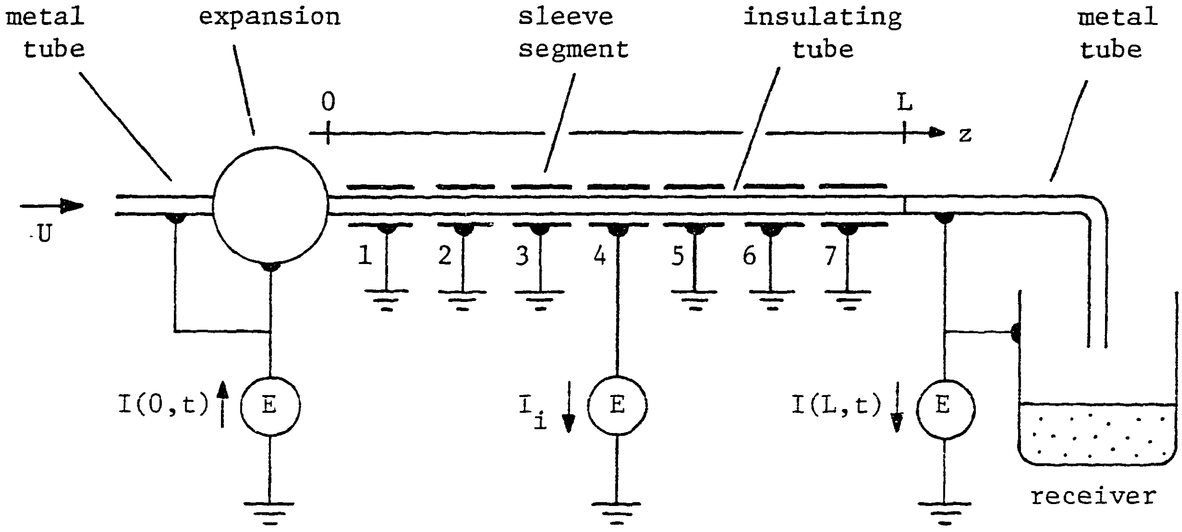

Fig. 5.1 Experimental arrangement for studying the convection current generated within an insulating tube. Electrometers E monitor influent and effluent currents and currents from individual sleeve segments.

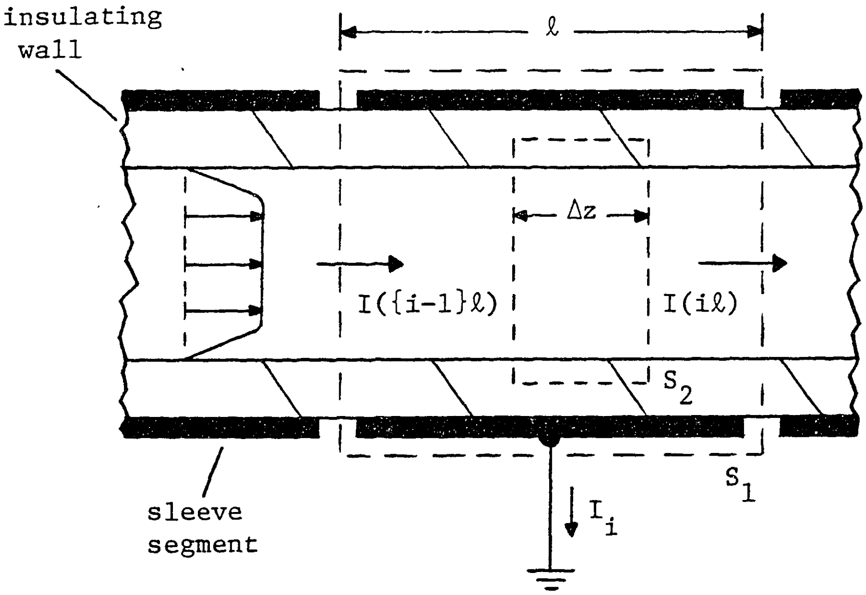

Fig. 5.2 Section of the insulating tube showing generators of the closed cylindrical surfaces S_1 and S_2. Not shown is a thin air gap between the outer surface of the insulating wall and the conducting sleeve.

$$\sum_{i=1}^{N} (\Delta_i I + I_i) = 0 \quad \rightarrow \quad I(0,t) - I(L,t) = \sum_{i=1}^{N} I_i(t)$$

as required by Eq. 5.1. Experiments consist of initiating the liquid flow and monitoring the currents $I(0,t)$, $I(L,t)$ and $I_i(t)$ as functions of time, with liquid conductivity and mean velocity as parameters. The axial current in the insulating tube at a distance $z = k\ell$ $(k = 1,2,\ldots, N-1)$ from the tube inlet is deduced from the measured values of $I(0,t)$ and I_i and repeated application of Eq. 5.1 with i ranging in succession from 1 to k. Finally, a smooth axial current profile is drawn through the discrete data points along the z-axis.

5.2.2 Results

Experimental results are divided into three groups. With the first group the objective is simply a clear demonstration of an internal charging mode that is independent of the original double layer; here a single sleeve segment suffices. The objective with the second group is to characterize the spatial development of the convection current; at least two segments are needed to reveal this distributed process. The third group spans the largest number of runs with a single tube sample, and it is here that axial conduction first comes into evidence.

Evidence of Internal Charging Mode: With expansion B of Table 4.1 at the inlet to the insulating tube (sample D; used in runs 90 through 109) the measured influent currents, summarized in Table 5.1, are small compared with those typical of experiments discussed in Sec. 3.3. Nevertheless, the characteristic form of the response, illustrated in Fig. 5.3 for run 106, is essentially the same as that in Fig. 3.7 and is subject to the same interpretation: the observed currents are due entirely to convection. The influent and effluent currents in Table 5.1 are the steady state values measured at the end of the run. A comparison of these currents for any given run indicates a departure from the migration limit which requires, according to Eq. 3.9, that the convection current decrease in magnitude in the flow direction.

TABLE 5.1

Evidence of Internal Charging Mode*

Run†	σ_ℓ	U	I(0,t)	I(L,t)	δ/λ_m	d_c/L	$\rho_w b/\sigma_\ell$
102 D	13.6	1.2	-0.008	+0.057	0.23	2.2	0.31
103 D	13.6	1.2	-0.013	+0.045	0.23	2.2	0.26
104 D	13.6	1.7	-0.004	+0.05	0.17	3.0	0.18
105 D	81.0	1.15	-0.037	+0.09	0.58	0.43	0.17
106 D	82.0	1.67	-0.05	+0.09	0.42	0.61	0.10
107 D	82.0	1.15	-0.028	+0.09	0.58	0.42	0.17
108 D	99.0	1.2	O(-0.01)	+0.20	0.62	0.37	0.32
109 D	99.0	1.7	-0.015	+0.15	0.45	0.52	0.14

* σ_ℓ in pS/m ; U in m/s ; I in nA

tube radius a = 1.3 (mm) and length L = 0.67 (m)

subscript 'c' denotes a calculated value

† letter identifies tube sample

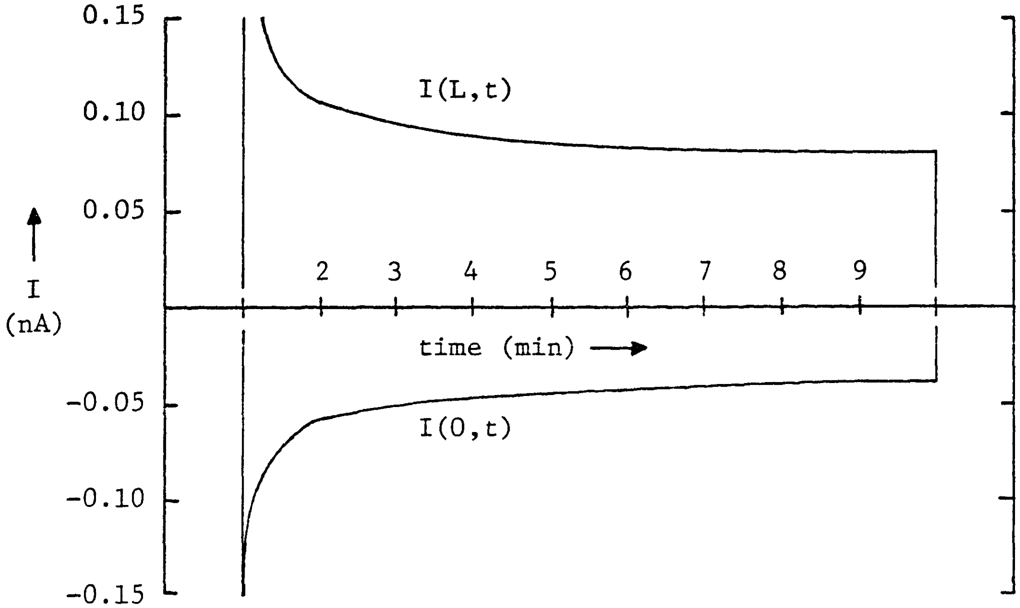

Fig. 5.3 Experimental results with the arrangement of Fig 5.1. Conditions are given in Table 5.1 as run 106.

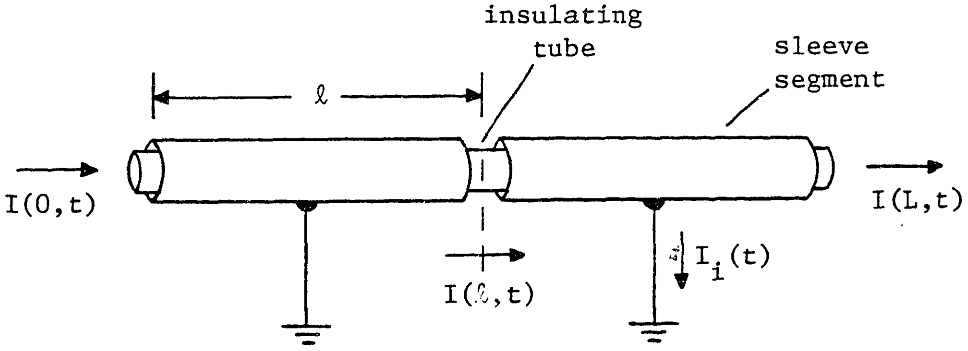

$$\Delta I_d \equiv I(L,t) - I(\ell,t) = -I_i(t)$$
$$\Delta I \equiv I(L,t) - I(0,t)$$

Fig. 5.4 Definitions of current differences whose ratio is tabulated in Table 5.2. Flow is from left to right.

A calculation of the charge contained in the diffuse part of the original double layer within the insulating tube now serves two purposes. First, for the conditions of run 106, Eq. 2.16 gives

$$Q_{dl} \simeq 2.0 \times 10^{-10} \text{ (C)}$$

while Eq. 2.18 gives for the amount by which the charge accumulated at time t ≃ 540.0 (s) exceeds that supplied at the tube inlet

$$\int_0^t |I(0,t) - I(L,t)|dt - \int_0^t |I(0,t)|dt \simeq 5.0 \times 10^{-8} \text{ (C)}$$

indicating that departures of the steady state convection currents from the migration limit are not attributable to the original double layer. Second, a comparison of the result for Q_{dl} with the area between the transient portion of either curve in Fig. 5.3 and the steady state portion extrapolated back to the time origin supports an interpretation of the transient as a sweeping out of the original diffuse layer. Consistent with this interpretation is an evaluation from Eq. 6.11 of the liquid transit time based on the length of the insulating tube and the velocity at the edge of the diffusion sublayer (which characterizes the velocity of the original diffuse layer). The result for run 106, $\tau_\delta \simeq$ 4.4 (s), is of the order of the time constant of the observed transient.

A more successful attempt to account for the steady state convection currents in Table 5.1 is based on Eqs. 2.11 and 2.15, which were applied to stainless steel tubes in Sec. 2.2.3. In the limit of $\delta \ll \lambda_m$ and identifying the convection current $I_s(z)$ with the measured current $I(z,t)$, elimination of $I_s(\infty)$ between these equations yields

$$\rho_w \simeq \frac{1}{Q}\left(1 + \frac{a\delta}{2\lambda_m^2}\right)\left(\frac{I(L,t) - I(0,t)\exp(-L/d)}{1 - \exp(-L/d)}\right)$$

where the development length d is given by Eq. 2.15b. The normalized wall charge density $\rho_w b/\sigma_\ell$ is calculated from this equation and tabulated in Table 5.1 for each run. Three observations are pertinent: (1) the tabulated values are consistent with Eq. 2.12, (2) they are fairly consistent with each other, and (3) they are of opposite sign to, and an order of magnitude smaller than, the experimental value for the stainless steel tube (-3.0; Fig. 2.5).

If this account of the steady state convection currents has merit, the results given in Table 3.2 must be reinterpreted. There, diffusion was neglected, and an adjustment of the calculated rate of change of net charge within the tube was based on a normalized wall charge density of $\rho_w b/\sigma_\ell \simeq 1.0$ and an enhanced liquid conductivity near the wall. However, with the values of the normalized wall charge density given in Table 5.1, the conductivity enhancement, according to Eq. 3.5, is negligible. Here, a further test of Eqs. 2.11 and 2.15 (in the limit $\delta \ll \lambda_m$) is applied by combining them with Eq. 3.45 to yield

$$\frac{dQ_t}{dt} = \left\{I(0,t) - I(\infty,t)\right\}\left\{1 - \exp(-L/d)\right\}$$

where

$$I(\infty,t) \simeq \rho_w Q\left\{1 + \frac{a\delta}{2\lambda_m^2}\right\}^{-1}$$

Now, using $\rho_w b/\sigma_\ell \simeq 0.1$, the mobility from Table 3.1, and other parameters from Table 3.2 this equation yields $Q_t/t \simeq -1.65$ (nC/min) for run 36 and $Q_t/t \simeq -4.36$ (nC/min) for run 37, which agree better with the measured values in Table 3.2 than do the originally calculated values.

<u>Evidence of Long Development Length</u>: As discussed in Sec. 2.2.2, Eqs. 2.11 and 2.15 are based on a limiting form ($\rho(a,z) \simeq \rho_w$) of the general boundary condition Eq. 2.10. That limit is applicable either where electrical conditions are fully developed (Sec. 2.2.1) or where the exchange

current density J_w is much greater than the normal current density at the wall $J_r(a,z)$. An indication of whether Eq. 2.15b correctly estimates the development length is based on the experimental arrangement shown in Fig. 5.4 and the results summarized in Table 5.2. The form of the response is still typified by that shown in Fig. 5.3, so the measured currents are regarded as due entirely to convection. The ratio tabulated in the last column is calculated from

$$\left(\frac{\Delta I_d}{\Delta I}\right)_c = \left[\frac{\exp(-\ell/d) - \exp(-L/d)}{1 - \exp(-L/d)}\right]$$

which is just an application of Eq. 2.15. Measured values of the same ratio are tabulated in the penultimate column, and are consistently larger than the calculated values. Because the calculated ratio is a monotonically *increasing* function of d, these results indicate that if a fully developed convection current exists, the associated development length is *longer* than that given by Eq. 2.15b. What makes this a fairly sensitive test is the condition satisfied in most of the runs that the value of d calculated from Eq. 2.15b is close to the length ℓ of the upstream sleeve segment. An implication of these results is that if the general boundary condition Eq. 2.10 is appropriate for the combination of materials under study, then the condition $J_r(a,z) \ll J_w$ implicit in Eq. 2.15b is not generally satisfied. A revised development length based on the general boundary condition is obtained in Sec. 5.3.1 below.

Evidence of Evolving Surface Conductivity: Currents measured in the two groups of experiments summarized in Tables 5.1 and 5.2 are regarded as entirely convective because their evolution is characterized by the single short transient attributable either to a process upstream of the insulating tube (Sec. 3.3.2) or perhaps to the original double layer in the insulating tube itself (see above). It was this circumstance that permitted a direct comparison with expressions for the streaming current developed for conducting tubes. In the group of experiments described next, there is evidence that conduction contributes significantly to the

TABLE 5.2

Evidence of Long Development Length[*]

Run[†]	σ_ℓ	U	L	ℓ	d_c	$\left(\frac{\Delta I_d}{\Delta I}\right)_m$	$\left(\frac{\Delta I_d}{\Delta I}\right)_c$
111 E	120.0	1.40	0.74	0.56	0.24	0.13	0.05
113 E	120.0	2.13	0.74	0.56	0.36	0.14	0.09
114 E	120.0	2.15	0.74	0.37	0.36	0.36	0.26
115 E	120.0	2.08	0.74	0.37	0.35	0.35	0.26
116 E	120.0	2.47	0.74	0.37	0.41	0.38	0.29
117 F	120.0	1.30	3.35	3.20	0.22	0.036	10^{-7}
118 F	120.0	1.65	3.35	3.20	0.28	0.041	10^{-6}

[*] σ_ℓ in pS/m ; U in m/s ; L, ℓ and d_c in m

tube radius a = 1.3 (mm)

subscripts 'm' and 'c' denote measured and calculated values

[†] letter identifies tube sample

axial current. This evidence takes two forms: the temporal response illustrated in Fig. 5.5, and the steady state current distribution illustrated in Fig. 5.6.

Because liquid is not continuously recirculated (Sec. 3.3.1) it must be periodically recycled back to the reservoir. Each segment of the temporal response of Fig. 5.5 corresponds to the flow time dictated by the size of the reservoir and the volume flow rate; the gaps between segments correspond to the time required to recycle the liquid. Commencement of the flow initiates a transient in the influent current $I(0,t)$ that is short enough to be completed before the liquid inventory is exhausted; this transient accounts for the "hook" shaped segments in Fig. 5.5 and may be associated with a process upstream of the insulating tube. If the flow segments are viewed as a continuous sequence a transient on a much longer time scale, about 60.0 minutes, is discernible, perhaps more clearly in the effluent current $I(L,t)$ than in the influent current. This slow exponential variation in the terminal currents contrasts dramatically with their rapid convergence to steady state values in Figs. 3.7 and 5.3, and strongly suggests that axial conduction is now competitive with convection. In support of this interpretation is the observation that the slow variation in the terminal currents is such as to reduce their difference, and hence reduce the rate of change of net charge given by Eq. 3.45. Moreover, the continuity of the flow segments evident in Fig. 5.5 is observed only if interruptions of the flow are short on the scale of the long transient; if the (liquid-filled) tube is left idle for longer periods the long transient is reinitiated when the flow commences again.

The sequence of runs shown in Fig. 5.5 is designated run 141, and bears comparison to similar sequences designated 133, 137, 145, 170, and 187 in Table 5.3. Anticipating a parallel with the charging transient described in Chapter 3, the time constants of these sequences are tabulated under the heading τ_1. In view of the decreasing value of τ_1 in successive sequences, it is pertinent to note that a single tube is

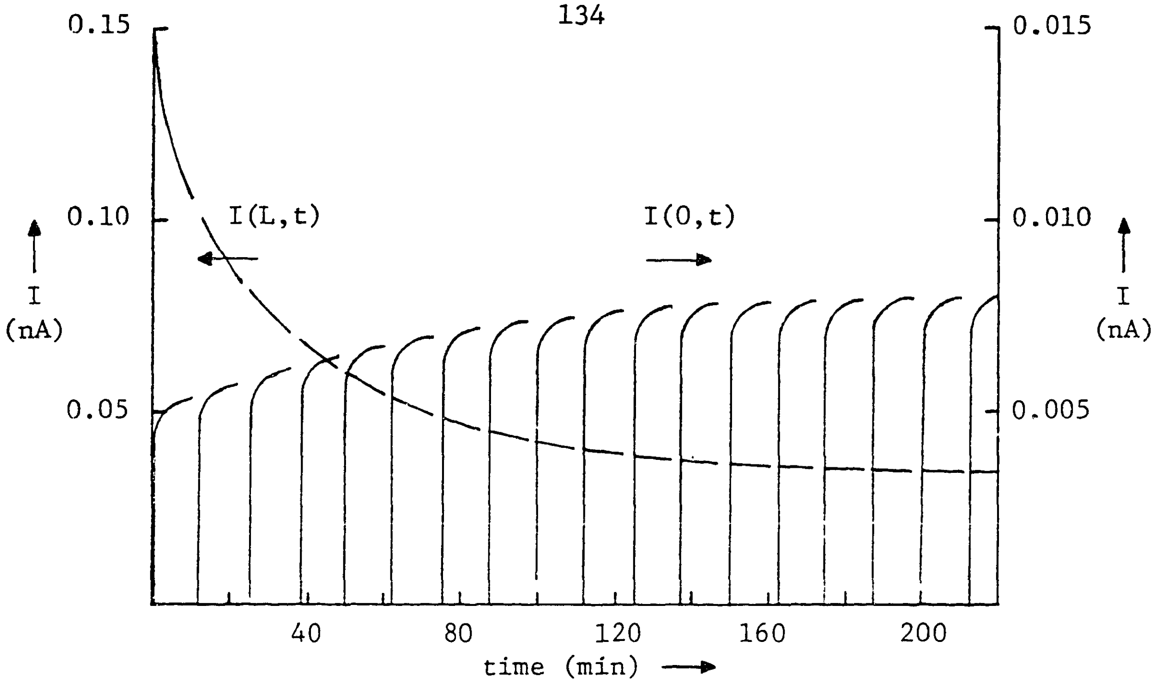

Fig. 5.5 Temporal evolution of measured influent and effluent currents. Conditions are given in Table 5.3 as run 141.

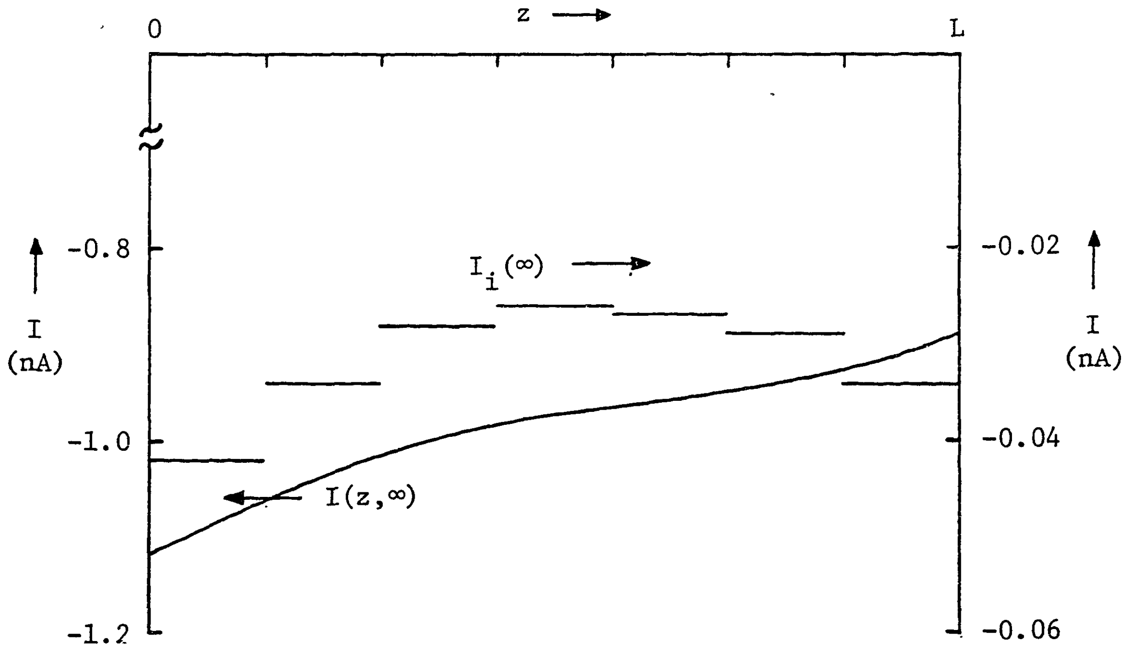

Fig. 5.6 Measured steady state currents from sleeve segments (discontinuous bars) and corresponding net axial current (continuous curve). Conditions are given in Table 5.3 as run 187.

TABLE 5.3

Evidence of Evolving Surface Conductivity[*]

Run[†]	σ_ℓ	U	τ_1	I(0,∞)	I(L,∞)	d_c/L	$\rho_w b/\sigma_\ell$
133 H	1.4	1.7	70.0	-0.009	+0.016	7.0	0.55
134 H	1.4	2.1	—	-0.015	+0.012	7.4	0.48
135 H	1.4	2.4	—	-0.023	+0.008	7.7	0.48
136 H	1.4	1.1	—	-0.002	+0.015	5.9	0.57
137 H	7.0	1.6	70.0	+0.002	+0.029	3.4	0.14
138 H	7.0	2.1	—	-0.001	+0.030	4.0	0.12
139 H	7.0	2.5	—	-0.001	+0.031	4.5	0.11
140 H	7.0	1.0	—	+0.005	+0.022	2.4	0.16
141 H	17.0	1.7	60.0	+0.008	+0.036	1.9	0.07
142 H	17.0	2.1	—	+0.004	+0.037	2.2	0.06
143 H	17.0	2.4	—	0.000	+0.037	2.5	0.06
144 H	17.0	1.1	—	+0.010	+0.030	1.3	0.09
145 H	110.0	1.7	25.0	+0.120	+0.250	0.35	0.20
146 H	110.0	2.1	—	+0.125	+0.280	0.43	0.16
147 H	110.0	2.4	—	+0.130	+0.300	0.49	0.14
148 H	110.0	1.1	—	+0.110	+0.185	0.23	0.32
170 H	7.6	1.4	14.0	-0.265	-0.180	2.9	0.05
172 H	7.6	1.6	—	-0.345	-0.250	3.2	0.01
173 H	7.6	1.9	—	-0.440	-0.330	3.6	0.01
187 H	57.0	1.0	2.0	-1.150	-0.875	0.40	-1.8

[*] σ_ℓ in pS/m ; U in m/s ; τ_1 in min. ; I in nA
tube radius a = 1.3 (mm) and length L = 0.89 (m)
subscript 'c' denotes a calculated value ; $\delta/\lambda_m < 0.7$ in all runs

[†] letter identifies tube sample
in runs 133-136 & 170-173 pure (undoped) Freon is used
runs 133-148 are with a liquid-filled expansion
in runs 170-173 expansion is packed with 3 mm diameter TFE spheres
in run 187 expansion is packed with fiberglass

involved: sample H which was used in runs 122 to 192. Runs listed in Table 5.3 for which no time constant is given represent segments at the tail end of the preceding sequence, where the steady state has already been established. Thus, for example, runs 142, 143, and 144 immediately follow the last segment in Fig. 5.5, with the liquid velocity set to the given values. In all of these runs the expansion in Fig. 5.1 is that designated E in Table 4.1.

The form of the axial current distribution illustrated in Fig. 5.6 is typical of the steady state distributions deduced from the currents from the seven sleeve segments shown in Fig. 5.1 by the procedure outlined in Sec. 5.2.1. The essential feature is the inflection point, which is absent if the current is entirely convective, regardless of whether it given by Eq. 2.15a or Eq. 3.9. A demonstration that the inflection point is consistent with an axial conduction process is given in Sec. 5.4.1 based on the model developed in Sec. 5.3.

Finally, as in Table 5.1, the normalized wall charge density is calculated from the measured currents in Table 5.3. However, that calculation can be meaningful only if the measured currents are entirely convective. Thus, a further indication that currents given in Table 5.1 represent convection alone while those of Table 5.3 include conduction is the slightly better consistency among $\rho_w b/\sigma_\ell$ in the former table, even if runs with undoped liquid are excluded from Table 5.3.

5.2.3 Preliminary Interpretation of the Temporal Transient

If axial conduction is an essential feature of the results summarized by Table 5.3 and Figs. 5.5 and 5.6, it is necessary to ask why convection currents were isolated in the experiments summarized in Sec. 3.3.2 and in Tables 5.1 and 5.2. As suggested in Sec. 3.3.2 and demonstrated in Sec 5.4.1, <u>bulk</u> conduction is negligible for the sleeve configuration; the relaxation time τ_l based on bulk conduction alone is found to be much longer than the times identified in Table 5.3. Thus, the importance of axial conduction stems from the presence of a significant surface conductivity σ_S. That surface conduction is not an intrinsic feature is indicated by the results of Sec. 3.3.3, but that it evolves under appropriate conditions is indicated by the decreasing time constants in Table 5.3. Finally, the fact that a steady state is eventually established (Fig. 5.5) indicates that the surface conductivity evolves over a longer time scale than the course of an experiment. A specific objective of the model developed next is a numerical evaluation of the surface conductivities implied by the observed range of τ_1.

Further insight into what is required of a model can be obtained by rewriting Eq. 5.1 as

$$I_i = - \int_{(i-1)\ell}^{i\ell} \frac{\partial I}{\partial z} dz \tag{5.2}$$

where in view of Eq. 3.8b

$$\frac{\partial I}{\partial z} = \pi a^2 \left[U \frac{\partial \bar{\rho}}{\partial z} + \sigma_e \frac{\partial E_z}{\partial z} \right] \tag{5.3}$$

It is already clear from Eq. 5.3 that axial conduction may explain the inflection point in Fig. 5.6. The steady state sleeve currents $I_i(\infty)$ in Fig. 5.6 are finite, so Eq. 5.2 implies that the two terms on the right in Eq. 5.3 sum to a constant in the steady state. As in case B of Sec. 3.2.5, the convection term is regarded as imposed, and thus the two terms are individually constant. In Sec. 5.3.2 the axial electric field is shown to be proportional to the local axial derivative of the surface charge density $\bar{\sigma}(z,t)$, so it remains to reconcile the steady state distribution $\bar{\sigma}(z,\infty)$ with the finite difference between the steady state influent and effluent currents in Table 5.3. In the model developed next, the tendency of the finite steady state net influent current to increase the surface charge density is balanced by a process of charge transfer across the liquid-insulating interface.

5.3 Model for the Temporal Transient

The model of this section is developed with two objectives. The first is to lend support to the contention in Sec. 5.2.3 that surface conduction is important, by showing that axial conduction is consistent with the inflection point in Fig. 5.6 and that bulk conduction is insufficient to account for the time constants in Table 5.3. The second is to identify conditions under which migration can be expected to dominate the normal current density at the liquid-insulating solid interface.

For the external conductor configuration the close fitting sleeve is retained to facilitate comparison with the experiments of Sec. 5.2, but three features are introduced into the present model that are omitted from the model of Sec. 3.2.5 (case B). First is the contribution of ion diffusion to the normal current density at the liquid-insulating solid interface. Second is the axial conduction process that is rendered important on the time scale of the experiments by a significant surface conductivity. Third is the finite conductivity of the tube wall. As discussed in Sec. 5.2.3, it is necessary to admit a current across the liquid-insulating solid interface to reconcile the steady state surface charge distribution with the finite difference between the steady state currents at the inlet and outlet of the insulating tube. In the absence of specific information, only the simplest description of charge transport in the wall is justified. Thus, the wall is assigned an ohmic conductivity which is low enough that (1) the wall carries a negligible fraction of the axial current, and (2) the wall can still be regarded as insulating on the time scale of the experiments of Sec. 3.3. Then with the exception of [d] and [f], the assumptions of Sec. 3.2.1 are retained.

5.3.1 Volume Charge Distribution

With the normal diffusion current included, the purpose of this section is to develop the counterpart of Eq. 3.9 for the volume charge distribution in the liquid along the axis of the tube. When the boundary condition $\rho(a,z) \simeq \rho_w$ is appropriate, the result is already given by Eq. 2.15. However, as discussed in Sec. 5.2.2, Eq. 2.15b underestimates the spatial development length for the materials under study, and this motivates use of the more general boundary condition Eq. 2.10.

Conservation of net charge is expressed by Eq. 4.1:

$$\frac{\partial\rho}{\partial t} = -\bar{v}\cdot\nabla\rho - \nabla\cdot\bar{J} \tag{5.4a}$$

where $\bar{v}$ is the mean liquid velocity and the net current density

$$\bar{J}(r,z) = \sigma_\ell\bar{E} - D_e\nabla\rho \tag{5.4b}$$

is expressed in terms of the uniform bulk conductivity σ_ℓ (assumption [e] of Sec. 3.2.1) and the local diffusivity D_e. As illustrated by Fig. 4.1 for the expansion region, Fig. 5.7 illustrates a turbulent core ($0 < r < a-\delta$) bounded by a diffusion sublayer ($a-\delta > r > a$). Equation 5.4 is specialized to these two regions by recognizing that turbulent diffusion renders the volume charge essentially uniform in the core while molecular diffusion dominates in the sublayer.

<u>Core Region</u>: With the differential form of Gauss' law inserted, and neglecting axial diffusion (in view of the large Peclet number LU/D_e) Eq. 5.4 becomes

$$\frac{\partial\rho}{\partial t} = -v_z\frac{\partial\rho}{\partial z} - \frac{\rho}{\tau_\ell} + \frac{1}{r}\frac{\partial}{\partial r}\left[rD_e\frac{\partial\rho}{\partial r}\right] \quad ; \quad \tau_\ell \equiv \frac{\varepsilon_\ell}{\sigma_\ell} \tag{5.5}$$

Following the development in Sec. 3.2.2, the time derivative in Eq. 5.5 is neglected in comparison with the convection term. Then integrating Eq. 5.5 over the cross section of the core region, where the mean velocity is essentially the superficial velocity, yields

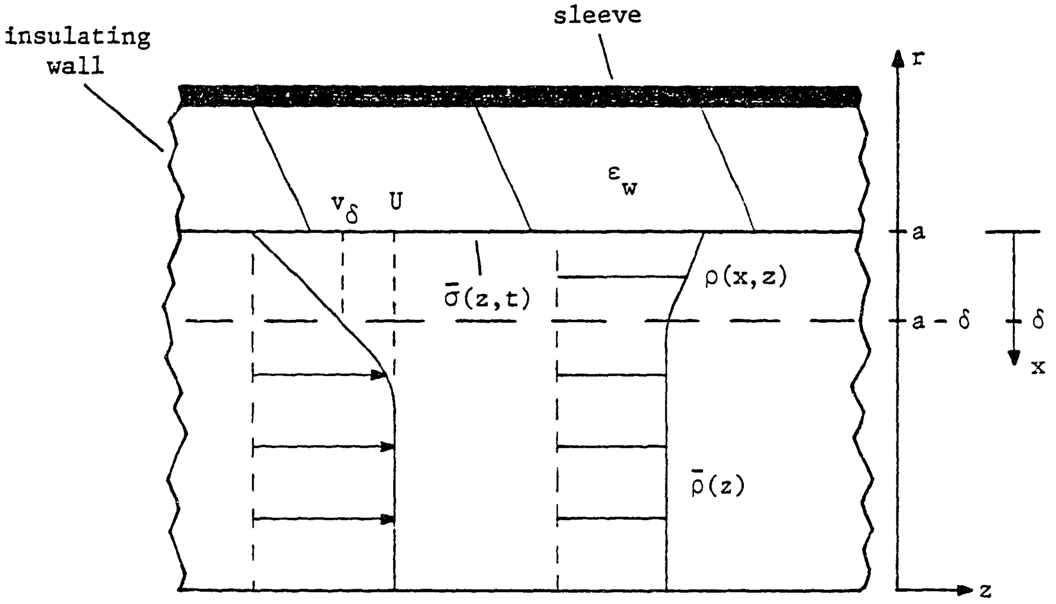

Fig. 5.7 Section of the insulating tube showing core region where $\rho = \bar{\rho}(z)$ and diffusion sublayer where $\rho = \rho(x,z)$. Turbulent velocity profile is shown and coordinate systems are defined. Diffusion sublayer is enlarged for clarity.

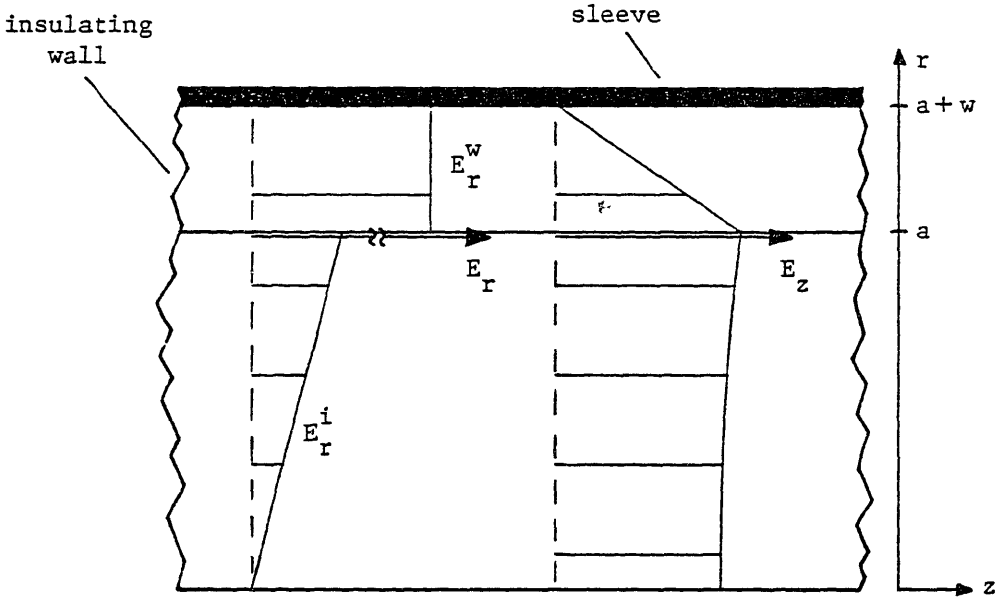

Fig. 5.8 Section of the insulating tube showing typical profiles of quasi-one-dimensional electric fields. Radial and axial field components are drawn to different scales. The small air gap between the outer surface of the tube wall and the inner surface of the sleeve is neglected.

$$U\frac{\partial\bar{\rho}}{\partial z} \simeq -\frac{\bar{\rho}}{\tau_\ell} + \frac{2}{a}D_m\frac{\partial\rho}{\partial r}\bigg|_{r=a-\delta} \qquad (5.6)$$

where $\bar{\rho}(z)$ is the net volume charge density averaged over the cross section of the core, and the diffusivity at the edge of the diffusion sublayer is approximated by the molecular diffusivity D_m. The second term on the right in Eq. 5.6 can be expressed in terms of $\bar{\rho}(z)$ and parameters characterizing the interface by solving Eq. 5.4 within the diffusion sublayer.

Diffusion Sublayer: Equation 5.4 is specialized to the diffusion sublayer by neglecting the time derivative, inserting Gauss' differential law, and using the molecular diffusivity for D_e. The sublayer thickness is small compared with the tube radius, so the result is written in terms of the planar sublayer coordinate $x = a - r$ which measures distance from the interface into the liquid (Fig. 5.7):

$$v_z(x)\frac{\partial\rho}{\partial z} \simeq -\frac{\rho}{\tau_\ell} + D_m\frac{\partial^2\rho}{\partial x^2} \quad ; \quad \rho = \rho(x,z) \qquad (5.7)$$

To justify neglect of the convection term, it is enough to show that the liquid transit time, based on the velocity at the edge of the sublayer (v_δ in Fig. 5.7) and whatever length characterizes the axial derivative in Eq. 5.7, is much longer than the relaxation time τ_ℓ. That length is the development length d which, according to Sec. 5.2.2, is at least as large as that (d_c) calculated from Eq. 2.15b. Thus

$$\tau_\delta \geq \frac{d_c}{v_\delta} = \frac{L}{v_\delta}\frac{d_c}{L} \simeq 11.0(L/U)\frac{d_c}{L}$$

As given by Eq. 6.10, the proportionality factor between v_δ and U is only weakly dependent on Reynolds number, so the final approximate equality applies to all of the experiments of Table 5.3. With d_c/L, σ_ℓ, U, and L given in Table 5.3 it is readily confirmed that τ_δ easily exceeds τ_ℓ. Thus, Eq. 5.7 becomes

$$D_m \frac{\partial^2 \rho}{\partial x^2} - \frac{\rho}{\tau_\ell} \simeq 0 \qquad (5.8)$$

With the turbulent diffusivity D_t given by Eq. 6.9 and a Reynolds number typical of the experiments of Table 5.3 ($R_y \simeq 10^4$), it may be shown that the turbulent Debye length ($\lambda_t \equiv \sqrt{\epsilon_\ell D_t/\sigma_\ell}$) is typically about two hundred times greater than the Debye length based on the molecular diffusivity, and that λ_t is comparable to or greater than the tube radius for these experiments. Thus, net charge in the turbulent core is essentially uniformly distributed and its value at the edge of the diffusion sublayer approximates the average value:

$$\rho(\delta,z) \simeq \bar{\rho}(z) \qquad (5.9)$$

The solution of Eq. 5.8 expressed in terms of the values of ρ at the boundaries of the sublayer is now

$$\rho(x,z) = \left[\frac{\bar{\rho}(z) - \rho(0,z)\cosh(\delta/\lambda_m)}{\sinh(\delta/\lambda_m)}\right]\sinh(x/\lambda_m) + \rho(0,z)\cosh(x/\lambda_m) \qquad (5.10)$$

where λ_m is the Debye length given by Eq. 2.9. Once $\rho(0,z)$ is determined from the boundary condition, the second term on the right in Eq. 5.6 can be obtained from Eq. 5.10 and the relation between derivatives:

$$\left.\frac{\partial \rho}{\partial r}\right|_{r=a-\delta} = -\left.\frac{\partial \rho}{\partial x}\right|_{x=\delta} \qquad (5.11)$$

consistent with the definitions of the coordinate systems in Fig. 5.7.

Boundary Condition: The general boundary condition Eq. 2.10 can be written in sublayer coordinates as

$$J_x(0,z) = -J_w\left(\frac{\rho(0,z) - \rho_w}{|\rho_w|}\right) \qquad (5.12)$$

As discussed in Sec. 2.2.2, the limiting form $J_w \gg J_x(0,z) \rightarrow \rho(0,z) \simeq \rho_w$ leads to a satisfactory description of the streaming currents generated by conducting tubes. There are two issues to address if Eq. 5.12 is to be applied to the insulating tube:

First, to account for the results of Table 5.2, it is necessary to retain the general form Eq. 5.12 because it leads to a longer development length than the limiting form. Some justification for this is available in the literature (53,54) where it is suggested on theoretical grounds that the exchange current density J_w should be lower for insulator electrodes than for metal ones. Experimental values of J_w for Teflon in contact with various redox systems in H_2SO_4 solutions range from less than 10^{-8} to better than 10^{-5} A/m^2 (55). While there is no basis for assuming that the same range applies to the present experiments, it is encouraging to compare this with the observed average current density

$$\langle J_x(0,z)\rangle = \left|\frac{I(0,t) - I(L,t)}{2\pi a L}\right|$$

This expression is valid only if surface conduction is excluded from $I(0,t)$ and $I(L,t)$, so these currents must be taken from Table 5.1 rather than Table 5.3. With the difference in currents typically 0.1 (nA) the average current density is 2.0×10^{-8} (A/m^2), which lies within the given range of exchange current densities.

Second, steady state conditions prevail in the conducting tube, so it is reasonable to regard ρ_w and J_w as fixed material parameters. In contrast, the accumulating surface charge and the evolving electric fields imply changing conditions at the interface between the liquid and the insulating tube. To make it plausible that these parameters remain fixed in the face of the accumulating surface charge it is necessary to show that only a small fraction of the available interfacial surface area may be occupied. If only one ionic species accounts for the surface charge, the minimum area occupied per (monovalent) ion is

$$\frac{e}{\epsilon_w\left(E_r^w\right)_{max}} \simeq \frac{1.6 \times 10^{-19}}{(2.3 \times 10^{-11})(5.0 \times 10^{7})} \simeq 10^{4}\ \mathring{A}^{2}$$

where the maximum electric stress is taken to be of the order of the dielectric strength of the insulating wall. This area is probably large enough compared with the actual area of the surface in contact with an ion to justify the use of Eq. 5.12 with fixed parameter values. However, if the same net surface charge arises from a small difference in the surface concentrations of two ionic species then the area occupied per ion is smaller. Moreover, parameters characterizing the interface may depend on the evolving electric fields or the evolving surface conductivity, so Eq. 5.12 is used with less confidence in the insulating tubes than in the conducting ones.

<u>Solution for the Volume Charge Distribution</u>: To apply the boundary condition Eq. 5.12, an expression for the normal current density within the sublayer is needed. From Eq. 5.4b

$$J_x(x,z) = \sigma_\ell E_x - D_m\frac{\partial\rho}{\partial x} \tag{5.13}$$

Substituting Eq. 2.31 for $-E_x$ yields

$$J_x(x,z) = \frac{a}{2}\left(-\frac{\bar{\rho}}{\tau_\ell} + \sigma_\ell\frac{\partial E_z}{\partial z} - \frac{2}{a}D_m\frac{\partial\rho}{\partial x} \right) \tag{5.14}$$

In Sec. 5.3.2 the axial field term is shown to be negligible compared with the first term on the right, so that with Eq. 5.10 substituted Eq. 5.14 yields

$$J_x(0,z) \simeq \frac{a}{2}\left(-\alpha\bar{\rho} + \beta\rho(0,z)\right) \qquad (5.15)$$

where

$$\alpha = \left[\frac{1}{\tau_\ell} + \frac{2D_m}{a\lambda_m}\operatorname{csch}(\delta/\lambda_m)\right] \quad ; \quad \beta = \left[\frac{2D_m}{a\lambda_m}\coth(\delta/\lambda_m)\right]$$

or in the limit $\delta/\lambda_m << 1$

$$\alpha = \frac{1}{\tau_\ell}\left(1 + \frac{2\lambda_m^2}{a\delta}\right) \quad ; \quad \beta = \frac{1}{\tau_\ell}\left(\frac{2\lambda_m^2}{a\delta}\right) \qquad (5.16)$$

Eliminate $J_x(0,z)$ between Eqs. 5.12 and 5.15 and obtain

$$\rho(0,z) = \frac{J_w(\rho_w/|\rho_w|) + (\alpha a/2)\bar{\rho}(z)}{J_w/|\rho_w| + \beta a/2} \qquad (5.17)$$

Substitute Eqs. 5.10 and 5.17 into Eq. 5.11, and insert the result into Eq. 5.6 to yield

$$U\frac{\partial\bar{\rho}}{\partial z} = (-\alpha\bar{\rho} + \beta\rho_w)\left[1 + \frac{a\beta|\rho_w|}{2J_w}\right]^{-1} \qquad (5.18)$$

This has the solution

$$\bar{\rho}(z) = \bar{\rho}(0)\exp(-z/d) + \bar{\rho}(\infty)\left(1 - \exp(-z/d)\right) \qquad (5.19)$$

where

$$\bar{\rho}(\infty) = \frac{\beta}{\alpha}\rho_w \quad ; \quad d = \frac{U}{\alpha}\left[1 + \frac{a\beta|\rho_w|}{2J_w}\right] \qquad (5.20)$$

Note that the development length d in Eq. 5.20 is greater than that given by Eq. 2.15b by the factor in parentheses which tends to unity in the limit of large J_w. Also the fully developed charge density $\bar{\rho}(\infty)$ is the same as that given by Eq. 2.11 in the limit $\delta \ll \lambda_m$, consistent with the fact that the boundary condition on $\rho(x,z)$ (Eq. 5.12) is independent of J_w in the fully developed region.

In case B of Sec. 3.2.5, the volume charge distribution is regarded as imposed if the inlet value $\bar{\rho}(0)$ is independent of the generated fields. Experiments discussed in Sec. 3.3.2 and in Chapter 6 indicate that this is so, at least for the close fitting sleeve configuration. Here, in addition to regarding $\bar{\rho}(0)$ as imposed, parameters characterizing the transverse boundary condition (ρ_w and J_w) are also considered independent of the surface charge transient, as discussed above. The volume charge distribution of Eqs. 5.19 and 5.20 plays the role of that given by Eq. 3.9 by driving a surface charge transient that is described in the following sections by an equation analogous to Eq. 3.10.

5.3.2 Axial Electric Field

As in Sec. 3.2.3 for the capped cylinder configuration, the objective here for the close fitting sleeve is a relation between the axial electric field within the liquid and the surface charge distribution at the liquid-solid interface. The first application of this relation is to justify neglect of the axial field term in Eq. 5.14. The second is in Sec. 5.3.3 where the axial field enters into an equation expressing conservation of surface charge.

A quasi-one-dimensional approximation (14, Sec. 4.12) for the radial electric field in the wall is motivated by the extreme aspect ratio of the tube and the proximity of the equipotential sleeve. The integral form of Gauss' law applied to the surface S_2 in Fig. 5.2 yields for the zero order field in the wall

$$E_r^w(z,t) \simeq \frac{1}{\epsilon_w}\left(\frac{\zeta\epsilon_\ell}{\lambda_m} + \bar{\sigma}(z,t) + \frac{a}{2}\bar{\rho}(z) \right) \simeq \frac{\bar{\sigma}}{\epsilon_w} \tag{5.21}$$

The first term represents the field of the fixed charge associated with the original double layer (Eq. 2.17), while the second and third terms arise from the surface and volume charge distributions induced by the flow. As implied by Eq. 5.21 and illustrated in Fig. 5.8, E_r^w is essentially independent of radial position. This is a consequence of the small wall thickness (w) compared with the radius of curvature (a) and the absence of space charge within the wall.

The first order axial electric field component follows from the requirement that the field be curl-free within the tube wall:

$$\frac{\partial E_z}{\partial r} = \frac{\partial E_r^w}{\partial z} \quad \rightarrow \quad E_z \simeq \big(r - (a + w)\big)\frac{\partial E_r^w}{\partial z} \tag{5.22}$$

The integration constant is adjusted to be consistent with the equipotential surface at the outer surface of the wall (Fig. 5.8). Neither the fixed double layer charge (see Eq. 2.17) nor the space charge $\bar{\rho}(z)$ contribute significantly to electrical stresses approaching the dielectric strength of the wall, so for most of the charging transient the surface charge density is the dominant term on the right in Eq. 5.21. Then combining Eqs. 5.21 and 5.22 yields

$$E_z \simeq \frac{-w}{\varepsilon_w}\frac{\partial \bar{\sigma}}{\partial z} \quad ; \quad r = a \tag{5.23}$$

for the axial field at the interface. The axial field profile sketched in Fig. 5.8 reflects both the continuity of this component across the interface and the symmetry condition on the axis of the tube. The approximate uniformity of E_z in the liquid is justified as follows. The field must be curl-free in the liquid as well as the in wall, so a relation analogous to Eq. 5.22 applies with E_r^w replaced by E_r^i, the radial field in the liquid. Then the fractional change in E_z between the tube axis and the interface is approximately

$$\frac{a}{E_z(a)} \frac{\partial E_z}{\partial r} \simeq \frac{a}{w} \frac{E_r^i}{E_r^w}$$

where Eq. 5.22 was used with r = a. The ratio of lengths on the right is about five, while the ratio of fields is small as soon as the surface charge density dominates the right side of Eq. 5.21. Thus, for most of the transient, the axial field is essentially uniform in the liquid.

To justify neglect of the axial field term in Eq. 5.14 it is enough to compare

$$\frac{\bar{\rho}}{\epsilon_\ell} \simeq \frac{I(L,0)}{\pi a^2 U \epsilon_\ell} > \frac{5.0 \times 10^{-11}}{(10^{-5})(2.1 \times 10^{-11})} = 2.0 \times 10^5$$

with

$$\frac{\partial E_z(a,z,t)}{\partial z} \simeq -w \frac{\partial^2 E_r^w}{\partial z^2} < \frac{w}{L^2}(10^7) \simeq 5.0 \times 10^3$$

A typical velocity of $U = 2.0$ is used, and to get a conservative test, the minimum $I(L,0)$ from Table 5.1 and a value for E_r^w that approaches the dielectric strength are used.

5.3.3 Conservation and Relaxation of Surface Charge

Exploiting the uniformity of the axial field in the liquid, an equation expressing conservation of surface charge is obtained from Eqs. 3.7 and 3.8:

$$\frac{\partial \bar{\sigma}}{\partial t} = -J_r^w - \frac{1}{2\pi a} \frac{\partial I}{\partial z} \tag{5.24a}$$

where

$$I \equiv \pi a^2 \left(U\bar{\rho} + \sigma_e E_z\right) \quad ; \quad \sigma_e \equiv \left(\sigma_\ell + \frac{2}{a}\sigma_s\right) \tag{5.24b}$$

The additional term J_r^w is the radial current density in the insulating wall evaluated at the liquid-solid interface. The time rate of change of the volume charge density is neglected in Eq. 5.24a because that term is small compared with the convection term retained as long as $\bar{\rho}(0)$ changes slowly on the scale of the liquid residence time L/U.

As discussed at the beginning of Sec. 5.3, the tube wall is assigned an ohmic conductivity σ_w so that using Eq. 5.21

$$J_r^w = \sigma_w E_r^w(a,z) = \frac{\bar{\sigma}}{\tau_w} \quad ; \quad \tau_w \equiv \frac{\epsilon_w}{\sigma_w} \tag{5.25}$$

Substituting Eqs. 5.23 and 5.25 into Eq. 5.24 yields

$$\frac{\partial\bar{\sigma}}{\partial t} + \frac{\bar{\sigma}}{\tau_w} - \left(\frac{aw\sigma_e}{2\epsilon_w}\right)\frac{\partial^2\bar{\sigma}}{\partial z^2} = -\frac{aU}{2}\frac{\partial\bar{\rho}}{\partial z} \tag{5.26}$$

which is the counterpart of Eq. 3.10.

<u>Surface Charge Relaxation</u>: The homogeneous form of Eq. 5.26 governs the surface charge relaxation that ensues when the flow is interrupted. As in the Sec. 3.2.4 the objective is an expression for the surface conductivity in terms of the time constant of the fundamental spatial mode. The series solution

$$\bar{\sigma}(z,t) = \sum_{n}^{\infty} \bar{\sigma}_n(t)\sin(k_n z) \quad ; \quad k_n = \frac{n\pi}{L} \tag{5.27}$$

guarantees that the integral constraint on the axial field

$$\int_0^L E_z(z)dz = \frac{-w}{\epsilon_w}\left(\bar{\sigma}(L,t) - \bar{\sigma}(0,t)\right) = 0 \tag{5.28}$$

is satisfied. The first equality follows from Eq. 5.23, while the integral constraint is due to the grounded terminations of the insulating tube. Substituting Eq. 5.27 into the homogeneous form of Eq. 5.26 yields

$$\frac{d\bar{\sigma}_n}{dt} + \frac{\bar{\sigma}_n}{\tau_n} = 0 \quad ; \quad \bar{\sigma}_n(t) = \bar{\sigma}_n(0)\exp(-t/\tau_n) \tag{5.29a,b}$$

where

$$\frac{1}{\tau_n} = \frac{1}{\tau_w} + \left(\frac{w\sigma_e a}{2\epsilon_w}\right)\left(\frac{n^2\pi^2}{L^2}\right) \tag{5.30}$$

The relaxation time τ_1 of the fundamental spatial mode is evidently the longest and hence corresponds to the observed time constants listed in Table 5.3. With $n = 1$, and recalling the definition of σ_e (Eq. 5.24b), Eq. 5.30 yields for the surface conductivity

$$\sigma_s = \left(\frac{\epsilon_w L^2}{w\pi^2}\right)\left(\frac{1}{\tau_1} - \frac{1}{\tau_w}\right) - \frac{a}{2}\sigma_\ell \tag{5.31}$$

It is clear from Eq. 5.30 that $\tau_w > \tau_1$. Thus, a lower limit on τ_w is the maximum value of τ_1 in Table 5.3: $\tau_w > 70.0$ minutes, corresponding to a bulk conductivity of $\sigma_w < 5.5 \times 10^{-15}$ (S/m). Now Eq. 5.31 can be applied to get an estimate of σ_s without specifying τ_w, by neglecting its reciprocal compared with $1/\tau_1$. This estimate becomes better as the smaller values of τ_1 from Table 5.3 are used. This upper limit on σ_w justifies the assumption implicit in Eq. 5.24 that the wall carries a negligible fraction of the axial conduction current.

5.3.4 Charging Transient and Electrical Stress

To facilitate application of the initial condition, the right hand side of Eq. 5.26 is written in the form of a Fourier series using Eqs. 3.29 and 5.19:

$$-\frac{aU}{2}\frac{\partial\bar{\rho}}{\partial z} = \sum_{n}^{\infty} A_n \sin(k_n z) \quad ; \quad k_n = \frac{n\pi}{L} \tag{5.32}$$

where

$$A_n = \frac{-aU}{2d}\left[\bar{\rho}(\infty) - \bar{\rho}(0)\right]e_n \tag{5.33}$$

with d (which also enters e_n) now given by Eq. 5.20. Substituting Eqs. 5.27 and 5.32 into Eq. 5.26 and solving the resulting ordinary differential equation subject to the initial condition $\bar{\sigma}(z,0) = 0$ yields

$$\bar{\sigma} = \sum_{n\ \mathrm{odd}}^{\infty} \left[\tau_n A_n \sin(k_n z)\left(1 - \exp(-t/\tau_n)\right)\right] \tag{5.34}$$

The electrical stress

$$E_r^w = \sum_{n\ \mathrm{odd}}^{\infty} \left[(\tau_n A_n/\epsilon_w)\sin(k_n z)\left(1 - \exp(-t/\tau_n)\right)\right] \tag{5.35}$$

follows from Eqs. 5.21 and 5.34.

5.3.5 Terminal Currents

Combining Eqs. 5.23 and 5.24b gives for the net axial current

$$I(z,t) = \pi a^2\left(\bar{\rho}(z)U - \frac{w\sigma_e}{\epsilon_w}\frac{\partial\bar{\sigma}}{\partial z}\right) \tag{5.36}$$

and with Eq. 5.34 inserted

$$I(z,t) = \pi a^2\left[\bar{\rho}(z)U - \frac{w\sigma_e}{\epsilon_w}\left(\sum_{n\ \mathrm{odd}}^{\infty} \tau_n A_n k_n \cos(k_n z)\left(1 - \exp(-t/\tau_n)\right)\right)\right] \tag{5.37}$$

where $\bar{\rho}(z)$ is given by Eq. 5.19. The terminal currents follow as

$$I(0) = \pi a^2\left[\bar{\rho}(0)U - \frac{w\sigma_e}{\epsilon_w}\left(\sum_{n\ \mathrm{odd}}^{\infty}\tau_n A_n k_n\left(1 - \exp(-t/\tau_n)\right)\right)\right] \tag{5.38}$$

and

$$I(L) = \pi a^2\left[\bar{\rho}(L)U + \frac{w\sigma_e}{\epsilon_w}\left(\sum_{n\ \mathrm{odd}}^{\infty}\tau_n A_n k_n\left(1 - \exp(-t/\tau_n)\right)\right)\right] \tag{5.39}$$

Finally, the currents drawn from the individual sleeve segments can be obtained from Eqs. 5.1 and 5.37. It can be shown that the net current given by Eq. 5.37 in the steady state is independent of axial position unless τ_w is finite. Thus, the experimental observation that the steady state axial derivative $\partial I/\partial z(z,\infty)$ is nonzero (Fig. 5.6) justifies the allowance for a nonzero wall conductivity in the model.

5.4 Comments on the Model

5.4.1 The Surface Conductivity

As discussed in Sec. 5.3.3, the surface conductivities can be estimated from

$$\sigma_s \simeq \frac{\epsilon_w L^2}{w\pi^2\tau_1} - \frac{a}{2}\sigma_\ell$$

With $\epsilon_w \simeq 2.6\epsilon_0$, $w \simeq 3.0 \times 10^{-4}$ and other parameters as given in Table 5.3, the range of surface conductivity in (S) is

$$1.5 \times 10^{-12} < \sigma_s < 5.1 \times 10^{-11}$$

while

$$9.1 \times 10^{-16} < (a\sigma_\ell/2) < 7.0 \times 10^{-14}$$

indicating that bulk conduction does not compete with surface conduction. Further evidence is available in Table 5.3 where the trend towards shorter time constants continues regardless of the direction of change in bulk conductivity.

In the steady state Eq. 5.37 yields

$$\frac{\partial^2 I}{\partial z^2} = \pi a^2 \left[\frac{\partial^2 \bar{\rho}(z)}{\partial z^2} U + \frac{w\sigma_e}{\varepsilon_w} \left(\sum_{n\ \mathrm{odd}}^{\infty} \tau_n A_n k_n^3 \cos(k_n z) \right) \right] .$$

The convection term on the right has an exponential z-dependence, and by itself cannot account for the inflection point in Fig. 5.6. With the conduction term included the right hand side does have a zero, which cannot be specified, however, without information about the interfacial parameters ρ_w and J_w.

Depending on one's picture of the origin of the surface conductivity, one may or may not expect it to be uniform over the entire tube as assumed in the analysis. It is not expected to be uniform if the rate of evolution is dependent on the local normal current density at the interface. However, the fact that a steady state is reached at all (Fig. 5.5) suggests that the surface conductivity is fixed for the duration of an experiment. Additional evidence that it evolves over a much longer time scale is provided in Chapter 6. If this is the case, then the rate of evolution must be independent of the normal current density which vanishes while the liquid is left stationary between experiments. Thus, the surface conductivity appears to originate simply in the long-term exposure of interface to the doped liquid, and the assumption of its uniformity is then reasonable.

5.4.2 The Continuum Approximation

In describing the charge distribution within the diffusion sublayer in terms of a smoothed volume density (Sec. 5.3.1), there is the implicit assumption that the dimensions over which variations in the density occur are large compared with the mean separation between ions. To examine this assumption, the mean ion separation

$$\ell_i = \left[\frac{e}{\rho_+ + \rho_-}\right]^{1/3} \simeq \left[eb/\sigma_\ell\right]^{1/3}$$

should be compared with the smaller of the Debye length and the diffusion sublayer thickness. For simplicity the former length is used:

$$\lambda_m = \left[\frac{\varepsilon_\ell D_m}{\sigma_\ell}\right]^{1/2}$$

To justify the continuum treatment the ratio ℓ_i/λ_m must be less than unity. Using the Einstein relation this ratio is

$$\frac{\ell_i}{\lambda_m} = \left[e\right]^{1/3}\left[\varepsilon_\ell v_t\right]^{-1/2}\left[\sigma_\ell/b\right]^{1/6}$$

With $e = 1.6 \times 10^{-19}$ (C), $\varepsilon_\ell = 2.1 \times 10^{-11}$ (F/m) and a room temperature thermal voltage of $v_t \simeq 0.027$ (V), this ratio is tabulated in Table 5.4 with ion mobility and liquid conductivity as parameters. For the mobility of Table 3.1 ($b \simeq 3.0 \times 10^{-8}$) and the conductivity range of interest (1-100 pS/m) the approximation appears justified. In defining the range of validity of the Debye-Huckel theory of the ionic atmosphere, the same criterion is usually expressed in terms of solute concentration rather than bulk conductivity (56).

5.5 Engineering Implications

There are two issues to disuss: first, how would the analysis of the capped cylinder configuration in Sec. 3.2 be revised to reflect the normal diffusion current, and second, when can that current be neglected in comparison with the migration current.

TABLE 5.4

Ratio of Mean Ion Separation to Debye Length

	b (m^2/V-s)			
σ_ℓ (S/m)	1.0×10^{-10}	1.0×10^{-9}	1.0×10^{-8}	1.0×10^{-7}
1.0×10^{-12}	0.33	0.23	0.15	0.11
3.2×10^{-12}	0.40	0.27	0.19	0.13
1.0×10^{-11}	0.49	0.33	0.23	0.15
3.2×10^{-11}	0.59	0.40	0.27	0.19
1.0×10^{-10}	0.72	0.49	0.33	0.23
3.2×10^{-10}	0.87	0.59	0.40	0.27
1.0×10^{-9}	1.1	0.72	0.49	0.33
3.2×10^{-9}	1.3	0.87	0.59	0.40
1.0×10^{-8}	1.5	1.1	0.72	0.49

5.5.1 Charging Transient with Capped Cylinder

The counterpart of the master equation (Eq. 3.10) of the migration model is obtained by substituting Eq. 5.19 into Eq. 3.8 with the result

$$\frac{\partial\lambda}{\partial t} + (\pi a^2\sigma_e)\frac{\partial E_z}{\partial z}(a,z,t) = \frac{\pi a^2 U}{d}\left[\bar{\rho}(0,t) - \bar{\rho}(\infty)\right]\exp(-z/d) \qquad (5.40)$$

where $\bar{\rho}(\infty)$ and d are given by Eq. 5.20. Thus, all of the results of Sec. 3.2 can be generalized to include diffusion by making the replacements

$$\bar{\rho}(0,t) \rightarrow \left[\bar{\rho}(0,t) - \bar{\rho}(\infty)\right] \quad ; \quad \tau_\ell U \rightarrow d \qquad (5.41)$$

In particular, the revised steady state result (Eq. 3.40)

$$\Phi_n = \frac{e_n U}{\sigma_e d B_n(R,a) k_n^2}\left[\bar{\rho}(0,\infty) - \bar{\rho}(\infty)\right] \qquad (5.42)$$

where e_n is given by Eq. 3.30, is called for in Sec. 7.1.1. As in Sec. 3.2.5, however, the assumption that $\rho(z,t)$ is independent of the generated fields is now more difficult to justify than in the case of the close fitting sleeve.

5.5.2 Range of Validity of the Migration Model

Conditions under which Eq. 5.40 reduces to Eq. 3.10 define the range of validity of the migration model of Chapter 3. These conditions are

$$\bar{\rho}(\infty) << \bar{\rho}(0,t) \qquad (5.43)$$

$$\delta << \lambda_m \qquad (5.44)$$

$$2\lambda_m^2/a\delta << 1 \qquad (5.45)$$

$$D_m|\rho_w|/\delta << J_w \qquad (5.46)$$

The first of these conditions ensures that most of the entrained charge originates upstream of the insulating tube. The last three conditions are just those for which $d \to \tau_\ell U$, where d is given by Eq. 5.20. The inequality of Eq. 5.44 is also assumed in the model of Chapter 3. The inequality of Eq. 5.45 implies that the diffusion time $(a\delta/D_m)$ is long compared with the charge relaxation time (τ_ℓ). Finally, the inequality of Eq. 5.46 ensures that charge transport through the liquid bulk is the rate limiting step in the spatial development. Of course, in the experiments reported in Sec. 5.2, the inequality of Eq. 5.43 is deliberately circumvented by means of the expansion element at the inlet to the insulating tube. However, Eq. 5.45 is satisfied for all of these experiments, except for those involving the lowest conductivities.

There are at least two situations where the normal diffusion and migration current densities may be comparable in an upstream metallic section while migration dominates in a dowstream insulating section:

<u>Equal Tube Radii and Unequal Wall Charge Densities</u>: With equal tube radii, the left side of Eq. 5.45 has the same value in both the metal and insulating sections, and this inequality is satisfied to the same degree in both. If diffusion and migration are in approximate balance near the outlet of the upstream metal section, then $\bar{\rho}(0,t)$ is essentially the fully developed volume charge density given by Eq. 5.16 and 5.20:

$$\bar{\rho}(0,t) \simeq \frac{(\rho_w)_u}{1 + a\delta/2\lambda_m^2} \quad ; \quad \bar{\rho}(\infty) \simeq \frac{\rho_w}{1 + a\delta/2\lambda_m^2} \qquad (5.47)$$

where the subscript 'u' associates the variable with the upstream section. Now, Eq. 5.43 is satisfied if $(\rho_w)_u >> \rho_w$. This is consistent with the results of Sec. 2.2.3 and those of Table 5.1 which suggest that $(\rho_w)_u \simeq -3.0(\sigma_\ell/b)$ for stainless steel while $\rho_w \simeq 0.1(\sigma_\ell/b)$ for Tefzel.

<u>Unequal Tube Radii and Equal Wall Charge Densities</u>: Even if $(\rho_w)_u$ and ρ_w are comparable, Eq. 5.43 will still be satisfied if the radius of the insulating tube exceeds that of the metal tube (see Sec. 7.1.1).

Chapter 6

STANDING-WAVE INTERACTION WITH IMPOSED FLOW

6.1 Introduction

There are both scientific and engineering incentives for the development of the technique described in this chapter. On the scientific side, the model of Chapter 5 remains tentative for lack of a physicochemical description of the liquid-solid interface. Thus, an independent experimental approach to the study of the surface conduction and the boundary condition on the volume charge would be of value. From the engineering standpoint, a comprehensive program for controlling the flow-induced electrical stresses should include real-time monitoring of the processes that are precursors of a hazardous condition.

The technique described in this chapter is one for probing the processes of interest near the liquid-insulating solid interface through capacitive interaction with the convecting part of the charge distribution. As analyzed in Sec. 5.3.1, the density of the naturally occuring volume charge in the liquid varies across the diffusion sublayer. This implies a variation in the liquid conductivity that is readily characterized where chemical equilibrium prevails, and makes it possible for an applied normal electric field to induce additional charge in the sublayer. Thus, a standing wave of potential imposed at the outer surface of the tube by means of an electrode structure like that pictured in Fig. 6.1 will induce a standing wave of perturbation charge within the sublayer where the liquid velocity is finite. The extent to which convection shifts the spatial phase of the induced charge distribution relative to the fixed electrode structure is a reflection of both the competition with conduction and the velocity profile within the sublayer. As in previous work (<u>57</u>) where the convecting charge was confined to a <u>free</u> liquid surface, the spatial phase shift is detected as an imbalance in image charges induced on segments of the same

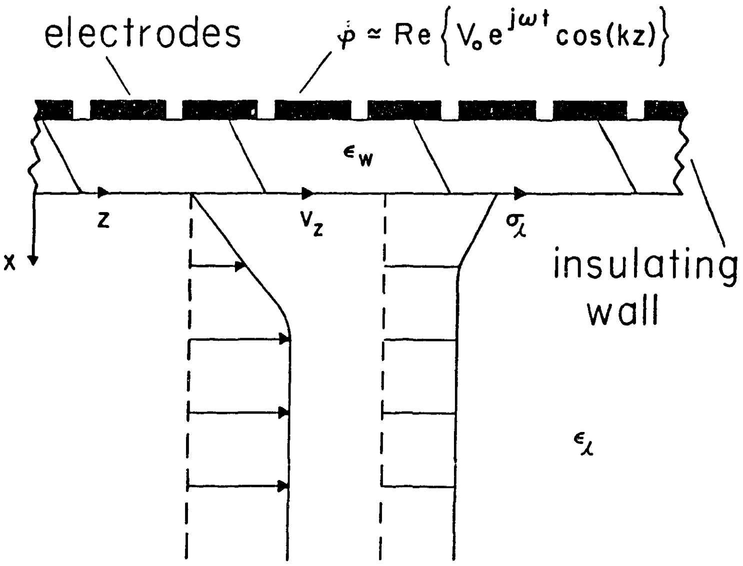

Fig. 6.1 An electrode structure on the outer surface of the insulating wall imposes a potential distribution there that approximates a standing-wave distribution. Typical velocity and conductivity profiles are as shown.

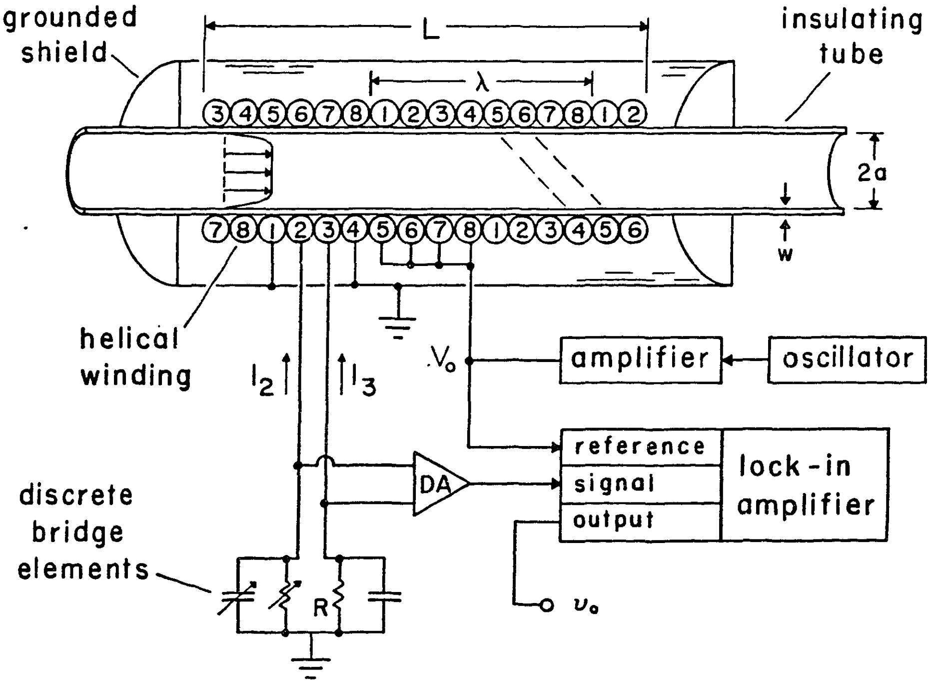

Fig. 6.2 Experimental configuration. Numbered circles identify wires of the helical winding. $L = 0.33$ (m), $\lambda = 0.01$ (m), $a = 1.3$ (mm), $w = 0.3$ (mm) and $R = 1.0$ MΩ.

electrode structure that imposes the standing wave.

Section 6.2 describes the experimental device for implementing this technique, and presents experimental results for the magnitude of the imbalance in image charges as a function of liquid velocity and standing wave frequency and amplitude. The frequency response predicted by the model developed in Sec. 6.3 exhibits the same trends discernible in the observed response. This success encourages use of the results to address two issues confronted in Chapter 5: the time scale for evolution of the surface conductivity, and the dependence of the convection current on the evolving surface charge. In addition, the sensitivity of the predicted response to the convection current suggests application of the technique to noninvasively monitor conditions in operating equipment.

6.2 Experiments

6.2.1 Arrangement

The most convenient form of the external electrodes to be used with the insulating tube is the helical winding illustrated in Fig. 6.2, which consists of eight individual wires. Exciting four adjacent electrodes (numbered 5-8) with an AC potential while the other four remain virtually grounded sets up a standing-wave of potential at the outer surface of the tube, with the wavelength of the spatial fundamental component as indicated in the figure. In the diffusion sublayer where the conductivity gradient is finite, a standing-wave component of net charge is induced, which in turn induces image charges on two of the unexcited electrodes (2,3). These image charges are detected as charging currents drawn primarily through bridge resistances across which the potential drop remains small compared with the excitation amplitude. To limit direct capacitive coupling between the excited and sensing electrodes, the intervening electrodes (1,4) are grounded, and a grounded shield encloses the winding.

With the initially liquid stationary, the charging currents are balanced by bridge adjustments. Then with the flow established, the standing wave distribution of induced charge is displaced downstream relative to the sensing electrodes, and the resulting imbalance in induced image charges is detected as a difference in the respective charging currents. The recorded experimental response is the magnitude υ_0 of the fundamental frequency component of the differential voltage across the resistances, as measured by a lock-in amplifier. Because flow-induced distension of the tube would modify interwinding capacities and produce a response that is independent of processes in the liquid, the tube and winding are clamped between v-grooves cut into plexiglas blocks which are rigidly attached to the grounded enclosure. No response is measured when the pressure in the tube is raised while a downstream valve blocks the flow, indicating that the response measured subsequently with the valve open can be attributed to convection effects.

6.2.2 Experimental Results

Experiments with Freon TF in turbulent flow through Tefzel tubes exhibit reproducible behavior. Figure 6.3 shows the typical response as a function of time. The observation of a steady signal indicates that the parameters that determine the response evolve over time scales much longer than the duration of an experiment. (However, as is readily demonstrated by circulating warm air against the grounded shield, this important feature can be obscured by temperature variations which slightly modify interwinding capacities.) Next, with the standing-wave amplitude V_0 fixed, the response is measured as a function of frequency with the results shown in Fig. 6.4. Note that as the mean velocity increases, the frequency that produces the peak response shifts towards higher values while the resonance broadens. Finally, Fig. 6.5 indicates a linear response as the standing-wave amplitude is varied with frequency fixed.

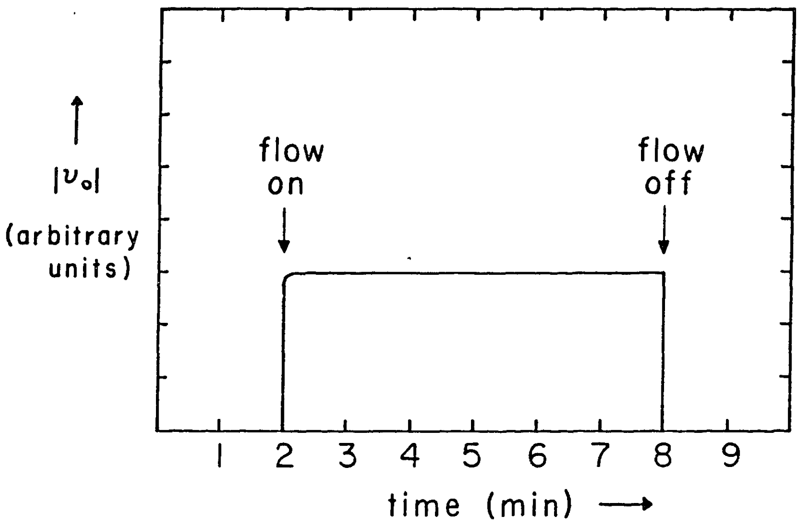

Fig. 6.3 Typical temporal response.

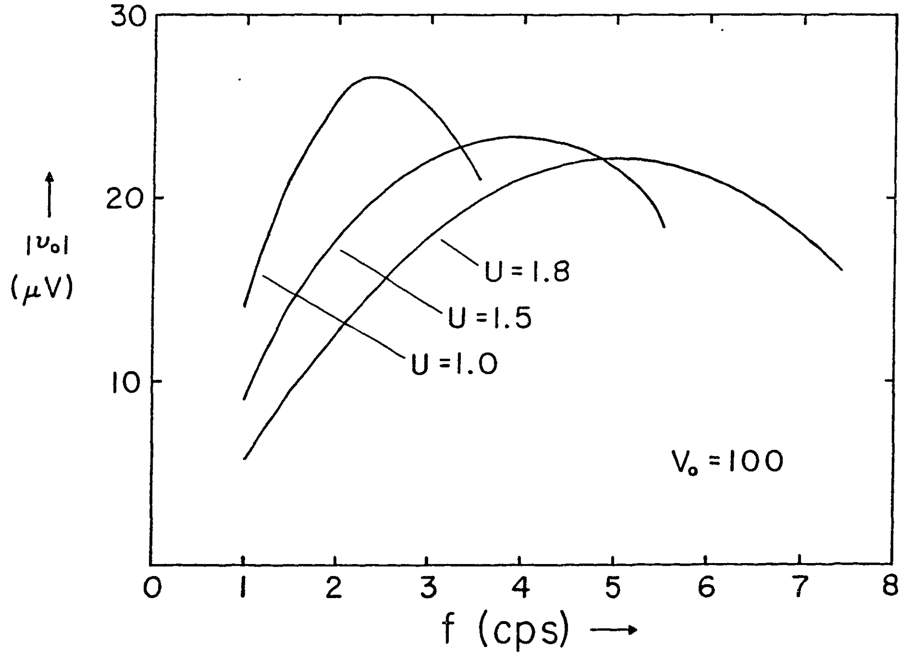

Fig. 6.4 Frequency response, illustrating resonances that broaden and shift towards higher frequencies with increasing flow rate U. σ_ℓ = 400.0 pS/m.

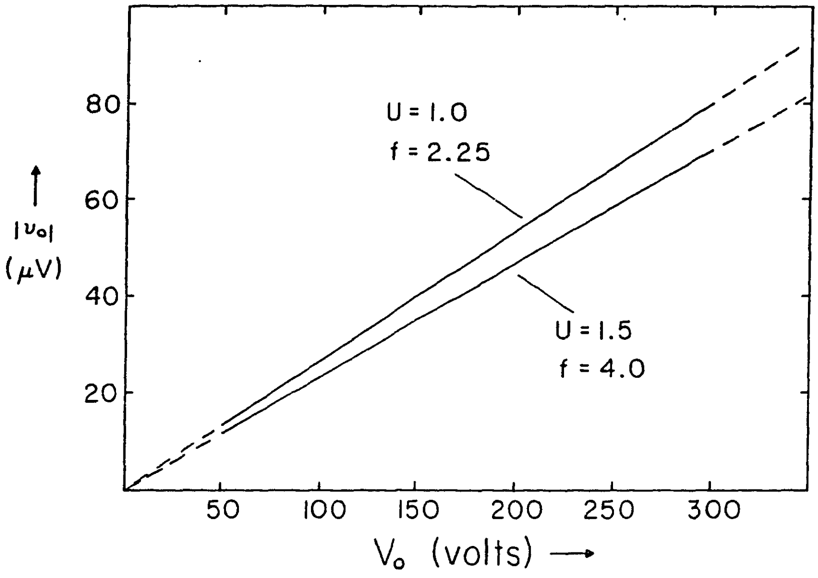

Fig. 6.5 Amplitude response. Frequencies (f) correspond to peak responses in Fig. 6.4.

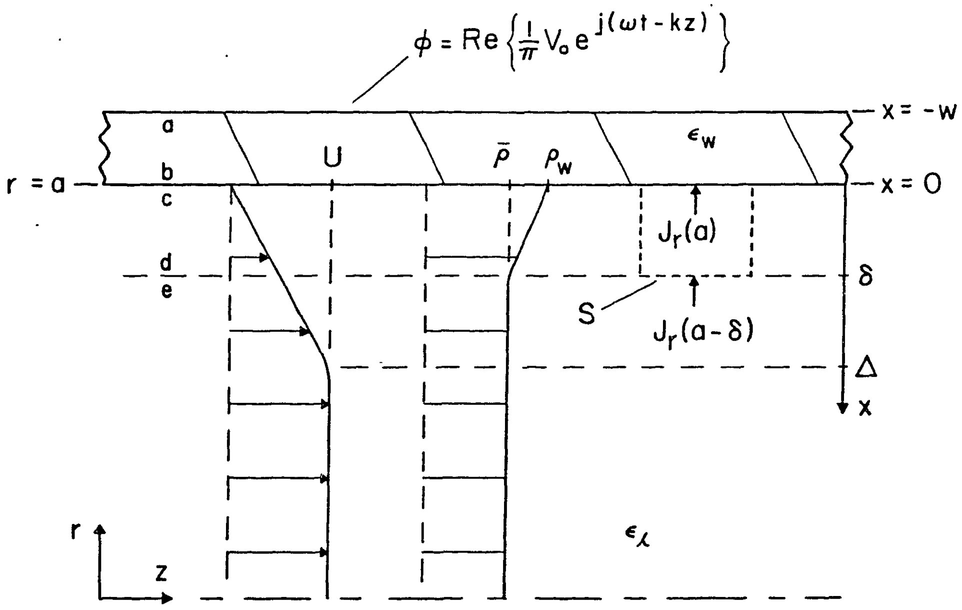

Fig. 6.6 Cross sectional view showing insulating wall and typical velocity and charge density profiles. Coordinate systems and surfaces (a - e) are defined.

6.2.3 Interpretation

The observed temporal (Fig. 6.3) and amplitude (Fig. 6.5) responses have simple interpretations that form the basis of a model for the frequency response. Once it is recognized that the unexcited helical winding must exert the same effect on the charging process as the close fitting sleeve (Fig. 3.1), it becomes clear that a charging transient like that shown in Fig. 3.7 is in progress even as the steady response shown in Fig. 6.3 is observed. Yet the reconciliation tends to support the pictures that underlie models for both of these experiments. With the charging process driven by a steady distribution of entrained volume charge, the observed transient reflects only a rate of change of the surface charge density at the liquid-solid interface. With the response υ_0 attributed to convection effects, the result in Fig. 6.3 indicates that electrical conditions are steady in the liquid volume where the velocity is finite, even if they are unsteady at the interface.

The linear dependence of the response on standing-wave amplitude (Fig. 6.5) indicates that, at least for the amplitude range investigated, a perturbation theory is appropriate in which the applied field induces charge in the diffusion sublayer by virtue of a conductivity gradient that is independent of that field. Thus, the conductivity gradient can be regarded as imposed by the steady distribution of the flow-induced volume charge.

6.3 Model

Consistent with the interpretation in the previous section, volume charge in the moving liquid is regarded as having two components: the background charge induced by the flow (Sec. 5.3.1), and the perturbation charge induced by the standing wave of potential. Once the assumptions and turbulent flow model are outlined, the response υ_0 is determined in two steps. First, the chemical equilibrium assumption is invoked to relate the conductivity gradient to the distribution of background charge within the diffusion sublayer (Sec. 6.3.3). Second, the radial component of the perturbation electric displacement induced within the tube by the applied potential is determined from the electroquasistatic field equations, and evaluated at the point of contact between the tube and the helical winding (Sec. 6.3.4). Gauss' law converts this result to expressions for the perturbation image charges induced on the winding and, in turn, for the charging currents drawn through the sensing resistors.

6.3.1 Assumptions

[a] The flow is turbulent and fully developed. Fully turbulent flow occurs for hydrodynamic Reynolds numbers in the approximate range

$$R_y \equiv \frac{2aU}{\nu} > 4000 \qquad (6.1)$$

while fully developed flow prevails beyond about 100 tube radii from the inlet.

[b] The Schmidt number is much greater than unity,

$$S_c \equiv \frac{\nu}{D_m} \gg 1 \qquad (6.2)$$

This is characteristic of the semi-insulating liquids of interest (see Tables 2.1 and 3.1).

[c] The Debye length exceeds the diffusion sublayer thickness,

$$\lambda_m^2 \gg \delta^2 \qquad (6.3)$$

The Debye length and diffusion sublayer thickness are defined by Eqs. 2.9 and 3.3, respectively. As a consequence of this inequality, the background volume charge distribution extends into the core region where the turbulent diffusivity is significant.

[d] The Debye length based on the turbulent diffusivity exceeds the tube radius,

$$\lambda_t > a \tag{6.4}$$

That is, the diffusion time based on the tube radius and the turbulent diffusivity (a^2/D_t) is exceeded by the charge relaxation time (τ_ℓ), and thus net charge in the core region ($0 < r < a - \delta$) will be essentially uniformly distributed.

[e] Within the diffusion sublayer the continuum approximation is valid (Sec. 5.4.2) and chemical equilibrium prevails for the unperturbed distribution of ions (Sec. A.2). Thus, the local conductivity within the sublayer is given by Eq. A.11:

$$\sigma_\ell(x,z) = \sigma_o\sqrt{1 + (\rho(x,z)b/\sigma_o)^2} \tag{6.5}$$

Implicit in Eq. 6.5 is the assumption of equal ion mobilities, which is reasonable for the antistatic additive of interest (Sec. 3.3.1). Also implicit is a condition on the strength of the applied fields (Sec. A.4, Eq. A.37c). As discussed in Sec. 6.2.3, experimental results suggest that the conductivity gradient is independent of the applied field. This implies a negligible contribution to the local conductivity from the perturbation charge, so there is no need to assume that perturbations of the background charge are consistent with chemical equilibrium. Thus, in the necessary condition for chemical equilibrium (Eq. A.73) τ is taken to be the liquid transit time based on the velocity at the edge of the diffusion sublayer (Sec. 6.3.2) rather than the period of the standing wave excitation.

6.3.2 Turbulent Flow Model

Accurate specification of the mean axial velocity profile is necessary only within the diffusion sublayer where the conductivity gradient, and hence the perturbation charge, is finite. While correctly representing the volume flow rate, the simplified profile based on the Blasius friction-factor correlation (18)

$$v_z = \begin{cases} U & 0 < r < (a - \Delta) \quad (6.6a) \\ \left(0.02\ R_y^{3/4}\ x/a\right)U & 0 < x < \Delta \quad (6.6b) \end{cases}$$

is most accurate near the wall ($x << \Delta$). The viscous sublayer thickness is given by (18)

$$\Delta = \left(118\ R_y^{-7/8}\right)a \tag{6.7}$$

The thickness of the diffusion sublayer is given by (18)

$$\delta = \left(S_c^{-1/3}\right)\Delta = \left(118\ R_y^{-7/8}\ S_c^{-1/3}\right)a \tag{6.8}$$

Thus, $\delta << \Delta$ in view of the high Schmidt number (assumption [b]), while $\Delta << a$ for the high Reynolds numbers (assumption [a]). Outside the diffusion sublayer ($x > \delta$), eddy diffusion dominates the thermal process, the eddy diffusivity being given by (22)

$$D_t = \left(0.01\ S_c\ R_y^{7/8}\right)D_m \tag{6.9}$$

As in Sec. 5.3.1, this expression for D_t can be used to show that Eq. 6.4 is generally satisfied for the experimental conditions. The velocity at the edge of the diffusion sublayer follows from Eqs. 6.6b and 6.8 as

$$v_z(\delta) = \left[2.36\, R_y^{-1/8}\, S_c^{-1/3}\right] U \qquad (6.10)$$

The liquid transit time based on this velocity and the length L of the helical winding

$$\tau_\delta = \frac{L}{v_z(\delta)} = \left[0.42\, R_y^{1/8}\, S_c^{1/3}\right](L/U) \qquad (6.11)$$

easily exceeds the charge relaxation time τ_ℓ ($\simeq$ 0.05 s) for the experiments of Sec. 6.2.2) and thus the necessary condition (Eq. A.73) for application of Eq. 6.5 is met.

6.3.3 Conductivity Gradient

By assumption [d], charge outside the diffusion sublayer is essentially uniformly distributed. Within the diffusion sublayer, the background charge density is distributed according to Eq. 5.10. Thus, in the limit where $\delta \ll \lambda_m$

$$\rho(x,z) = \begin{cases} \bar{\rho}(z) & 0 < r < (a - \delta) \qquad (6.12a) \\ \frac{x}{\delta}\left[\bar{\rho}(z) - \rho(0,z)\right] + \rho(0,z) & 0 < x < \delta \qquad (6.12b) \end{cases}$$

Figure 6.7 illustrates the velocity and charge density profiles represented by Eqs. 6.6 and 6.12. Substituting Eq. 6.12b into Eq. 6.5 yields

$$\sigma_\ell(x,z) \simeq \Sigma(z) + \gamma(z)x \qquad (6.13a)$$

where

$$\Sigma(z) \equiv \sigma_o\left[1 + \frac{1}{2}\left[\frac{\rho(0,z)b}{\sigma_o}\right]^2\right] \qquad (6.13b)$$

and

$$\gamma(z) \equiv \frac{-\sigma_o}{\delta}\left[\frac{\rho(0,z)b}{\sigma_o}\right]^2 \left[\frac{\rho(0,z) - \bar{\rho}(z)}{\rho(0,z)}\right] \tag{6.13c}$$

to linear terms in the fractional change in $\rho(x,z)$ across the sublayer. To apply the boundary condition Eq. 5.15 it is necessary to revert from boundary layer coordinates to cylindrical coordinates, so that $\rho(0,z) \rightarrow \rho(a,z)$. Two cases are considered. First, suppose the convection current is still developing, in which case $\rho(a,z)$ is expressed in terms of $\bar{\rho}(z)$ by Eq. 5.17:

$$\rho(a,z) = \frac{J_W(\rho_W/|\rho_W|) + (\alpha a/2)\bar{\rho}(z)}{J_W/|\rho_W| + \beta a/2} \tag{6.14}$$

where α and β are given by Eq. 5.14. In the second case, the convection current is fully developed so that $J_r(a,z) = 0$ (see Sec. 2.2.1) and now Eqs. 2.10 and 5.20 give

$$\rho(a,z) = \frac{\alpha}{\beta}\bar{\rho}(\infty) = \rho_W \tag{6.15}$$

In the fully developed case Eq. 6.13c becomes (with $\delta << \lambda_m$)

$$\gamma = \frac{-\sigma_o}{\delta}\left[\frac{\rho_W b}{\sigma_o}\right]^2 \left[1 + \frac{2\lambda_m^2}{a\delta}\right]^{-1} \tag{6.16a}$$

Where electrical conditions are still developing, and if J_W is sufficiently small that $\rho(a,z) \simeq \rho_W$, the conductivity gradient becomes

$$\gamma = \frac{-\sigma_o}{\delta}\left[\frac{\rho_W b}{\sigma_o}\right]^2 \left[1 - \frac{\bar{\rho}(z)}{\rho_W}\right] \tag{6.16b}$$

If the development length d (Eq. 5.18) is long compared with the axial extent of the interaction region defined by the length L of the helical winding, then the conductivity gradient γ is essentially uniform along the axis, in addition to being independent of time (Sec.6.2.3).

6.3.4 Perturbation Analysis

To determine the response υ_0 (defined in Fig. 6.2), it is convenient to divide the tube cross section into three coaxial regions, within each of which the perturbation potentials and normal components of the electric displacements are governed by equations specialized to the given region. The outermost region is the tube wall, with bounding surfaces denoted 'a' and 'b' in Fig. 6.6. Innermost is the core region bounded by the surface 'e' which lies at the radius $r = (a - \delta)$. In between lies the diffusion sublayer with bounding surfaces 'c' and 'd' adjacent to the wall and the core regions, respectively. In what follows, superscripted variables are evaluated at the surface (in Fig. 6.6) corresponding to the superscript.

The spatial harmonics associated with the actual square-wave potential distribution imposed at surface 'a' by the electrodes do not contribute significantly to the potential at surface 'b' (and hence within the interaction region) partly because their amplitudes at surface 'a' are reduced relative to the spatial fundamental component, and partly because the amplitudes fall off more rapidly with distance from the electrodes. With harmonics neglected, and with one half of the electrodes per wavelength remaining virtually grounded (Fig. 6.2), the potential imposed at 'a' is

$$\Phi^a = \mathrm{Re}\left[\frac{2V_o}{\pi}\exp(j\omega t)\cos(kz)\right] - \mathrm{Re}\left[\frac{2V_o}{\pi}\exp(j\omega t)\right] \qquad (6.17)$$

Implicit in this axisymmetric form is a neglect of winding pitch that is justified as long as the circumference of the tube exceeds the wavelength of the excitation. Because the second term in Eq. 6.17 represents a uniform distribution, it makes no contribution to the potential within the liquid. Thus, only the first term is retained, and this is represented as the sum of two traveling waves:

$$\Phi^a = \mathrm{Re}\left[\frac{V_o}{\pi}\left(\exp(j\omega t-jkz) + \exp(j\omega t+jkz)\right)\right] \tag{6.18}$$

Because the potentials are described by linear equations, the responses to these two traveling-wave components can be found independently and then superposed. The response to the forward traveling wave

$$\Phi^a = \mathrm{Re}\left(\hat{\Phi}^a \exp(j\omega t-jkz)\right) \quad ; \quad \hat{\Phi}^a = V_o/\pi \tag{6.19}$$

is sought first. Since they are solutions to linear equations, the perturbation displacements and potentials assume the same traveling-wave form. The present objective is to express the normal displacment at the surface 'a' explicitly in terms of that part of the imposed potential given by Eq. 6.19.

In the insulating tube wall, the potential is governed by Laplace's equation. With the wall thickness small compared to the tube radius, the region can be regarded as electrically planar so that the complex amplitudes of the perturbation potentials ($\hat{\Phi}$) and normal displacements ($\hat{D}_x = -\epsilon\partial\hat{\Phi}/\partial x$) evaluated at the boundaries of the region are related by (14, Sec. 2.16)

$$\begin{bmatrix} \hat{D}_x^a \\ \hat{D}_x^b \end{bmatrix} = \epsilon_w k \begin{bmatrix} \coth(kw) & -\mathrm{csch}(kw) \\ \mathrm{csch}(kw) & -\coth(kw) \end{bmatrix} \begin{bmatrix} \hat{\Phi}^a \\ \hat{\Phi}^b \end{bmatrix} \tag{6.20}$$

Within the liquid core there is no conductivity gradient, and hence no perturbation charge. Thus, the perturbation potential there is also governed by Laplace's equation, and perturbation amplitudes at the boundary of the core region are related by the cylindrical harmonic (14, Sec. 2.16)

$$\hat{D}^e_x = -\hat{D}^e_r = \epsilon_\ell k\left[\frac{I_0'(ka)}{I_0(ka)}\right]\hat{\Phi}^e = \epsilon_\ell k\left[\frac{I_1(ka)}{I_0(ka)}\right]\hat{\Phi}^e \tag{6.21}$$

where I_n is the nth order modified Bessel function of the first kind, and the prime denotes differentiation with respect to the argument.

Although Laplace's equation no longer applies, relations analogous to those obtained for the wall and core regions are sought for the diffusion sublayer. Axial diffusion of perturbation charge arises from spatial variations on the scale of the wavelength (λ) and hence is characterized by the a diffusion time (λ^2/D_m) that is long enough on the scale of the charge relaxation time (τ_ℓ) that axial diffusion can be neglected. It is left to the Sec. 6.3.5 to show that diffusion of perturbation charge in the direction normal to the phase boundary can be neglected as well. Then using Poisson's equation to convert Eq. A.9 to an equation for the perturbation potential yields

$$\epsilon_\ell\left[\frac{\partial}{\partial t} + (v_z)\frac{\partial}{\partial z} + \frac{1}{\tau_\ell}\right]\nabla^2\Phi + \nabla\Phi\cdot\nabla\sigma_\ell = 0 \tag{6.22}$$

which is linear in Φ because σ_ℓ is regarded as independent of the applied field (Sec. 6.2.3). Substituting the traveling-wave form (see Eq. 6.19), and again regarding the layer as electrically planar yields an ordinary differential equation for the complex amplitude:

$$\left[j\epsilon_\ell(\omega - kv_z) + \sigma_\ell\right]D^2\hat{\Phi} + D\hat{\Phi}D\sigma_\ell = 0 \tag{6.23}$$

where $D \equiv \partial/\partial x$. Neglect of the term $k^2\hat{\Phi}$ compared with $D^2\hat{\Phi}$ is justified as long as the wavelength λ is much greater than the diffusion sublayer thickness δ, and leads to a first order equation for the normal electric displacement. Substituting Eqs. 6.6b and 6.13a into Eq. 6.23 and noting that $D\hat{\Phi} = -\hat{D}_x/\epsilon_\ell$ yields

$$D\hat{D}_x + \hat{D}_x\left(A + Bx\right)^{-1} = 0 \tag{6.24a}$$

where

$$A \equiv \frac{\Sigma + j\epsilon_\ell \omega}{\gamma} \quad ; \quad B \equiv 1 - j\left(\frac{0.02\epsilon_\ell kUR_y{}^{3/4}}{\gamma a}\right) \tag{6.24b}$$

and Σ and γ are defined by Eq. 6.13. Equation 6.24 is separable and readily integrated to yield

$$\hat{D}_x(x) = \hat{D}_x^c\left(1 + Bx/A\right)^{-1/B} \tag{6.25}$$

Evaluated at $x = \delta$, Eq. 6.25 yields the first of two relations that play the role for the diffusion sublayer that Eqs. 6.20 play for the wall:

$$\hat{D}_x^d = \hat{D}_x^c\left(1 + B\delta/A\right)^{-1/B} \tag{6.26}$$

It can be shown that the differentiation involving complex constants needed to verify that Eq. 6.25 satisfies Eq. 6.24a can proceed as though the constants were real (58). To complete the electrical description of the diffusion sublayer, the relation

$$\hat{\Phi}^d \simeq \hat{\Phi}^c \tag{6.27}$$

is added which recognizes that in the long wave limit ($\lambda >> \delta$) only a small fractional change in potential across the diffusion sublayer is possible. Together with Eqs. 6.20 and 6.21, these last two equations complete specification of the bulk equations for the three regions, which must be supplemented by boundary conditions at the interfaces between regions. At the d-e interface

$$\hat{\Phi}^d = \hat{\Phi}^e \quad ; \quad \hat{D}_x^d = \hat{D}_x^e \tag{6.28}$$

The first condition expesses continuity of the potential as required by Faraday's law, the second reflects the absence of a charge singularity at the d-e interface. Next, the boundary conditions at the b-c interface

$$\hat{\Phi}^c = \hat{\Phi}^b \tag{6.29a}$$

and

$$\frac{\partial\bar{\sigma}}{\partial t} = \left[-\frac{\partial}{\partial z}(\sigma_s E_z) - \frac{D_x^c}{\tau_\ell} \right] \rightarrow \hat{D}_x^c = \frac{j\omega\tau_\ell \hat{D}_x^b - k^2\sigma_s\tau_\ell\hat{\Phi}^b}{1 + j\omega\tau_\ell} \tag{6.29b}$$

express, respectively, continuity of the potential and conservation of perturbation surface charge. Solving Eqs. 6.20, 6.21, and 6.26-6.29 for the complex amplitude of the normal displacement at surface 'a' in terms of the potential at the same surface yields

$$\hat{D}_x^a = T_+\hat{\Phi}^a \tag{6.30}$$

where

$$T_+ = (\epsilon_w k)\coth(kw) + \frac{-(\epsilon_w k)^2 \operatorname{csch}^2(kw)}{P_+ + (\epsilon_w k)\coth(kw)}$$

and

$$P_+ = \left(\frac{1 + j\omega\tau_\ell}{j\omega\tau_\ell}\right)\left(\frac{\epsilon_\ell k I_1(ka)}{I_0(ka)}\right)\left(1 + \frac{B\delta}{A}\right)^{1/B} + \frac{k^2\sigma_s}{j\omega}$$

The response to the backward traveling-wave component in Eq. 6.18 can be found from Eq. 6.30 simply by making the replacement k → -k, which amounts to replacing B by its complex conjugate. Denoting the resulting coefficient by T_-, superposing the two responses, and recalling Eq. 6.19 to express $\hat{\Phi}^a$ in terms of the standing wave amplitude gives for the normal component of the electric displacement at surface 'a'

$$D_x^a = \mathrm{Re}\left[\frac{V_o}{\pi}\left(T_+\exp(-jkz) + T_-\exp(+jkz)\right)\exp(j\omega t)\right] \qquad (6.31)$$

Because the spacing between the wire electrodes is small compared with their distance from the grounded enclosure (Fig. 6.2), the electrodes intercept all of the normal flux at surface 'a.' Thus, the wire electrodes can be regarded as flat, as pictured in Fig. 6.1, in applying Gauss' law to express the charging currents defined in Fig. 6.2:

$$i_2 = \frac{\ell}{k}\int_{3\pi/4}^{\pi} \frac{\partial D_x^a}{\partial t}\, d(kz) \;+ i_d(t) \qquad (6.32a)$$

$$i_3 = \frac{\ell}{k}\int_{\pi}^{5\pi/4} \frac{\partial D_x^a}{\partial t}\, d(kz) \;+ i_d(t) \qquad (6.32b)$$

where because of the balancing procedure, the current $i_d(t)$ associated with any direct coupling between the excited and the sensing electrodes is identical for each of the latter. Finally, upon substituting Eq. 6.31 into Eq. 6.32, and carrying out the indicated integrations, the response (in volts) follows as

$$|v_o| = R|i_2 - i_3| = \frac{(2-\sqrt{2})}{\pi}\frac{\omega\ell R}{k}|T_+ - T_-|V_o \qquad (6.33)$$

Once it is recognized, either by inspection or by physical argument,*

---

* e.g. Eqs. 6.20 and 6.21 apply for any frequency (within the quasistatic limit), including zero frequency in which case the normal electric displacements arising from an applied potential of the form of Eq. 6.19 are clearly invariant under the replacement k → -k.

that the coefficients of $\hat{\Phi}$ in Eqs. 6.20 and 6.21 are even functions of k, it is easily shown that $P_+ = P_-$ when $U = 0$. It quickly follows that $\upsilon_o = 0$ when $U = 0$, indicating that the response is generated by the flow. A computer program performed the complex algebra called for in Eq. 6.33, and yielded the theoretical frequency response curves shown in Fig. 6.7 with $\bar{\rho}$ fixed and U as a parameter, and in Fig. 6.8 with U fixed and $\bar{\rho}$ as a parameter (59). For these figures, σ_s is taken to be negligible, while the conductivity gradient is essentially that given by Eq. 6.16b.

6.3.5 Diffusion of Perturbation Charge

Neglect of diffusion in Eq. 6.22 is justified here in retrospect by showing that the magnitude of the omitted term is typically much less than that of the conduction term retained. The equation in question equates the time rate of decrease of the local net perturbation charge density to the divergence of the perturbation current density $\bar{J}$ where

$$\bar{J} = \rho v_z \hat{i}_z - \sigma_\ell \nabla\Phi - D_m \nabla\rho \tag{6.34}$$

with $\hat{i}_z$ representing the axial unit vector. As noted in connection with Eqs. 6.22 and 6.23, the axial components of the last two terms on the right do not contribute significantly to the divergence, and so it is appropriate to focus on the normal component of $\bar{J}$ which has the complex amplitude

$$\hat{J}_x = \left[\frac{\sigma_\ell}{\epsilon_\ell} - D_m\left(\frac{\partial^2}{\partial x^2} - k\frac{\partial}{\partial x}\right)\right]\hat{D}_x \simeq \left[\frac{\sigma_\ell}{\epsilon_\ell} - D_m\frac{\partial^2}{\partial x^2}\right]\hat{D}_x \tag{6.35}$$

Here, the potential and the charge density have been expressed in terms of the displacement, the first as in Eq. 6.24a, and the second using Gauss' law. The second approximate equality recognizes that space derivatives must be characterized by lengths scales shorter than the excitation wavelength in order to be significant. To assess the

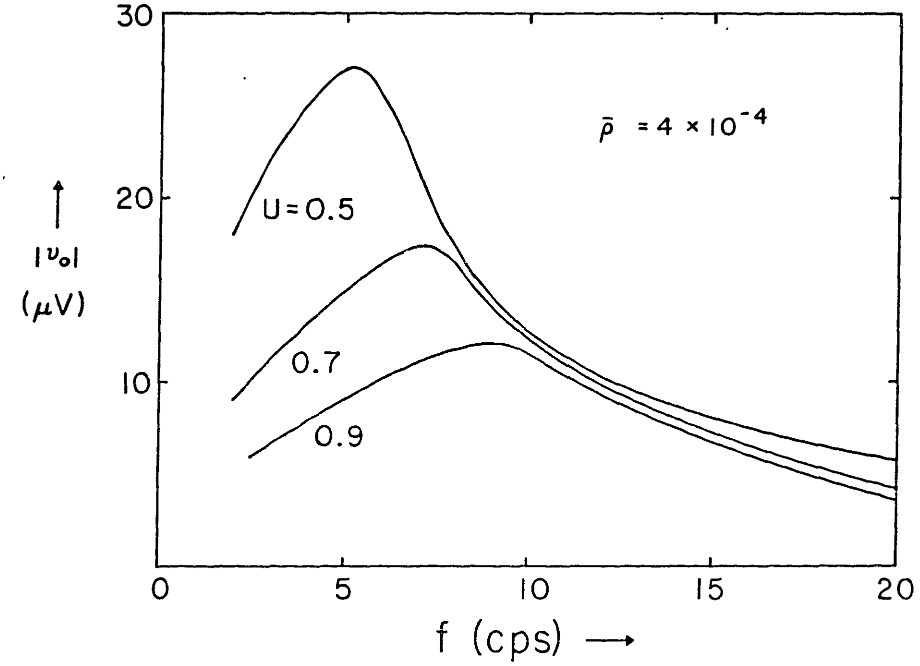

Fig. 6.7 Theoretical frequency response. Entrained volume charge density is fixed while flow rate varies.

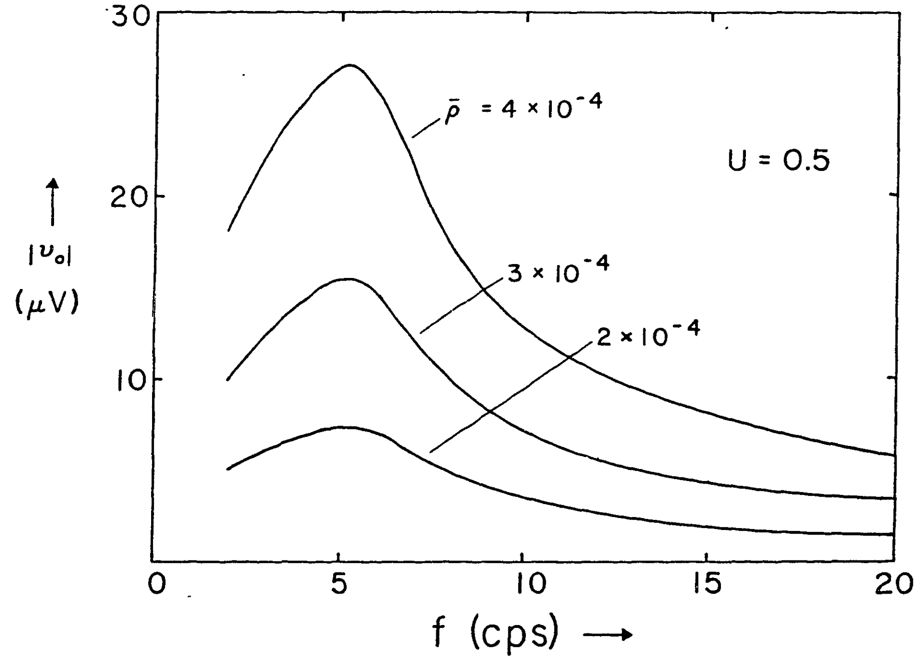

Fig. 6.8 Theoretical frequency response. Flow rate is fixed while entrained volume charge, and hence convection current, varies.

importance of diffusion, Eq. 6.25 is substituted into Eq. 6.35 and the ratio of the magnitude of the diffusion current to that of the conduction current is formed:

$$\lambda_m^2\left|\frac{1+B}{A^2}\right|\left|1+\frac{Bx}{A}\right|^{-2} \tag{6.36}$$

This has a maximum M at $x = 0$ given by

$$M = \lambda_m^2\,\frac{|1+B|}{|A^2|} \tag{6.37}$$

Substituting Eqs. 6.13b and 6.24b yields

$$M = \left[\frac{\lambda_m^2\gamma^2}{\sigma_o^2|1+j\omega\tau_\ell|^2}\right]\left|2 - j\left[\frac{0.02\epsilon_\ell kUR_y{}^{3/4}}{\gamma a}\right]\right| \tag{6.38}$$

where the approximation $\Sigma \simeq \sigma_o$ used is justified as long as $\rho(0,z)b/\sigma_o$ is of the order of or less than unity (see Eq. 2.12). For hydrodynamic Reynolds numbers of the order of 10^3 to 10^4,

$$\frac{0.02R_y{}^{3/4}U}{a} = \frac{2.4R_y{}^{-1/8}U}{118R_y{}^{-7/8}a} \simeq \frac{U}{\Delta} \tag{6.39}$$

where Eq. 6.7 was used. Furthermore, since an upper bound for M is sought, $\omega\tau_\ell$ can be neglected in the denominator in Eq. 6.38. Thus, with Eq. 6.39 substituted and with γ as given in Eq. 6.13c, Eq. 6.38 becomes

$$M = \left[\frac{\bar{\rho}b}{\sigma_o}\right]^4\left[\frac{\delta}{\lambda_m}\right]^2\left|2 + j\left(\frac{U}{\Delta}\,\frac{\tau_\ell k\lambda_m^2}{\delta(\bar{\rho}b/\sigma_o)^2}\right)\right| \tag{6.40}$$

Now according to Eqs. 2.12 and 6.3, the leading factor on the right in Eq. 6.40 is much less than unity, and thus to determine whether M approaches unity, it is enough to examine the magnitude of M′ where

$$M < M' = \left(\frac{\bar{\rho}b}{\sigma_o}\right)^4 \left(\frac{\delta}{\lambda_m}\right)^2 \left(\frac{U}{\Delta}\,\frac{\tau_\ell k\lambda_m^2}{\delta\left(\bar{\rho}b/\sigma_o\right)^2}\right) = \left(\frac{\bar{\rho}b}{\sigma_o}\right)^2 \frac{\delta\tau_\ell kU}{\Delta} \qquad (6.41)$$

In view of the high Schmidt number (Eq. 6.8) and for the present experimental conditions,

$$\delta < \Delta \quad ; \quad \tau_\ell kU = O(1)$$

Then since the leading factor on the far right in Eq. 6.41 is of the order of or less than unity (see for example Table 5.1), so is M′. Thus, the correction that would be introduced by including diffusion in Eq. 6.22 would be small.

6.4 Discussion

The temporal and amplitude responses illustrated in Figs. 6.3 and 6.5 respectively are perhaps most valuable because they can be interpreted without reference to the model, and because they tend to support some of the assumptions invoked Chapters 3 and 5. Without a <u>free</u> liquid surface, the observation of a response to liquid convection (see Sec. 6.2.1) is clear indication that the technique is sensitive to conditions in the liquid <u>bulk</u>. The steady temporal response and the linear amplitude response reveal three aspects of the phenomena initiated the flow:

(1) As long as chemical equilibrium can be assumed to prevail in the diffusion sublayer, the electrically-induced charge corresponds to a specific distribution of flow-induced net volume charge. Thus, the steady temporal response (Fig. 6.3) reveals this distribution to be

imposed, at least for sleeve configuration, in the sense assumed in Secs. 3.2.5 and 5.3.1. The linear amplitude response (Fig. 6.5) confirms that at least for the modest applied voltages used here, the volume charge distribution is determined by the flow conditions and not the external field.

(2) Regardless of the electrical description of conditions in the liquid bulk, the response (see Eq. 6.30) is attenuated by a significant surface conductivity at the liquid-solid interface (surface 'c' in Fig. 6.6) because it will tend to exclude the applied field from the liquid bulk. Thus, if a significant surface conductivity is present, the steady response of Fig. 6.3 indicates that it does not evolve on the time scale of the experiment (consistent with assumption in Sec. 5.3).

(3) Though not independent of (1), it is worth emphasizing that since the steady temporal response overlaps a charging transient like that illustrated in Fig. 3.7, the latter is attributable entirely to surface charge accumulation.

Two factors prevent a quantitative comparison between the experimental (Fig. 6.4) and theoretical (Fig. 6.7) frequency responses. First, the experimental Debye length λ_m and diffusion sublayer thickness δ are of the same order in conflict with a condition of the theory (Eq. 6.3). To be consistent with this condition, the model (Eq. 6.33) is applied with the flow rates indicated in Fig. 6.7 and a value of the bulk conductivity that is an order of magnitude less than the experimental value. Second, the influent convection current $I(0) = Q\bar{\rho}(0)$ needed to determine the background charge density $\bar{\rho}$ was not recorded. The value for $\bar{\rho}$ indicated in Fig. 6.7 is based on measurements under corresponding experimental conditions (see Chapters 3 and 5). Despite the use of parameter values to evaluate Eq. 6.33 that differ from experimental values, a qualitative correspondence between the theoretical (Fig. 6.7) and experimental (Fig. 6.4) frequency responses is clearly discernible. Both exhibit a resonance which broadens and shifts towards higher frequencies with increasing superficial velocity. Furthermore, the theoretical results indicate resonant frequencies in the same range as those observed experimentally, and peak amplitudes of the same order of magnitude.

This qualitative correspondence encouraged an examination of the dependence on convection current at fixed flow velocity. Figure 6.8 indicates that while the shape and position on the frequency axis remain unchanged, the amplitude of the response varies essentially as the square of the convection current at a given flow rate. Although this quadratic relation is not evident in the expressions for the response, it appears to hold for a wide range of hypothetical conditions. Thus, the interaction could provide the basis for sensitive detection of convection current levels downstream of current generators or upstream of insulating elements that tend to collect charge.

The standing-wave technique is useful as a means for studying the natural processes in the volume because the induced charge constitutes only a perturbing influence on the original charge distribution within the sublayer. Thus, the applied fields are typically much smaller than those that can be generated by the flow and which would be expected to account for charge injection across the liquid-insulating solid interface from one bulk region to the other. To investigate the injection process, much higher potentials are applied when the external electrode structure is exploited again in Appendix B. There, to help distinguish injected charge from that induced by the flow, the liquid is initially stationary, and then it is the mechanical response elicited by an imposed traveling-wave of potential that is of interest.

Chapter 7

ENGINEERING IMPLICATIONS

By confirming expected trends of the time (τ_1) that characterizes the charging transient (see Sec. 2.1) the experimental results of Chapters 3, 4 and 5 tend to support the picture of the flow-induced electric field generation in the insulating tube wall as the result of charge generation and accumulation processes as they are opposed by charge leakage. While the clearest support for the basic ideas comes from study of the transient, design issues are best addressed in terms of the ultimate electrical stress which results when these competing processes reach a balance. Thus, the objectives of Sec. 7.1.1 are to sort out the dependencies of these processes, and hence of the ultimate electrical stress, on system parameters, and to clarify the implications for configurations other than the capped cylinder. Of particular interest, is the dependence on parameters that can be controlled, namely, the bulk and surface conductivities, the tube radius, and the influent convection current. In Sec. 7.1.2 the conclusions of Sec. 7.1.1 are consolidated and phrased in the form of design suggestions.

7.1.1 Dependence of Ultimate Electrical Stress on System Parameters

For the capped cylinder configuration, the steady state wall stress E_r^W (see Fig. 3.3) is given in the form of a superposition of spatial modes by the combination of Eqs. 3.22, 3.23 and 5.42. Examination of the mode amplitudes (see Eqs. 3.19, 3.26, 3.30 and 3.32) indicates that the magnitude of the stress is essentially that of the fundamental mode. Thus, for discussion purposes, only the first term of the series need be retained, and this is evaluated at z = L/2 to yield the maximum stress:

$$E_r^W(L/2,\infty) \simeq \frac{\varepsilon_0}{\varepsilon_W}\left(\frac{e_1 U C_1(R,a)}{\sigma_e d B_1(R,a) k_1}\right)\left(\bar{\rho}(0,\infty) - \bar{\rho}(\infty)\right) \qquad (7.1)$$

The usefulness of this result is hampered by the inclusion of phenomenological parameters (the wall charge density ρ_w and the exchange current density J_w which enter $\bar{\rho}(\infty)$ and d, Eq. 5.20) and a parameter which refers to a specific external conductor configuration (the cylinder radius R). In what follows these parameters are eliminated in exchange for an upper limit to the stress that will be remain useful provided that limit is not too conservative. From Eq. 3.30

$$e_1 = \frac{2}{\pi}\left[\frac{1 + \exp(-L/d)}{1 + (L/\pi d)^2}\right] < \frac{4}{\pi} \tag{7.2}$$

In the limit $k_1 a << 1$ implicit in the model (see footnote to Eq. 3.24) and provided that $k_1 R$ is not too small, it can be shown that

$$\frac{C_1(R,a)}{B_1(R,a)} \rightarrow \frac{-1/2}{(k_1 a/2)\ell n(k_1 a/2)} > 0 \tag{7.3}$$

where B_1 and C_1 are given by Eqs. 3.17 and 3.20 respectively. While the condition on $k_1 R$ excludes the impractical case of the sleeve (Fig. 3.1), the condition on $k_1 a$ (which amounts to $a << L$) is fairly unrestrictive. The ratio in Eq. 7.3 is independent of R, and decreases with $k_1 a$ in the range $0 < k_1 a/2 < 1/e$ ($\simeq 0.37$). Finally, from Eqs. 5.16 and 5.20 in the limit $\delta << \lambda_m$

$$d = \frac{U}{\alpha}\left[1 + \frac{a\beta|\rho_w|}{2J_w}\right] > \tau_\ell U\left[1 + \frac{2\lambda_m^2}{a\delta}\right]^{-1} \tag{7.4}$$

Once Eq. 7.2 is inserted into Eq. 7.1, the development length d appears only in the denominator, so a <u>lower</u> limit on d is appropriate. Thus, ρ_w and J_w are readily eliminated because the shortest development corresponds to a process limited by transport through the liquid bulk, while these parameters enter only when J_w is small enough that the spatial development is controlled by an interfacial process. In view of the last three equations an upper limit for the stress is

$$E_r^w(L/2,\infty) \;<\; \frac{2L\varepsilon_0}{\varepsilon_w\varepsilon_\ell}\left(\frac{1 + 2\lambda_m^2/a\delta}{1 + 2\sigma_s/a\sigma_\ell}\right)\left(\frac{\bar{\rho}(0,\infty) - \bar{\rho}(\infty)}{(-k_1a/2)\ell n(k_1a/2)}\right) \tag{7.5}$$

where the definition of σ_e from Eq. 3.8b is recalled. Because the insulating tube makes only a small contribution to the total length of the coolant flow path, the volume flow rate Q is perhaps best regarded as constrained, so the liquid velocity (U) is not independent of the tube radius (a). Hence, the design parameters remaining in Eq. 7.5 are the radius (a), the bulk (σ_ℓ) and surface (σ_s) conductivities, and perhaps the tube length (L) which enters both the leading factor and k_1 ($\equiv \pi/L$). It remains to estimate the influent and fully developed volume charge densities, $\bar{\rho}(0,\infty)$ and $\bar{\rho}(\infty)$, in order to apply Eq. 7.5 and to determine whether the former is sufficiently greater that an expansion section (Chapter 4) will be effective.

<u>Volume Charge Densities</u>. To make the discussion concrete, two assumptions are made. First, the influent convection current $Q\bar{\rho}(0,\infty)$ is fully developed near the exit of the upstream charge generating element, and is governed by Abedian and Sonin's theory (Eq. 2.11). This envisions an upstream element such as a heat sink with the liquid flowing through a winding channel that is long compared with the development length d. Second, the channel radius is much less than that of the insulating tube. This is motivated by the expectation that the liquid velocity is much greater in the upstream element where heat is being transferred to the liquid. Then given that the inequality $\delta \ll \lambda_m$ is satisfied in the insulating tube (see Sec. 3.2.1), it is also satisfied in the upstream section because at fixed flow rate δ varies essentially as the square of the tube radius (see Eq. 7.8 below). In this limit, Eq. 2.11 yields

$$\frac{\bar{\rho}(0,\infty)}{(\rho_w)_u} \simeq \left[1 + \frac{(a\delta)_u}{2\lambda_m^2}\right]^{-1} \tag{7.6}$$

where the subscript 'u' associates the variable with the upstream section. For the fully developed convection current in the insulating tube Eqs. 5.16 and 5.20 yield in the same limit

$$\frac{\bar{\rho}(\infty)}{\rho_w} = \frac{\beta}{\alpha} \simeq \left[1 + \frac{a\delta}{2\lambda_m^2}\right]^{-1} \tag{7.7}$$

Regarding ρ_w and $(\rho_w)_u$ as generally comparable and of the order given by Eq. 2.12, it remains to determine the dependence of the quantity $(a\delta)$ on tube radius at fixed flow rate. In view of Eq. 3.3

$$a\delta \propto a^2\, Ry^{-7/8} \simeq \frac{a\nu}{2U} \propto \frac{a^3\nu}{2Q} \tag{7.8}$$

Then with the given assumptions $a\delta \gg (a\delta)_u$, and because $a\delta/2\lambda_m^2$ is typically greater than unity Eqs. 7.6 and 7.7 indicate that $\bar{\rho}(0,\infty) \gg \bar{\rho}(\infty)$.

This result completes the discussion of Sec. 5.5.2 by showing how Eq. 5.43 can be satisfied even when the metallic and insulating sections are characterized by comparable wall charge densities (ρ_w). Thus, either of the conditions $(\rho_w)_u \gg \rho_w$ or $a_u \ll a$ imply that $\bar{\rho}(0,\infty) \gg \bar{\rho}(\infty)$, that is, the generated electrical stress (Eq. 7.5) is due to charge that originates primarily <u>upstream</u> of the insulating tube. As long as the <u>influent</u> convection current $(\bar{\rho}(0,\infty)Q)$ dominates in Eq. 7.5 an expansion volume (Chapter 4) will be effective in reducing the generated stress.

Now the upper limit Eq. 7.5 can be further clarified using Eq. 7.6:

$$\left[\bar{\rho}(0,\infty) - \bar{\rho}(\infty)\right] \simeq \bar{\rho}(0,\infty) \simeq (\rho_w)_u\left[1 + \frac{(a\delta)_u}{2\lambda_m^2}\right]^{-1} \tag{7.9}$$

Then taking $(\rho_w)_u$ to be of the order of σ_ℓ/b (Eq. 2.12) Eq. 7.5 becomes

$$E_r^w(L/2,\infty) < \frac{2L\varepsilon_o\sigma_\ell}{\varepsilon_w\varepsilon_\ell b}\left(\frac{(1 + 2\lambda_m^2/a\delta)/(1 + (a\delta)_u/2\lambda_m^2)}{(1 + 2\sigma_s/a\sigma_\ell)(-k_1a/2)\ell n(k_1a/2)}\right) \tag{7.10}$$

With typical parameter values and with $k_1a/2 \simeq 1/e$ the right side of Eq. 7.10 is $O(10^{18}\sigma_\ell$ V/m), or $O(10^8$ V/m) for the largest bulk conductivity ($\sigma_\ell \simeq 10^{-10}$ S/m) consistent with the limit $\delta \ll \lambda_m$ under the present experimental conditions.

7.1.2 Control of Ultimate Electrical Stress

The following strategies are suggested by the development of the previous section:

Inhibit Charge Generation. To the extent that conditions are electrically developed (Sec. 2.2) in the flow element immediately upstream of an insulating tube, that element determines the convection current supplied to the tube. Thus, one approach to limiting the convection current at the inlet to the insulating tube would be a modification of the surface of the upstream element (typically a heat sink), perhaps in the manner described in Sec. 4.5. But now the side effects of the modified surface on heat transfer become a concern. An alternative is to use an antistatic agent in sufficient concentration that the operating point is to the right of the peak in the "bell" curves in Fig. 2.5. (The eventual decrease in convection current with increasing liquid conductivity is not reflected in Eq. 7.6 because only the limit $\delta \ll \lambda_m$ has been considered.) However, it is preferable to avoid the addition of a substance that may be taken up by solid surfaces in the flow loop with as yet unknown side effects.

Charge Trapping. There are two contributions to the charge that accumulates at the inner surface of the insulating wall: that which originates upstream of the insulating tube (external mode), and that which accumulates in the absence of upstream sources (internal mode). It is the first contribution that is emphasized by the migration model of Chapter 3, and which can be diverted from the insulating tube by means of an expansion section operating as a charge trap (Chapter 4). Conditions under which the external mode is dominant are identified in

Secs. 5.5.2 and 7.1.1, and are likely to be met in practice. When a charge trapping expansion section is inserted at the inlet to the insulating tube, the expression for the ultimate electrical stress (Eq. 7.10) must be multiplied by a factor of (1 - E) where E is the trapping efficiency given by Eq. 4.9.

Enhance Leakage. As discussed in Sec. 3.4 the external conductor configuration must be tailored to avoid "hotspots" where a conductor in close proximity to the insulating tube attenuates the local axial electric field and the associated leakage current. In contrast to the bulk conductivity, a controlled surface conductivity ($\sigma_s > a\sigma_\ell/2$) at the inner surface of the insulating tube enhances the leakage proceess without influencing the charge generation process in the upstream element. This accounts for the single occurence of σ_s in the denominator of Eq. 7.10.

Enlarge Insulating Tube Radius. Unless the surface conductivity is significant, the right side of Eq. 7.10 decreases as the radius (a) of the insulating tube increases in the range $0 < k_1a/2 < 1/e$ ($\simeq 0.37$). There are two issues to bear in mind as the radius is increased (with the volume flow rate fixed). First is the possible transition to laminar flow conditions, due either to the reduction in Reynolds number or to the increase in diffusion sublayer thickness (relative to the Debye length). Second is the greater energy stored by the accumulated charge when the electric stress equals the dielectric strength. That is, while the ultimate field is expected to be smaller in a larger insulating tube, physical damage is more likely in the larger tube if the dielectric strength is exceeded.

Appendix A

CHEMICAL EQUILIBRIUM

A.1 Introduction

A theme of Secs. 1.3 and 2.2 is the existence of ionization equilibrium in the liquid bulk where electrical conditions are fully developed (Sec. 2.2.1), and the departures from equilibrium that characterize the region of spatial development (Sec. 2.2.2). There it is stressed that treatment of the nonequilibrium process calls for additional specific data in the form of rate constants. Section A.2 shows how this distinction has its origin in the smaller (by one) number of partial differential equations needed to describe the conservation of reacting species in the equilibrium case. It is this analytical simplification that provides the strong incentive to clarify the conditions under which chemical equilibrium may be assumed to prevail.

Classical studies of chemical rate processes have their empirical basis in experiments that ideally maintain homogeneous distributions of the chemical reactants. Following a disturbance, equilibrium sets in after a transient having a duration τ_{cr} that can be expressed in terms of the chemical rate constants and the equilibrium concentrations (60). In convective systems, the inhomogeneous and dissimilar distributions of ionic reactants imply additional rate processes (diffusion and migration) that may inhibit the local chemical equilibration even if processes in the liquid bulk remain stationary as viewed in the laboratory frame. Nevertheless, Sec. A.3 argues that in the region of fully developed electrical conditions chemical equilibrium prevails regardless of the time scale τ_{cr}. However, Sec. A.4 shows that if treatment of the electrical development is to avail itself of the analytical simplification outlined in Sec. A.2, this time scale must be short relative to those that characterize diffusion and migration.

The condition on time constants that justifies the assumption of local chemical equilibrium is expressed in Sec. A.4 as a lower limit on the ion recombination rate k_R. Section A.5 identifies an upper limit on k_R that is approached when diffusion is the rate limiting step in the recombination process, and which is independent of specific chemical attributes of the reactants. It is left to Sec. A.6 to compare for dielectric media this upper limit k_{12} with the lower limit of Sec. A.4. Thus, the price paid for neglecting specific aspects of the reaction is a condition for chemical equilibrium that is necessary but not sufficient.

A.2 The Chemical Equilibrium Assumption

If only three reactive species, two ionic and one neutral, are present in significant concentrations, the two simplest ionization reactions are

$$A^+ + B^- \rightleftarrows iC \quad ; \quad i = 1,2 \tag{A.1}$$

where i = 1 or 2 for a uni- or bimolecular dissociation process, respectively. The conservation equations that govern the associated charge densities and neutral concentration attribute local time rates of change to divergences of diffusion, migration and convection flux densities:

$$\frac{\partial \rho_+}{\partial t} = -\nabla \cdot \bar{J}_+ + G - R \quad ; \quad \bar{J}_+ = +\rho_+\bar{v} + b_+\rho_+\bar{E} - D_+\nabla\rho_+ \tag{A.2}$$

$$\frac{\partial \rho_-}{\partial t} = +\nabla \cdot \bar{J}_- + G - R \quad ; \quad \bar{J}_- = -\rho_-\bar{v} + b_-\rho_-\bar{E} + D_-\nabla\rho_- \tag{A.3}$$

$$\frac{\partial n}{\partial t} = -\nabla \cdot \bar{\Gamma}_n - (G - R)\frac{i}{e} \quad ; \quad \bar{\Gamma}_n = n\bar{v} - D_n\nabla n \tag{A.4}$$

These equations are coupled through Gauss' law and the generation (G) and recombination (R) terms which reflect the rates of the homogeneous reaction Eq. A.1. To ensure charge conservation, the same net generation rate (G - R) appears in both of the ion conservation statements. It is to satisfy mass conservation that the same net rate, multiplied by i/e (for monovalent ions), enters into Eq. A.4 for the neutral species.

Appropriate forms for the generation and recombination terms follow from inspection of the homogeneous chemical rate equation:

$$\frac{d}{dt}[A^+] = \frac{d}{dt}[B^-] = \left(k_D[C]^i - k_R[A^+][B^-]\right) = -\frac{d}{dt}\left(\frac{[C]}{i}\right) \qquad (A.5)$$

With the identifications (for monovalent ions)

$$n = [C] \quad ; \quad \rho_+ = e[A^+] \quad ; \quad \rho_- = e[B^-] \qquad (A.6)$$

the generation and recombination terms must be

$$G = ek_D n^i \quad ; \quad R = \frac{k_R \rho_+ \rho_-}{e} \qquad (A.7)$$

where k_D and k_R are the effective dissociation and recombination rate constants, respectively.

The chemical equilibrium assumption regards the generation and recombination terms (Eq. A.7) as large enough compared with other terms in the conservation equations that they balance separately, with the result

$$\rho_+\rho_- \simeq e^2 K n^i \quad ; \quad K \equiv k_D/k_R \qquad (A.8)$$

where K is the equilibrium constant. In Eq. A.8 the approximate equality means the difference between the two terms is small compared with either individual term. To exploit this independent algebraic constraint among the dependent variables, the conservation equations A.2-A.4 must be used in combinations for which the net generation rate (G - R) does not appear. Thus, subtracting Eq. A.3 from Eq. A.2 and inserting the differential form of Gauss' law yields

$$\frac{D\rho}{Dt} = -\bar{E}\cdot\nabla\sigma_\ell - \frac{\sigma_\ell \rho}{\epsilon_\ell} + \nabla\cdot(D_e\nabla\rho) \quad ; \quad \frac{D}{Dt} \equiv \frac{\partial}{\partial t} + \bar{v}\cdot\nabla \qquad \text{(A.9)}$$

where

$$\rho \equiv \rho_+ - \rho_- \quad \text{and} \quad \sigma_\ell \equiv b(\rho_+ + \rho_-) \qquad \text{(A.10)}$$

are the net charge density and the local conductivity, and for simplicity equal ion mobilities (see Sec. 3.3.1) and incompressible flow are assumed. Eliminating the individual charge densities from Eqs. A.8 and A.10 leaves the conductivity expressed in terms of the net charge density

$$\sigma_\ell = \sigma_o\sqrt{1 + (\rho b/\sigma_o)^2} \quad ; \quad \sigma_o \equiv 2be\sqrt{Kn^i} \qquad \text{(A.11)}$$

Here σ_o is the conductivity where the net charge vanishes. The generation term in Eq. A.4 can likewise be expressed in terms of the neutral density and the new dependent variables ρ and σ_ℓ. Note the simplification achieved: the three original partial differential equations are replaced by the two partial differential equations A.4 and A.9 supplemented by the algebraic equation A.11.

Further simplification is possible for dielectric media where ionizable solutes remain so weakly dissociated that the neutral density suffers a much smaller fractional departure from its equilibrium value than do the ions. Then n can be approximated as fixed and uniform so that the conservation equation for the neutral species is extraneous. Now when Eq. A.8 is justified, the original three partial differential equations are replaced by the single partial differential equation (A.9) supplemented by a single algebraic equation (A.11). Note also that the rate constants do not enter, only the equilibrium constant does through Eq. A.11.

A.3 Fully Developed Electrical Conditions

The demonstration that Eq. A.8 holds where electrical conditions are fully developed regardless of the reaction rates is based on three assumptions:

1. Total solute concentration is fully developed. This is consistent with the fully developed electrical condition.
2. Ion generation and recombination processes are confined to the liquid bulk. That is, the reactions of Eq. A.1 do not take place at the interface, and any transformation of one of the species A^+, B^- or C at the interface results in a different chemical species. For example, the polymeric neutral solute of Table 1.1 is thought to undergo a proton transfer reaction of the form of Eq. A.1 with i = 2 (44). If the resulting ions individually participate in electron transfer at the interface, the neutral entities so produced will have lower molecular weights than the original neutral form.
3. Rate constants of the ionization reaction are uniform. Because k_D and k_R are temperature dependent this assumption presumes isothermal conditions, certainly reasonable in a convecting turbulent liquid. Furthermore, if the recombination process is diffusion controlled, then the mean separation between reactants must be small relative to the scale of the turbulence so that the uniform molecular diffusivity is controlling regardless of the local turbulence intensity (61).

A corollary is the demonstration that radial ionic flux densities vanish identically.

Equation 2.7 implies the first of the two equalities among the radial flux densities

$$\Gamma_r^+(r,\infty) = \Gamma_r^-(r,\infty) = \frac{-1}{i}\Gamma_r^n(r,\infty) \equiv \Gamma_r(r,\infty) \qquad \text{(A.12)}$$

where i = 1,2 for uni- and bimolecular dissociation, respectively (see Eq. A.1). If the net generation rate (G - R) is eliminated between the steady, fully developed forms of Eqs. A.3 and A.4 the result

$$\frac{1}{r}\frac{d}{dr}\left(r\Gamma_r^n\right) = -\frac{i}{r}\frac{d}{dr}\left(r\Gamma_r^-\right) \tag{A.13}$$

shows that Γ_r^- and Γ_r^n can differ only by the term A/r where A is a constant. However, to avoid a singularity on the axis, A must be identically zero, and the second equality in Eq. A.12 follows immediately.

In view of the first two assumptions above the individual flux densities in Eq. A.12 must vanish at the interface: $\Gamma_r(a,\infty) = 0$. Otherwise, the finite value of $\Gamma_r(a,\infty)$ would, by the second assumption, imply a change in form of the solute, which the first assumption precludes. Then integrating the steady, fully developed form of any one of Eqs. A.2 to A.4 over the tube cross section yields

$$\int_0^a (G - R)2\pi r dr = 0 \tag{A.14}$$

The stronger statement that the integrand vanishes identically is based on manipulation of the expressions in Eqs. A.2 to A.4 for the radial flux densities:

$$\Gamma_r(r,\infty) = \pm b_\pm c_\pm E_r - D_e\frac{dc_\pm}{dr} \quad ; \quad i\Gamma_r(r,\infty) = D_e\frac{dn}{dr} \tag{A.15a,b,c}$$

where the definition in Eq. A.12 has been used, and the same D_e appears in each case reflecting the dominance of the nonspecific eddy diffusivity over most of the cross section. Multiply Eqs. A.15a and A.15b by c_- and c_+ respectively and sum the results to obtain

$$(c_+ + c_-)\Gamma_r = c_+c_-E_r(b_+ - b_-) - D_e\frac{d}{dr}(c_+c_-) \tag{A.16}$$

Now, multiply Eqs. A.15c and A.16 by k_D and k_R respectively and sum the results to yield

$$k_R(c_+ + c_- + iK)\Gamma_r = D_e\frac{d}{dr}\left(k_D n - k_R c_+ c_-\right) + k_R c_+ c_- E_r(b_+ - b_-) \qquad (A.17)$$

where $K \equiv k_D/k_R$ is the equilibrium constant. Note that the third assumption above has been invoked to bring the rate constants inside the derivative to form the net generation rate in the first term on the right.

To argue that $\Gamma_r(r,\infty)$ and the net generation rate vanish for $0 < r < a$, it is enough to show that otherwise Eq. A.17 is generally violated. First, suppose the ion mobilities are identical, to eliminate the second term on the right in Eq. A.17. If $\Gamma_r > 0$ (say) then there is net generation in the core of the flow and, to satisfy Eq. A.14, net recombination near the wall. But this implies a negative radial derivative of the net generation rate, while the left hand side of Eq. A.17 is positive by assumption. The same contradiction arises if $\Gamma_r < 0$ is assumed. To allow for a difference in ion mobilities it must be shown that the previously neglected term remains much less than one of those retained. The ratio of the two terms in Eq. A.17 that contain the product c_+c_- is

$$\frac{aE_r(b_+ - b_-)}{v_T b(D_t/D_m)} \qquad (A.18)$$

where the tube radius a is assumed to characterize the radial derivative, b is the average ion mobility, and v_T is the thermal voltage introduced by the Einstein relation. From Sec. 3.2.2 the ratio of the turbulent to molecular diffusivities is of the order of 10^4 for Schmidt and Reynolds numbers of the order of 10^3, while the fractional difference in mobilities is at most of the order of unity. Finally, with the typical space charge fields ($a\bar{\rho}/2\varepsilon_{\ell}$) encountered in the experiments of the previous chapters, the typical potential drop between the tube axis and inner wall does not exceed the thermal voltage by nearly as much as D_t exceeds D_m. Thus the ratio Eq. A.18 is small, and the original conclusions holds that the approximate equality Eq. A.8 is satisfied in the sense that both sides ~~vastly~~ exceed their difference.

A.4 Chemical Equilibrium in Inhomogeneous Systems

The simplification of the coupled conservation equations (A.1-A.3) outlined in Sec. A.2 hinges on the assumption that the generation (G) and recombination (R) terms are individually much greater in magnitude than any other term. To investigate this assumption without actually solving the equations requires that they be cast into normalized form. This section addresses the questions: what characteristic times are implicit in the normalized conservation equations, how can they be specialized to dielectric solvents, and what ordering of these times justifies the equilibrium assumption.

Define a characteristic length ℓ and time scale of interest τ so that

$$r = \underline{r}\ell \quad ; \quad t = \underline{t}\tau \quad ; \quad v = \underline{v}(\ell/\tau) \qquad \text{(A.19)}$$

It will be supposed that the net charge density is small in the sense that differences between instantaneous ion concentrations and their respective equilibrium values remain small compared with those values, a condition usually satisfied in practical bipolar systems. Thus, σ_o (defined with Eq. A.9) is the characteristic conductivity, $\sigma_o/2b$ is the typical value for $\rho_{\pm}$, and the typical neutral density is determined from the equilibrium condition Eq. A.8.

$$\sigma = \underline{\sigma}\sigma_o \quad ; \quad \rho_\pm = \underline{\rho}_\pm \frac{\sigma_o}{2b} \quad ; \quad n^i = \underline{n}^i \frac{k_R \sigma_o{}^2}{4e^2 b^2 k_D} \tag{A.20}$$

where i = 1 or 2 corresponding to the uni- or bimolecular reactions of Eq. A.1. The absence of an applied potential, and the contribution of an evolving surface charge distribution to the electric field make it difficult to to specify a typical field strength. For purposes of normalization, the characteristic field is taken to be that associated with one species of ion when the counterions are discharged. From Gauss' law

$$E = \underline{E}\,\frac{\ell}{\epsilon_\ell}\cdot\frac{\sigma_o}{2b} \tag{A.21}$$

However, because the two ion concentrations are in fact comparable, the normalized field is likely to satisfy

$$\underline{E} << 1 \tag{A.22}$$

In normalizing the conservation equations to these characteristic values the rate constant

$$k_L = \frac{e(b_+ + b_-)}{\epsilon_\ell} \quad (m^3/s) \tag{A.23}$$

emerges, which is the recombination rate constant predicted by Langevin for gases at high pressure (62).

Given this normalization, what characteristic times emerge, and for what ordering of these times will an observer following a liquid element through the region of interest find that chemical equilibrium is maintained in the approximate sense of Eq. A.8? The answers are discerned from a normalized equation for the convective derivative of the net generation rate (G - R). Multiplying Eqs. A.2 and A.3 by ρ_- and ρ_+, respectively, substituting Eq. A.7, and adding the results yields

$$\frac{D\rho_+\rho_-}{Dt} = \frac{\tau}{\tau_\ell}\frac{\bar{E}}{2}\cdot(\rho_+\nabla\rho_- - \rho_-\nabla\rho_+) + \frac{\tau}{\tau_\ell}\frac{2k_R}{k_L}\sigma(n^i - \rho_+\rho_-) + \frac{\tau}{\tau_D}(\rho_+\nabla^2\rho_- + \rho_-\nabla^2\rho_+) \quad ; \quad i = 1,2 \tag{A.\underline{24}}$$

where for simplicity incompressible flow and equal ion mobilities are assumed, and the underlined equation number indicates that all variables in the equation are normalized to the characteristic values defined in Eqs. A.19 to A.21. The relaxation and diffusion times are defined by

$$\tau_\ell \equiv \frac{\varepsilon\ell}{\sigma_o} \quad ; \quad \tau_D \equiv \ell^2/D_e \tag{A.25}$$

Because of the exponent i in Eq. A.7, the uni- and bimolecular reactions must be considered separately when normalizing the conservation equation for the neutral species.

Unimolecular Dissociation: With $i = 1$, Eq. A.4 has the normalized form

$$\frac{Dn}{Dt} = -\tau k_D(n - \rho_+\rho_-) + \frac{\tau}{\tau_d}\nabla^2 n \quad ; \quad \tau_d \equiv \frac{\ell^2}{D_n} \tag{A.\underline{26}}$$

Subtracting Eq. A.24 from Eq. A.26 yields the convective derivative of the normalized net generation rate

$$\frac{D}{Dt}(n - \rho_+\rho_-) = -\frac{\tau}{\tau_{cr}}(n - \rho_+\rho_-) - \frac{\tau}{\tau_\ell}\frac{\bar{E}}{2}\cdot(\rho_+\nabla\rho_- - \rho_-\nabla\rho_+) - \frac{\tau}{\tau_D}(\rho_+\nabla^2\rho_- + \rho_-\nabla^2\rho_+) + \frac{\tau}{\tau_d}\nabla^2 n \quad ; \tag{A.\underline{27}}$$

where

$$\frac{\tau}{\tau_{cr}} = \frac{2\tau k_R}{\tau_\ell k_L}\left(\frac{be}{\sigma_o}K + 1\right) = \frac{2\tau k_R}{\tau_\ell k_L}\left(\frac{K}{2\gamma s} + 1\right) \tag{A.28}$$

where Eq. A.23 and the definition of τ_ℓ were used, and both $\underline{n}$ and $\underline{\sigma}$ were approximated by unity. The equilibrium degree of dissociation γ was introduced by recognizing that $\sigma_o = 2eb[A^+] = 2eb\gamma s$, where s is the total solute concentration. To specialize the chemical relaxation time to dielectric media it proves convenient to eliminate K from Eq. A.28 and express the chemical relaxation time in terms of k_R and γ alone. To that end note that

$$[A^+] = [B^-] = \gamma s \quad ; \quad [C] = (1 - \gamma)s \tag{A.29}$$

and that in equilibrium Eq. A.5 (with i = 1) requires that

$$\gamma^2(s/K) + \gamma - 1 = 0 \quad \rightarrow \quad \frac{K}{2\gamma s} + 1 = \frac{1 - \gamma/2}{1 - \gamma} \tag{A.30}$$

where the second relation follows after some algebra. Now Eq. A.28 becomes

$$\frac{\tau}{\tau_{cr}} = \frac{2\tau k_R}{\tau_\ell k_L}\,\frac{1 - \gamma/2}{1 - \gamma} \approx \frac{2\tau k_R}{\tau_\ell k_L}(1 - \gamma)^{-1} \tag{A.31}$$

The approximate equality recognizes that $(1 - \gamma/2) = 0(1)$ since $0 < \gamma < 1$.

<u>Bimolecular Dissociation</u>: After multiplication by 2n, and with i = 2, Eq. A.4 assumes the normalized form

$$\frac{Dn^2}{Dt} = -\frac{\tau}{\tau_\ell}\frac{4n}{k_L}\sqrt{k_R k_D}\,(n^2 - \rho_+\rho_-) + \frac{\tau}{\tau_d}2n\nabla^2 n \tag{A.32}$$

Subtracting Eq. A.24 from Eq. A.32 yields for the convective derivative of the net generation rate

$$\frac{D}{Dt}(n^2 - \rho_+\rho_-) = -\frac{\tau}{\tau_{cr}}(n^2 - \rho_+\rho_-) - \frac{\tau}{\tau_\ell}\frac{\bar{E}}{2}\cdot(\rho_+\nabla\rho_- - \rho_-\nabla\rho_+)$$

$$- \frac{\tau}{\tau_D}(\rho_+\nabla^2\rho_- + \rho_-\nabla^2\rho_+) + \frac{\tau}{\tau_d}2n\nabla^2 n \qquad (A.\underline{33})$$

where

$$\tau/\tau_{cr} = \frac{2\tau k_R}{\tau_\ell k_L}\left(2\sqrt{K} + 1\right) \qquad (A.34)$$

As before K is eliminated in favor of k_R and γ. The equilibrium implied by Eq. A.5 with i = 2 is

$$\gamma^2 - K(1-\gamma)^2 = 0 \quad \rightarrow \quad 2\sqrt{K} + 1 = \frac{1+\gamma}{1-\gamma} \qquad (A.35)$$

where the second relation follows after manipulation of the first. Now Eq. A.34 becomes

$$\tau/\tau_{cr} = \frac{2\tau k_R}{\tau_\ell k_L}\left(\frac{1+\gamma}{1-\gamma}\right) \simeq \frac{2\tau k_R}{\tau_\ell k_L}\left(1-\gamma\right)^{-1} \qquad (A.36)$$

where the fact was used that $(1+\gamma) = 0(1)$. Note that Eqs. A.31 and A.36 are the same.

In view of Eqs. A.27 and A.33 the same criterion for maintenance of chemical equilibrium applies in both the uni- and bimolecular cases:

$$\tau/\tau_D \leq 0(1) \quad ; \quad \tau/\tau_d \leq 0(1) \quad ; \quad (\tau/\tau_\ell)\underline{E} \leq 0(1) \qquad (A.37a,b,c)$$

while

$$\frac{\tau}{\tau_{cr}} \gg 1 \qquad (A.38)$$

Note that as long as Eq. A.22 holds, Eq. A.37c will be met for a wide range of τ/τ_ℓ. Thus, the "universal" criterion for chemical equilibrium in dielectric media for which $\gamma << 1$ is

$$\frac{2\tau k_R}{\tau_\ell k_L} >> 1 \tag{A.39}$$

Given τ and τ_ℓ, this is a lower limit on the recombination rate k_R.

A.5 Physical Significance of the Rate Constants

If the criterion for chemical equilibrium Eq. A.39 is to be applied to poorly characterized solutes, it is natural to ask what can be said about the recombination rate constant k_R without referring to specific reactants. In this section the reaction of Eq. A.1 is resolved into two component steps, one of which is identifiable as a diffusion-controlled process, and the other a chemical transformation. The overall reaction proceeds more slowly than any of its component steps, and thus the apparent recombination rate k_R is bounded from above by the forward rate of the diffusion step k_{12}. It is left to Sec. A.6 to compare Debye's prediction for the limiting recombination rate k_{12} with Langevin's rate k_L.

As the basis for a description of <u>macroscopic</u> effects, Eqs. A.2 to A.4 imply an ionization process in which only two ionic and one neutral species have significant concentrations. The identification of component reaction steps introduces a fourth reaction participant that helps elucidate the mechanisms implicit in the overall reaction Eq. A.1, but also serves notice that Eqs. A.2 to A.4 are not always adequate. Equation A.1 is elaborated as follows:

$$\begin{array}{ccccc} & \text{step 1} & & \text{step 2} & \\ A^+ + B^- & \underset{k_{21}}{\overset{k_{12}}{\rightleftarrows}} & C_E & \underset{k_{32}}{\overset{k_{23}}{\rightleftarrows}} & iC_T \\ \text{free ions} & & \begin{array}{c}\text{encounter}\\ \text{complex}\end{array} & & \begin{array}{c}\text{transformed}\\ \text{complex}\end{array} \end{array} \quad . \qquad (A.40)$$

where i = 1 or 2 for uni- or bimolecular dissociation, respectively. The encounter (C_E) and transformed (C_T) complexes are neutral species in the sense that they make no contribution to conduction.

With nothing implied regarding its stability, the encounter complex is defined here as what results from the mutual approach of two oppositely charged ions and contact between their solvation shells, <u>before</u> any change occurs in the solvation pattern or any other structural feature. The transformed complex is defined as any neutral species, present in significant concentration, that results from modification of the encounter complex. Defined this way, the encounter complex is the product of Coulomb interactions in competition only with the thermal energy, while production of the transformed complex generally involves Coulomb and short-range interactions and a desolvation process.

Whether Eqs. A.2 to A.4 remain sufficient hinges on whether Eq. A.5 can represent the two-step reaction. The present objective is to identify limiting cases where this is so, and to express the effective rate constants (k_D and k_R) and the concentration of the "observable" neutral species [C] in terms of the rate constants and concentrations of neutral complexes defined in Eq. A.40. The relation between the overall forward rate constant (k_R) and that of the first step (k_{12}) is of particular interest because the former enters into the equilibrium criterion (Eq. A.39) while the latter is the subject of the theory of Debye.

For the homogeneous chemical reaction Eq. A.40, the two ion concentrations remain equal ($[A^+] = [B^-] \equiv [I]$), and the rate equations are

$$\frac{d}{dt}[I] = -k_{12}[I]^2 + k_{21}[C_E] \tag{A.41}$$

$$\frac{d}{dt}[C_E] = k_{12}[I]^2 - (k_{21} + k_{23})[C_E] + k_{32}[C_T]^i \tag{A.42}$$

$$\frac{d}{dt}[C_T] = i\left(k_{23}[C_E] - k_{32}[C_T]^i\right) \tag{A.43}$$

This set of equations can be reduced to the two represented by Eq. 5

$$\frac{d}{dt}[I] = \left(k_D[C]^i - k_R[I]^2\right) = -\frac{d}{dt}([C]/i) \tag{A.44}$$

in three of the four limiting cases considered below.

(A) Negligible concentration of transformed complex: $[C_E] \gg [C_T]$
The identifications

$$k_D = k_{21} \quad ; \quad k_R = k_{12} \quad ; \quad [C] = [C_E] \tag{A.45}$$

are the obvious ones. It is tempting to anticipate the relative concentrations of the encounter and transformed complexes by comparing the free energy gained upon desolvation to the loss in free energy secured by minimizing the coulombic potential as a result of removing intervening solvent molecules. This would suggest that case A refers to solvents of moderate to high polarity, but the possibility that specific solvation effects and short-range interactions may be important precludes generalization. Nevertheless, in one case a more definite statement is possible: bimolecular dissociation is clearly excluded because by the definition of the encounter complex it is produced at the rate of only one per encounter.

(B) Negligible concentration of encounter complex: $[C_E] \ll [C_T]$
In the case of bimolecular dissociation, an encounter between two free ions produces two neutral entities. Thus charge transfer must be involved, and the neutral status is maintained by covalent bonds rather

than Coulomb attraction. Here, the ion pair represents an intermediate form, present in small concentration, that is still produced at the rate of one per encounter. For unimolecular dissociation, this ordering of concentrations reflects an instability of the encounter complex, and is perhaps more typical than case A when the solvent polarity is low.

A common and generally successful approximation in chemical kinetics is the Bodenstein steady state approximation (63) for which Hirschfelder (64) has provided justification. In this, the relatively small concentration of an unstable intermediate species is approximated as constant. Thus with $d[C_E]/dt \simeq 0$, Eq. A.42 yields

$$[C_E] = \frac{k_{12}[I]^2 + k_{32}[C_T]^i}{k_{21} + k_{23}} \tag{A.46}$$

Using this to eliminate $[C_E]$ from Eqs. A.41 and A.43 leads to equations of the form of Eq. A.44 if the identifications are made

$$k_D = \frac{k_{21}k_{32}}{k_{21} + k_{23}} \quad ; \quad k_R = \frac{k_{12}k_{23}}{k_{21} + k_{23}} \quad ; \quad [C] = [C_T] \tag{A.47}$$

in agreement with Eigen et al (65). Note that $k_R \le k_{12}$ with the equality approached only in the limit of $k_{23} >> k_{21}$ when the forward rate of the transformation step is fast enough that production of the transformed complex is limited by the forward rate of the first step.

(C) First step is rate limiting

Now allowance is made for significant concentrations of both neutral complexes, and it is striking that a single effective neutral species can be identified. Only for unimolecular dissociation ($i = 1$) can Eqs. A.41 to A.43 be reduced to Eq. A.44. On the relatively slow time scale of changes in the ion concentrations [I], the two neutral species remain in instantaneous equilibrium:

$$[C_T] \doteq K_2[C_E] \quad ; \quad K_2 = \frac{k_{23}}{k_{32}} \tag{A.48}$$

This relationship can be inserted in Eq. A.41, but not in Eq. A.42 where the faster time scale is also implicit. To obtain equations of the form of Eq. A.44, Eqs. A.42 and A.43 are summed yielding (with i = 1)

$$\frac{d}{dt}\left([C_E] + [C_T]\right) = k_{12}[I]^2 - k_{21}[C_E] \tag{A.49}$$

which is -d[I]/dt as required by mass conservation. Next, advantage is taken of Eq. A.48 to write

$$k_{21}[C_E] = \frac{k_{21}}{1 + K_2}\left([C_E] + [C_T]\right) \tag{A.50}$$

Substituting Eq. A.50 into Eq. A.49 shows that the desired form has been obtained if the identifications are made

$$k_D = \frac{k_{21}}{1 + K_2} \quad ; \quad k_R = k_{12}$$

and (A.51)

$$[C] = [C_E] + [C_T] = [C_E](1 + K_2)$$

In the analysis of case B, the small concentration of the intermediate form was assumed to remain constant. Here, the intermediate participates in the fast second step, and its rate of change cannot be neglected. Thus, at least as analyzed here, cases B and C are mutually exclusive. On the other hand, when $K_2 << 1$ cases A and C are indistinguishable, and they remain so as concerns the equilibrium criterion (Eq. A.39) even when K_2 is not small.

(D) Second step is rate limiting

Now the concentrations of the two neutral forms are not instantaneously coupled as in case C, and two independent conservation equations are required in addition to those for the ionic species. Now Eqs. A.2-A.5 are insufficient. This case may have practical importance when the ions have localized or inaccessible charge groups. In the former case the transformation step may involve a reorientation process that is inhibited by the confining effects of the solvent molecules.

In summary, Eqs. A.2 to A.5 represent the two-step reaction (Eq. A.40) in three limiting cases, and in general $k_R \leq k_{12}$. Because k_R enters into the equilibrium criterion (Eq. A.39) and is bounded from above by k_{12}, the rate of formation of the encounter complex is of special interest. Fortunately, as discussed in the next section, k_{12} represents a process that is amenable to a simple model.

A.6 Limiting Recombination Rate

The equilibrium criterion Eq. A.39 calls for a lower limit on the overall recombination rate constant k_R, while Sec. A.5 identifies the forward rate constant of the first step (Eq. A.40) k_{12} as an upper limit for k_R. Thus, a <u>necessary</u> condition for Eq. A.39 to hold is

$$\frac{2\tau k_{12}}{\tau_e k_L} \gg 1 \qquad \text{(A.52)}$$

This section reviews the classical theory of Smoluchowski and Debye for the diffusion-controlled encounter frequency, with a view towards a comparison of k_{12} and k_L for dielectric solvent media.

For the purpose of modeling its rate of formation, the definition of the encounter complex given in Sec. A.5 yields two benefits, even if the concentration of that complex (so defined) is negligible. First, because the complex is the <u>initial</u> product of an encounter between solvated ions, the constant (k_{12}) that governs this rate reflects a diffusion process and not any specific chemical attributes of the reactants or the solvent. Thus, provided the average initial separation between ions equals many solvent molecule diameters, a continuum description of the solvent, though provisional, ought to suffice. Second, the probability that an encounter complex will result from the mutual approach of and contact between two solvated ions is unity, and thus the rate of formation of the encounter complex is identical to the frequency of encounters. In contrast, models for the transformation step in Eq. A.40 cannot be phrased in terms of macroscopic parameters because specific short range forces and the discreteness of the solvent come into play.

Smoluchowski's model for the frequency of encounters between uncharged particles in thermal motion (66) was developed to describe the rate of coagulation in colloidal systems. As discussed by Overbeek, the original model does not account for double layer repulsion forces, evolving particle size, and the spectrum of particle sizes. The simplicity of the original model proved a virtue, however, for the omission of refinements pertinent only to the colloidal system encouraged its adaptation to other physical contexts. Not surprisingly, Debye's adaptation of the model to ionic reaction rates in solution by including a general long-range interaction between reactants raises a different set of issues. These issues are identified by the subheadings in the overview of Debye's theory given below.

Boundary Condition at the Reaction Radius: The Smoluchowski-Debye artifice designates one member of one of the reactive species, A^+ (say), as a reference ion, and represents its reactivity by replacing it with a sink that consumes members of the B^- species when the latter encounter the edge of the sink. The diameter α of the sink corresponds to the distance between centers of the reactants when they form an encounter complex, while its charge and diffusivity are those of the reference ion.

In the frame of the sink, the B^- species diffuse and migrate in spherically symmetric fashion with diffusion coefficient D_-. This isotropy on the molecular scale reflects the continuum approximation. To exploit this symmetry, the sink is regarded as stationary and situated at the center of a spherical coordinate system, and its thermal motion is accounted for by replacing the diffusivity of the B^- species by the sum of the diffusivities $2D = D_+ + D_-$.

The frequency of encounters between the reference ion and the B^- ions is given by the net inward flux $-4\pi r^2 \Gamma_b(r,t)$ of the latter across a closed surface coincident with the edge of the sink at $r = \alpha$. The <u>net</u> rate of disappearance of B^- ions is the net flux associated with a single sink multiplied by the concentration $[A^+]$ of sinks:

$$\frac{d}{dt}[B^-] = [A^+] 4\pi\alpha^2 \Gamma_b(\alpha,t) \equiv -k_{12}[A^+][B^-] \qquad (A.53)$$

The rate constant follows as

$$k_{12}(t) = -\frac{4\pi\alpha^2 \Gamma_b(\alpha,t)}{[B^-]} \qquad (A.54)$$

The radial flux density $\Gamma_b(r,t)$ and the local concentration $c_b(r,t)$ of B^- ions are coupled through Fick's first and second laws:

$$\Gamma_b(r,t) = -2D\left(\frac{\partial c_b}{\partial r} + \frac{c_b}{kT}\frac{\partial U}{\partial r}\right) \quad ; \quad \frac{\partial c_b}{\partial t} = \frac{-1}{r^2}\frac{\partial}{\partial r}\left(r^2 \Gamma_b\right) \qquad (A.55a,b)$$

where U is the potential of the average force between ions. Solutions of Eqs. A.55 are subject to the boundary conditions

$$c_b(\alpha,t) = 0 \quad ; \quad U(\alpha,t) = -\infty \qquad (A.56a,b)$$

$$c_b(\infty,t) = [B^-] \quad ; \quad U(\infty,t) = 0 \qquad (A.57a,b)$$

$$c_b(r,0) = [B^-] \quad (r > \alpha) \qquad (A.58)$$

The widely expressed criticism (67,68) of the boundary condition Eq. A.56a stems from the failure on the part of these authors to define an intermediate complex consistent with that condition, and their insistence that the theory apply to the formation of what has been called here a transformed complex (Eq. A.40). They regard the transformed complex as the only reaction product that is present in significant concentration, a situation modeled here by case B of Sec. A.5. In order to represent the reaction with one step, they require a boundary condition that equates the inward flux of B^- at the "reaction radius" $r = \alpha$ to a "reaction flux" that reflects a net rate in the second step in Eq. A.40. The intermediate consisting of a B^- ion at the reaction radius is not identified as a distinct species, and thus $c_b(\alpha,t)$ is nonzero.

With the present definitions (Sec. A.5), $c_b(\alpha,t)$ must be zero because the entity formed by two ions with centers separated by a distance α constitutes an encounter complex which is regarded as distinct. It is the introduction of such a complex that, despite its relatively small concentration, permits application of the Smoluchowski-Debye method with the original boundary condition (Eq. A.56a), while necessitating separation of the reaction into two steps. When case B of Sec. A.5 applies, the two approaches are reconcilable, as they must be since the negligible concentration of the intermediate complex implies that it has no unique representation.

Conditions for Quasistationary Reaction Rate: When $U = 0$, Eqs. A.55 have the solution

$$c_b(r,t) = [B^-]\left\{1 - \frac{\alpha}{r}\,\mathrm{erfc}\left[\frac{r-\alpha}{\sqrt{8Dt}}\right]\right\} \tag{A.59}$$

The rate constant follows from Eqs. A.54, A.55a (with $U = 0$), and A.59

as

$$k_{12}(t) = \frac{8\pi\alpha^2 D}{[B^-]} \left.\frac{\partial c_b}{\partial r}\right|_\alpha = 8\pi\alpha D\left[1 + \frac{\alpha}{\sqrt{2\pi D t}}\right] \tag{A.60}$$

Collins and Kimball (69) note that Fick's second law is applicable only for $t \gg \nu^{-1} = \langle s^2 \rangle/6D$, where ν is the frequency of random "jumps" of the diffusing molecules and $\langle s^2 \rangle$ is the mean square jump length. Thus the singularity in k_{12} at $t = 0$ must be ignored. These authors calculate the initial reaction rate based on random walk diffusion equations, and find that it does not significantly differ from the stationary rate (given by Eq. A.60 with $t \to \infty$) when the ratio $\alpha/\langle s \rangle \simeq 1$. As this ratio increases, so does the ratio $k_{12}(0)/k_{12}(\infty)$, and k_{12} can be regarded as a constant only on time scales long compared with the time

$$\tau_\alpha = \frac{\alpha^2}{2\pi D} \tag{A.61}$$

that characterizes relaxation of the concentration distribution. In particular, τ_α must be short compared with the time characterizing changes in the average concentration $[B^-]$, which from Eqs. A.53 and A.60 is

$$\tau_c = \left(k_{12}[A^+]\right)^{-1} = \left(8\pi\alpha D[A^+]\right)^{-1} \tag{A.62}$$

Thus k_{12} is quasistationary if

$$\tau_\alpha \ll \tau_c \quad \to \quad \alpha \ll d_r \tag{A.63}$$

where $d_r \equiv [A^+]^{-1/3}$ is the mean spacing between reactive ions. Note that this condition is consistent with the original continuum approximation for the solvent.

No solution of the <u>time dependent</u> Eqs. A.55 is available when the interaction energy U is significant. However, the usefullness of the long time solution with U = 0 encourages solution of the <u>steady state</u> equation directly. Thus, with r_b regarded as a constant, Eq. A.55a is readily integrated subject to Eqs. A.57:

$$c_b(r) = \exp(-U/kT)\left[[B^-] + \frac{r^2 r_b(r)}{2D} \int_r^\infty \exp(U/kT)\, \frac{dr}{r^2}\right] \tag{A.64}$$

Finally, with Eqs. A.56 applied, Eqs. A.54 and A.64 yield

$$k_{12} = 8\pi D\alpha_{eff} \quad ; \quad \alpha_{eff} \equiv \left(\int_\alpha^\infty \exp(U/kT)\, \frac{dr}{r^2} \right)^{-1} \tag{A.65}$$

which is Debye's general result. Definition of an effective ion size α_{eff} points up the similarity between Eq. A.65 and Eq. A.60 when the quasistationary condition Eq. A.63 holds, and suggests that the latter be generalized to

$$\alpha_{eff} << d_r \tag{A.66}$$

When the interaction is attractive ($U < 0$), $\alpha_{eff} > \alpha$, and thus while Eq. A.66 is more tentative than Eq. A.63, it is also more restrictive.

<u>Application to Turbulent Flows</u>: When the conservation equations (A.2 to A.4) are applied to turbulent flows, the diffusivities that appear explicitly in those equations must include the eddy contribution. If the recombination rate (R) is still to be modeled the question arises whether Eq. A.65 still applies since a diffusion process is also implicit in the latter. As in the third assumption in Sec. A.3, the answer hinges on whether the smallest eddies, within which molecular effects prevail, are still large enough to contain many reactants (<u>61</u>). Thus the ordering of lengths

$$\alpha_{eff} << d_r << \text{turbulence scale} \tag{A.67}$$

appears necessary.

Nature of the Concentration Gradient: Collins and Kimball (67) questioned the nature of the postulated concentration gradient that helps maintain a flux of reactants towards the sink. If the gradient develops because a reaction has depleted the local concentration of reactants, then the gradient is no longer of interest because the reference ion has already been discharged. These authors proceed to resolve this dilemma by showing that the knowledge that a given ion has not yet reacted at a given time diminishes the probability of a reactive partner being in the immediate neighborhood. The probable distributions are still governed by Fick's laws, and in that sense the postulated gradients are real and must be recognized by treatments of chemical kinetics.

Interaction Energy: Equation A.65 expresses the limiting recombination rate k_{12} in terms of the general interaction energy (U) and the ion size parameter (α). Now U is specified, the rate constant is evaluated, and the result is compared to Langevin's rate. Consistent with Eq. A.67 the concentration of reactants is assumed sufficiently dilute that they are randomly distributed, and thus the time average electric potential in the vicinity of the reference ion is that of a point charge, so that

$$U(r) = \frac{z_i z_j e^2}{4\pi\epsilon_\ell r} \tag{A.68}$$

Debye (70) carries out the integration called for in Eq. A.65 and finds

$$k_{12} = 8\pi\alpha D \frac{U(\alpha)/kT}{\exp(U(\alpha)/kT) - 1} \tag{A.69}$$

Inserting Eq. A.68 and the Einstein relations into Eq. A.69, and forming a ratio with Eq. A.23 yields

$$\frac{k_{12}}{k_L} = \frac{1}{1 - \exp(-b_{ij}/\alpha)} \quad ; \quad \frac{-z_i z_j e^2}{4\pi\varepsilon_\ell kT} \tag{A.70}$$

where b_{ij} is the separation between ions of valence z_i and z_j at which the coulomb and thermal energies are equal. Note that $b_{ij} > 0$ when $z_i z_j < 0$, and that the predicted rate constant exceeds Langevin's rate to a degree that is significant when

$$(b_{ij}/\alpha) \leq 0(1) \tag{A.71}$$

that is, when the coulomb energy of two oppositely charged reactants in contact has a magnitude of the order of or less than the thermal energy.

To appreciate the reason, it should be noted that both Langevin's and Debye's rates account for the coulomb interaction, but while Langevin's evidently represents a point charge solution, Debye models the finite size of the reactants. That Debye's rate is the larger reflects the fact that Brownian motion will ultimately bring together two finite-sized molecules even without the coulomb attraction. However, this additional mechanism for producing an encounter can only be noticeable when the coulomb interaction fails to dominate the thermal energy, as is the case when Eq. A.71 holds.

For a monovalent electrolyte at room temperature, find that

$$\frac{b_{ij}}{\alpha} = \frac{5.6 \times 10^{-8}}{\varepsilon_r \alpha} \tag{A.72}$$

where $\varepsilon_r = \varepsilon_\ell/\varepsilon_o$ is the relative permittivity of the solvent. With α of the order of 10 Å, Eq. A.72 indicates that the finite size is unimportant when ε_r is less than about A.71, and thus $k_{12} \approx k_L$ for dielectric media. For less dilute solutions, the interaction is screened by the Debye-Huckel ionic atmosphere and $k_{12} \leq k_L$. Thus, the necessary condition for chemical equilibrium Eq. A.52 reduces to

$$\tau_{\ell} << \tau \tag{A.73}$$

In Chapters 5 and 6 the characteristic time τ is a liquid transit time based on the liquid velocity at the edge of the diffusion sublayer in a tube and the length of the tube ($\tau \rightarrow \tau_{\delta} = L/v_{\delta}$).

Appendix B

TRAVELING-WAVE PUMPING OF LOW VISCOSITY LIQUIDS

B.1 Introduction

Like the standing-wave interaction of Chapter 6, the technique described below for probing the liquid-insulating solid interface avoids direct liquid-electrode contact by capacitive coupling between excited external electrodes and an internal charge distribution. Again, the electrical frequency (ω) and wavenumber (k) are imposed, but now the applied potential is a traveling wave rather than the superposition of forward and backward waves that comprise the standing wave (Eq. 6.18). However, whereas in the induction sensor the flow is also imposed, and the combined effects of convection and conduction on the field-induced volume charge distribution are sensed electrically, now the motions of the initially quiescent liquid are induced by the applied field. The helical winding remains a convenient way to constrain the potential at the outer surface of the insulating tube, and in the experiment described in Sec. B.2 the induced motion is detected as a pressure difference developed across the ends of the winding. The applied fields needed to induce observable motion are typically of the order of those inadvertently generated by an imposed flow (see Chapter 3), and hence the technique is intended as one for studying natural processes under controlled conditions.

Like the standing-wave interaction, the traveling-wave pump has its origins in a study (71) of a free liquid surface. There, the pumping is accounted for by a model that regards the liquid as having a uniform conductivity and permittivity, and thereby confines the net charge and hence the electromechanical coupling to the free surface. In the presence of thermal gradients in the liquid, which imply gradients in electrical conductivity, an ohmic model (72) still predicts pumping even if a free surface is absent, because the applied field can induce a net charge in the liquid bulk.

However, the ohmic model cannot account for the observed bulk electromechanical coupling in a (presumably) isothermal liquid. In a model (73) for the pumping of relatively viscous liquids, the fundamental species conservation equations predict that a net charge is induced in a thin liquid layer at the interface while the bulk of the liquid remains charge-free. With the thickness of the coupling layer determined by the migration length ($L_m = bE\tau$) based on the excitation period τ, applicability is restricted to relatively viscous liquids by the requirement that L_m be small enough compared with the excitation wavelength to justify a quasi-one-dimensional description of field quantities and the neglect of convection effects on the induced charge. For example, with an absolute room temperature viscosity of $\eta \simeq 0.1$, a typical ion mobility in dioctyl-phthalate is $b \simeq 2 \times 10^{-10}$. With E and τ of the order of 10^6 V/m and 1.0 s respectively, the thickness of the coupling layer ($L_m \simeq 200$ μm) is easily exceeded by the wavelength associated with the wire electrodes used in practice.

In the low viscosity liquids typical of cooling applications the larger ion mobilities (see Table 3.1) imply migration lengths that may be comparable to both the excitation wavelength and the tube diameter. Thus, the electromechanical coupling is distributed throughout the liquid bulk and now neither the quasi-one dimensional model nor the neglect of convection effects is appropriate. The model outlined in Sec. B.3 pictures the net charge in the liquid bulk as being due to ions ejected from the liquid-solid interface under the influence of the normal component of the applied field. The ions may originate in a charge double layer or they may result from charge transfer across the interface. At least as pictured by the model, the pumping interaction hinges on the same physical process that underlies electrodialysis, namely, the passage of ions between the solution and the interface (or even the solid phase). However, while in electrodialysis the passage is detected as a current in an external circuit or by an effect on the liquid conductivity, in the traveling-wave pump the extent of ion injection into the liquid bulk is reflected by the electrical force exerted, and the motion induced, by the tangential component of the applied field.

B.2 Experimental Arrangement and Preliminary Results

Figure B.1 illustrates the pump experiment. A helical winding on a section of insulating tube supports a traveling wave of potential that advances essentially along the tube length. The tube extends beyond both ends of the winding and rises vertically to contain the liquid in the fashion of a manometer. Exciting the winding induces a time-average longitudinal electrical force density in the liquid bulk. The pressure difference developed as a result between the ends of the winding is then determined from liquid displacement in the vertical sections.

Figure B.2 illustrates the pattern of response typical of the extensive data acquired for Freon in Tefzel tubes. Pumping is said to be forward when the average electrical force is in the same direction as that in which the traveling wave advances. Backward pumping corresponds to the force and the phase velocity being oppositely directed. As the phase velocity and traveling wave amplitude are varied, regimes of both forward and backward pumping are observed.

Apparatus for the traveling wave pumping of liquid through a two-foot glass column packed with insulating particles has also been constructed. Preliminary tests with Teflon particles typically 3mm in diameter indicate that pressure differences can be developed which are comparable to those observed for the thirty-foot length of open tube. However, pumping through the column appears to be significant over a much narrower range of liquid conductivities.

There are two questions one would like to have answered by the experiments. First, is the flow the fully developed laminar one assumed

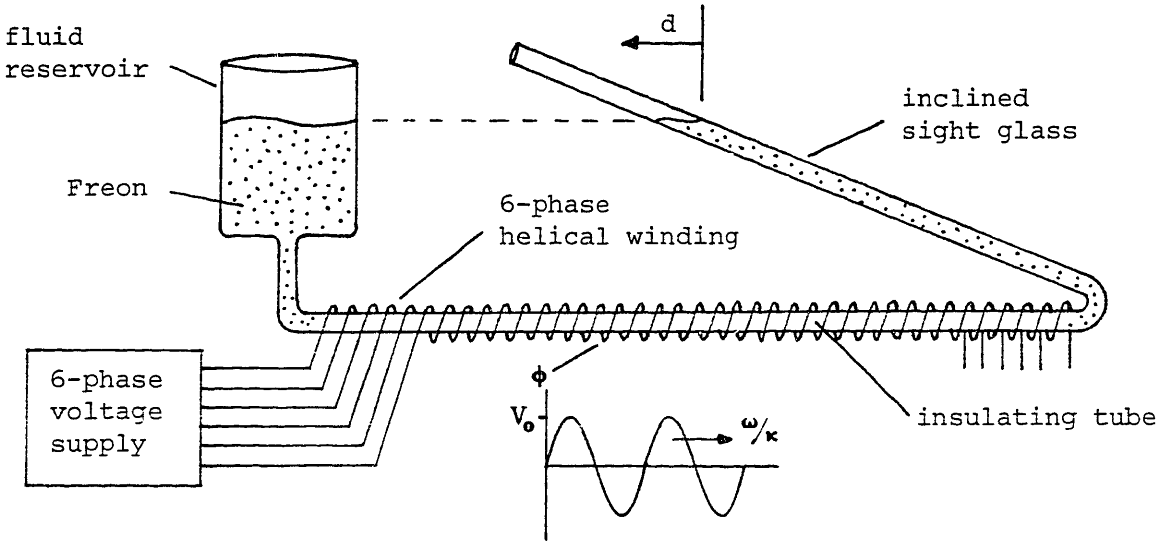

Fig. B.1 Experimental arrangement for traveling-wave pumping.

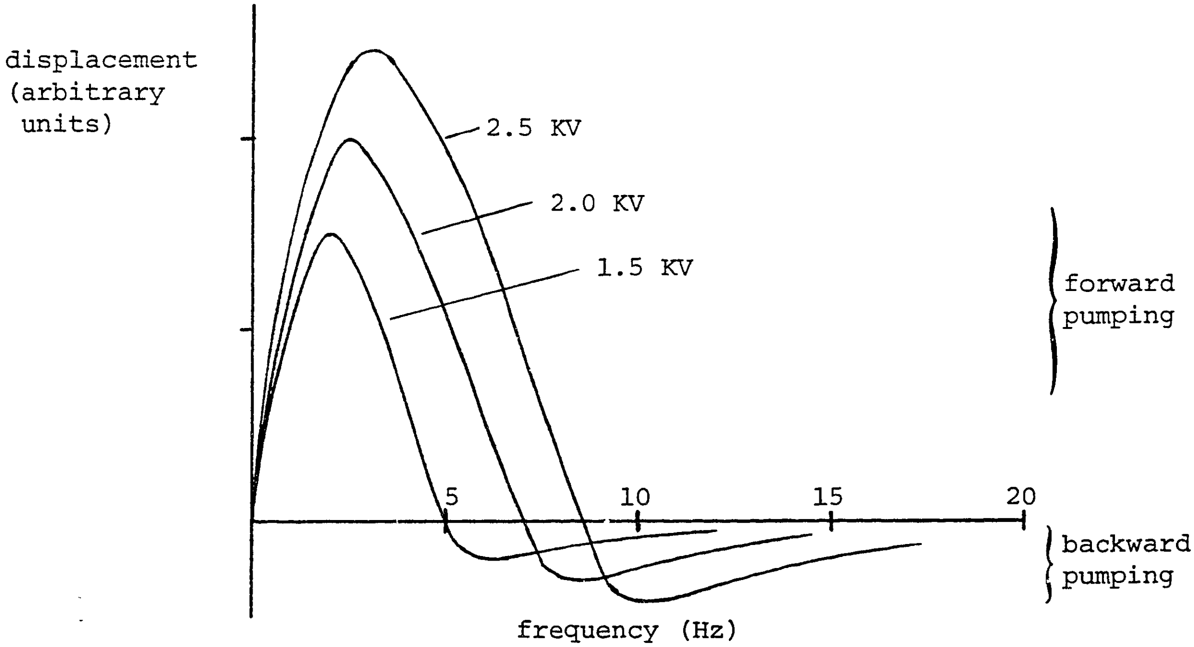

Fig. B.2 Typical dependence of displacement d (Fig. B.1) on traveling-wave amplitude and frequency.

in the model of the next section. Theoretical considerations may indicate whether the laminar flow is likely to be unstable. Alternatively, an experimental approach is possible using a laser Doppler anemometer to reveal the details of the liquid motions. The second question is whether there is any evidence of charge injection. This evidence might take two forms: a threshold field for pumping, and a qualitative change in behavior when the migration length L_m is of the order of the tube radius. An unambiguous threshold proved difficult to observe, partly because the liquid was slow to settle completely after a disturbance. However, a strong indication that charge injection is involved is the correlation between the cross-over points in Fig. B.2 and the excitation periods obtained by setting the migration length $L_m = bkV\tau$ equal to the tube radius. Here, k is the wavenumber $2\pi/\lambda$, where λ is the excitation wavelength.

B.3 Model Outline and Preliminary Numerical Results

The simple model for the pumping presented below is intended to apply when the dominant source of net charge in the liquid bulk is ion injection from the liquid-insulating solid interface. The net charge density is assumed tenuous enough that the electric field in the liquid is essentially that imposed by the applied potential. Thus, the injected ions travel along characteristic lines determined by the imposed field and an initially unknown velocity profile that must be consistent with the average <u>tangential</u> electric force density. To specify the net charge density (and hence the force density) at a given point, the ion trajectory through that point must be traced back to the interface where the <u>normal</u> field component determines the magnitude of the injected charge through a (trial) "injection law." The interface is continually "replenished" as the ions eventually return to the interface where it intercepts a characteristic line.

Because the velocity profile is needed to evaluate the force density which then determines that profile, a trial profile must be specified to initialize the analysis. In what may or may not generally be a convergent procedure, the predicted velocity profile then becomes the new trial profile in the succeeding iteration. A self-consistent result is obtained when the trial and predicted velocity profiles agree.

The penetration of injected ions into the bulk of the low viscosity liquid makes it difficult to develop a model that is "universal" in the sense of being applicable to a general configuration of the liquid container. For its simplicity, and because it represents the tube configuration whenever the tube radius (a) is large compared with the excitation wavelength, a planar half-space of liquid (Fig. B.3) is the context for presenting the model. Four assumptions are made:

[a] The fluid mechanical response is a fully developed laminar flow of low enough Reynolds number that the velocity profile satisfies a creep-flow model. Thus, in the configuration of Fig. B.3 the velocity field takes the form $\vec{v} = v_z(x)\hat{z}$ and a stream function can be defined such that

$$v_z(x) = \frac{d\phi}{dx} \quad ; \quad \phi(x) = \int_0^x v_z dx \quad ; \quad \phi(0) \equiv 0 \qquad (B.1)$$

[b] The volume charge density remains small enough that the applied electric field dominates the space charge field. In this weak injection limit the potential in the liquid half-space satisfies Laplace's equation subject to boundary conditions that specify the potential at the interface and require the potential to vanish far from the interface:

$$\Phi(x,z,t) = V_0\cos(ky)\exp(-kx) \quad ; \quad ky \equiv (\omega t - kz) \qquad (B.2)$$

Without loss of generality, the thickness (w) of the insulating wall is regarded as small compared with the excitation wavelength ($2\pi/k$) so that the potential at the liquid-solid interface is essentially that at the

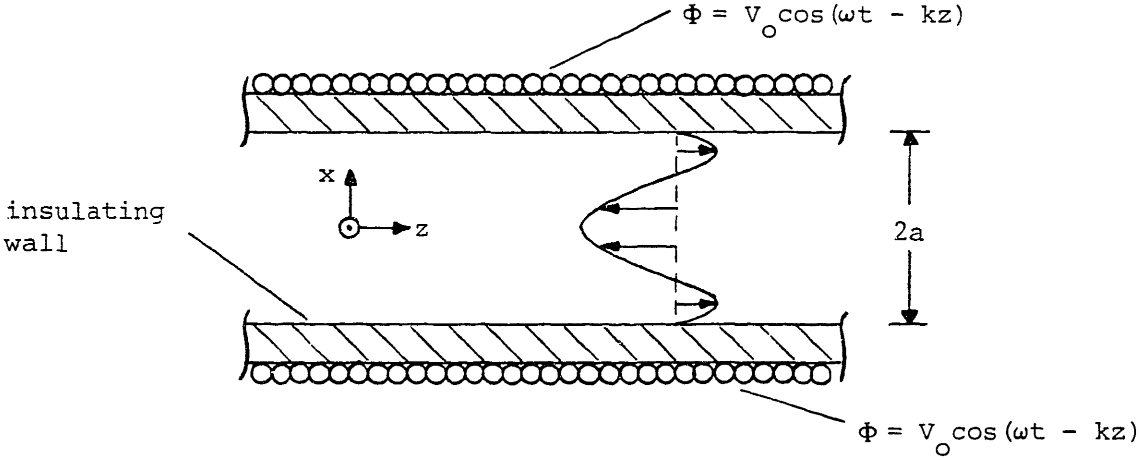

Fig. B.3 Planar model with channel half-width (a) much greater than excitation wavelength (λ).

electrodes. If kw is not small, the amplitude and phase of the potential at the interface relative to that at the electrodes is readily determined from "transfer relations" like those used in Sec. 6.3.4.

[c] Ion diffusion is negligible. This is justified if the diffusion time (λ^2/D_m) vastly exceeds the transit time (λ/bE_0; $E_0 \equiv kV_0$), a condition that is equivalent to requiring the applied potential to vastly exceed the thermal voltage.

[d] The transit time (λ/bE_0) is short compared with the charge relaxation time ($\tau_\ell \equiv \epsilon_\ell/\sigma_\ell$). Thus, injected ions are not neutralized by conduction processes. When recombination is Langevin the chemical relaxation time τ_{cr} is of the order of the charge relaxation time τ_ℓ (see Eq. A.31 with $k_R \rightarrow k_L$ and $\gamma \rightarrow 0$). Thus, the transit time is also exceeded by the time that characterizes ion recombination, and hence the injected charge density retains its initial magnitude over the entire trajectory.

Bernoulli's equation relates the measurable lateral displacement to the pressure gradient induced by the traveling wave of potential:

$$\Delta d = \cot(\theta)\Delta h = \frac{\cot(\theta)}{\rho_m g}\Delta p = \left(\frac{\cot(\theta)L}{\rho_m g}\right)\frac{dp}{dz} \qquad (B.3)$$

Here Δp is the pressure difference between points in the liquid just beyond the ends of the winding (of length L) where the velocity is negligble. Consistent with the fully developed velocity profile (assumption [a]), the final equality in Eq. B.3 implies a uniform pressure gradient along the excited section of the tube. In the planar coordinates appropriate to the developed model of Fig. B.3 the creep-flow limit of the Navier-Stokes equation relates the pressure gradient to the electrical force density:

$$\frac{dp}{dz} = F_z + \eta\frac{d^2v_z}{dx^2} \qquad (B.4)$$

This is to be solved subject to the no-slip condition at the wall and the condition that the shear stress vanish at the plane of symmetry a distance from the interface equal to the tube radius (a):

$$v_z(0) = 0 \quad ; \quad \frac{dv_z}{dx}(a) = 0 \tag{B.5}$$

For the static head measurement, there is no net flow across any plane normal to the z-axis:

$$\int_0^a v_z(x)dx = 0 \tag{B.6}$$

Subject to these conditions, Eq. B.4 is integrated twice to give

$$v_z(x) = \frac{1}{\eta}\left[\int_0^x \int_{x'}^a F_z(\tilde{x})d\tilde{x}\, dx' - \left(ax - x^2/2\right)\frac{dp}{dz}\right] \tag{B.7}$$

and integrated third time to give

$$\frac{dp}{dz} = \frac{3}{a^3}\int_0^a \int_0^x \int_{x'}^a F_z(\tilde{x})d\tilde{x}\, dx'\, dx \tag{B.8}$$

The electric force density is the averaged one

$$F_z(x) = \int_{-\pi}^{+\pi} \rho(x,y)E_z(x,y)d(ky) = 0 \tag{B.9}$$

With assumption [b], field components in the half-space are consistent with the Laplacian potential Eq. B.2

$$E_x = E_o\cos(ky)\exp(-kx) \quad ; \quad E_z = -E_o\sin(ky)\exp(-kx) \tag{B.10a,b}$$

where $E_0 \equiv kV_0$. In view of assumption [c] the inertialess ions are transported only by migration and convection. Thus, their trajectories or characteristic lines are described by

$$\frac{dx}{dt} = \pm bE_x = \pm bE_0\cos(ky)\exp(-kx) \tag{B.11}$$

$$\frac{dy}{dt} = \left[v_p - \frac{dz}{dt}\right] = \left(v_p - v_z(x) \pm bE_0\sin(ky)\exp(-kx)\right] \tag{B.12}$$

where $v_p \equiv \omega/k$ is the phase velocity of the traveling wave and the upper and lower signs correspond to positive and negative ions, respectively. If now dt is eliminated between Eqs. B.11 and B.12 the result

$$\begin{aligned} &dx\left(v_p - v_z(x) \pm bE_0\sin(ky)\exp(-kx)\right] \\ &\qquad + dy\left(\mp bE_0\cos(ky)\exp(-kx)\right] = 0 \end{aligned} \tag{B.13}$$

is a perfect differential because the time dependence is eliminated with the definition of (ky) in Eq. B.2. In what amounts to a determination of vector potentials (in the frame of the traveling wave) for the solenoidal flow and field, Eq. B.13 is integrated to give

$$xv_p - \Phi(x) \mp (bE_0/k)\sin(ky)\exp(-kx) = C_\pm \tag{B.14}$$

where Φ is defined in Eq. B.1 and $C_\pm$ are integration constants. With a view towards application of an injection law, these constants are expressed in terms of the position $(x,y) = (0,y_0^\pm)$ on the interface where the characteristic lines are intercepted:

$$\mp\left[\frac{(kx)v_p - k\Phi(x)}{bE_0}\right] + \sin(ky)\exp(-kx) = \sin(ky_0^\pm) \tag{B.15}$$

In general, of the two solutions of Eq. B.15 for $y_0^\pm$ ($-\pi < y_0^\pm < \pi$) the desired one is that corresponding to the point of entry of the characteristic line. Near the interface where the liquid velocity is negligible, characteristic lines and field lines coincide, and thus positive (negative) charge can be injected only where the normal field E_x is directed into (out of) the liquid bulk. However, in the present case it proves unnecessary to distinguish between the two solutions because the normal field has the same magnitude where a given characteristic line both enters and leaves the liquid bulk. Thus, with the proviso that a charged species can be injected from only one end of a characteristic line, the injected charge densities have the functional form

$$\rho_\pm = f_\pm\left(\left|E_x(0,y_0^\pm)\right| \right) \tag{B.16}$$

where the normal field intensity (Eq. B.10a) evaluated at the point of entry is

$$\left|E_x(0,y_0^\pm)\right| = \left|E_0\cos(ky_0^\pm)\right| = E_0\left(1 - \sin^2(ky_0^\pm)\right)^{1/2} \tag{B.17b}$$

Thus, given assumption [d] and a trial stream function $\psi(x)$, the charge density at (x,y) is the algebraic sum of the individual charge densities $\rho_\pm$ determined by eliminating $E_x(0,y_0^\pm)$ and $\sin(ky_0^\pm)$ between Eqs. B.15, B.16 and B.17.

As might be expected intuitively, there are points (x,y) in the liquid (different for the two species) for which Eq. B.15 has no (real) solutions. For the planar half-space, this implies that the characteristic line through that point does not intercept the injecting wall, and it is expedient to simply set the charge density (and hence the force density) there to zero. However, with a view towards generalizing the model to the more complicated case of a liquid channel bounded by two injecting walls spaced closely enough that the characteristic line through a given point may intercept the more distant wall, it is more instructive to interpret the absence of solutions in terms of critical points and critical characteristic lines. Critical points $(x_c^{\pm}, y_c^{\pm})$ are points of zero force, and hence satisfy

$$(v_z(x_c^{\pm}) - v_p)\hat{z} \pm b\bar{E}(x_c^{\pm}, y_c^{\pm}) = 0 \qquad (B.18)$$

Thus while $y_c^{\pm} = \pi/2$ and $-\pi/2$, $x_c^{\pm}$ is given implicitly by

$$(v_z(x_c^{\pm}) - v_p) \mp bE_0 \sin(ky_c^{\pm})\exp(-x_c^{\pm}) = 0 \qquad (B.19)$$

Critical characteristic lines are those which pass through the critical points. For the planar half-space the critical lines (again, different for the two species) set off regions of the liquid which are not accessible to injected charge. For the liquid channel with two injecting and interacting walls, the critical lines define regions of four types corresponding to combinations of the two possible origins and two possible destinations of charge on the enclosed characteristic lines. This situation is complicated by the fact that the critical points do not lie on the channel plane of symmetry.

With all of the quantities of interest expressed as integrals over space (Eqs. B.7 to B.9), acceptable accuracy can be expected from evaluation of the net charge density on a relatively coarse grid of points. Once the net charge density is determined at each grid point from Eqs. B.15 to B.17, the average longitudinal force density, the pressure gradient and the velocity profile are obtained in succession from Eqs. B.9, B.8 and B.7. The predicted velocity profile generates the new trial stream function through Eq. B.1, and the procedure is repeated until either the trial and predicted profiles are in satisfactory agreement or it becomes clear that the two profiles are not converging.

In a preliminary computer implementation of this procedure, the two profiles did converge. The results indicate that at least for some excitation amplitudes and frequencies, both forward and backward pumping are simultaneously consistent with the model. Because backward pumping is predicted for the initially quiescent liquid, backward pumping appears to be the only accessible final state, provided it is a stable one. There is, however, some suggestion from experimental observation that backward pumping is not always a stable state, and thus forward pumping may result even when it is not directly accessible from the initial state. At excitation frequencies and amplitudes for which forward pumping is actually recorded, an initial backward displacement is sometimes observed before the forward pumping sets in, particularly when the excitation is applied abruptly.

NOTATION

(MKS units are used unless otherwise noted)

a	tube inside radius (m)
A	cross sectional area of dead-end channels (Sec. 4.2.3)
A	(Sec. 6.3.4)
A^+	positive ionic species (Sec. A.5)
b	average ion mobility $(b_+ + b_-)/2$
$b_\pm$	positive and negative ion mobilities $(m^2/V\text{-}s)$
b_{ij}	effective range of coulombic interaction (Sec. A.6)
B	(Sec. 6.3.4)
B_n	(Eq. 3.17)
B^-	negative ionic species (Sec. A.5)
c_b	local concentration of B^- (m^{-3}) (Sec. A.6)
c_i	concentration of inert ions (Sec. A.6)
c_r	concentration of reactive ions (Sec. A.6)
$c_\pm$	molar concentrations of ionic species $(moles/m^3)$
C	neutral solute species (Sec. A.5)
C_n	(Eq. 3.20)
C_E	encounter complex (Sec. A.5)
C_T	transformed complex (Sec. A.5)
d	development length (m)
d_r	mean separation of reactive ions (m) (Sec. A.6)
D	$\equiv \partial/\partial x$

D_e	local effective diffusivity (m^2/s)
D_m	average molecular diffusivity (m^2/s)
D_n	diffusivity of neutral species (m^2/s)
D_t	eddy diffusivity (m^2/s)
$D_\pm$	diffusivity of ionic species (m^2/s)
$\hat{D}_r$	complex amplitude of perturbation radial electric displacment
$\hat{D}_x$	$-\hat{D}_r$
e	electronic charge, 1.6×10^{-19} (C)
e_n	Fourier coefficients (Eq. 3.30)
E	expansion efficiency (Eq. 4.9)
$\bar{E}$	electric field (V/m)
E_w	electric field within expansion wall (Sec. 4.2.3)
E_r^i	radial electric field in liquid at tube wall (V/m)
E_r^o	radial electric field in gas at tube wall (V/m)
E_r^w	radial electric field inside tube wall (V/m)
E_z	axial component of electric field (V/m)
F	Faraday's constant, 96,500 (C/mole)
F_n	(Eqs. 2.2 and 3.27)
F_z	time-averaged axial electric force density (Sec. B.3)
G	generation rate ($C/s\text{-}m^3$) (Sec. A.2)
G, G_i	conductance of dead-end channel (Sec. 4.2.3)
i_2, i_3	charging currents (A)
I	total axial current (A)
I_i	current from the ith sleeve segment to ground (A)
I_ℓ	axial current carried by liquid bulk (A)

I_n	modified Bessel function of the first kind and nth order
I_s	convection or streaming current (A)
I_w	axial current carried by the tube wall (A)
I_N	leakage current carried by dead-end channels (A)
j	$\sqrt{-1}$
$\bar{J}$	current density (A/m^2)
$\bar{J}_\pm$	current densities carried by positive and negative ions (A/m^2)
J_w	exchange current density at liquid-solid interface (A/m^2)
J_r^w	radial current density inside wall (A/m^2)
k	Boltzman's constant, 1.38×10^{-23} (J/K°)
k	wave number ($2\pi/\lambda$)
k_m	mass transfer coefficient (m/s)
k_n	wave number ($\equiv n\pi/L$)
K_n	modified Bessel function of the second kind and nth order
k_D	effective dissociation constant (Sec. A.2)
k_L	Langevin's recombination coefficient (m^3/s)
k_R	effective recombination constant (m^3/s) (Sec. A.2)
k_{12}	recombination rate constant (m^3/s)
k_{21}	dissociation rate constant (m^3/s)
k_{23}	rate constant (s^{-1})
k_{32}	rate constant (s^{-1} ; i=1) or (m^3/s ; i=2)
K	equilibrium constant ($K = k_D/k_R$)
K_1	equilibrium constant ($K_1 = k_{12}/k_{21}$)
K_2	equilibrium constant ($K_2 = k_{23}/k_{32}$)
K^+	coefficient (m/s)

K^-	coefficient (m/s)
ℓ	length of a sleeve segment (Chapter 5)
ℓ	length of one wire electrode (Chapter 6)
ℓ	characteristic length (Sec. A.4)
L	tube length (m)
L	axial length of helical winding (m)
L_e	linear expansion dimension (m)
n	density of neutral species (m^{-3}) (Sec. A.2)
N	number of dead-end channels (Sec. 4.2.3)
p	liquid pressure ($Kg/m\text{-}s^2$) (Sec. B.3)
p_i	liquid pressure in expansion inlet channel ($Kg/m\text{-}s^2$)
p_o	liquid pressure in expansion outlet channel ($Kg/m\text{-}s^2$)
P	power (W)
$P_\pm$	coefficients (Sec. 6.3.4)
Q	volume flow rate (m^3/s)
Q_{dl}	total charge in diffuse part of double layer (C)
Q_e	total charge in insulating expansion (C)
Q_t	total charge in insulating tube (C)
r	radial coordinate
R	radius of external conducting cylinder (m)
R	resistance (Fig. 6.2)
R	recombination rate ($C/s\text{-}m^3$) (Sec. A.2)
$Re(Z)$	real part of the complex argument Z
R_e	electric Reynolds number ($\equiv \epsilon U/\sigma L$)
R_y	hydrodynamic Reynolds number ($\equiv 2aU/\nu$)

s	total solute concentration (m^{-3}) (Sec. A.4)
S	surface area (m^2)
S_c	Schmidt number ($\equiv \nu/D_m$)
S_h	Sherwood number ($\equiv k_m L_e/D_m$)
T	absolute temperature (K°)
$T_\pm$	coefficients (Sec. 6.3.4)
U	mean liquid velocity (m/s)
U	potential of the average force (Sec. A.6)
v_p	phase velocity (m/s)
v_x	local time-averaged velocity (m/s)
v_z	local time-averaged velocity (m/s)
v_T	thermal voltage ($kT/e \simeq 0.027$ V)
v_δ	liquid velocity at edge of diffusion sublayer (m/s)
V	volume (m^3)
V_o	standing wave amplitude (V)
w	thickness of the insulating wall of a tube or expansion (m)
x	coordinate measuring distance from interface into liquid
z	axial coordinate
z_i	unsigned ionic valence (Sec. 2.3.3)
z_i, z_j	signed ionic valence (Sec. A.6)
α	(Sec. 5.3)
α	ion size parameter (Sec. A.6)
α_{eff}	effective ion size parameter (Sec. A.6)
β	(Sec. 5.3)
ϵ_ℓ	liquid permittivity (F/m)

ϵ_o	permittivity of free space (F/m)
ϵ_w	permittivity of tube wall (F/m)
σ_e	effective conductivity ($\equiv \sigma_\ell + (2/a)\sigma_s$)
σ_ℓ	local liquid conductivity (S/m)
σ_o	liquid bulk conductivity where $\rho = 0$ (S/m)
σ_s	surface conductivity (S)
σ_w	conductivity of tube wall (S/m)
$\bar{\sigma}(z,t)$	surface charge density averaged over tube circumference (C/m^2)
$\bar{\bar{\sigma}}(t)$	surface charge density averaged over entire tube (C/m^2)
$\bar{\sigma}_\pm$	surface charge densities (C/m^2)
Σ	conductivity (Sec. 6.3.3)
γ	conductivity gradient (Sec. 6.3.3)
γ	degree of dissociation in equilibrium (Appendix A)
Γ_b	radial flux density of B$^-$ ions (m^{-2}s^{-1}) (Appendix A)
Γ_n	flux density of neutral species (m^{-2}s^{-1}) (Appendix A)
$\Gamma_r^\pm$	radial flux density of ionic species (m^{-2}s^{-1})
Φ	electric potential (V)
Φ_n	Fourier coefficients (V)
$\hat{\Phi}$	complex amplitude of perturbation potential (V)
τ	time characterizing evolution of surface charge in expansion (s)
τ	characteristic time (Appendix A)
τ	temporal period of traveling-wave excitation (Appendix B)
τ_1	time characterizing charging transient in insulating tube (Secs. 2.1, 3.2, 5.3)

τ_1	time characterizing evolution of surface charge in expansion (Sec. 4.2.3)
τ_a	relaxation time of the ion distribution (Appendix A)
τ_c	relaxation time of the average ion concentration (Appendix A)
τ_{cr}	chemical relaxation time (Appendix A)
τ_d	diffusion time for neutral species (Appendix A)
τ_D	diffusion time for ionic species (Appendix A)
τ_{ex}	duration of an experiment
τ_ℓ	charge relaxation time in liquid ($\equiv \epsilon_\ell/\sigma_\ell$)
τ_m	migration time (Appendix A)
τ_n	time characterizing the nth Fourier mode (s)
τ_r	liquid residence time in expansion ($\equiv V/Q$)
τ_w	shear stress at interface ($Kg/m\text{-}s^2$)
τ_w	charge relaxation time in wall (ϵ_w/σ_w)
τ_δ	transit time (L/v_δ)
$\rho(r,z)$	local volume charge density (C/m^3)
$\rho(x,z)$	volume charge density in diffusion sublayer in tube (C/m^3)
$\rho(x,t)$	volume charge density in diffusion sublayer in expansion (C/m^3)
$\bar{\rho}(z,t)$	volume charge density averaged over tube cross section (C/m^3)
$\bar{\rho}(t)$	volume charge density in turbulent core of expansion (C/m^3)
$\bar{\rho}_i(t)$	volume charge density at expansion inlet (C/m^3)
ρ_m	mass density (Kg/m^3)
ρ_o	$= \sigma_o/2eb$ (Appendix A)
ρ_w	volume charge density at liquid-solid interface ($\equiv \rho(a,z)$)
$\rho_\pm$	$= e[A^+]$, $e[B^-]$ (C/m^3) (Appendix A)

λ	effective line charge density (C/m)
λ	wavelength of standing- or traveling-wave excitation ($2\pi/k$)
λ_m	molecular Debye length (m)
λ_n	Fourier coefficients (C/m)
λ_t	turbulent Debye length (m) ($\equiv \sqrt{\varepsilon_\ell D_t/\sigma_\ell}$)
δ	diffusion sublayer thickness (m)
Δ	viscous sublayer thickness (m)
η	absolute viscosity (Kg/m-s)
ν	kinematic viscosity (m^2/s)
$\bar{\upsilon}$	mean axial ion velocity (m/s)
υ_o	response in volts (Chapter 6)
ω	angular frequency (s^{-1})
ζ	zeta potential (V)

REFERENCES

1. Tamura, R. et al. "Static Electrification by Forced Oil Flow in Large Power Transformers," IEEE Transactions, PAS-99, 335 (1980).

2. Oommen, T.V. and E.M. Petrie. "Electrostatic Charging Tendency of Transformer Oils," Paper 84 WM 164-0 of IEEE PES Winter Meeting, Texas, 1984.

3. Klinkenberg, A. and J.L. Van der Minne. Electrostatics in the Petroleum Industry. Amsterdam: Elsevier, 1958.

4. Klinkenberg, A. "Theoretical Aspects and Practical Implications of Static Electricity in the Petroleum Industry," in J.J. McKetta (ed.). Advances in Petroleum Chemistry and Refining. New York: John Wiley & Sons, 1964, vol. 8, chapt. 2.

5. Leonard, J.T. "Generation of Electrostatic Charge in Fuel Handling Systems: A Literature Survey," NRL Report 8484, September 1981.

6. Denbow, N. and A.W. Bright. "The Design and Performance of Novel On-Line Electrostatic Charge-Density Monitors, Injectors, and Neutralisers for Use in Fuel Systems," in Lowell, J. (ed.). Electrostatics, 1979. London: The Institute of Physics, 1979, pp. 171-179.

7. Ginsburgh, I. "The Static Charge Reducer," J. Colloid Interface Sci. 32, 424 (1970).

8. Klinkenberg, A. and B.V. Poulston. "Antistatic Additives in the Petroleum Industry," J. Inst. Petrol., 44, 379 (1958).

9. Leonard, J.T. and H.F. Bogardus. "Pro-Static Agents in Jet Fuels," NRL Report 8021, August 1976.

10. Carruthers, J.A. and K.J. Marsh. "Charge Relaxation in Hydrocarbon Liquids Flowing Through Conducting and Non-Conducting Pipes," J. Inst. Petroleum 48, 169 (1962).

11. Abedian, B. "Electrostatic Charge Relaxation in Tank Filling Operations," J. Electrostatics, 14, 35 (1983).

12. Asano, K. "Electrostatic Potential and Field in a Cylindrical Tank Containing Charged Liquid," Proc. IEE, 124, 1277 (1977).

13. Carruthers, J.A. and K.J. Marsh. "The Estimate of Electrostatic Potentials, Fields, and Energies in a Rectangular Metal Tank Containing Charged Fuel," J. Inst. Petroleum 48, 180 (1962).

14. Melcher, J.R. Continuum Electromechanics. Cambridge: The M.I.T. Press, 1981.

15. Boumans, A.A. "Streaming Currents in Turbulent Flows and Metal Capillaries. III. Experiment (1). Aim and Procedure," Physica, 23, 1038 (1957).

16. Overbeek, J.Th.G. in H.R. Kruyt (ed.). Colloid Science, Vol. 1. Amsterdam: Elsevier, 1952, Chapters 4 and 5.

17. Hunter, R.J. Zeta Potential in Colloid Science. London: Academic Press, 1981.

18. Probstein, R.F., A.A. Sonin, and E. Gur-Arie. "A Turbulent Flow Theory of Electrodialysis," Desalination, 11, 165 (1972).

19. Fischer, F.E., A. Glassanos, and N.G. Hingorani. "HVDC Link to Test Compact Terminals," Electrical World, February 1, 1977, p. 40.

20. Varga, I.K. "Voltage Generation Through Flow of Liquid in Dielectric Tubes," J. Phys. D: Appl. Phys. 14, 1395 (1981).

21. Parsons, R. "The Electrical Double Layer, Electrode Reactions and Static," in Davies, D.K. (ed.). Static Electrification, 1971. London: The Institute of Physics, 1971, pp 124-137.

22. Abedian, B. and A.A. Sonin. "Theory for Electric Charging in Turbulent Pipe Flow," J. Fluid Mech. 120, 199 (1981).

23. Pribylov, V.N. and L.T. Chernyi. "Electrization of Dielectric Liquids Flowing in Tubes," Fluid Dynamics 14, 844 (1979).

24. Walmsley, H.L. and G. Woodford. "The Generation of Electric Currents by the Laminar Flow of Dielectric Liquids," J. Phys. D: Appl. Phys. 14, 1761 (1981).

25. Walmsley, H.L. "The Generation of Electric Currents by the Turbulent Flow of Dielectric Liquids: I. Long Pipes," J. Phys. D: Appl. Phys. 15, 1907 (1982).

26. Walmsley, H.L. "The Generation of Electric Currents by the Turbulent Flow of Dielectric Liquids: II. Pipes of Finite Length," J. Phys. D: Appl. Phys. 16, 553 (1983).

27. Abedian, B. "Electric Charging of Low Conductivity Liquids in Turbulent Flows Through Pipes," Ph.D. Thesis, MIT, Cambridge, Mass., 1980.

28. Taylor, D.M. "Outlet Effects in the Measurement of Streaming Currents," J. Phys. D: Appl. Phys. 7, 394 (1974).

29. Keller, H.N. and H.E. Hoelscher. "Development of Static Charges in a Nonconducting System," Ind. Eng. Chem. 49, 1433 (1957).

30. Rutgers, A.J., M. De Smet, and W. Rigole. "Streaming Currents with Nonaqueous Solutions," J. Colloid Sci. 14, 330 (1959).

31. Shafer, M.R. et al. "Electric Currents and Potentials Resulting From the Flow of Charged Liquid Hydrocarbons Through Short Pipes," J. Research NBS 69C, 307 (1965).

32. Gibson, N. "Static in Fluids," in Davies, D.K. (ed.). Static Electrification, 1971. London: The Institute of Physics, 1971, pp 71-83.

33. Gibbings, J.C. and G.S. Saluja. "Electrostatic Streaming Current and Potential in a Liquid Flowing Through Insulating Pipes," Int. Meeting on Electrostatic Charging, Frankfurt, Germany, March 29, 1973.

34. Von Engel, A. Ionized Gases, 2nd ed. London: Oxford University Press, 1965, p. 249.

35. Gibbings, J.C. and E.T. Hignett. "Dimensional Analysis of Electrostatic Streaming Current," Electrochimica Acta 11, 815 (1966).

36. Gibbings, J.C., G.S. Saluja and A.M. Mackey. "Electrostatic Charging Current in Stationary Liquids," in Davies, D.K. (ed.). Static Electrification, 1971. London: The Institute of Physics, 1971, pp. 93-108.

37. Mason, P.I. and W.D. Rees. "Hazards from Plastic Pipes Carrying Insulating Liquids," J. Electrostatics 10, 137 (1981).

38. Gasworth, S.M., J.R. Melcher, and M. Zahn. "Flow-Induced Charge Accumulation and Field Generation in Thin Insulating Tubes," Conference on Interfacial Phenomena in Practical Insulating Systems, National Bureau of Standards, Gaithersburg, Maryland, September 19-20, 1983.

39. Tefzel Fluoropolymer, Design Handbook. E.I. du Pont de Nemours & Co., Inc., Wilmington, Delaware, 1973.

40. Kirk-Othmer Encyclopedia of Chemical Technology. 3rd ed., New York: John Wiley & Sons, 1980, vol. 11, pp. 35-41.

41. Freon Solvent Data. Bulletin No. FST-1, E.I. du Pont de Nemours & Co., Inc., Wilmington, Delaware, 1980.

42. "Ethyl" Distillate Conductivity Additive 48. Ethyl Corporation., Houston, Texas.

43. Gemant, A. Ions in Hydrocarbons. New York: John Wiley & Sons, 1962.

44. Devins, J.C. and S.J. Rzad. Private communication.

45. Calderbank, P.H. "Mass Transfer," in V.W. Uhl and J.B. Gray (eds.). Mixing. New York: Academic Press, 1967, vol. II.

46. Bird, R.B., W.E. Stewart, and E.N. Lightfoot. Transport Phenomena. New York: John Wiley & Sons, 1960.

47. Uhl, V.W. "Mechanically Aided Heat Transfer," in V.W. Uhl and J.B. Gray (eds.). Mixing. New York: Academic Press, 1966, vol. I.

48. White, F.M. Fluid Mechanics. New York: McGraw-Hill, 1979.

49. Rohsenow, W.M. and H.Y. Choi. Heat, Mass, and Momentum Transfer. Englewood Cliffs, New Jersey: Prentice-Hall, 1961.

50. Koopal, L.K. and J. Lyklema. "Characterization of Polymers in the Adsorbed State by Double Layer Measurements. The Silver-Iodide + Poly(vinyl Alcohol) System," Faraday Discussions 59, 230 (1975).

51. Kavanagh, B.V., A.M. Posner and J.P. Quirk. "Effect of Polymer Adsorption on the Properties of the Electrical Double Layer," Faraday Discussions 59, 242 (1975).

52. Deslouis, C., I. Epelboin, B. Tribollet and L. Viet. "Electrochemical Methods in the Study of the Hydrodynamic Drag Reduction by High Polymer Additives," Electrochimica Acta 20, 909 (1975).

53. Mehl, W. and J.M. Hale. "Insulator Electrode Reactions," in P. Delahay and C.W. Tobias (eds.). Advances in Electrochemistry and Electrochemical Engineering. Vol. 6. New York: Interscience, 1967, p. 399.

54. Mehl, W. and F. Lohmann. "Exchange Currents for Redox Reactions at Organic and Inorganic Insulator Electrodes," Electrochimica Acta 13, 1459 (1968).

55. Boguslavsky, L.I. "Insulator/Electrolyte Interface," in J.O'M. Bockris, B.E. Conway, and E. Yeager (eds.). Comprehensive Treatise of Electrochemistry. Vol. 1. New York: Plenum Press, 1980, Chap. 7.

56. Frank, H.S. and P.T. Thompson. "A Point of View on Ion Clouds," in W.J. Hamer (ed.), The Structure of Electrolytic Solutions. New York: John Wiley & Sons, 1959, pp. 113-134.

57. Melcher, J.R. "Charge Relaxation on a Moving Liquid Interface," Phys. Fluids 10, 325 (1967).

58. Churchill, R.V. Complex Variables and Applications, 2nd ed., New York: McGraw-Hill, 1960.

59. Gasworth, S.M., J.R. Melcher, and M. Zahn. "Induction Sensing of Electrokinetic Streaming Current," Conference on Interfacial Phenomena in Practical Insulating Systems, National Bureau of Standards, Gaithersburg, Maryland, September 19-20, 1983.

60. Eigen, M. and L. De Maeyer. "Relaxation Methods," in A. Weissberger (ed.), Technique of Organic Chemistry, 2nd ed. New York: Wiley, 1963, Part II, Chapt. 18.

61. Levich, V.G. Physicochemical Hydrodynamics. Englewood Cliffs, N.J.: Prentice-Hall, 1962, Sec. 41.

62. Cobine, J.D. Gaseous Conductors. New York: Dover, 1958, Sec. 4.9.

63. Livingston, R. "Evaluation and Interpretation of Rate Data," in A. Weissberger (ed.), Technique of Organic Chemistry, 2nd ed., New York: Wiley, 1963, Part I.

64. Hirschfelder, J.O. "Pseudostationary State Approximation in Chemical Kinetics," J. Chem. Phys. 26, 271 (1957).

65. Eigen, M., W. Kruse, G. Maass, L. De Maeyer. "Rate Constants of Protolytic Reactions in Aqueous Solution," Progr. Reaction Kinetics 2, 285 (1964).

66. Overbeek, J.Th.G. "Kinetics of Flocculation," in H.R. Kruyt (ed.), Colloid Science, vol. I, Amsterdam: Elsevier, 1952, Chapt. VII.

67. Collins, F.C. and G.E. Kimball. "Diffusion-Controlled Reaction Rates," J. Colloid Sci. 4, 425 (1949).

68. Schurr, J.M. "The Role of Diffusion in Bimolecular Solution Kinetics," Biophys. J. 10, 700 (1970).

69. Collins, F.C. and G.E. Kimball. "Diffusion-Controlled Reactions in Liquid Solutions," Ind. Eng. Chem. 41, 2551 (1949).

70. Debye, P. "Reaction Rates in Ionic Solutions," Trans. Electrochem. Soc. 82, 265 (1942).

71. Melcher, J.R. "Traveling-Wave Induced Electroconvection," Phys. Fluids 9, 1548 (1966).

72. Melcher, J.R. and M.S. Firebaugh "Traveling-Wave Bulk Electroconvection Induced across a Temperature Gradient," Phys. Fluids 10, 1178 (1967).

73. Ehrlich, R.M. and J.R. Melcher. "Bipolar Model for Traveling-Wave Induced Nonequilibrium Double-Layer Streaming in Insulating Liquids," Phys. Fluids 25, 1785 (1982).